The Dissertation Committee for Junmin Wang Certifies that this is the approved version of the following dissertation:

Coordinated and Reconfigurable Vehicle Dynamics Control

Committee:

Raul G. Longoria, Supervisor

Joseph J. Beaman, Jr.

Robert H. Bishop

Benito Fernández-Rodriguez

S. V. Sreenivasan

Coordinated and Reconfigurable Vehicle Dynamics Control

by

Junmin Wang, B.E.A.E.; M.S.P.M.E.; M.S.M.E.; M.S.E.E.

Dissertation

Presented to the Faculty of the Graduate School of

The University of Texas at Austin

in Partial Fulfillment

of the Requirements

for the Degree of

Doctor of Philosophy

The University of Texas at Austin

May 2007

Dedication

To my parents, my wife, Junyan, and my entire family.

Acknowledgements

First and foremost, I thank my advisor, Professor Raul Longoria, for offering continuous guidance and support in academic and many other aspects throughout my Ph.D. program and dissertation process.

I also express my sincere appreciations to all other members of my doctoral committee for their valuable suggestions, comments, helps, and time on this research. I thank Professor Benito Fernández for insight gained into nonlinear control theory from his class. I express my appreciation to Professor Joseph Beaman for the valuable suggestions on system evaluation methodologies employed in this dissertation. My thanks also go to Professor Robert Bishop for beneficial conversations on aircraft control allocation methods, to Professor S. V. Sreenivasan for suggestions on computational efforts regarding real-time applications.

In addition, I also thank Professor Maruthi Akella for insight into adaptive control theory as learned from his class at UT.

Ms. Cindy Raman and Ms. Ruth Schwab in the Department of Mechanical Engineering are especially appreciated for their help and conveniences provided to me over my Ph.D. program at UT.

Finally, I am very grateful for my wife, Junyan, and my entire family. Their sustained love and support made this dissertation possible.

Coordinated and Reconfigurable Vehicle Dynamics Control

Publication No._____

Junmin Wang, Ph.D.

The University of Texas at Austin, 2007

Supervisor: Raul G. Longoria

This dissertation describes a coordinated and reconfigurable vehicle dynamics control system. With the continuous development of vehicle actuation/sensing technologies, coordinating all the available actuation resources to improve system performance and expand system operational envelope has become an active research topic that has received significant attention from both academia and industry. Given the complex nature of tire forces that are relied upon for inducing generalized forces for vehicle motion control, the main challenge is how to coordinate all the tire forces in a unified and optimal manner to achieve the overall control objectives even under adverse conditions.

In this dissertation, a hierarchically-coordinated and reconfigurable vehicle dynamics control system is proposed. A higher-level robust nonlinear controller is designed to produce the generalized forces/moment for controlling vehicle planar motions. An innovative control allocation scheme is designed to distribute the generalized forces/moment to slip and slip angle of each tire with the considerations of vehicle dynamics and environmental variations. Individual tire slip and slip angles are

selected as the control variables to resolve the inherent tire force nonlinear constraints which otherwise may make the system more complex and computationally expensive. A real-time adaptable, computationally efficient accelerated fixed-point method with improved convergence rate when actuation saturates is proposed to solve the amplitude and rate constrained quadratic programming (QP) control allocation problem. To track the desired allocated slip and slip angle of each tire and therefore the required tire longitudinal and lateral forces to fulfill the control objectives, a combined tire slip and slip angle tracking control system is developed to manipulate the driving/braking/steering actuation of each wheel independent to vehicle body states. The overall system is evaluated on a commercial full-vehicle model provided by CarSim® under various adverse driving conditions including scenarios where vehicle actuator failures occur. Compared with those of existing vehicle control systems, significantly expanded system operational envelop and greatly reduced driver efforts were observed.

Table of Contents

List of Tables

List of Figures

Chapter 1: Introduction

Control of nonlinear systems with redundant and constrained actuation is a relatively new research area. Here the system actuation redundancy means the number of actuators is greater then the number of system controlled outputs. Current nonlinear control design methods cannot be directly applied for these kinds of systems due to their often required "square" property. However, many engineering systems, such as ground vehicles, aircraft, marine vessels, and robotic systems, are redundantly actuated. In order to avoid conflicts, improve safety and reliability as well as expand the system operational envelope, those redundant actuators need to be utilized in an optimal and coordinated manner subject to their constraints. A ground vehicle dynamics control system is a typical nonlinear system with redundant and constrained actuation.

This dissertation aims at developing a systematic coordinated and reconfigurable vehicle dynamics control system to expand the system operational envelope. In this chapter, the background and motivations are presented, followed by the research goals and contributions. An outline of the dissertation is given at the end of this chapter.

1.1 BACKGROUND AND MOTIVATIONS

Over the past 20 years, the goal of vehicle dynamics control (VDC) or vehicle stability control (VSC) has been focused on improving vehicle handling, maneuverability, and stability. It is reported that more than 10,000 fatal crashes could be prevented by vehicle stability control systems annually in the US [ESP-NHTSA]. Under adverse driving conditions, the average driver may exhibit panic reactions and may not generate appropriately coordinated steering/braking/throttle commands to control the vehicle in a time effective manner. In addition, as more actuation become available (e.g., independent four-wheel steering/braking and four wheel driving), it is difficult to imagine

that a human driver would be able to appropriately utilize these actions without significant assistance. The VDC was introduced to anticipate and correct problems before they occur or are even noticed by the driver. Reacting after the vehicle becomes unstable is unreliable.

The VDC should help to achieve predictable and transparent responses to greatly enhance vehicle active safety and maneuverability. With the continuous advancement of vehicle actuation and sensing technologies (such as independent four-wheel braking/steering/driving and GPS/IMU), vehicle dynamics control approaches are also evolving correspondingly. Conventional vehicles' yaw / lateral motions are controlled by hand-steering wheel, and longitudinal motion is controlled by accelerator/brake pedals. The state-of-the-art vehicles are equipped with many x-by-wire sub-systems whose control authorities overlap among the controlled variables. This greatly increases the number of degrees of freedom in the systems and makes them essentially redundantly actuated. It is expected that coordinating all the available actuation resources could provide great potentials in improving system responses and expanding its operational envelope even for adverse driving conditions and/or actuator failure/degradation scenarios. This new generation of VDC is generally referred to as *coordinated vehicle dynamics control* (CVDC) and has recently received significant research attention from both industry and academia. Given the complex nature of tire forces that are relied upon for inducing generalized forces/moments for vehicle motion control, the main challenge is how to coordinate all the tire forces in a unified and optimal manner to achieve the overall control objectives.

Control allocation (CA) techniques in conjunction with nonlinear control design methods can provide a rigorous approach for dealing with nonlinear systems with redundant and constrained actuation, as expected in CVDC. Applications of this kind of

control strategies can be found in aircrafts systems and marine vessels. Recently, the control allocation has become more pertinent as the development of the VDC propagates and is employed in the CVDC in this dissertation.

1.2 RESEARCH GOALS

The goal of this research is to develop a coordinated and reconfigurable control system to utilize all the available actuation resources, namely tire forces, to improve performance of vehicle control system. Coordinated control directs all the sub-systems/resources toward the same overall control objectives, while reconfigurable control ensures system control objectives are best achieved even when some actuators/sub-systems fail. It is expected that the coordination among actuation can expand the system operational envelope and alleviate driver effort even under adverse driving conditions, which implicitly will improve vehicle active safety.

Here, the system operational envelope is not explicitly defined but it is implied through performance comparisons against different existing vehicle control systems responding to various vehicle benchmarking test maneuvers.

While the focus of this research is on control design, system states including vehicle motions and tire-road friction coefficient are assumed available through sensors and/or estimators.

1.3 MAIN CONTRIBUTIONS OF THE RESEARCH

This dissertation presents a coordinated and reconfigurable control system for nonlinear redundantly-actuated constrained ground vehicle systems. The contributions of this research are:

1) Developed a coordinated and reconfigurable vehicle dynamics control system to utilize redundant actuation resources in a unified manner to significantly

expand system operational envelope and reduce driver's effort under adverse driving conditions.

2) Designed an accelerated fixed-point control allocation algorithm with improved convergence speed when actuation saturations occur.
3) Proposed a novel control allocation scheme specifically for ground vehicle systems. Different from the existing control allocation used for VDC where the generalized control efforts are allocated to tire forces, the generalized control efforts are allocated to tire slip and slip angle, which made the system physically-realistic and simplified the optimization problem.
4) Combined tire slip and slip angle tracking control system is developed. The system manipulates the driving/braking/steering actuation of each wheel to track the desired slip and slip angle independent of vehicle states to simplify control tasks and enable coordinated control.
5) Introduced an integral action into the vehicle yaw motion control to reduce the vehicle heading residual caused by yaw rate tracking error.

1.4 GUIDE TO THIS DISSERTATION

The content of this dissertation is organized as follows: Chapter 2 provides a review of relevant vehicle dynamics theory and existing vehicle dynamics control approaches. Chapter 3 presents tracking control for nonlinear systems with actuation constraints and the proposed coordinated vehicle dynamics control (CVDC) system structure. Chapter 4 presents the control allocation methods with emphasis put on the proposed accelerated fixed-point control allocation. Chapter 5 describes the control allocation scheme specifically for CVDC systems. Chapter 6 presents the combined tire slip and slip angle tracking control. Chapter 7 mainly shows virtual experimental evaluation results of the proposed CVDC compared with different existing systems under

various adverse driving conditions. Chapter 8 summarizes the dissertation and suggests future work.

Chapter 2: Vehicle Dynamics and Control

This Chapter briefly reviews the vehicle dynamics theory and the art of vehicle dynamics control systems. Vehicle dynamics terms relevant to this research will be defined for usage in the following chapters. We will start with the tire forces/moments and tire models, in which several well-known tire models will be described. Vehicle body dynamics will be followed with the focus on control-oriented modeling. In the last portion, a review of the art of the current VDC will be given.

2.1 TIRE FORCES AND MOMENTS

Tires are the only vehicle components generating external forces that can be effectively manipulated to affect vehicle motions, and thus they are crucial for vehicle dynamics and control. In order to study vehicle dynamics and design the control systems, it is important to have a good understanding of tire mechanics. As pneumatic tires are universally used for on-road ground vehicles, they will be the subject tires in this chapter.

There are several different tire axis systems used in literature. One of the commonly used axis system is defined by Society of Automotive Engineers (SAE) [SAE J670e]. Here, we will adopt the axis system as shown in Figure 2.1, which is consistent with the one defined by CarSim®, a commercial vehicle dynamics simulation package used in this dissertation. The only difference of these two systems is the direction of the Z axis.

Besides the driving/braking/steering torques applied on the wheel by vehicle actuators, there are three forces and three moments induced by the tire interacting with the ground. The longitudinal force F_{xi} is the component of the resultant ground force acting on the tire along its X_w direction. The tire lateral force F_{yi} is the component in the Y_w direction, and F_{zi} is the tire normal force perpendicular to the contact patch between

tire and ground. M_{xi} is the overturning moment acting on the tire about its X_w axis from the ground. M_{yi} is the rolling resistance moment about Y_w axis. M_{zi} is the tire aligning moment about the Z axis. In this dissertation, to distinguish from vehicle generalized forces and moments composed by all the tire forces and moments, we will use $F_{(x,y,z)i}$ to denote the forces of an individual tire and $M_{(x,y,z)i}$ to indicate the moments on an individual tire. Here,

$$i \in Q := [fl \quad fr \quad rl \quad rr], \tag{2.1}$$

is the index indicating one of the four tires on the front-left, front-right, rear-left, and rear-right corners of a vehicle, respectively.

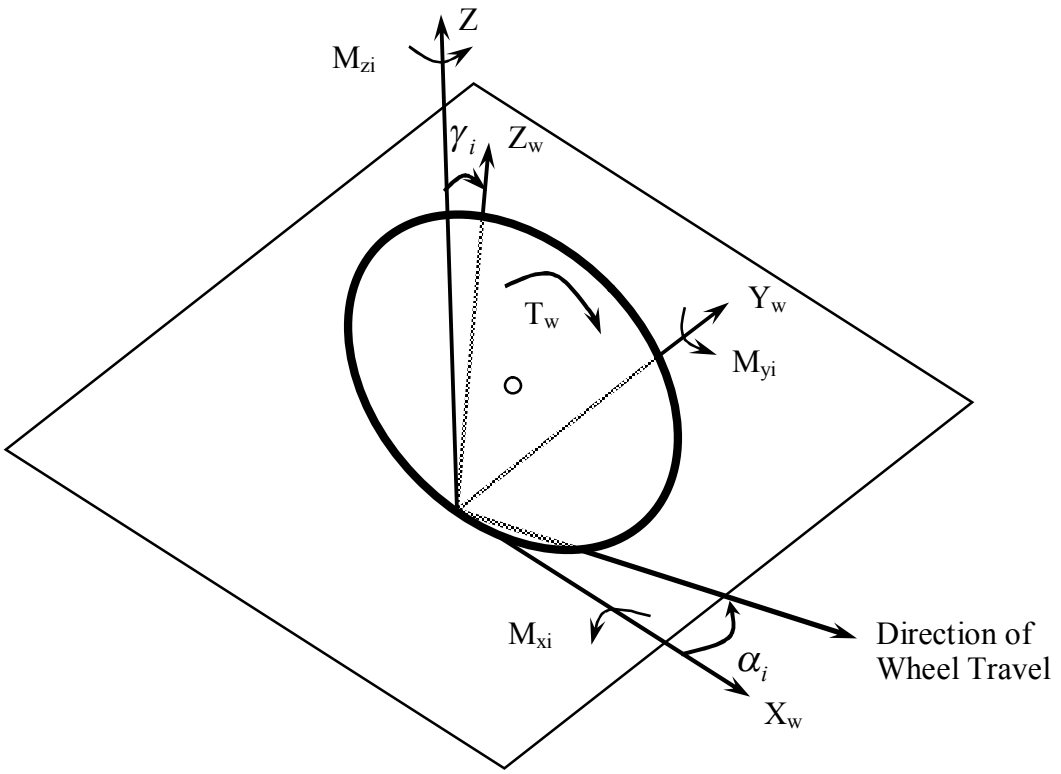

Figure 2.1 Tire axis system

In Figure 2.1, two important angles, the slip angle α_i and the camber angle γ_i, for a rolling tire are graphically illustrated. The tire slip angle is the angle between the direction of wheel travel and orientation of the tire. Camber angle is formed by the plane perpendicular to tire-ground contact surface and the tire plane. In the following sub-sections, we will describe the characteristics of these tire forces/moments.

2.1.1 Tire Rolling Resistance

Tire rolling resistance is usually ignored in vehicle dynamics control because during critical maneuvers its magnitude is small compared with the tractive or braking forces exerted on tires from the ground. Rolling resistance is primarily caused by the hysteresis in tire materials due to the deflection and mainly affected by several factors such as tire structure/materials, tire normal force, road surface conditions, inflation pressure, rolling speed, and temperature etc. [Wong, 2001]. Tire rolling resistance magnitude can be described using the following equation,

$$F_{ri} = F_{zi} f_r, \tag{2.2}$$

where, F_{ri} is the tire rolling resistance, F_{zi} is the tire normal load, and f_r is the tire rolling resistance coefficient, which can be fitted as a function of tire longitudinal speed based on experimental data as,

$$f_r = a_r + b_r V_{xi}^2 . \tag{2.3}$$

where, V_{xi} is tire center longitudinal speed in km/h, a_r is a coefficient in the order of 1.0e-2, b_r is a coefficient in the order of 1.0e-8. Typical passenger car tire rolling resistance coefficient is therefore in the order of 1.0e-2 and weakly depends on speed [Wong, 2001]. Note that tire resistance is an energy loss of the overall vehicle systems.

2.1.2 Tire Tractive / Braking Forces

Given certain tire normal force and tire-road friction level, when a driving or braking torque is applied to a wheel, a tire will induce a tractive or braking force from the ground, respectively. When driven or braked, tire center speed does not equal to its circumferential speed. This phenomena is referred as tire longitudinal slip (or slip ratio) s_i, which is defined as the relative difference between tire circumferential speed and tire center speed [SAE J670e] as,

$$s_i = \frac{\omega_{wyi} R_i - V_{xi}}{V_{xi}} = \frac{\omega_{wyi} R_i}{V_{xi}} - 1, \tag{2.4}$$

where, ω_{wyi} is the tire longitudinal rotational speed in rad/s and R_i is the tire effective rolling radius in meter. When no driving/braking torque acts on a tire, slip $s_i = 0$. Under driving conditions, tire circumferential speed is greater than tire center speed, so $s_i > 0$, while in braking conditions, tire circumferential speed is less than tire center speed and thus $s_i < 0$.

Tire longitudinal force (either tractive or braking force) is a function of tire longitudinal slip. Figure 2.2 shows a typical relationship between slip and tire longitudinal force under 4000 (N) normal force on a surface with a friction coefficient of 0.9, which is about the friction level of a dry concrete or asphalt surface. At small slip levels, longitudinal force is mainly caused by the elastic deformation of the tire tread and its magnitude increases with slip almost linearly. If the slip further increases, tire tread sliding occurs and the relationship between longitudinal force and slip becomes nonlinear. Once the longitudinal force reaches its peak value, further increasing of the slip will result in an unstable operation where the longitudinal force decreases quickly with increasing slip.

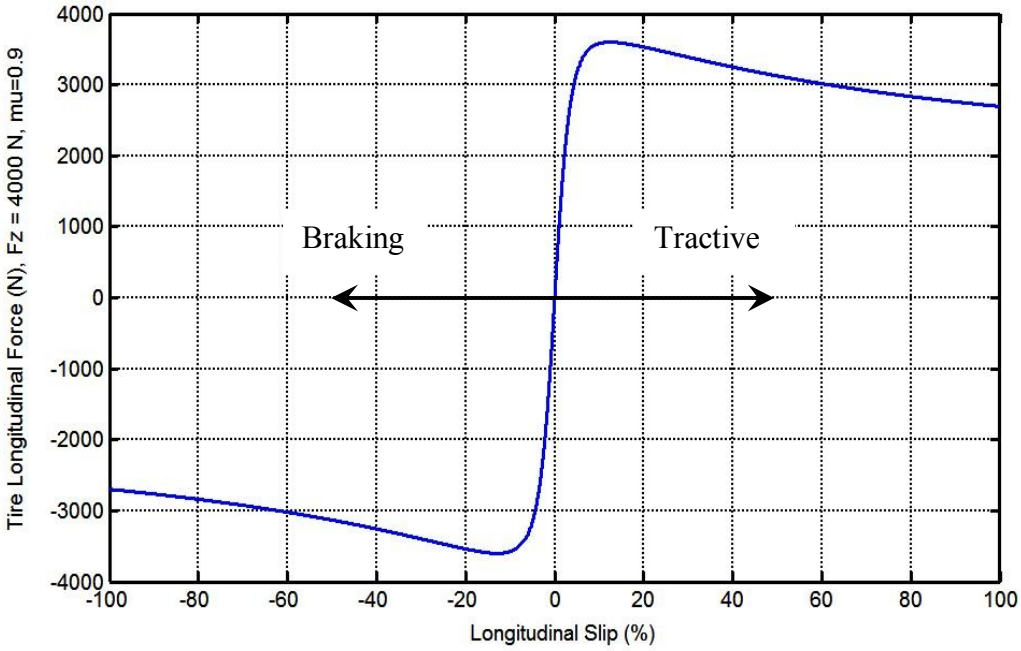

Figure 2.2 Tire longitudinal force vs. tire longitudinal slip

Tire longitudinal force is also greatly affected by the tire normal force, tire-road friction coefficient, and tire lateral force. In general, tire longitudinal force decreases with decreasing normal force and friction coefficient but with increasing lateral force. The details of these relationships will be discussed in the tire model section later. In Figure 2.2, tire lateral force is assumed zero.

2.1.3 Tire Lateral Force

When a tire is not traveling along the wheel plane (i.e., tire slip angle is non-zero), a lateral force will be developed at the tire-road contact patch due to lateral tire deformation. Lateral force is also called cornering force, which is a function of tire slip angle and analogous to the relationship between tire longitudinal force and slip. Figure 2.3 shows a typical relationship between tire lateral force and tire slip angle under 4000 (N) normal force on a surface with a friction coefficient of 0.9. No longitudinal force is

involved. Notice here the polarity of the slip angle and lateral force is opposite, consistent with the definition used in the CarSim® vehicle dynamics simulation package employed in this dissertation.

At small slip angle values, lateral force is approximately a linear function of slip angle. After reaching a maximum lateral force at a particular slip angle, it decreases with increased slip angle.

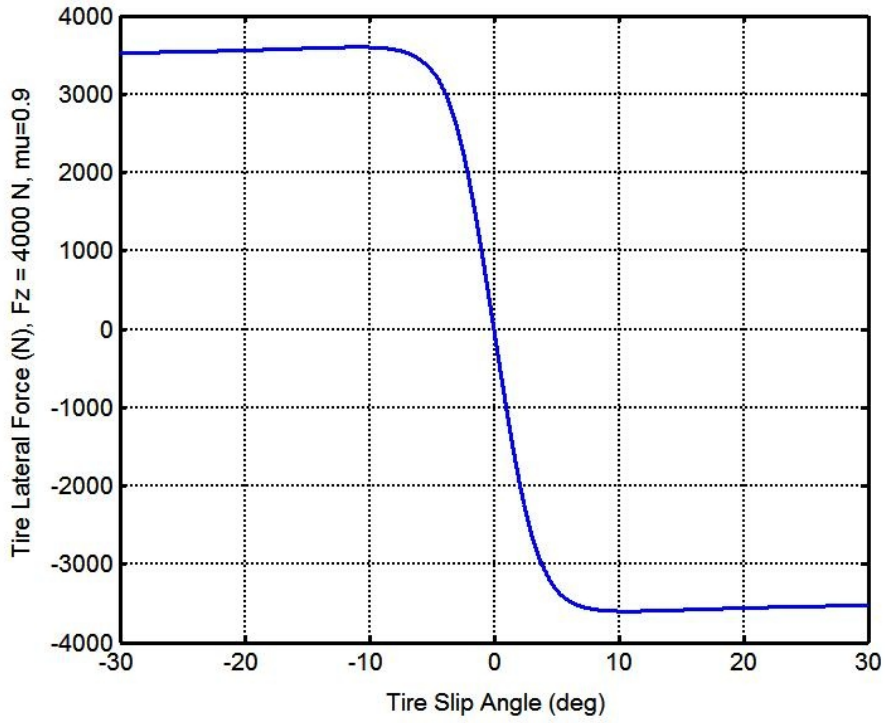

Figure 2.3 Tire lateral force vs. tire slip angle

Lateral force is also greatly affected by tire normal force, tire-road friction coefficient and tire longitudinal force. The lateral force decreases with normal force and tire-road friction coefficient. Non-zero tire longitudinal force decreases the tire lateral force.

2.1.4 Tire Self-Aligning Moment

Pneumatic tire self-aligning (or aligning) moment is primarily generated by two sources: the characteristics of the side deformation of a forward moving tire with non-zero slip angle, and the steering geometry. The resultant lateral force from the ground acts behind the wheel center in the ground plane as shown in Figure 2.4. It then forms a torque with tendency to align the wheel plane with the direction of wheel travel. The distance t_p is called pneumatic trail as shown in Figure 2.4.

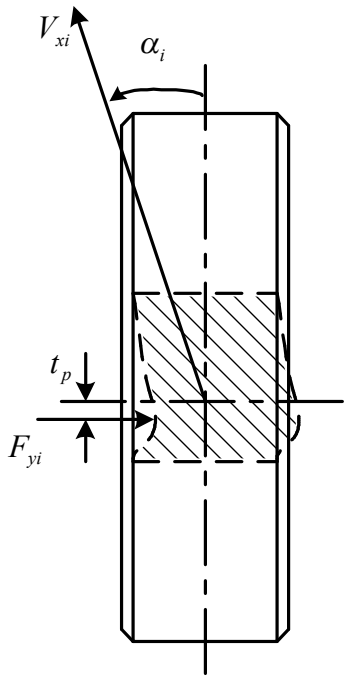

Figure 2.4 Tire deformation during cornering

Another contribution to the tire self-aligning moment is from the mechanical steering geometry, particularly the caster angle, which is the angular displacement, θ_c, between tire steering axis and vertical direction as shown in Figure 2.5. The distance between the center of tire-ground contact patch and the intersection point of steering axis with ground is called mechanical trail, t_m, which is determined by the steering geometry

and tire dimensions. Therefore the lateral force applied on the tire contact patch forms a torque against the steering direction.

In general, these two contributions add to yield the tire self-aligning moment as,

$$M_{zi} = F_{yi}(t_p + t_m). \tag{2.5}$$

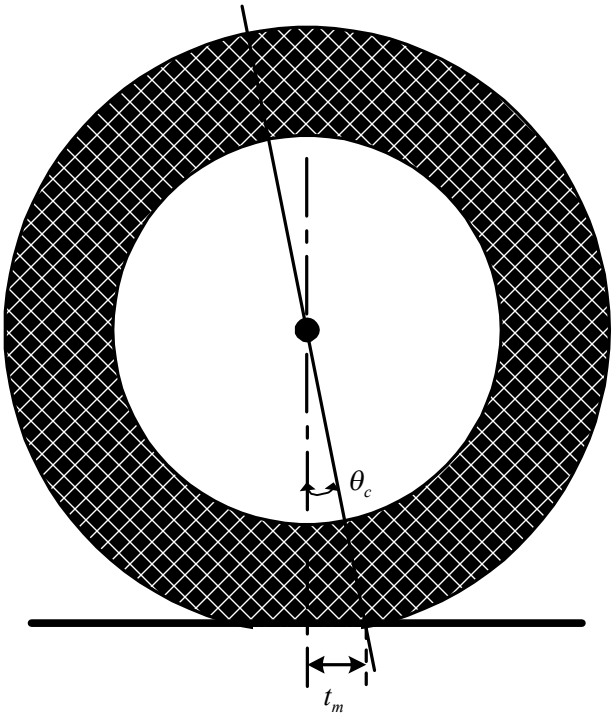

Figure 2.5 Steering tire caster angle and mechanical trail.

A typical tire self-aligning moment as a function of tire slip angle is shown in Figure 2.6. At small slip angle values, the self-aligning moment is associated with slip angle linearly. However, as the slip angle becomes large, the relationship becomes very nonlinear and the self-aligning moment peaks and then decreases dramatically at large slip angle. The self-aligning moment helps the steered tire return to its original position after a turn action and it is important for vehicle handling stability. It is the main torque acting against the steering actuation.

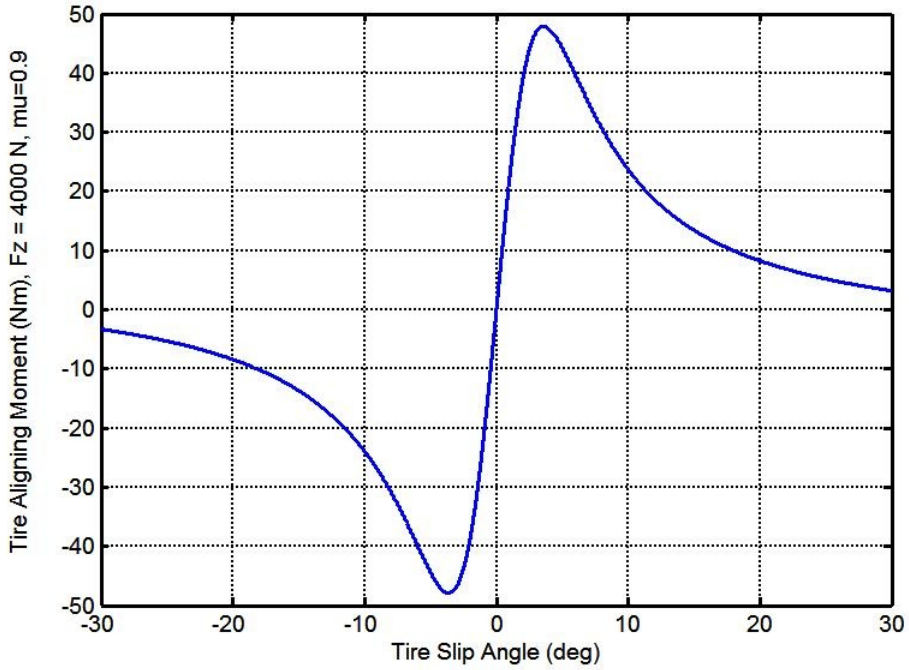

Figure 2.6 Tire self-aligning moment due to pneumatic trail.

In addition to being connected with tire slip angle, self-aligning effects are also subject to other factors such as tire normal force, tire-road friction coefficient, and longitudinal force.

2.1.5 Coupling Effects between Tire Longitudinal and Lateral Forces

In the above discussion on tire forces and moments, we did not explicitly describe the coupling effects between tire longitudinal and lateral forces. However, it is very common that a tire experiences both longitudinal and lateral forces such as during accelerating/braking in a turn maneuver. The coupling effects between tire longitudinal and lateral forces are important in coordinated vehicle dynamics control where both tire longitudinal and lateral forces need to be utilized simultaneously.

Generally, the presence of tractive or braking force will reduce the tire lateral force that can be generated for a given slip angle, normal load, and friction coefficient. For small tractive or braking force, the reduction of the lateral force is mainly due to the reduction of the tire cornering stiffness. In the case of large tractive or braking force cases, significant decrease of the lateral force is mainly caused by the reduced adhesion in the lateral direction [Wong, 2001]. Tire lateral forces also affect the longitudinal forces in a similar manner.

Although the tire longitudinal and lateral forces vary with slip and slip angle as well as their interactive effects, the achievable longitudinal and lateral forces are approximately limited by an enveloping curve which is often called friction ellipse as shown in Figure 2.7 [Wong, 2001].

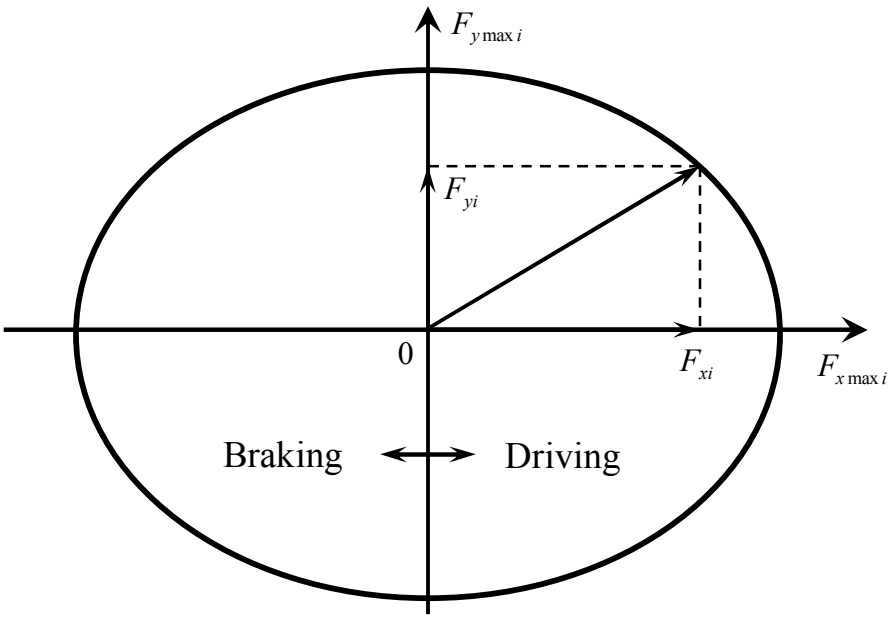

Figure 2.7 The friction ellipse concept for achievable tire longitudinal and lateral forces

In a friction ellipse, tire longitudinal and lateral forces approximately follow the nonlinear constraint,

$$\left(\frac{F_{xi}}{C_{xi}}\right)^2 + \left(\frac{F_{yi}}{C_{yi}}\right)^2 \le (\mu_i F_{zi})^2, \tag{2.6}$$

with $F_{x\max i} = C_{xi}\mu_i F_{zi}$ and $F_{y\max i} = C_{yi}\mu_i F_{zi}$ being the maximal tire longitudinal and lateral forces, respectively. The sum of the weighted squares of tire longitudinal force and lateral force is physically limited by the tire normal load and tire-road friction coefficient. From the friction ellipse, one can determine the maximum lateral force to a given longitudinal force, and vice versa.

2.2 TIRE MODELS

Since tire forces are crucial for vehicle dynamics, it is very desirable to have some mathematical models for estimating the complex tire behaviors for both simulation and control design purposes. Significant research efforts have been dedicated to the development of tire models over the last several decades. Many different tire models exist in literature derived from the physical nature of the tire and/or empirical formulations based on experimental data [Dugoff et al., 1970], [Pacejka and Bakker, 1993], [Pasterkamp and Pacejka, 1994], [Pasterkamp and Pacejka, 1997], [Deur, Asgari, and Hrovat, 2001], [Claeys et al., 2001], [Tsiotras et al., 2004], [Bozdog and Olson, 2005], [Cafvert and Svendenius, 2005], [Shifrin 2006]. These models have different emphases, shortcomings, accuracies, and complexities. Here, we will just present two tire models with details placed on the Magic Formula tire model as it will be used in the control design of this dissertation.

2.2.1 Dugoff's Tire Model

The Dugoff's tire model was developed in 1970's. Thanks to its simple formulation and capability of describing longitudinal and lateral force coupling effect, it

is popularly used in vehicle control systems [Guvenc et al., 2003], [Zhang et al., 2003], [Wang and Longoria, 2006a], [Wang and Longoria, 2006c]. The model is expressed as,

$$F_{xi} = f_i C_{xi} s_i , \tag{2.7}$$

$$F_{yi} = f_i C_{yi} \alpha_i , \tag{2.8}$$

$$f_i = \begin{cases} 1 & , F_{Ri} \le \dfrac{\mu_i F_{zi}}{2} \\ (2 - \dfrac{\mu_i F_{zi}}{2F_{Ri}}) \dfrac{\mu_i F_{zi}}{2F_{Ri}} & , F_{Ri} > \dfrac{\mu_i F_{zi}}{2} \end{cases} , \tag{2.9}$$

with $F_{Ri} = \sqrt{(C_{xi} s_i)^2 + (C_{yi} \alpha_i)^2}$, and C_{xi} and C_{yi} being the tire longitudinal and lateral stiffness, respectively. F_{zi} is the tire normal force and μ_i is the tire-road friction coefficient.

One can find that when combined longitudinal and lateral force F_{Ri} is small (less than half of the maximal force), the tire longitudinal and lateral forces given from the Dugoff's model are independent and linear to slip and slip angle, respectively. From the model, as F_{Ri} further increasing (greater than half of the maximal force), the coupling effect between tire longitudinal and lateral forces starts showing up.

The Dugoff's tire model is simple and with only two calibration parameters, C_{xi} and C_{yi}. It works well for small slip / slip angle regions. However, there are some concerns regarding its accuracy for vehicle control, particularly for the applications where the tire may need to work in large slip / slip angle regions.

1) The tire self-aligning moment description is absent in this model.
2) There are only two calibration parameters, tire longitudinal and lateral stiffness. It is difficult to describe the complex tire behaviors accurately enough, especially for highly nonlinear behaviors at large slips and slip angles. As shown in Figure 2.8, the amplitude of the calculated tire longitudinal force increases with tire slip monotonically even at large slip region, which is inconsistent with experimental

tire behavior. Similar discrepancies can be found for the tire lateral force vs. slip angle relationships.

3) Tire longitudinal and lateral force coupling effects are not well modeled especially at high slip / slip angle regions. Comparing the calculated tire longitudinal forces for zero slip angle and 2 deg slip angle in Figure 2.8, one can see that there are some coupling effects at small slip regions. However, as the slip increases, the coupling effects diminish and disappear, unlike what is observed in general trends of tire behaviors.

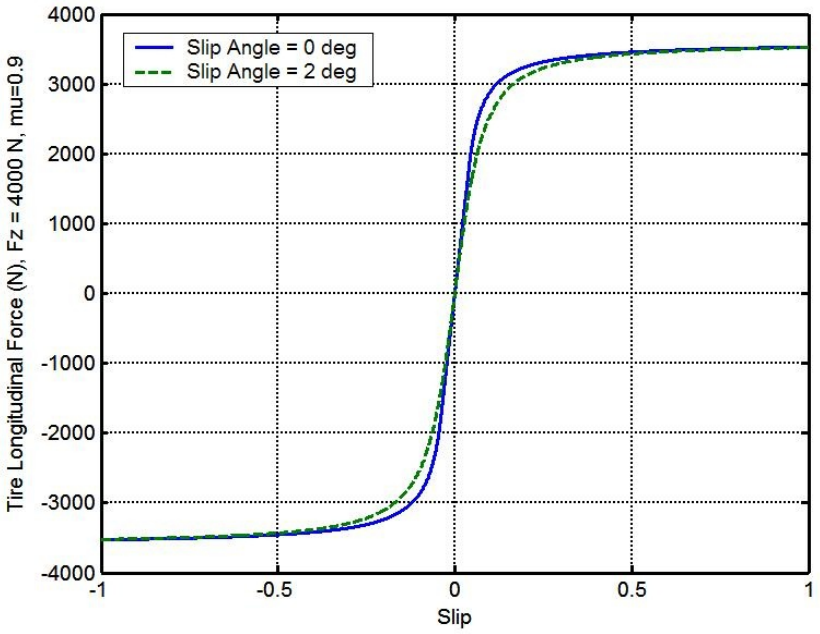

Figure 2.8 Longitudinal force vs. slip calculated from the Dugoff's model

With these observations in mind, we choose a much more accurate tire model, Magic Formula tire model, for the control design in this dissertation, even though its formulations are more complex than those of Dugoff's model. The Magic Formula tire models are presented in the next sub-section.

2.2.2 Magic Formula Tire Model

One of the most well-known tire models is Pacejka's Magic Formula tire model [Pacejka and Bakker, 1993]. The Magic Formula tire model is an empirical method for characterizing tire behavior, which can be effectively fit to experimental data [Oosten and Bakker, 1993] and is widely used for vehicle dynamics simulations and analyses [Wong, 2001]. The model employs a general and smooth form called Magic Formula to describe the tire longitudinal force, lateral force, and self-aligning moment. The basic equations are,

$$y(x) = D\sin\{C\arctan[Bx - E(Bx - \arctan Bx)]\}, \tag{2.10a}$$

$$Y(X) = y(x) + S_v, \tag{2.10b}$$

$$x = X + S_h, \tag{2.10c}$$

where $Y(X)$ represents tire longitudinal force, lateral force, or self-aligning moment, X is tire slip or slip angle. Coefficient B is the stiffness factor, C is the shape factor, D is the peak factor, and E is the curvature factor. S_h and S_v denote the horizontal shift and vertical shift, respectively. These coefficients are tuned to fit experimental data for a given tire on a test patch.

Experimental test results have shown that the Magic Formula tire model is capable of generating tire characteristics that closely match measured data for all longitudinal force, lateral force, and self-aligning moment over large ranges of slip and slip angle [Bakker et al., 1989]. The Magic Formula tire model for the case of combined slip and slip angle can be described by,

$$\begin{aligned} F_{xi} = {} & D_{x\alpha i}\cos[C_{x\alpha i}\arctan(B_{x\alpha i}\alpha_i)]\{\mu_0 F_{zi}\sin\{C_{xi}\arctan \\ & [B_{xi}s_{xi} - E_{xi}(B_{xi}s_{xi} - \arctan(B_{xi}s_{xi}))]\} + S_{vxi}\} \end{aligned}, \tag{2.11a}$$

$$s_{xi} = s_i + S_{hxi}, \tag{2.11b}$$

$$F_{yi} = D_{ysi}\cos[C_{ysi}\arctan(B_{ysi}s_i)]\{\mu_0 F_{zi}\sin\{C_{yi}\arctan [B_{yi}\alpha_{yi} - E_{yi}(B_{yi}\alpha_{yi} - \arctan(B_{yi}\alpha_{yi}))]\} + S_{vyi}\}, \quad (2.11c)$$

$$\alpha_{yi} = \alpha_i + S_{hyi}, \quad (2.11d)$$

$$M_{zi} = D_{zsi}\cos[C_{zsi}\arctan(B_{zsi}s_i)]\{\mu_0 F_{zi}\sin\{C_{zi}\arctan [B_{zi}\alpha_{zi} - E_{zi}(B_{zi}\alpha_{zi} - \arctan(B_{zi}\alpha_{zi}))]\} + S_{vzi}\}, \quad (2.11e)$$

$$\alpha_{zi} = \alpha_i + S_{hzi}, \quad (2.11f)$$

where $i \in Q := [fl, \quad fr, \quad rl, \quad rr]$ refers to a given tire. F_{xi} is the tire longitudinal force, F_{yi} is the tire lateral force, and M_{zi} is the tire self-aligning moment. The parameters B_*, C_*, D_*, E_* are obtained by fitting to experimental data for a specific tire and specific road condition. For different road surfaces with different friction levels, these parameters need to be determined experimentally. In this dissertation, we use a set of parameters that were fit for a surface with nominal friction level in [Wong, 2001]. The friction similarity technique [Pasterkamp and Pacejka, 1994] was used to approximate the effects of variations of friction level on tire forces/moment.

The friction similarity technique can be described as follows. Define the friction ratio as, $R_{\mu i} = \mu_i / \mu_0$, where μ is the tire-road friction coefficient for a different surface, μ_0 is the nominal tire-road friction coefficient on which the parameters of the Magic Formula tire model are identified to match with the experimental data. Define $s_{\mu i} = s_i / R_\mu$ and $\alpha_{\mu i} = \alpha_i / R_\mu$, where s_i and α_i are measured slip and slip angle, the longitudinal force, lateral force and aligning moment become,

$$F_{xi} = D_{x\alpha i}\cos[C_{x\alpha i}\arctan(B_{x\alpha i}\alpha_{\mu i})]\{R_\mu \mu_0 F_{zi} \sin\{C_{xi}\arctan[B_{xi}s_{\mu xi} - E_{xi}(B_{xi}s_{\mu xi} - \arctan(B_{xi}s_{\mu xi}))]\} + S_{vxi}\}, \quad (2.12a)$$

$$s_{\mu xi} = s_{\mu i} + S_{hxi}, \quad (2.12b)$$

$$F_{yi} = D_{ysi}\cos[C_{ysi}\arctan(B_{ysi}s_{\mu i})]\{R_\mu \mu_0 F_{zi} \sin\{C_{yi}\arctan[B_{yi}\alpha_{\mu yi} - E_{yi}(B_{yi}\alpha_{\mu yi} - \arctan(B_{yi}\alpha_{\mu yi}))]\} + S_{vyi}\}, \quad (2.12c)$$

$$\alpha_{\mu yi} = \alpha_{\mu i} + S_{hyi}, \quad (2.12d)$$

$$M_{zi} = D_{zsi}\cos[C_{zsi}\arctan(B_{zsi}s_{\mu i})]\{R_{\mu}\mu_0 F_{zi} \sin\{C_{zi}\arctan[B_{zi}\alpha_{\mu zi} - E_{zi}(B_{zi}\alpha_{\mu zi} - \arctan(B_{zi}\alpha_{\mu zi}))]\} + S_{vzi}\}, \quad (2.12e)$$

$$\alpha_{\mu zi} = \alpha_{\mu i} + S_{hzi}. \quad (2.12f)$$

To visualize the Magic Formula tire model, Figure 2.9 and Figure 2.10 show the tire longitudinal force vs. slip with different slip angles and lateral force vs. slip angle with different slips, respectively.

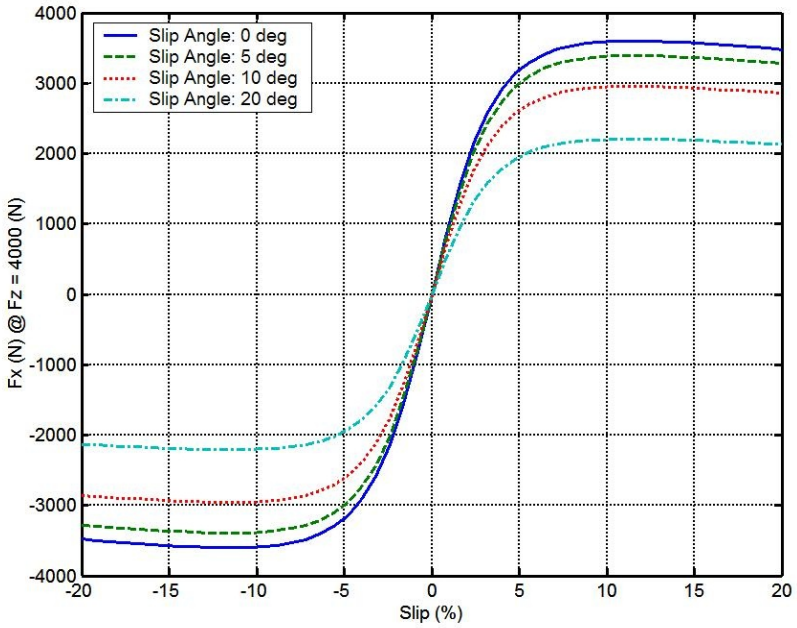

Figure 2.9 Magic Formula tire model longitudinal force vs. slip at different slip angles

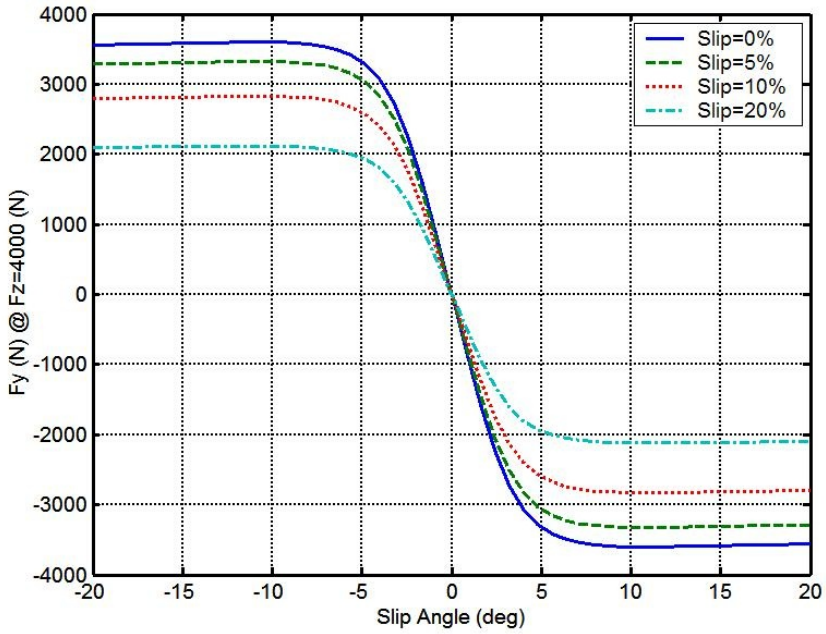

Figure 2.10 Magic Formula tire model lateral force vs. slip angle at different slips

The effects of the tire-road friction level variations modeled by the friction similarity technique for longitudinal force and lateral force are shown in Figure 2.11 and Figure 2.12, respectively. $\mu = 0.8 \sim 0.9$ is the typical friction level for dry concrete or asphalt surfaces, $\mu = 0.5 \sim 0.7$ is for the wet surface, $\mu = 0.3 \sim 0.5$ is for hard snow surface, and $\mu = 0.1 \sim 0.3$ is perhaps about the friction level for icy surface [Wang et al., 2004]. As shown in the figures, the Magic Formula tire model with friction similarity can capture the trends of the effects of tire-road friction levels fairly well.

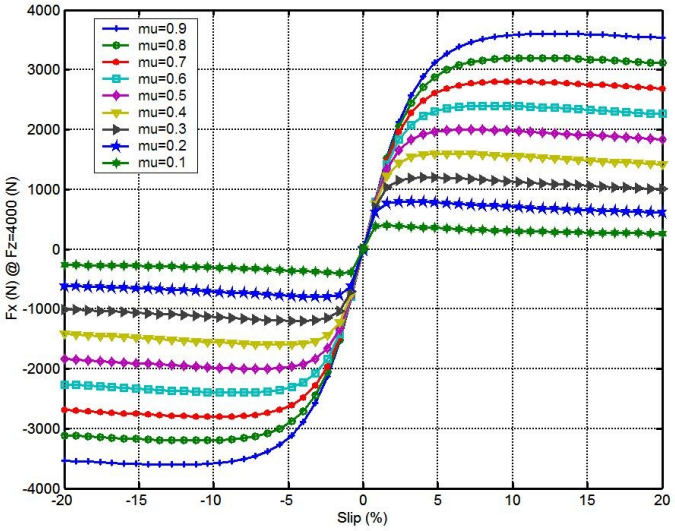

Figure 2.11 Effects of friction level on tire longitudinal force modeled by the friction similarity

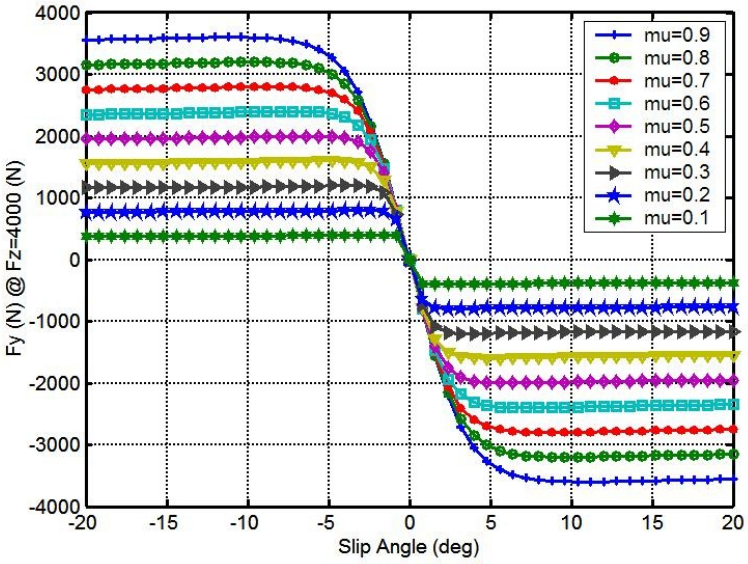

Figure 2.12 Effects of the friction level on tire lateral force modeled by the friction similarity

Another merit about the Magic Formula tire models is that they are continuously differentiable, which is suitable for control design purposes, and we will see more on this

in Chapter 5 and Chapter 6. It should be noted that the slip is defined in percentages and slip angle is defined in degrees for the Magic Formula tire model.

2.3 VEHICLE DYNAMICS

Vehicle as a complex mechanical system consists of many components. Roughly, it can be divided into two groups: sprung part and unsprung part. Sprung part includes all the components supported by the suspensions such as vehicle body, internal components, passengers, and cargo, but not the mass of the suspension components themselves. Unsprung part includes the suspensions, wheels, and other components directly connected to them. For passenger cars and commercial vehicles, a majority of the vehicle mass is sprung. The larger the ratio of sprung mass to unsprung mass, the less the body and vehicle occupants are affected by road bumps, dips, and other surface imperfections. The vehicle sprung mass can be lumped as a rigid body as shown in Figure 2.13. Its motions comprise *X*, *Y*, and *Z* motions, as well as yaw, roll, and pitch motions.

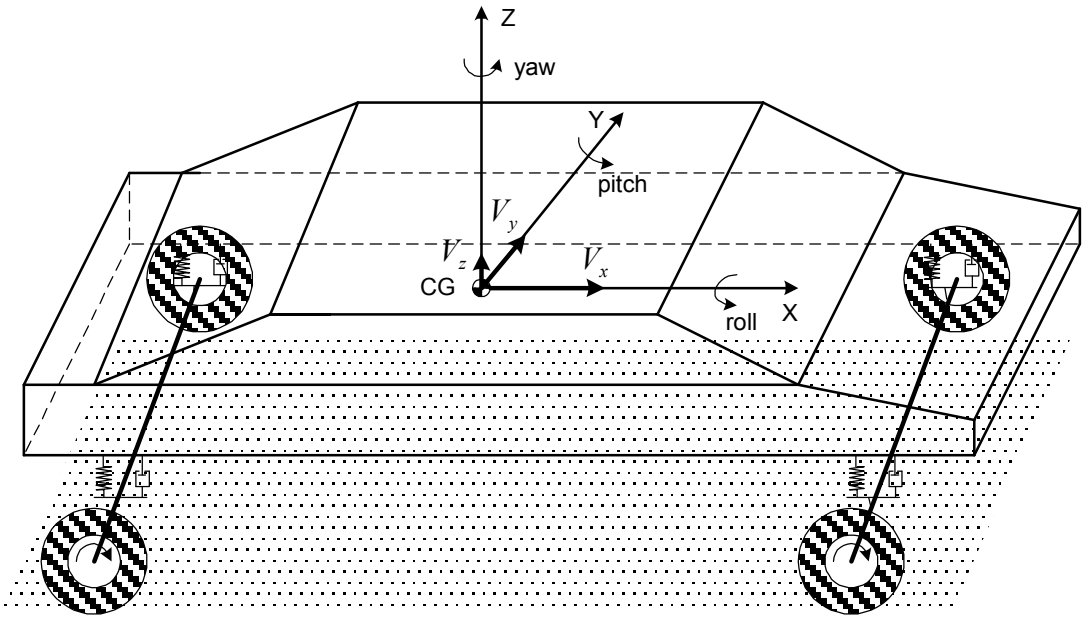

Figure 2.13 Vehicle body motions

In this section, vehicle dynamics are presented with emphasis put on the control-oriented vehicle dynamic model.

2.3.1 Vehicle Rigid Body Dynamics

If we consider the overall vehicle system as a rigid body, then the equations of motion can be derived as follows. Using the vehicle body fixed coordinates at the center of gravity as shown in Figure 2.13, define the body fixed translational and angular velocities with respect to the *X*, *Y*, and *Z* axes as,

$$V = \begin{bmatrix} V_x & V_y & V_z \end{bmatrix}^T, \tag{2.13}$$

$$\Omega = \begin{bmatrix} \Omega_x & \Omega_y & \Omega_z \end{bmatrix}^T, \tag{2.14}$$

where V_x is the vehicle longitudinal velocity, V_y is the lateral velocity, V_z is the vertical velocity, Ω_x is the roll velocity, Ω_y is the pitch velocity, and Ω_z is the yaw velocity.

The translational and angular momenta are then defined, respectively, as,

$$p = MV, \tag{2.15}$$

$$h = I\Omega, \tag{2.16}$$

where M is the mass of the vehicle, and I is the moment inertia. Based on Newton's second law, the dynamics along each axis can be found from the equations,

$$F = \left.\frac{dp}{dt}\right|_{xyz} + \Omega \times p, \tag{2.17}$$

$$T = \left.\frac{dh}{dt}\right|_{xyz} + \Omega \times h, \tag{2.18}$$

and,

$$F_x = \dot{p}_x + \Omega_y p_z - \Omega_z p_y = M\dot{V}_x + M\Omega_y V_z - M\Omega_z V_y, \tag{2.19}$$

$$F_y = \dot{p}_y + \Omega_z p_x - \Omega_x p_z = M\dot{V}_y + M\Omega_z V_x - M\Omega_x V_z, \tag{2.20}$$

$$F_z = \dot{p}_z + \Omega_x p_y - \Omega_y p_x = M\dot{V}_z + M\Omega_x V_y - M\Omega_y V_x, \tag{2.21}$$

$$T_x = \dot{h}_x + \Omega_y h_z - \Omega_z h_y = I_x\dot{\Omega}_x + I_z\Omega_y\Omega_z - I_y\Omega_z\Omega_y, \tag{2.22}$$

$$T_y = \dot{h}_y + \Omega_z h_x - \Omega_x h_z = I_y \dot{\Omega}_y + I_x \Omega_z \Omega_x - I_z \Omega_z \Omega_x , \tag{2.23}$$

$$T_z = \dot{h}_z + \Omega_x h_y - \Omega_y h_x = I_z \dot{\Omega}_z + I_y \Omega_x \Omega_y - I_x \Omega_y \Omega_x . \tag{2.24}$$

For planar motion of passenger vehicles, the vertical motion V_z, pitch motion Ω_y, and roll motion Ω_x are considered small. If we ignore those three motions, the resultant vehicle dynamics will only include longitudinal motion V_x, lateral motion V_y, and yaw motion Ω_z, and the planar dynamics can be described as,

$$M\dot{V}_x = M\Omega_z V_y + F_x , \tag{2.25}$$

$$M\dot{V}_y = -M\Omega_z V_x + F_y , \tag{2.26}$$

$$I_z \dot{\Omega}_z = T_z . \tag{2.27}$$

Equations (2.25 – 2.27) capture the dominant motions of a ground vehicle and are simple enough for control design purposes [Guvenc et al., 2003], [Hac et al., 2006], [Wang and Longoria, 2006a]. They are usually regarded as the control-oriented vehicle dynamic model.

It should be noted that in the dynamic model above, the entire vehicle (both sprung mass and unsprung mass) is treated as a rigid body, instead of modeling the sprung mass and unsprung mass separately. The interactions between sprung mass and unsprung mass, suspension dynamics, roll and pitch motions of the sprung mass etc. are not described. Models describing the dynamics of the sprung mass and unsprung mass separately are certainly more accurate [Feng et al., 1998], [Ikenaga et al., 2000], [Lin et al., 2004], however, as we are interested in the control-oriented model, simple models describing the dominant dynamics are preferred. It is worthwhile to point out that CarSim® involves a full-vehicle multibody dynamics model that is much more complete and complex, and can produce response characteristics that have shown favorable comparison with experimental data taken from real vehicles [CarSim User Manual,

2003]. The CarSim® vehicle dynamics simulation package will be used as the test platform in this dissertation.

2.3.2 Tire Normal Load

From the tire model described previously, it is clear that the amplitudes of the tire longitudinal and lateral forces directly depend on its normal force F_{zi}. The static tire normal load can be calculated from the equations,

$$F_{zfl0} = \frac{m_v g l_r}{2(l_f + l_r)}, \tag{2.28}$$

$$F_{zfr0} = \frac{m_v g l_r}{2(l_f + l_r)}, \tag{2.29}$$

$$F_{zrl0} = \frac{m_v g l_f}{2(l_f + l_r)}, \tag{2.30}$$

$$F_{zrr0} = \frac{m_v g l_f}{2(l_f + l_r)}. \tag{2.31}$$

For vehicle dynamics control systems, the effect of the load transfers due to vehicle sprung mass longitudinal and lateral accelerations will need to be considered in order to closely approximate the actual tire normal load during operations. For simplicity, assume the front and rear roll center heights of the vehicle (sprung mass and unsprung mass) are same. The dynamic load transfer of each tire can be calculated from,

$$\delta F_{zfl} = -\frac{m_v a_x h_g}{2(l_f + l_r)} - \frac{m_v a_y h_r \kappa_f}{2 l_s}, \tag{2.32}$$

$$\delta F_{zfr} = -\frac{m_v a_x h_g}{2(l_f + l_r)} + \frac{m_v a_y h_r \kappa_f}{2 l_s}, \tag{2.33}$$

$$\delta F_{zrl} = \frac{m_v a_x h_g}{2(l_f + l_r)} - \frac{m_v a_y h_r \kappa_r}{2 l_s}, \tag{2.34}$$

$$\delta F_{zrr} = \frac{m_v a_x h_g}{2(l_f + l_r)} + \frac{m_v a_y h_r \kappa_r}{2 l_s}, \tag{2.35}$$

where, κ_f, κ_r are the roll stiffness factor of the front and rear suspension, respectively and $\kappa_f + \kappa_r = 1$. In this estimation approach, the vehicle body longitudinal and lateral accelerations are needed, and it is assumed that these quantities can be easily measured by widely available inertial sensors. The bias issues associated with the inertial sensors can be overcome by sensor fusion methods as described in [Wang et al., 2004] and [Bevly et al., 2000].

2.3.3 Aerodynamic Forces and Moments

Aerodynamic forces and moments are considerable in vehicle dynamics when vehicles are running at highway speeds and/or wind gust is strong. Aerodynamic resistance is mainly due to the pressure drag, which arises from the component of the normal pressure on the vehicle body acting against the motion of the vehicle. This force can usually be expressed as,

$$R_a = \frac{\rho}{2} C_D A_f V_r^2, \tag{2.36}$$

where ρ is the mass density of the air, C_D is the aerodynamic resistance coefficient, and A_f is a characteristic area of the vehicle, which is the projected area of the vehicle in its direction of travel, and V_r is the relative speed between vehicle and wind. For modern passenger cars, typical values are $A_f \approx 2.0\,\mathrm{m}^2$ and $C_D \approx 0.4$ [Wong, 2001].

Aerodynamic lift is another effect that can act on the vehicle when its relative speed to wind is high enough. The aerodynamic lift is mainly caused by the pressure differential across the vehicle body from the bottom to the top. Similar as the aerodynamic resistance, the aerodynamic lift can be approximated as,

$$R_L = \frac{\rho}{2} C_L A_f V_r^2, \tag{2.37}$$

where C_L is the aerodynamic lift coefficient with typical values as 0.2 ~ 0.5 for passenger cars [Wong 2001].

Aerodynamic resistance and aerodynamic lift acting on the vehicle also result in a moment about the vehicle's CG, which is commonly called aerodynamic pitching moment. This moment can cause normal load transfer from one axle to the other. The aerodynamic pitching moment can be calculated as,

$$M_a = \frac{\rho}{2} C_M A_f L_c V_r^2, \tag{2.38}$$

where C_M is the aerodynamic pitching moment coefficient, and L_c is the characteristic length of the vehicle. For passenger vehicles, the values of the C_M are in the range of 0.05 ~ 0.20 [Wong 2001].

The vehicle to wind relative velocity V_r has important influence on both the magnitudes and directions of the aerodynamic forces and moments. However, the wind velocity can only be treated as an external disturbance signal because it is uncontrollable. Aerodynamic forces and moments together with the generalized ground forces and moments from tires affect the vehicle dynamics. It should be noted that the effects of aerodynamic forces and moments are well modeled in the CarSim® models.

2.4 CURRENT VEHICLE DYNAMICS CONTROL SYSTEMS

Many different VDC/VSC systems have been introduced into the automotive market and/or proposed in the technical literature. Those VDC systems can be loosely classified into four categories according to their actuation modes, and these are reviewed in this section.

2.4.1 Steering-Based Vehicle Stability Control

Given the road condition and tire normal force, the lateral force produced from the tire is a function of the tire slip ratio and slip angle. Changing the steering angle

(front wheels and/or rear wheels) will affect the vehicle lateral dynamics. A class of steering-based vehicle stability control systems has been studied.

Halanay et al. analyzed the stability and maneuverability of a vehicle with a yaw rate feedback compensator to control the rear wheel steering [Halanay et al., 1994]. An adaptive law was used to account for uncertainty in the tire stiffness. Simulations illustrated that both the vehicle stability and maneuverability can be improved by the feedback controller. Hebden et al. investigated a front wheel steer-by-wire control approach in conjunction with a conventional anti-lock braking system (ABS) to improve the vehicle stability during braking on a split-μ surface scenario [Hebden et al., 2004]. The controller was designed based on a linearized vehicle model at a steady-state operating point with the assumption that the friction coefficient was known. Simulation studies showed that active front wheel steering control can effectively reduce the yaw angle and lateral position deviation. Mammar and Koenig designed a H_∞ active front wheel steering controller based on a linearized vehicle model to improve the vehicle handling performance [Mammar and Koenig, 2002]. The controller exhibits enhancement of the vehicle stability and robustness properties in simulation of lane-changing and aquaplaning maneuvers with variations in the system parameters. Hayama et al. proposed an approach to control the front-wheel steering angle based on the difference between front-wheel rotational speeds to account for the undesirable motion caused at split-μ condition [Hayama et al., 2000]. Better maneuverability compared with the conventional steering-by-wire system was demonstrated on a split- μ test.

Remarks: For the steering-based stability control, a common shortcoming is that the control effectiveness relies on the tire lateral forces only. It makes the system less effective when the tires approach the limits of adhesion [Shibahata et al., 1993] as well as

when tire longitudinal slip is present. In adverse driving situations, the steering-based VDC system alone may not be sufficient to control the vehicle states as desired.

2.4.2 Differential Braking Vehicle Stability Control

A yaw moment can be generated from the transverse distribution of the tire longitudinal forces (driving or braking) as well. Vehicle stability control systems via torque distribution actuation are the most common approach in [Liu et al., 2002], [Zanten, 2000], [Shimada and Shibahata, 1994]. This type of VDC is usually referred as direct yaw-moment control (DYC) [Heinzl et al., 2002], [Hisaoka et al., 1999], [Kageyama and Jo, 1997]. The longitudinal forces at the right and left side wheels are offset to create the required yaw moment to control the vehicle yaw motion. Most of the commercially available VDC are based on this approach because existing standard actuators, such as ABS, can be directly used for this purpose [Guvenc et al., 2003].

Drakunov et al. suggested a yaw control algorithm with biased distribution of the brake force on the left and right sides of the vehicle [Drakunov et al., 2000]. A periodic switching function is used to handle the uncertainty of the tire friction force. However, this approach could potentially cause unreachable sliding mode and oscillations in the vehicle motion. Guvenc et al. studied an individual wheel braking based yaw stability control [Guvenc et al., 2003]. The vehicle speed and tire-road friction were assumed to be constant for all time to make the system time invariant for controller design. The effectiveness of this braking based yaw controller is demonstrated based on simulation studies using a nonlinear vehicle model. Hallowell and Ray designed an all-wheel independent torque controller to improve the vehicle stability with respect to the uncertainty of the road condition [Hallowell and Ray, 2003]. The controller was designed based on the assumption that the four wheel torque can be individually controlled through four wheel-side electric motors. Simulation results based on an 8-

DOF nonlinear vehicle model show that the torque distribution system can provide good stability and traction control with variation on the road surface condition. Shim and Margolis studied a differential braking control strategy using yaw rate feedback and tire road friction coefficient feed-forward [Shim and Margolis, 2001]. The tire road friction coefficient was obtained from an assumed online friction estimator. Simulation results show that knowledge of friction coefficient can offer significant improvement in vehicle maneuverability compared with that of a yaw rate controller alone.

Remarks: Compared with a steering-based approach, the control capability of the longitudinal differential braking-based vehicle stability control is higher, especially in the nonlinear range near the saturation [Furukawa and Abe, 1997]. However, a common disadvantage of this kind of systems is that the generation of yaw moment depends on the distribution of the braking force on the vehicle wheels. Vehicle generalized longitudinal force could be sacrificed and the longitudinal motion will be affected as well. For example, in the case of split-μ scenario, the longitudinal forces from the wheels on the high μ surface have to be reduced to match with the saturated ones from the wheels on the low μ surface in order to prevent the generation of unexpected yaw moment or compensate the yaw moment disturbance, which, however, could significantly sacrifice the vehicle longitudinal deceleration performance. Active wheel steering can provide additional lateral forces to reject yaw and roll disturbances rising from asymmetric longitudinal forces and side wind etc. In addition, from the disturbance to the driver point of view, the steering-based systems are much less perceptible to the driver compared with the brake-based DYC systems, because the brake actuations could cause vehicle longitudinal speed change and audible noise [Bedner and Chen, 2004], [Mammar and Koenig, 2002].

2.4.3 Coordinated Steering and DYC Vehicle Stability Control

As mentioned above, both steering-based systems and DYC systems have authority on control of the vehicle stability, having their own strengths and shortcomings. Thus, it seems nature to assume that a combination of these two systems would compensate for any drawbacks in each, improve the performance of the vehicle stability control, and keep the vehicle behavior closer to that expected by the driver even at adverse driving situations [Heinzl et al., 2002], [Hisaoka et al., 1999], [Kageyama and Jo, 1997]. Several research activities have been carried on at this front.

Guvenc et al. proposed a vehicle yaw stability control approach coordinating steering and individual wheel braking actuations [Guvenc et al., 2003]. The authors argued that the best performance can be achieved only by coordinated steering and individual wheel braking control. A simple coefficient $0 \le \lambda \le 1$ was used to distribute the control effort between steering angle and braking torque. Chen and Tomizuka studied the lateral control for a tractor-semitrailer commercial vehicle with coordinated steering and braking [Chen and Tomizuka, 2000]. It was assumed that the road reference information was available all the time for the controller to track. Simulation results based on a vehicle model show that the coordinated front wheel steering and trailer braking control can noticeably reduce the yaw error compared with the steering control only. However, the tire-road friction condition and actuator limitations were not considered in the controller. Heinzl et al. compared three different control strategies: active front wheel steering, active front wheel steering plus unilateral braking, and active rear wheel steering plus unilateral braking for vehicle dynamics control in a severe cornering and braking maneuver situation in simulation [Heinzl et al., 2002]. The results reveal advantages of the combined steering and unilateral braking strategies. Mokhiamar and Abe also compared different combinations of DYC with active front wheel steering (AFS), active

rear wheel steering (ARS), and AFS+ARS in simulation [Mokhiamar and Abe, 2002]. The combination of DYC with AFS/AFS+ARS exhibits superior performance in maximizing vehicle stability limit. Bedner et al. proposed a supervisory control approach to manage both brake and four-wheel-steering (4WS) system for vehicle stability control [Bedner and Chen, 2004]. A common reference model is used to distribute the control action to the two systems. The test results demonstrated that the proposed coordinated control of brakes and 4WS can improve the system performance in terms of stability, driver workload, driver comfort, and deceleration time compared with the brake-only system. However, the detailed control algorithm was not described in the paper. Nagai et al. proposed an integrated control system of active front steering (AFS) and DYC to control the vehicle yaw rate and sideslip angle using a model-matching controller designed based on a linearized vehicle model [Nagai et al., 2002]. Simulation study shows that the vehicle's yaw rate and sideslip motion were considerably improved compared with the system with DYC only. The control action includes both feed-forward and feedback portions with the feed-forward action coming from the reference model while the feedback effort compensating for the parameter uncertainties and disturbances. It was shown that the feed-forward action can effectively reduce control error and stabilization period. Yu and Moskwa designed a 4WS and independent wheel torque control system to enhance the vehicle maneuverability and safety [Yu and Moskwa, 1994]. Simulation results show that the vehicle stability was improved while the driver's workload is reduced by coordinating the steering and braking commands. In this study, the optimization of the steering and braking was not considered. The road friction coefficient was assumed to be known and constant, and the actuator dynamics were ignored. Brennan and Alleyne proposed an integrated front wheel steering and individual wheel torque controller to govern vehicle lateral position using frequency-

weighted coordination [Brennan and Alleyne, 2001]. Classical SISO approaches were utilized to solve the MISO problem while the wheel torque input acting at high-frequency and front steering for low-frequency.

Remarks: It is expected that the coordinated steering and torque-biased VDC could potentially enhance the vehicle performance better than any of the two alone. However, as several sub-systems all have control authorities on the controlled vehicle motions, coordination is essential. Without good coordination, conflicting actions may occur among the different sub-systems. As more and more advanced actuation systems are equipped on vehicles, a unified and optimal control approach to globally coordinate all the available actuation resources to best fulfill the VDC control tasks are then desirable.

2.4.4 Active Suspension-Based Vehicle Stability Control Systems

In addition to the VDC system using steering and/or longitudinal force distribution, there exist other systems using active suspensions to enhance the vehicle stability and maneuverability. For example, Elbeheiry et al. investigated the integration between active front steering system and active roll moment control (ARMC) system to enhance the vehicle controllability in hard emergency situations [Elbeheiry et al., 2001]. The ARMC system actively differentiates the front and rear axles' vertical suspension forces to change the vehicle yaw rate and reduce the vehicle roll motion. A 2-DOF nonlinear vehicle model is used for the controller design. Simulation studies show that the vehicle yaw rate control performance can be improved with coordination between the AFS and ARMC.

2.5 SUMMARY

In this chapter, tire forces/moments and tire models are discussed. The well-known Magic Formula tire model is selected for this dissertation due to its capability in

accurately describing complex tire behaviors. Vehicle dynamic is introduced with the emphasis placed on the control-oriented vehicle dynamics model.

A review of existing vehicle dynamics control approaches is given and it motivated the following research goals:

1) Develop a globally coordinated vehicle dynamics control system.
2) The control system should be able to coordinate all the possible actuation in a unified and optimal manner.
3) The control system should fulfill multiple vehicle control tasks simultaneously. If they are not achievable at the same time, an appropriate prioritization mechanism should be included in the control system.
4) Reconfigurable control needs to be adapted in the system to best achieve the control tasks in case some actuation degrades and/or fails.
5) The overall performance of the developed system should be superior compared with the existing vehicle control approaches especially under adverse driving conditions.

Chapter 3: Tracking Control for Nonlinear Systems

In this chapter, we discuss the problem of tracking control for nonlinear dynamical systems with and without actuation constraints. Different nonlinear control law design methods will be discussed. A modular control structure with control allocation to resolve actuation redundancy and constraints will be described. The overall coordinated vehicle dynamics control (CVDC) structure employing control allocation will be proposed. The higher-level nonlinear controller for the CVDC system will be designed as well.

Controlling the outputs of a given system to track a desired time-varying trajectory is one of the most common and important problems for both control theory research and engineering practice. Since the 1980s', nonlinear control theories and design methods have been significantly advanced. For a class of nonlinear systems without actuation constraints, several well-known control design approaches have been applied, namely feedback linearization, sliding mode control, backstepping control design, and adaptive control etc. Nonlinear control design methods are almost exclusively based upon Lyapunov theory. For tracking control, the goal is to construct a control law that can bring the system states to, or close enough to, desired time-varying values. In other words, we aim at making the desired states equilibrium of the closed-loop system.

Systems with actuation constraints are very common in practice. The most popular actuation constraints are amplitude saturation and rate limits. Exceeding actuation amplitude and rate limits could cause closed-loop tracking performance deterioration such as integral windup, and even affect system stability properties such as leading to limit cycling and unstable responses. For some actuators, exceeding the

actuation constraints may induce their unstable modes. In literature, several control approaches are proposed to deal with nonlinear systems with actuation constraints, but mostly for actuation amplitude saturation type constraint only. The control systems utilizing control allocation methods can address both actuation amplitude saturation and actuation rate limits as well as optimally resolve actuation redundancy. This approach will be introduced at the end of this chapter and in the following chapters.

Even though we only consider nonlinear tracking control systems in this chapter, it should be pointed out that substantial theoretical advancements in the area of feedback control of linear dynamical systems subject to actuation and/or state constraints have been made. Most of them focus on regulation problems with time-invariant constraints for linear systems [Nguyen and Jabbari, 2000], [Angeli et al., 2000], [Sussmann et al., 1994]. However, nonlinear tracking control with actuation constraints remains a research topic.

3.1 LYAPUNOV THEORY

We briefly present the definitions and tools for proving system stability in the sense of Lyapunov. More detailed materials can be found in [Slotine and Li, 1991] and [Sastry and Bodson, 1989]. Consider the following general system,

$$\dot{x} = f(t, x), \qquad x(t_0) = x_0, \tag{3.1}$$

where $x \in \Re^n, t \geq 0$. The system above is called *autonomous* (or *time-invariant*) if f does not explicitly depend on time t, and *non-autonomous* (or *time-varying*), otherwise. Here, we only consider autonomous systems,

$$\dot{x} = f(x) \qquad x(t_0) = x_0. \tag{3.2}$$

We define the $x = x_e$ be an equilibrium of the system if $f(x_e) = 0$. The stability properties of the equilibrium point can be characterized by the following definitions.

Definition 3.1 (Stability in the Sense of Lyapunov) The equilibrium point $x = x_e$ of (3.2) is stable in the sense of Lyapunov (ISL), if $\forall \varepsilon > 0$, there exists $\delta(t_0, \varepsilon) > 0$ such that,

$$\|x(t_0) - x_e\| < \delta \;\Rightarrow\; \|x(t) - x_e\| < \varepsilon, \qquad \forall t \geq t_0 . \tag{3.3}$$

The system is unstable if it is not stable.

Definition 3.2 (Uniform Stability) x_e is call a *uniformly stable* equilibrium point of (3.2) if δ in Definition 3.1 is independent of t_0.

We can notice that the stability requirement can only ensure the system states are not going to move away from the equilibrium point with time. However, it does not guarantee systems have the tendency of going to the equilibrium point when started close to it enough, which will be captured by the following definition.

Definition 3.3 (Asymptotic Stability) x_e is an *asymptotically stable* (AS) equilibrium point of (3.2), if

a) x_e is a stable equilibrium point ISL,
b) $\forall t_0 \geq 0$, there exists $\delta(t_0)$, such that $\|x_0 - x_e\| < \delta \;\Rightarrow\; \lim_{t\to\infty} x(t) = x_e$.

If x_e is AS and $\lim_{t\to\infty} x(t) = x_e$ holds for all $x_0 \in \Re^n$, it is called a *globally asymptotically stable* (GAS) equilibrium point of (3.2).

Note that for the asymptotic stability property, the speed of convergence is not quantified in the definition. The following definition requires at least exponential convergence rate.

Definition 3.4 (Exponential Stability) x_e is called an exponentially stable equilibrium point of (3.2) if there exist $\alpha > 0$ and $\forall \varepsilon > 0$, $\exists \delta(\varepsilon)$, such that the solution of the system satisfies

$$\|x(t) - x_e\| \leq \varepsilon e^{-a(t-t_0)} \|x_0 - x_e\|, \text{ whenever } \|x_0 - x_e\| \leq \delta . \tag{3.4}$$

Exponential stability (ES) is the strongest form in stability. For nonlinear control systems, it is sometime challenging to design a control law to achieve ES.

In the above definitions, $x(t)$ is the solution of (3.2) starting from x_0 and t_0. In general, it is difficult to find $x(t)$ analytically, which makes it difficult to evaluate the stability properties directly. Fortunately some alternative ways for proving stability have been developed. A. M. Lyapunov, a Russian mathematician and engineer, introduced the idea of condensing the system state vector $x(t)$ into a scalar function $V(x)$ to measure how far the states are from the equilibrium point. If the function $V(x)$ decreases with time, the system must be moving towards the equilibrium. This approach is often refereed to as Lyapunov's direct stability method (or second method) and widely used to prove stability for nonlinear control systems.

Before presenting the Lyapunov stability theory, let us give some more useful definitions.

Definition 3.5 (Locally Positive Definite Functions) A continuous function $V(x)$ is called a *locally positive definite function* (LPDF) if, for some $\delta > 0$, and some $\alpha(\cdot) \in K$ ($\alpha(\cdot)$ is a class K function, i.e. $\alpha(\cdot)$ is continuous and strictly increasing with $\alpha(0) = 0$), such that,

$$V(0) = 0 \quad \text{and} \quad V(x) \geq \alpha(|x|) \quad \text{for all } \|x - x_e\| \leq \delta . \tag{3.5}$$

The function is called a *positive definite function* (PDF) if (3.5) holds for $x \in \Re^n$. $V(x)$ is said to be *negative definite* if $-V(x)$ is positive definite.

Definition 3.6 (Radially Unbounded Functions) A function $V(x)$ with $V(0) = 0$ is said to be *radially unbounded* if there exists a function $\phi(\cdot) \in KR$ ($\phi(\cdot)$ is a class KR function, i.e. $\phi(\cdot) \in K$ and $\lim_{r \to \infty} \phi(r) = \infty$), such that,

$$V(x) \geq \phi(\|x\|) \quad \text{for all } x \in \Re^n . \tag{3.6}$$

Now we are ready to state the basic theorem of Lyapunov for global asymptotic stability.

Theorem 3.1 (Theorem of Lyapunov) For the system (3.2) and let $f(0) = 0$. Let $V(x)$ be a positive definite, radially unbounded, and continuously differentiable scalar function. If

$$\dot{V}(x) = \frac{dV(x)}{dx} f(x) < 0, \quad \text{for } x \neq 0, \tag{3.7}$$

then $x = 0$ is a globally asymptotically stable (GAS) equilibrium point.

A positive definite function $V(x)$ whose derivative satisfies $\dot{V}(x) \leq 0$ is said to be a Lyapunov function of the system. The radially unboundedness requirement is necessary to guarantee that the GAS property holds globally. If $V(x)$ is locally PD, the system will be locally AS as well.

3.2 NONLINEAR TRACKING CONTROL WITHOUT ACTUATION CONSTRAINTS

Feedback linearization, sliding mode control, and backstepping are the most well-known nonlinear control design methods. Even though actuation constraints are not considered in these design methodologies, they are widely used for a class of nonlinear systems in engineering practice. Here, we briefly describe the backstepping design method and sliding mode control.

3.2.1 Backstepping Method

Theorem 3.1 implies that the closed-loop asymptotic stability can be achieved by constructing a control law with an appropriate Lyapunov function. Consider the system with a control input as,

$$\dot{x} = f(x, u), \quad u = c(x). \tag{3.8}$$

The closed-loop system can then be written as,

$$\dot{x} = f(x, c(x)) \tag{3.9}$$

If we can construct a control law $u = c(x)$ along with an appropriate Lyapunov function $V(x)$ such that,

$$\dot{V} = \frac{dV}{dx} f(x, c(x)) < 0, \quad \text{for } x \neq 0, \tag{3.10}$$

the closed-system can be guaranteed to be AS. The corresponding Lyapunov function is called *control Lyapunov function* (CLF) [Krstic et al., 1995]. However, in practice, finding the appropriate CLF and control law is not trivial and often depends on the imagination and experience of the designers. For a class of nonlinear systems, backstepping offers a systematic method for nonlinear control design through a recursive design procedure which gives a Lyapunov function and the associated control law. The backstepping design method is well documented in [Krstic et al., 1995] and here we briefly review the method. The main idea in backstepping is to make some states act as "virtual control inputs" of others and design the control law in a cascade way. Consider the system below,

$$\begin{aligned}
\dot{x}_1 &= f_1(x_1) + x_2 \\
\dot{x}_2 &= f_2(x_1, x_2) + x_3 \\
&\vdots \\
\dot{x}_{n-1} &= f_{n-1}(x_1, x_2, \cdots, x_{n-1}) + x_n \\
\dot{x}_n &= f_n(x_1, x_2, \cdots, x_n) + u
\end{aligned} \tag{3.11}$$

$$y = x_1$$

The backstepping procedure is to design control for x_i using x_{i+1} as a virtual control input and define a Lyapunov function for each step. At the final step, augment all the Lyapunov function at each stage and derive the actual control law. More specifically, at step 1, let us assume x_2 as the virtual control input. Design x_2 as a stabilizing control to make x_1 asymptotically stable. For example, the desired x_2 could be

$$g_1(x_1) := -f_1(x_1) - \lambda_1 x_1, \quad \lambda_1 > 0. \tag{3.12}$$

We can let the Lyapunov function for step 1 as,

$$V_1(x_1) = \frac{1}{2}x_1^2, \tag{3.13}$$

$$\dot{V}_1 = x_1\left[f_1(x_1) + x_2\right] = x_1\left[-g_1(x_1) - \lambda_1 x_1 + x_2\right] = -\lambda_1 x_1^2 + x_1\underbrace{\left[x_2 - g_1(x_1)\right]}_{z_2}. \tag{3.14}$$

Thus, at step 2, control should be designed to drive $z_2 \to 0$, which makes $\dot{V}_1$ negative definite. Define a coordinate transform as: $(x_1, x_2) \to (x_1, z_2)$, and $z_2 = x_2 - g_1(x_1)$ is the difference between the actual state x_2 and its desired value $g_1(x_1)$. We then have,

$$\begin{aligned}
\dot{x}_1 &= f_1(x_1) + z_2 + g_1(x_1) = -\lambda_1 x_1 + z_2 \\
\dot{z}_2 &= \dot{x}_2 - \frac{\partial g_1}{\partial x_1}\left[f_1(x_1) + x_2\right] = f_2(x_1, x_2) - \frac{\partial g_1}{\partial x_1}\left[f_1(x_1) + x_2\right] + x_3 . \\
&= \bar{f}_2(x_1, z_2) + x_3
\end{aligned} \tag{3.15}$$

By augmenting the Lyapunov function, we have,

$$V_2(x_1, z_2) = V_1(x_1) + \frac{1}{2}z_2^2, \tag{3.16}$$

$$\dot{V}_2 = -\lambda_1 x_1^2 + x_1 z_2 + z_2\left[\bar{f}_2(x_1, z_2) + x_3\right]. \tag{3.17}$$

A proper virtual control for x_3 can be selected as,

$$g_2(x_1, z_2) := -\bar{f}_2(x_1, z_2) - x_1 - \lambda_2 z_2, \tag{3.18}$$

which gives

$$\dot{V}_2 = -\lambda_1 x_1^2 - \lambda_2 z_2^2 + z_2 z_3 . \tag{3.19}$$

where $z_3 := x_3 - g_2(x_1, z_2)$ is defined as the difference between actual state x_3 and the desired one. The transformed system is then given as,

$$\begin{aligned}
\dot{x}_1 &= -\lambda_1 x_1 + z_2 \\
\dot{z}_2 &= \bar{f}_2(x_1, z_2) + x_3 = -x_1 - \lambda_2 z_2 + z_3
\end{aligned}. \tag{3.20}$$

Follow the same fashion, we can have

$$\begin{aligned}\dot{z}_3 &= \dot{x}_3 - \left(\frac{\partial g_2}{\partial x_1}\dot{x}_1 + \frac{\partial g_2}{\partial z_2}\dot{z}_2\right) \\ &= f_3(x_1, x_2, x_3) - \left(\frac{\partial g_2}{\partial x_1}\dot{x}_1 + \frac{\partial g_2}{\partial z_2}\dot{z}_2\right) + x_4 \\ &= \bar{f}_3(x_1, z_2, z_3) + x_4\end{aligned} . \tag{3.21}$$

Augment the Lyapunov function as,

$$V_3(x_1, z_2, z_3) = V_2(x_1, z_2) + \frac{1}{2}z_3^2, \tag{3.22}$$

$$\dot{V}_3 = -\lambda_1 x_1^2 - \lambda_2 z_2^2 + z_2 z_3 + z_3\left[\bar{f}_3(x_1, z_2, z_3) + x_4\right]. \tag{3.23}$$

This suggests a virtual control for x_4 as,

$$g_3(x_1, z_2, z_3) := -\bar{f}_3(x_1, z_2, z_3) - z_2 - \lambda_3 z_3. \tag{3.24}$$

Following the same procedure, we can reach the last step and have,

$$\begin{aligned}\dot{x}_1 &= -\lambda_1 x_1 + z_2 \\ \dot{z}_2 &= -x_1 - \lambda_2 z_2 + z_3 \\ &\vdots \\ \dot{z}_n &= \dot{x}_n - \left(\frac{\partial g_{n-1}}{\partial x_1}\dot{x}_1 + \frac{\partial g_{n-1}}{\partial z_2}\dot{z}_2 + \cdots\right) \\ &= f_n(x_1, x_2, \cdots, x_n) - \left(\frac{\partial g_{n-1}}{\partial x_1}\dot{x}_1 + \frac{\partial g_{n-1}}{\partial z_2}\dot{z}_2 + \cdots\right) + u \\ &= \bar{f}_n(x_1, z_2, \cdots, z_n) + u\end{aligned} . \tag{3.25}$$

The final augmented Lyapunov function is,

$$\begin{aligned}V_n(x_1, z_2, z_3, \cdots) &= V_{n-1}(x_1, z_2, \cdots, z_{n-1}) + \frac{1}{2}z_n^2 \\ &= \frac{1}{2}\left(x_1^2 + z_2^2 + \cdots + z_n^2\right)\end{aligned} , \tag{3.26}$$

$$\dot{V}_n = -\lambda_1 x_1^2 - \sum_{k=2}^{n-1}\lambda_k z_k^2 + z_{n-1}z_n + z_n\left[\bar{f}_n(x_1, z_2, \cdots, z_n) + u\right]. \tag{3.27}$$

If we choose $u = -\bar{f}_n(x_1, z_2, \cdots, z_n) - z_{n-1} - \lambda_n z_n$, then,

$$\dot{V}_n = -\lambda_1 x_1^2 - \sum_{k=2}^{n} \lambda_k z_k^2 , \tag{3.28}$$

which is negative definite for $\lambda_k > 0$. Thus, this control law can ensure asymptotical convergence of x_1 to 0.

Remarks:

1) As we can see from the above description, the systems need to be triangular cascade (strict feedback form) in order to apply backstepping design method.
2) In derivation of the control law, virtual controls of previous steps need to be analytically differentiated. It may result in proliferation of terms for the final control law.
3) Robustness of the resultant control law w.r.t. system parametric uncertainties and un-modeled dynamics is not explicitly revealed.

The backstepping method presented above can be used for trajectory tracking control as shown in the following example.

Example 3.1 Backstepping tracking control Consider the following nonlinear system,

$$\begin{aligned} \dot{x}_1 &= x_2 + (x_1 - a)^2 \\ \dot{x}_2 &= x_1 + u \end{aligned} , \tag{3.29}$$

where u is control input and we want the system state x_1 to track a desired time-varying trajectory given by $r = b\sin(\omega t)$.

Let's define the tracking error as $\tilde{x}_1 = x_1 - r$. Then we have

$$\dot{\tilde{x}}_1 = \dot{x}_1 - \dot{r} = x_2 + (x_1 - a)^2 - \dot{r} = x_2 + f_1 , \tag{3.30}$$

where $f_1 = (\tilde{x}_1 + r - a)^2 - \dot{r}$. We want to treat x_2 as a virtual control to drive the tracking error $\tilde{x}_1$ to zero for the trajectory tracking purpose. Consider the Lyapunov function candidate,

$$V_1(\tilde{x}_1) = \frac{1}{2}\tilde{x}_1^2, \tag{3.31}$$

$$\dot{V}_1 = \tilde{x}_1\dot{\tilde{x}}_1 = \tilde{x}_1(x_2 + f_1). \tag{3.32}$$

It provides the hint to choose the virtual control (or desired x_2) as $g_1(\tilde{x}_1, r, \dot{r}) = -f_1 - \lambda_1\tilde{x}_1$, $\lambda_1 > 0$ Then,

$$\dot{V}_1 = \tilde{x}_1[x_2 - \lambda_1\tilde{x}_1 - g_1(\tilde{x}_1, r, \dot{r})] = -\lambda_1\tilde{x}_1^2 + \tilde{x}_1[x_2 - g_1(\tilde{x}_1, r, \dot{r})]. \tag{3.33}$$

Define the difference between actual state x_2 and the desired one as $z = x_2 - g_1(\tilde{x}_1, r, \dot{r})$. We then take the derivative of z as,

$$\begin{aligned}\dot{z} &= \dot{x}_2 - \frac{\partial g_1}{\partial \tilde{x}_1}\dot{\tilde{x}}_1 - \frac{\partial g_1}{\partial r}\dot{r} - \frac{\partial g_1}{\partial \dot{r}}\ddot{r} \\ &= x_1 + u - \frac{\partial g_1}{\partial \tilde{x}_1}(x_2 + f_1) - \frac{\partial g_1}{\partial r}\dot{r} - \frac{\partial g_1}{\partial \dot{r}}\ddot{r}. \\ &= f_2 + u\end{aligned} \tag{3.34}$$

Consider the augmented Lyapunov function candidate,

$$V_2(\tilde{x}_1, z) = V_1(\tilde{x}_1) + \frac{1}{2}z^2. \tag{3.35}$$

Take its derivative, we can have,

$$\begin{aligned}\dot{V}_2 &= -\lambda_1\tilde{x}_1^2 + \tilde{x}_1[x_2 - g_1(\tilde{x}_1, r, \dot{r})] + z(f_2 + u) \\ &= -\lambda_1\tilde{x}_1^2 + \tilde{x}_1 z + z(f_2 + u)\end{aligned}. \tag{3.36}$$

It becomes clear that if we choose the control law as $u = -f_2 - \tilde{x}_1 - \lambda_2 z$, $\lambda_2 > 0$ then

$$\dot{V}_2 = -\lambda_1\tilde{x}_1^2 + \tilde{x}_1 z + z(f_2 + u) = -\lambda_1\tilde{x}_1^2 - \lambda_2 z^2, \tag{3.37}$$

which is negative definite. Therefore, both $\tilde{x}_1$ and z converge to zero asymptotically. The resultant control law is given by,

$$
\begin{aligned}
u &= -f_2 - \tilde{x}_1 - \lambda_2 z \\
&= -2x_1 + \frac{\partial g_1}{\partial \tilde{x}_1}(x_2 + f_1) + \frac{\partial g_1}{\partial r}\dot{r} + \frac{\partial g_1}{\partial \dot{r}}\ddot{r} + r - \lambda_2\left[x_2 - g_1(\tilde{x}_1, r, \dot{r})\right] \\
&= -2x_1 + \left[-2(\tilde{x}_1 + r - a) - \lambda_1\right]\left[x_2 + (\tilde{x}_1 + r - a)^2 - \dot{r}\right] - 2(\tilde{x}_1 + r - a)\dot{r} \\
&\quad + \ddot{r} + r - \lambda_2\left[x_2 + (\tilde{x}_1 + r - a)^2 - \dot{r} + \lambda_1\tilde{x}_1\right]
\end{aligned}
\qquad (3.38)
$$

One can find that there are already many terms involved in the control law for such a simple system.

The system is simulated with the parameters $a = b = \omega = 1$, and $\lambda_1 = \lambda_2 = 2$. In the simulation, the initial condition is set as $x_0 = \begin{bmatrix} 1 & -1 \end{bmatrix}^T$. Figure 3.1 shows the simulation results. The system output x_1 can track the reference trajectory well.

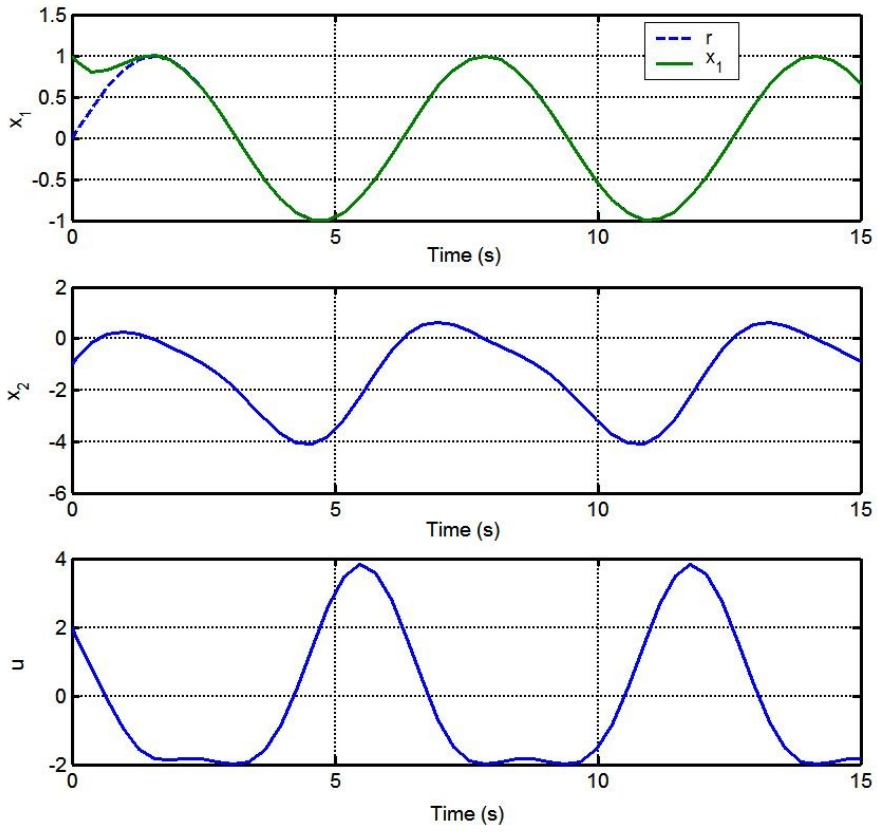

Figure 3.1 Simulation results of the backstepping control for Example 3.1

3.2.2 Sliding Mode Control

Feedback linearization and sliding mode control (SMC) share some similar design procedures. Insensitivity and robustness of sliding mode control to plant disturbances, parametric uncertainties, and un-modeled dynamics make it attractive for many engineering applications [Slotine and Li, 1991], [Fernandez and Hedrick, 1987], [Utkin, 1992]. Here we describe the SMC method introduced in [Slotine and Li, 1991].

Consider the SISO nonlinear system described below,

$$\begin{aligned} \dot{x} &= f(x) + g(x)u + g_w(x)w \\ y &= h(x) \end{aligned}, \tag{3.39}$$

where $y \in \Re$ is the output, $u \in \Re$ is the input, and $w \in \Re$ is an unknown disturbance. Assume the system has *relative degree* of n with respect to both control input u and unknown disturbance w, which means the output function $y = h(x)$ needs to be differentiated n times to have input u and disturbance w show in its expression. The system then can be transformed into controller canonical form as,

$$\begin{aligned} \dot{z}_1 &= z_2 \\ \dot{z}_2 &= z_3 \\ &\vdots \\ \dot{z}_{n-1} &= z_n \\ \dot{z}_n &= L_f^n h(x) + L_g L_f^{n-1} u + L_{gw} L_f^{n-1} w = a(x) + b(x)u + b_w(x)w . \end{aligned} \tag{3.40}$$

where $L_f h(x) = \dfrac{\partial h}{\partial x} f(x)$ is the Lie derivative or directional derivative of h in the direction of the vector field $f(\cdot)$. $z_1 = h(x)$ and $z_i = L_f^{i-1} h(x)$ for $i = 2, 3, \cdots, n$ consist of the coordinate transformation of the original system.

We want the control system to achieve asymptotic tracking, which is $y(t) \to y_d(t)$ as $t \to 0$. Define the tracking errors as,

$$e_1 = z_1 - y_d = y - y_d ,$$

$$e_2 = z_2 - \dot{y}_d = \dot{y} - \dot{y}_d,$$
$$\vdots$$
$$e_n = z_n - y_d^{(n-1)} = y^{(n-1)} - y_d^{(n-1)}. \tag{3.41}$$

Notice that $\dot{e}_k = e_{k+1}$ holds for $k = 1, \cdots, n-2$. We can define a sliding surface as:

$$S = e_n + a_{n-2}e_{n-1} + a_{n-3}e_{n-2} + \cdots + a_1 e_2 + a_0 e_1, \tag{3.42}$$

where a_k, $k = 0, \cdots, n-2$ can be chosen to be the coefficients of a polynomial which is Hurwitz. These coefficients determine the dynamic behavior of the sliding surface. For example, the coefficients can be selected as the following stable cascade of first-order polynomials with the same pole,

$$(s+p)^{n-1} = s^{n-1} + a_{n-2}s^{n-2} + a_{n-3}s^{n-3} + \cdots + a_1 s + a_0, \tag{3.43}$$

where $-p < 0$ is the common pole.

Take the derivative of the sliding surface, we can have,

$$\dot{S} = \dot{e}_n + \sum_{k=0}^{n-2} a_k e_{k+2}. \tag{3.44}$$

The tracking errors will go to zero as $S \to 0$. Consider the Lyapunov function candidate,

$$V = \frac{1}{2}S^2. \tag{3.45}$$

Taking the derivative, we have,

$$\begin{aligned} \dot{V} &= S\dot{S} \\ &= S\left(\dot{e}_n + \sum_{k=0}^{n-2} a_k e_{k+2} \right) \\ &= S\left(\dot{z}_n - y_d^{(n)} + \sum_{k=0}^{n-2} a_k e_{k+2} \right) \\ &= S\left(a(x) + b(x)u + b_w(x)w - y_d^{(n)} + \sum_{k=0}^{n-2} a_k e_{k+2} \right) \end{aligned} \tag{3.46}$$

An appropriate control law can therefore be selected as,

$$u(t) = \frac{1}{\bar{b}(x)}\left[-\bar{a}(x) - \overline{b_w(x)w(t)} + y_d^{(n)} - \sum_{k=0}^{n-2} a_k e_{k+2} - K(t)\,\mathrm{sgn}(S) \right]. \tag{3.47}$$

where $\bar{a}(x)$, $\bar{b}(x)$, and $\overline{b_w(x)w(t)}$ are the estimates of $a(x)$, $b(x)$, and $b_w(x)w(t)$, respectively. Note that in order to keep the relative degree unchanged, we require $b(x) \in [b_{\min}, \ b_{\max}]$ should not change sign despite the parameter uncertainties. In other words, $b(x) \neq 0$. We can define the discrepancy of the control caused by uncertainties as,

$$d(t) = \left[a(x) - \frac{b(x)}{\bar{b}(x)}\bar{a}(x) \right] + \left(\frac{b(x)}{\bar{b}(x)} - 1 \right)\left[y_d^{(n)} - \sum_{k=0}^{n-2} a_k e_{k+2} \right] - \left[\frac{b(x)}{\bar{b}(x)}\overline{b_w(x)w(t)} - b_w(x)w(t) \right] \tag{3.48}$$

Substitute (3.47) and (3.48) into (3.46), we can then have,

$$\begin{aligned} \dot{V} &= S\left[d(t) + \frac{b(x)}{\bar{b}(x)} K(t)\,\mathrm{sgn}(S) \right] \\ &= S\,\mathrm{sgn}(S)\left[d(t)\,\mathrm{sgn}(S) + \frac{b(x)}{\bar{b}(x)} K(t) \right]. \\ &\leq |S|\left[|d(t)| + \frac{b(x)}{\bar{b}(x)} K(t) \right] \end{aligned} \tag{3.49}$$

Since $V = \frac{1}{2}S^2 = \frac{1}{2}|S|^2$,

$$\dot{V} = |S|\frac{d|S|}{dt}. \tag{3.50}$$

If $|S|\frac{d|S|}{dt} \leq -\eta|S|$ can be satisfied, then we have,

$$\frac{d|S|}{dt} \leq -\eta, \tag{3.51}$$

whenever $S \neq 0$. It implies that $|S| \to 0$ within a finite time given by $|S(t=0)|/\eta$. This is refereed to as the reaching phase, and $\eta > 0$ is the design parameter. Once the sliding surface becomes zero, it will remain at zero thereafter, which is called the sliding phase. In order to satisfy (3.51), the gain $K(t)$ in (3.49) needs to be sufficiently large. However, unnecessarily large gain may cause noise sensitivity issue.

Let $\bar{b}(x)$ be the geometric mean of the upper and lower bounds of $b(x)$ [Slotine and Li, 1991],

$$\bar{b}(x) = \text{sgn}(b(x))\sqrt{b_{\min} b_{\max}} \ . \tag{3.52}$$

We then have,

$$\beta^{-1} \le \frac{b(x)}{\bar{b}(x)} \le \beta \text{, and } \beta = \sqrt{\frac{b_{\max}}{b_{\min}}} \ . \tag{3.53}$$

Based on this, we can obtain the lower bound on the gain as,

$$K(t) \ge \left(|d(t)| + \eta\right)\beta \ . \tag{3.54}$$

This gain can guarantee $\dot{V} \le -\eta|S|$ and therefore the attractiveness of the sliding surface, which in turn gives desired system tracking performance.

Ideal SMC requires infinitely fast switching around the sliding surface because of the involvement of $\text{sgn}(S)$ in the control law, which may lead to control chattering in practical digital computer implementation. If the chattering frequency is within the structural bandwidth of the system, it may trigger problematic responses due to un-modeled dynamics. However, if the control switching frequency is much higher than any of system structural modes, the chatter may not cause noticeable effects [Li, 2002]. In practical implementation of SMC, the chattering can be avoided by introducing continuous approximation of the switching function [Esfandiary and Khalil, 1991], [Slotine and Li, 1991]. For example, the sgn function can be replaced by a saturation function as,

$$\text{sgn}(S) \approx sat\left(\frac{S}{\Omega}\right), \tag{3.55}$$

where Ω is the boundary layer thickness. The saturation function is defined as,

$$sat(x) = \begin{cases} 1 & x \ge \Omega \\ x & |x| < \Omega \\ -1 & x \le -\Omega \end{cases} . \tag{3.56}$$

The control law then becomes,

$$u(t) = \frac{1}{\bar{b}(x)}\left[-\bar{a}(x) - \overline{b_w(x)w(t)} + y_d^{(n)} - \sum_{k=0}^{n-2} a_k e_{k+2} - K(t)sat(S/\Omega) \right]. \tag{3.57}$$

The continuous approximations usually cause bounded steady-state tracking error. Instead of converging to the origin, the tracking error will converge to a neighborhood of the origin whose size is $o(\Omega)$ [Seshagiri and Khalil, 2002]. However, if desired, the steady-state tracking error can be eliminated by introducing integral actions in sliding surface [Seshagiri and Khalil, 2002], [Mantz et al., 1999], [Cheng and Miu, 1999].

Notice that the control law includes the calculation of e_{k+2}, which requires the measured output signal be differentiated for $k+1$ times. For systems with high relative degrees, high-order differentiating of the output signal that is usually contaminated by measurement noise may cause some undesirable behaviors.

3.2.3 MIMO Nonlinear Systems

Control design methods for nonlinear multi-input-multi-output (MIMO) systems are not as readily available as for SISO systems. As mentioned before, almost all the nonlinear control methodologies rely on using Lyapunov theories to prove stability. For MIMO nonlinear systems, obtaining successful Lyapunov functions is much more challenging than for SISO systems. *Uniform detectable obstacles* are often encountered in the derivations of control laws for MIMO systems [Akella, 2006]. General robust MIMO nonlinear control is still a research topic. If the control inputs are decoupled, or in other words, each output channel corresponds to only one and different control input, the design methods for SISO systems can be readily extended to MIMO systems by simply treating them as several SISO systems put together. However, if the control inputs are coupled, extending to MIMO system is not trivial. Under certain circumstances, some of the nonlinear control design methods for the SISO systems can be extended to the MIMO

systems. But it is often requisite that the MIMO systems have the same number of control inputs and controlled outputs, or the systems are square. Consider the following time-invariant MIMO nonlinear system with linear in the controls,

$$\dot{x} = f(x) + \sum_{k=1}^{m} g_k(x) u_k \,,$$

$$\begin{pmatrix} y_1 \\ y_2 \\ \vdots \\ y_m \end{pmatrix} = \begin{pmatrix} h_1(x) \\ h_2(x) \\ \vdots \\ h_m(x) \end{pmatrix}. \tag{3.58}$$

where $x \in \Re^m$. It is a m-input-m-output system. Assume each output channel y_k has a smallest relative degree r_k with respect to any input u_i, $i = 1, \cdots, m$. This means that,

$$y_k^{(r_k)} = L_f^{r_k} h_k(x) + L_g L_f^{r_k - 1} h_k(x) u \,, \tag{3.59}$$

where $L_g L_f^{r_k - 1} h_k(x) \in \Re^{1 \times m}$, has at least one non-zero element. Combine all the m equations, and we can have,

$$\begin{pmatrix} y_1^{(r_1)} \\ y_2^{(r_2)} \\ \vdots \\ y_m^{(r_m)} \end{pmatrix} = A(x) + B(x) u \,, \tag{3.60}$$

where $A(x) \in \Re^{m \times 1}$ and $B(x) \in \Re^{m \times m}$. In order to apply SMC or feedback linearization, it is required that the system satisfies the *matching condition*, i.e. $B(x)$ is invertible.

A MIMO system is said to have a *vector relative degree* $\begin{bmatrix} r_1 & r_2 & \cdots & r_m \end{bmatrix}^T$ if individual output y_k has a relative degree of r_k and $B(x)$ is invertible. If the vector relative degree satisfies $r_1 + r_2 + \cdots + r_m = r = n$, then the output y_k and its derivatives can construct n independent coordinate functions, there will be no any internal (or zero) dynamics. If $r < n$, then we need to ensure that the internal dynamics are stable. The MIMO sliding mode control design methodology is well documented in [Fernández and Hedrick, 1987].

3.3 NONLINEAR TRACKING CONTROL WITH ACTUATION CONSTRAINTS

The nonlinear control synthesis methods presented in the previous section provide powerful control design strategies for a large class of nonlinear systems. However, the actuation constraints are not considered in the control law design. For systems where violations of actuation constraints are highly undesirable or prohibitive, explicitly addressing the actuation constraints would be necessary. For nonlinear systems with actuation constraints, control designs are performed on a case-by-case basis. In this section, we present several approaches for handling actuation constraints, mainly amplitude saturation constraint.

3.3.1 Incorporation of Actuation Saturation in Control Laws

Hyperbolic functions are used to design control laws for some nonlinear systems having input saturation constraints [Akella, 2006] and [Wallsgrove and Akella, 2005]. Here we show the spirit of the method through an example. Consider the pendulum system shown below.

Example 3.2 Pendulum system tracking control with actuation saturation constraint For the simplified pendulum system, suppose we have an input force whose amplitude is muL and always acts in the positive direction perpendicular to the link as shown in Figure 3.2.

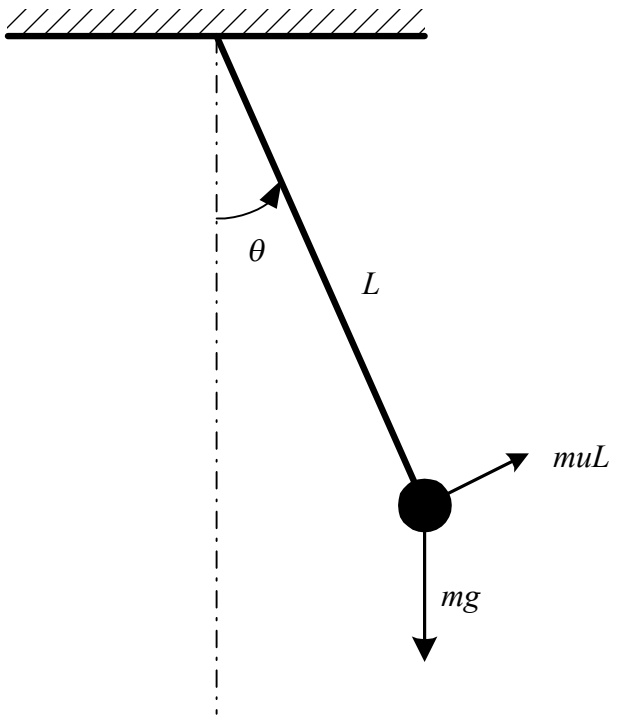

Figure 3.2 The simple pendulum system

The system dynamics can be written in state space form as,

$$\begin{aligned} \dot{x}_1 &= x_2 \\ \dot{x}_2 &= -\frac{g}{L}\sin(x_1) + u \end{aligned}, \tag{3.61}$$

where $x_1 = \theta$, $x_2 = \dot{\theta}$, g is the acceleration due to gravity, m is the mass of the ball, and L is the constant length of the cable. There exists a saturation constraint on the input as,

$$|u| \le u_{\max}. \tag{3.62}$$

We want to design a controller to make θ track a desired time-varying reference signal r without violating the control saturation.

Proposition 3.1: For the above pendulum tracking control problem subject to input saturation constraint, assume the reference signal satisfies $\sup_t |\ddot{r}(t)| \le C < u_{\max}$ and let

$\tilde{u}_m = u_{\max} - \frac{g}{L} - C > 0$, the following controller can achieve asymptotic tracking without violating the input saturation.

$$u = \ddot{r} - \beta\tilde{u}_m \tanh(\lambda_1 e_1) + \frac{g}{L}\sin(e_1 + r) - (1-\beta)\tilde{u}_m \tanh\left[\lambda_2(e_2 + ke_1)\right], \tag{3.62}$$

with

$$\dot{k} = -r_k(1-\beta)\tilde{u}_m e_1\left\{\tanh\left[\lambda_2(e_2 + ke_1)\right] + \tanh(\lambda_1 k e_1)\right\}, \tag{3.63}$$

for any $k(0) \in \Re$, λ_1, λ_2, $r_k > 0$, and $\beta \in (0, \quad 1)$.

Proof: The proof is based on a Lyapunov-like analysis. First, from the above control law, we note that,

$$|u| \le C + \beta\tilde{u}_m + \frac{g}{L} + (1-\beta)\tilde{u}_m = u_{\max}. \tag{3.64}$$

Thus, the actuation saturation constraint is met. Define the tracking error dynamics as,

$$\begin{aligned} e_1 &= x_1 - r \\ e_2 &= x_2 - \dot{r} \end{aligned} \quad \Rightarrow \quad \begin{aligned} \dot{e}_1 &= e_2 \\ \dot{e}_2 &= \dot{x}_2 - \ddot{r} = -\frac{g}{L}\sin(e_1 + r) + u - \ddot{r} \end{aligned}. \tag{3.65}$$

Choose the Lyapunov function candidate as,

$$V = \frac{\beta\tilde{u}_m}{\lambda_1}\log\left[\cos(\lambda_1 e_1)\right] + \frac{1}{2}e_2^2 + \frac{1}{2r_k}k^2. \tag{3.66}$$

It is easy to see that V is radially unbounded and positive definite. Take the derivative of V, we can have,

$$\begin{aligned} \dot{V} &= \beta\tilde{u}_m \tanh(\lambda_1 e_1)e_2 - \frac{g}{L}e_2\sin(e_1 + r) + e_2 u - e_2\ddot{r} + \frac{1}{r_k}k\dot{k} \\ &= e_2\left[\beta\tilde{u}_m \tanh(\lambda_1 e_1) - \frac{g}{L}\sin(e_1 + r) + u - \ddot{r}\right] + \frac{1}{r_k}k\dot{k} \\ &= (e_2 + ke_1)\left[\beta\tilde{u}_m \tanh(\lambda_1 e_1) - \frac{g}{L}\sin(e_1 + r) + u - \ddot{r}\right] \\ &\quad - ke_1\left[\beta\tilde{u}_m \tanh(\lambda_1 e_1) - \frac{g}{L}\sin(e_1 + r) + u - \ddot{r}\right] + \frac{1}{r_k}k\dot{k} \end{aligned}. \tag{3.67}$$

Substitute u and $\dot{k}$ into the above equation, we can have,

$$\begin{aligned}\dot{V} &= -(1-\beta)\tilde{u}_m(e_2+ke_1)\tanh[\lambda_2(e_2+ke_1)] \\ &\quad + \frac{k}{r_k}\left\{\dot{k} + r_k e_1(1-\beta)\tilde{u}_m \tanh[\lambda_2(e_2+ke_1)]\right\} \\ &= -(1-\beta)\tilde{u}_m(e_2+ke_1)\tanh[\lambda_2(e_2+ke_1)] - (1-\beta)\tilde{u}_m ke_1 \tanh(\lambda_1 ke_1)\end{aligned} \quad . \tag{3.68}$$

Since $x\tanh(x) \geq 0,\ \forall x \in \Re$, and $x\tanh(x) = 0 \ \Leftrightarrow \ x = 0$, we have $\dot{V} \leq 0$. From $V \geq 0$ and $\dot{V} \leq 0 \ \Rightarrow\ V$ is a lower bounded and non-increasing function $\Rightarrow\ V \in L_\infty$ $\Rightarrow\ e_1,\ e_2,\ k \in L_\infty$ and $\lim_{t\to\infty} V \overset{\Delta}{=} V_\infty$ exists and is finite. Also we can have, $\lim_{t\to\infty} V = \lim_{t\to\infty}\int_0^t \dot{V}d\tau + V(0) \ \Rightarrow\ \lim_{t\to\infty}\int_0^t \dot{V}d\tau = V_\infty - V(0)$ exists and it is finite, $\lim_{t\to\infty}\int_0^t (e_2+ke_1)\tanh[\lambda_2(e_2+ke_1)]d\tau$ exists and is finite, and $\lim_{t\to\infty}\int_0^t ke_1 \tanh(\lambda_1 ke_1)d\tau$ exists and is finite.

$$\begin{aligned}\frac{d}{dt}\{(e_2+ke_1)\tanh[\lambda_2(e_2+ke_1)]\} &= (e_2+\dot{k}e_1+k\dot{e}_1)\tanh[\lambda_2(e_2+ke_1)] \\ &\quad + (e_2+ke_1)\operatorname{sech}^2[\lambda_2(e_2+ke_1)]\lambda_2(\dot{e}_2+k\dot{e}_1+\dot{k}e_1)\end{aligned} \quad . \tag{3.69}$$

is a function of $e_1,\ e_2,\ k,\ \dot{e}_1,\ \dot{e}_2,\ \dot{k}$. From (3.62) and (3.65), we can have,

$$e_1, e_2, k \in L_\infty \ \Rightarrow\ u \in L_\infty \ \Rightarrow\ \dot{e}_2 \in L_\infty . \tag{3.70}$$

From (3.63), we know $\dot{k}$ is a function of $e_1, e_2, k \ \Rightarrow\ \dot{k} \in L_\infty$. Thus, $\frac{d}{dt}\{(e_2+ke_1)\tanh[\lambda_2(e_2+ke_1)]\} \in L_\infty \ \Rightarrow\ (e_2+ke_1)\tanh[\lambda_2(e_2+ke_1)]$ is uniformly continuous.

Similarly,

$$\begin{aligned}\frac{d}{dt}[ke_1\tanh(\lambda_1 ke_1)] &= \dot{k}e_1\tanh(\lambda_1 ke_1) + k\dot{e}_1\tanh(\lambda_1 ke_1) \\ &\quad + ke_1\operatorname{sech}^2(\lambda_1 ke_1)\lambda_1(k\dot{e}_1+\dot{k}e_1)\end{aligned}, \tag{3.71}$$

is a function of $e_1,\ k,\ \dot{e}_1,\ \dot{k} \in L_\infty \Rightarrow \frac{d}{dt}[ke_1\tanh(\lambda_1 ke_1)] \in L_\infty \Rightarrow ke_1\tanh(\lambda_1 ke_1)$ is uniformly continuous. Therefore, from Barbalat's Lemma, we can have,

$$\begin{cases} \lim_{t\to\infty}\{(e_2 + ke_1)\tanh[\lambda_2(e_2 + ke_1)]\} = 0 \\ \lim_{t\to\infty}[ke_1 \tanh(\lambda_1 ke_1)] = 0 \end{cases}$$

$$\Rightarrow \begin{cases} \lim_{t\to\infty}(e_2 + ke_1) = 0 \\ \lim_{t\to\infty}(ke_1) = 0 \end{cases} . \tag{3.72}$$

$$\Rightarrow \lim_{t\to\infty} e_2 = 0$$

Note $\lim_{t\to\infty} e_2 = \lim_{t\to\infty}\int_0^t \dot{e}_2 d\tau + e_2(0) \Rightarrow \lim_{t\to\infty}\int_0^t \dot{e}_2 d\tau = \lim_{t\to\infty} e_2 - e_2(0) = -e_2(0)$

exists and is finite.

$$\begin{aligned} \ddot{e}_2 &= -\frac{g}{L} e_2 \cos(e_1 + r) + \dot{u} - \ddot{r} \\ &= -\frac{g}{L} e_2 \cos(e_1 + r) + \ddot{r} - \beta\tilde{u}_m \operatorname{sech}^2(\lambda_1 e_1)\lambda_1 \dot{e}_1 + \frac{g}{L} e_2 \cos(e_1 + r) \\ &\quad - (1-\beta)\tilde{u}_m \operatorname{sech}^2[\lambda_2(e_2 + ke_1)]\lambda_2(\dot{e}_2 + k\dot{e}_1 + \dot{k}e_1) - \ddot{r} \\ &= -\beta\tilde{u}_m \operatorname{sech}^2(\lambda_1 e_1)\lambda_1 \dot{e}_1 - (1-\beta)\tilde{u}_m \operatorname{sech}^2[\lambda_2(e_2 + ke_1)]\lambda_2(\dot{e}_2 + k\dot{e}_1 + \dot{k}e_1) \end{aligned} \tag{3.73}$$

We can easily see that $\ddot{e}_2 \in L_\infty \Rightarrow \dot{e}_2$ is uniformly continuous. Barbalat's Lemma dictates that $\lim_{t\to\infty} \dot{e}_2 = 0$. We also know that,

$$\begin{aligned} 0 = \lim_{t\to\infty} \dot{e}_2 &= \lim_{t\to\infty}\left[-\frac{g}{L}\sin(e_1 + r) + u - \ddot{r} \right] \\ &= \lim_{t\to\infty}\{-\beta\tilde{u}_m \tanh(\lambda_1 e_1) - (1-\beta)\tilde{u}_m \tanh[\lambda_2(e_2 + ke_1)]\} \\ &= -\beta\tilde{u}_m \lim_{t\to\infty}[\tanh(\lambda_1 e_1)] - (1-\beta)\tilde{u}_m \lim_{t\to\infty}\{\tanh[\lambda_2(e_2 + ke_1)]\} \end{aligned} \tag{3.74}$$

Since $\lim_{t\to\infty}\{\tanh[\lambda_2(e_2 + ke_1)]\} = 0$, we can have,

$$\lim_{t\to\infty}[\tanh(\lambda_1 e_1)] = 0 \Rightarrow \lim_{t\to\infty} e_1 = 0. \tag{3.75}$$

From (3.72) and (3.75), we can conclude that the system tracking errors go to zero as $t \to \infty$. ■

Figure 3.3 below shows the simulation results of the system with reference signal as $r = \sin(t)$ (rad), and parameters being selected as $\lambda_1 = 6.0$, $\lambda_2 = 2.0$, $r_k = 1.0$, $\beta = 0.6$, $L = 0.5$. The control law developed above is used in the simulation. The initial

conditions are set as $x_1(0) = 2.0\,(\text{rad}) = 114.5916^\circ$, $x_2(0) = 3.0\,(\text{rad/s}) = 171.8873\,(\text{deg/s})$, and $k(0) = 0.0$. Two cases with different actuation saturation upper bounds $u_{\max 1} = 22.0$ and $u_{\max 2} = 40.0$ are presented.

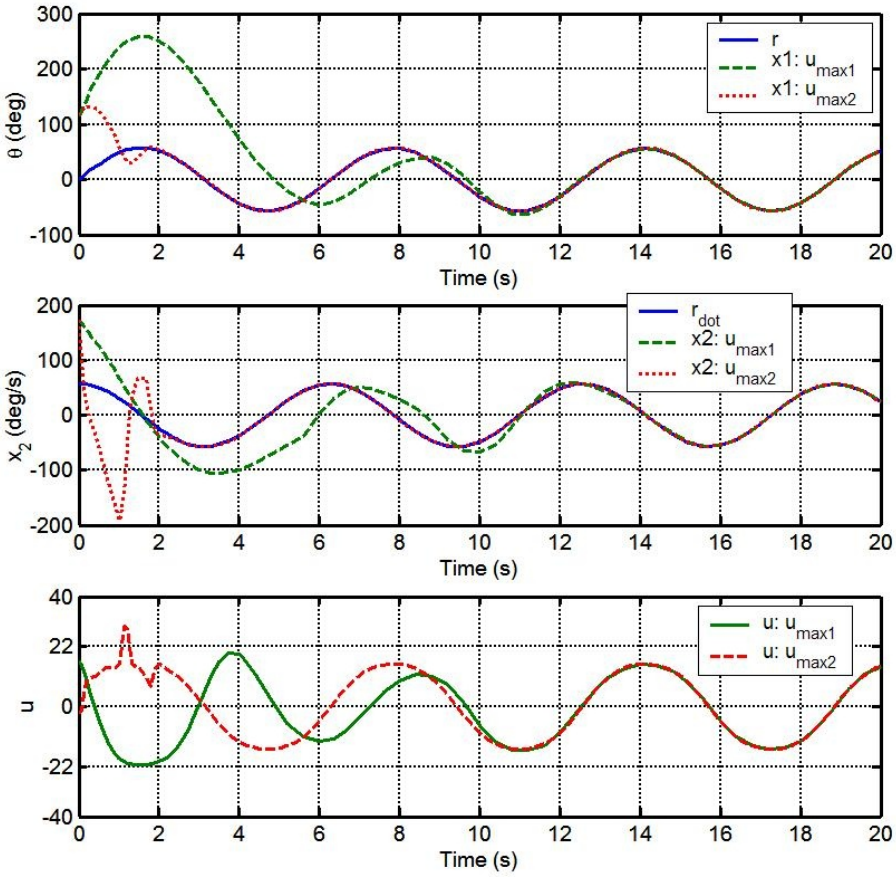

Figure 3.3 Controller example for the pendulum system with actuation saturation

The first row in Figure 3.3 compares the reference angle and actual angle of the pendulum. The second row shows the $\dot{r}$ and actual state x_2. As one can see, the errors decay to zero with time. The bottom row shows the control input u for two cases. We can find that the control inputs obey the saturation constraints $|u| \le u_{\max 1} = 22.0$ and $|u| \le u_{\max 2} = 40.0$, respectively. Note the control input signal is directly generated by

the control law without passing through any limitations. However, the convergence rate for the case with greater saturation value is significantly faster than the one with smaller saturation value.

Remarks: The proposed control law can guarantee the tracking errors go to zero with time while obeying the input saturation constraint. However, from practical control system design and implementation points of view, the following aspects need to be considered.

1) The selection of control law tuning parameters (λ_1, λ_2, r_k) and their influence on the control system performance in terms of convergence rate etc. are not forthright. It is difficult to relate the control performance directly to the tuning parameter values.
2) Actuation rate limits, which are commonly encountered in practice, cannot be explicitly incorporated in this control design.
3) System performance, especially convergence rate varies with control input amplitude constraint.
4) Limitations have to be put on the reference signals in order to meet the control saturation constraints based on this kind of control laws.
5) Control robustness with respect to system parametric uncertainties are not specifically addressed in the control law.

3.3.2 Reference Management

Another class of design methods to cope with actuation saturations is through reference management/governor. The basic idea of these methods is to modify the originally supplied reference signal based on system states to avert the occurrence of constraint violations. These types of approaches are mostly developed for linear systems [Bemporad et al., 1997], [Niu and Tomizuka, 2001], [Gilbert et al., 1995]. The

conceptual structure of the reference management/governor is shown in Figure 3.4, where $x(t)$ is the system states, $y(t)$ is the system outputs, $r_d(t)$ is the original desired reference signal, and $r_a(t)$ is the modified reference signal actually fed to the closed-loop system. Modification of the reference signal is based on the desired reference and system states. Predictive mechanism such as *receding horizon control* methodology is often used to generate the modified reference signal.

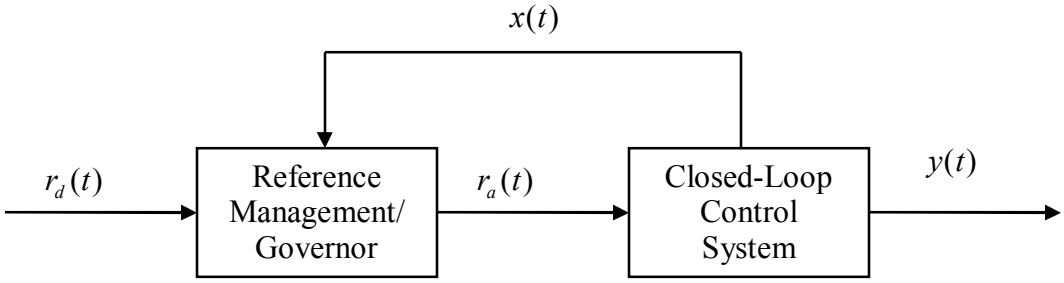

Figure 3.4 Control systems with reference management/governor

For nonlinear systems, using reference management to deal with actuation constraints is not popular mainly because of the complexity involved in solving the on-line nonlinear optimization problems for generating the modified reference signals [Bemporad, 1997].

Dealing with actuation constraints through reference management/governor requires knowledge of the future evolution of the reference signal [Bemporad et al., 1997], which could be available for some applications with preset references such as industrial robots. However, the reference signals may not be available for some applications such as VDC where references are generated in real-time.

3.4 SYSTEMS WITH REDUNDANT AND CONSTRAINED ACTUATION

In the previous sections, we discussed nonlinear tracking control. As being pointed out, to apply the nonlinear control methods for MIMO systems, it is often

required that the dimensions of system input and controlled output are same. However, in practice, using redundant actuation (the number of control inputs is greater than the number of controlled outputs) is a common approach to satisfy the continuously increasing demand on system performance and reliability in a large variety of engineering systems such as aircraft, automobiles, and robotic systems [Part etc., 2003], [Hammett 1999], [Bedner and Chen, 2004], [Bishop and Spong, 1998], [Antonelli and Chiaverini, 1998], [Bodson 2002]. The nonlinear control design methods presented in the previous sections may not be directly applicable for redundantly actuated systems. Another advantage for redundantly actuated systems is to achieve reconfigurable control. Here, reconfigurable control refers to a system in which a control law can maintain and/or minimize loss of the closed-loop performance in the events of some actuator failures or control effectiveness degradations. It is a valuable feature for safety-critical systems such as aircrafts and ground vehicles.

In addition to the actuation amplitude saturation constraints, practical systems commonly have actuation rate limit constraints as well. It means the rate of change for an actuator needs to be inside a certain range. A too fast movement may cause physical damage of the actuators or give rise to unstable modes of the sub-control systems if they are treated as actuators in the overall systems. Furthermore, actuation (amplitude and rate) constraints may vary with changes on environment and system operating conditions. For instance, in ground vehicle systems, tire effective slip range lessens with decreasing tire-road friction coefficient. Therefore, control of nonlinear systems with redundant and constrained actuation is practically meaningful and still remains as an open research topic.

Consider the following class of nonlinear systems with redundant and constrained actuation,

$$\dot{x} = f(x) + g(x)v, \tag{3.76a}$$

$$y = h(x), \tag{3.76b}$$

$$v = k(U), \tag{3.76c}$$

where $x \in \Re^n$ is the system state vector, $v \in \Re^m$ is the virtual (or generalized) control input vector (different from the concept of the virtual control in the backstepping design), $y \in \Re^m$ is the system output vector, $U \in \Re^p$ is the actual control vector, $p > m$. The elements of the vector U subject to corresponding amplitude and rate limit constraints. (3.76c) is a constrained control effectiveness mapping $k : \Re^p \mapsto \Re^m$. In other words, the elements of the virtual control vector are generalized by every actual actuator through the control effectiveness mapping while obeying their corresponding constraints.

If we treat v as control input vector and the system consisting of (3.76a) and (3.76b) satisfies the matching condition, then the MIMO SMC control design methodology can be applied to specify the control laws in terms of desired virtual control v_d. A *control allocation* can be employed to optimally distribute the v_d to each available actuator. While the control allocation will be discussed in detail in Chapter 4, Figure 3.5 below shows the overall structure of this modulated control system. It consists of a higher-level feedback tracking control law to yield appropriate v_d to make the system outputs track the desired reference signal r, and a control allocation module to resolve the actuation redundancy while obeying both actuation amplitude and rate constraints. This control methodology has been studied for control of aircrafts and marine vessels where redundant and constrained actuators are common [Bodson, 2002], [Luo and Serrani et al., 2004], and [Harkegard and Glad, 2005].

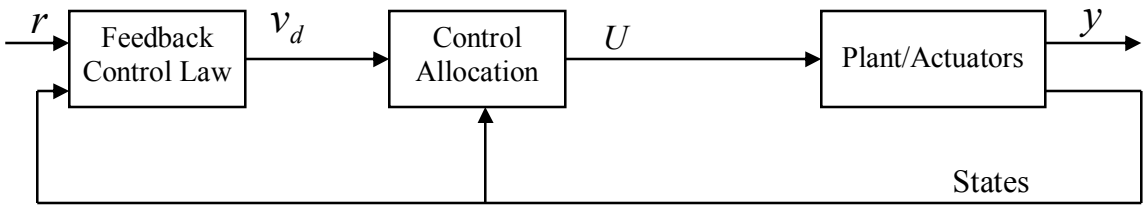

Figure 3.5 Modulated control structure with control allocation

3.5 COORDINATED VEHICLE DYNAMICS CONTROL

In this section, we present the overall control structure for the proposed coordinated vehicle dynamics control (CVDC) using the modulated structure to deal with actuation redundancy and constraints. A higher-level sliding mode controller for the CVDC is also designed.

3.5.1 Overall Structure of CVDC

If we consider the vehicle as a rigid body, it has six degrees of freedom as shown in Figure 2.13 in Chapter 2, three translations, V_x, V_y, and V_z along the X, Y, and Z axes, and rotations, roll, pitch, and yaw about these axes as well. The primary motions for vehicle dynamics control in this dissertation are longitudinal, lateral, and yaw motions, or planar motion as shown in Figure 3.6.

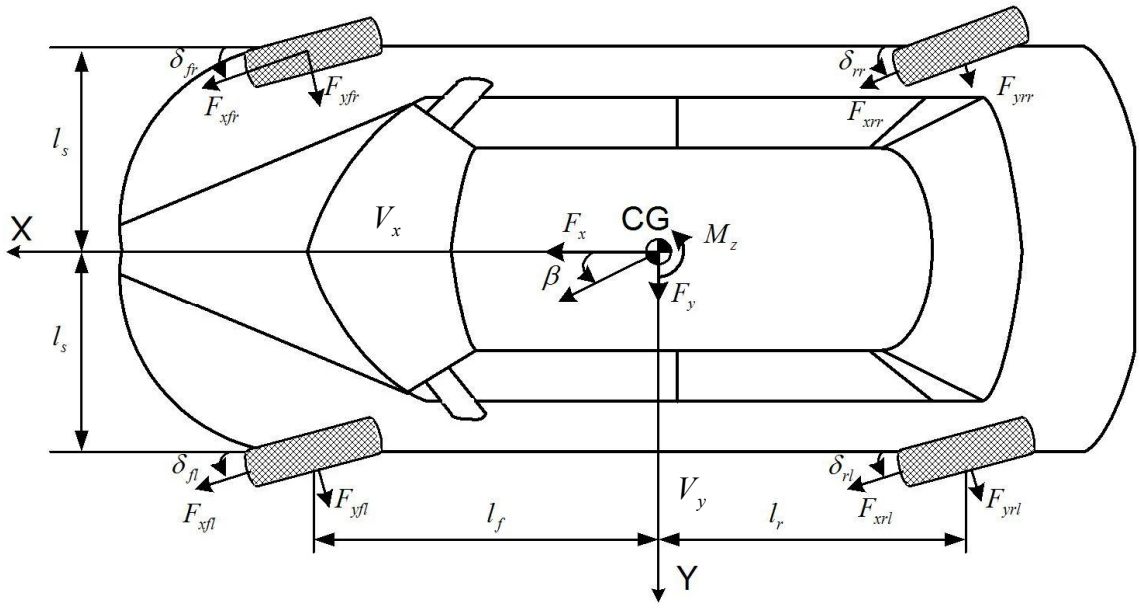

Figure 3.6 The ground vehicle planar dynamic motions

In Chapter 2, we developed the control-oriented vehicle dynamic model (2.25-27). As the longitudinal aerodynamic resistance may become considerable at high vehicle speeds, we include it in the equation of motion with the assumption that wind speed is zero. We can rewrite the equations of motions in state-space form as,

$$\dot{x} = \begin{pmatrix} x_2 x_3 - \dfrac{\rho}{2M} C_D A_f x_1^2 \\ -x_1 x_3 \\ 0 \end{pmatrix} + \begin{pmatrix} \dfrac{1}{M} & 0 & 0 \\ 0 & \dfrac{1}{M} & 0 \\ 0 & 0 & \dfrac{1}{I_z} \end{pmatrix} \begin{pmatrix} F_{xd} \\ F_{yd} \\ M_{zd} \end{pmatrix}. \tag{3.77}$$

Define the system states as $x_1 = V_x$, $x_2 = V_y$, and $x_3 = \Omega_z$. Let the system output as $y = [x_1 \quad x_2 \quad x_3]^T$ and the input vector as $v_d = [F_{xd} \quad F_{yd} \quad M_{zd}]^T$, which defines the desired generalized forces/moment constituted by the longitudinal and lateral forces of all the tires by the following equations,

$$\begin{aligned} F_x = {} & F_{xfl}\cos\delta_{fl} - F_{yfl}\sin\delta_{fl} + F_{xfr}\cos\delta_{fr} - F_{yfr}\sin\delta_{fr} \\ & + F_{xrl}\cos\delta_{rl} - F_{yrl}\sin\delta_{rl} + F_{xrr}\cos\delta_{rr} - F_{yrr}\sin\delta_{rr} \end{aligned}, \tag{3.78}$$

$$F_y = F_{xfl}\sin\delta_{fl} + F_{yfl}\cos\delta_{fl} + F_{xfr}\sin\delta_{fr} + F_{yfr}\cos\delta_{fr} + F_{xrl}\sin\delta_{rl} + F_{yrl}\cos\delta_{rl} + F_{xrr}\sin\delta_{rr} + F_{yrr}\cos\delta_{rr}, \tag{3.79}$$

$$\begin{aligned} M_z = {} & l_s(-F_{xfl}\cos\delta_{fl} + F_{yfl}\sin\delta_{fl} - F_{xrl}\cos\delta_{rl} + F_{yrl}\sin\delta_{rl}) \\ & + l_s(F_{xfr}\cos\delta_{fr} - F_{yfr}\sin\delta_{fr} + F_{xrr}\cos\delta_{rr} - F_{yrr}\sin\delta_{rr}) \\ & + l_f(F_{xfl}\sin\delta_{fl} + F_{yfl}\cos\delta_{fl} + F_{xfr}\sin\delta_{fr} + F_{yfr}\cos\delta_{fr}) \\ & + l_r(-F_{xrl}\sin\delta_{rl} - F_{yrl}\cos\delta_{rl} - F_{xrr}\sin\delta_{rr} - F_{yrr}\cos\delta_{rr}) \end{aligned}, \tag{3.80}$$

where F_{xi} and F_{yi} for $i \in Q := [fl, \quad fr, \quad rl, \quad rr]$ are the tire longitudinal and lateral forces, respectively. The slip angle of each wheel can be calculated from the equations below.

$$\alpha_{fl} = -\delta_{fl} + \tan^{-1}\left(\frac{V_y + \dot{\psi} l_f}{V_x - \dot{\psi} l_s}\right) \tag{3.81a}$$

$$\alpha_{fr} = -\delta_{fr} + \tan^{-1}\left(\frac{V_y + \dot{\psi} l_f}{V_x + \dot{\psi} l_s}\right) \tag{3.81b}$$

$$\alpha_{rl} = -\delta_{rl} + \tan^{-1}\left(\frac{V_y - \dot{\psi} l_r}{V_x - \dot{\psi} l_s}\right) \tag{3.81c}$$

$$\alpha_{rr} = -\delta_{rr} + \tan^{-1}\left(\frac{V_y - \dot{\psi} l_r}{V_x + \dot{\psi} l_s}\right) \tag{3.81d}$$

The speeds at the center of each tire are,

$$V_{fl} = (V_x - \dot{\psi} l_s)\cos\delta_{fl} + (V_y + \dot{\psi} l_f)\sin\delta_{fl} \tag{3.82a}$$

$$V_{fr} = (V_x + \dot{\psi} l_s)\cos\delta_{fr} + (V_y + \dot{\psi} l_f)\sin\delta_{fr} \tag{3.82b}$$

$$V_{rl} = (V_x - \dot{\psi} l_s)\cos\delta_{rl} + (V_y - \dot{\psi} l_r)\sin\delta_{rl} \tag{3.82c}$$

$$V_{rr} = (V_x + \dot{\psi} l_s)\cos\delta_{rr} + (V_y - \dot{\psi} l_r)\sin\delta_{rr} \tag{3.82d}$$

At a given tire normal load and tire-road friction coefficient, the tire longitudinal and lateral forces can be controlled by varying slip and slip angle in limited ranges through appropriate manipulation of the wheel driving/braking/steering torques, as presented in Chapter 2. Therefore, the system is a MIMO nonlinear system with redundant and constrained actuation. Here, we let

$$U = [s_{fl} \quad \alpha_{fl} \quad s_{fr} \quad \alpha_{fr} \quad s_{rl} \quad \alpha_{rl} \quad s_{rr} \quad \alpha_{rr}]^T, \tag{3.83}$$

be the actual control vector populated by slip and slip angle of each tire. We thus propose a control structure for the CVDC system as shown in Figure 3.7.

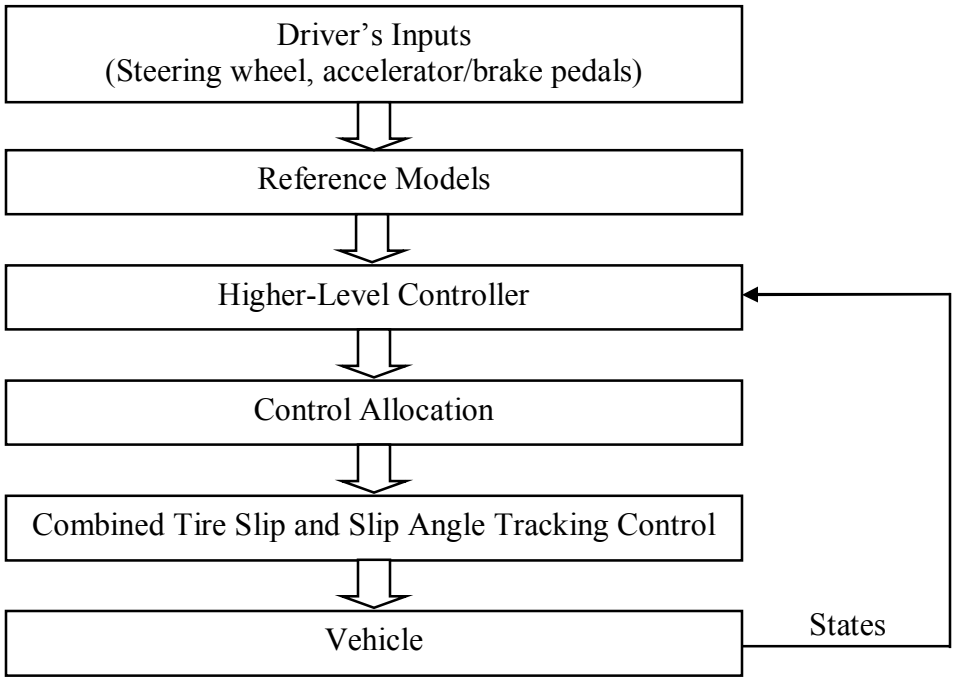

Figure 3.7 Overall structure of the coordinated vehicle dynamics control system

In this kind of coordinated VDC systems, the reference model provides vehicle reference/desired motions based on driver commands. The higher-level controller produces the generalized control efforts such as imposed forces and moments required to track the desired vehicle states. Details of the control design will be presented in the following sub-section. Control allocation optimally *distributes* the generalized control efforts to *slip* and *slip angle* of each tire to simultaneously induce desired longitudinal and lateral forces under the constraints (will be discussed in Chapter 4 and Chapter 5). The task of a combined tire slip and slip angle tracking controller (will be described in Chapter 6) is to manipulate driving/braking torque and steering angle of all wheels, independent of the vehicle body states, so each tire's slip and slip angle track desired

values dictated by a control allocation algorithm. The corresponding vehicle states are fed back to the higher-level controller to close the loop for stability.

Remarks: Compared with the existing vehicle control approaches discussed in Chapter 2, several advantages of this CVDC structure are worthy to be highlighted.

1) Coordination: the above control structure provides a systematic and unified approach to globally coordinate all the available resources to improve the system performance and expand the operational envelope in extreme situations. Potential conflicts among different actuators can be avoided by including them into this integrated structure.
2) Actuation constraints: both actuation amplitude and rate constraints can be addressed in the control allocation algorithm. Variations of control effectiveness due to changes of operating conditions and environment can be readily incorporated. Here, slip and slip angles of the tires are treated as the actuation. Details will be described in Chapter 4 and Chapter 5.
3) Reconfigurablity: the CVDC control structure enables reconfigurable control; i.e., in case of actuation failure, the system can automatically utilize the rest of the actuators to best fulfill the control tasks without redesigning the control laws. The reconfigurable control of the CVDC will be demonstrated in Chapter 7.
4) Task prioritization: in the presence of actuation failure or under adverse driving conditions, the high-level control tasks may not be accomplished simultaneously due to the degraded or reduced control authority. This CVDC control structure allows task prioritization by utilizing the available actuation to achieve the corresponding generalized control efforts with priorities. For example, in some emergency hard braking situations, vehicle longitudinal motion is more critical than yaw motion. Then, the tire forces can be generated to formulate the desired

generalized longitudinal force as the primary goal while putting the generalized lateral force and yaw moment as the secondary objectives.

3.5.2 Higher-Level Controller for CVDC

It is apparent that the matrix $diag\left(\begin{bmatrix} \frac{1}{M} & \frac{1}{M} & \frac{1}{I_z} \end{bmatrix}\right)$ is invertible and the system (3.77) has a *vector relative degree* $\begin{bmatrix} 1 & 1 & 1 \end{bmatrix}^T$. As the dimension of the state vector equals to the sum of the relative degree of each output channel, there is no zero dynamics involved in the system.

Compared with the actual full vehicle model, we know that there are un-modeled dynamics and disturbances, such as wind gust, involved. Moreover, the system parameters are uncertain because M and I_z vary with change of vehicle load. Based on these considerations, we select SMC to ensure system robustness. Since the control inputs are decoupled, the system (3.77) can be partitioned into three SISO systems as,

$$\dot{x}_1 = x_2 x_3 - \frac{\rho}{2M} C_D A_f x_1^2 + \frac{1}{M} v_1 + w_1, \tag{3.84}$$

$$\dot{x}_2 = -x_1 x_3 + \frac{1}{M} v_2 + w_2, \tag{3.85}$$

$$\dot{x}_3 = \frac{1}{I_z} v_3 + w_3, \tag{3.86}$$

where $v_1 = F_{xd}$, $v_2 = F_{yd}$, and $v_3 = M_{zd}$. The terms $w_{1,2,3}$ represent the disturbance of each channel. Assume vehicle mass and yaw moment of inertia variation ranges are $M \in [M_{\min}, \ M_{\max}]$ and $I_z \in [I_{z\min}, \ I_{z\max}]$, respectively. Let $\overline{M} = \sqrt{M_{\min} M_{\max}}$ and $\bar{I}_z = \sqrt{I_{z\min} I_{z\max}}$ be the nominal values of the vehicle mass and yaw moment of inertia, respectively. As the relative degree for each output channel is 1, we can define the sliding surface to make the outputs track corresponding desired values as,

$$S_1 = e_1 = x_1 - x_{1d}, \tag{3.87}$$

$$S_2 = e_2 = x_2 - x_{2d}\,, \tag{3.88}$$

$$S_3 = e_3 = x_3 - x_{3d}\,. \tag{3.89}$$

The errors will go to zero as $S_{1,2,3} \to 0$. For channel 1, consider the Lyapunov function candidate,

$$V_1 = \frac{1}{2} S_1^2\,. \tag{3.90}$$

Take its derivative, we can have,

$$\dot{V}_1 = S_1 \dot{S}_1 = S_1(\dot{x}_1 - \dot{x}_{1d}) = S_1\left(x_2 x_3 - \frac{\rho}{2M} C_D A_f x_1^2 + \frac{1}{M} v_1 + w_1 - \dot{x}_{1d} \right). \tag{3.91}$$

Select the control law as,

$$v_1 = \overline{M}\left(- x_2 x_3 + \frac{\rho}{2\overline{M}} C_D A_f x_1^2 - \overline{w}_1 + \dot{x}_{1d} - K_1 \operatorname{sgn}(S_1) \right), \tag{3.92}$$

where $\overline{w}_1$ is the nominal value of the disturbance. Substitute it into (3.91), it becomes

$$\dot{V}_1 = S_1\left[\left(1 - \frac{\overline{M}}{M} \right) x_2 x_3 + w_1 - \frac{\overline{M}}{M} \overline{w}_1 + \left(\frac{\overline{M}}{M} - 1 \right) \dot{x}_{1d} - \frac{\overline{M}}{M} K_1 \operatorname{sgn}(S_1) \right]. \tag{3.93}$$

From the selection of nominal mass $\overline{M}$, we can have,

$$\beta_1^{-1} \le \frac{\overline{M}}{M} \le \beta_1\,, \quad \beta_1 = \sqrt{\frac{M_{\max}}{M_{\min}}} \ge 1\,. \tag{3.94}$$

Let $\overline{\beta}_1 = \max\left(\left| 1 - \beta_1^{-1} \right|, \quad \left| 1 - \beta_1 \right| \right)$. Assume the disturbance term has a bound of

$$\left| w_1 - \frac{\overline{M}}{M} \overline{w}_1 \right| \le w_{1u}\,, \tag{3.95}$$

and the derivative of the desired state has an upper bound as,

$$\left| \dot{x}_{1d} \right| \le \overline{\dot{r}}_1\,. \tag{3.96}$$

The above two assumptions are reasonable because in practice the disturbance terms caused by aerodynamics are physically bounded and the desired vehicle states

generated by the reference models as shown in Figure 3.6 are smooth. Equation (3.93) then becomes,

$$\begin{aligned}\dot{V}_1 &= S_1\left[\left(1-\frac{\overline{M}}{M}\right)x_2x_3 + w_1 - \frac{\overline{M}}{M}\overline{w}_1 + \left(\frac{\overline{M}}{M}-1\right)\dot{x}_{1d} - \frac{\overline{M}}{M}K_1\,\mathrm{sgn}(S_1)\right] \\ &= S_1\,\mathrm{sgn}(S_1)\left[\mathrm{sgn}(S_1)\left(1-\frac{\overline{M}}{M}\right)x_2x_3 + \mathrm{sgn}(S_1)\left(w_1 - \frac{\overline{M}}{M}\overline{w}_1\right) + \mathrm{sgn}(S_1)\left(\frac{\overline{M}}{M}-1\right)\dot{x}_{1d} - \frac{\overline{M}}{M}K_1\right] \\ &\le |S_1|\left[\overline{\beta}_1|x_2x_3| + w_{1u} + \overline{\beta}_1\overline{\dot{r}}_1 - \frac{\overline{M}}{M}K_1\right]. \end{aligned} \tag{3.97}$$

To achieve the desired attractive behavior of the sliding surface, we want to accomplish,

$$\dot{V}_1 = |S_1|\frac{d|S_1|}{dt} \le -\eta_1|S_1|, \text{ or } \frac{d|S_1|}{dt} \le -\eta_1, \tag{3.98}$$

where $\eta_1 > 0$ is a design parameter determining the convergence speed of the sliding surface. This implies that $|S_1| \to 0$ whenever it is not zero. Compare (3.97), in order to achieve (3.98), it is then required that,

$$K_1 \ge \beta_1\left(\overline{\beta}_1|x_2x_3|_m + w_{1u} + \overline{\beta}_1\overline{\dot{r}}_1 + \eta_1\right), \tag{3.99}$$

where $|x_2x_3|_m = \max\left(|x_2x_3|\right)$ is physically upper limited. This gain will ensure that the control law (3.92) can make the sliding surface S_1 attractive under disturbance and parametric variations.

In practical implementation, to avoid the chattering effects caused by the sign switching function, we replace it by a saturation function with a boundary layer whose thickness is Φ_1 as (3.55 – 3.56). Thus, the control law becomes,

$$v_1 = F_{xd} = \overline{M}\left[-x_2x_3 + \frac{\rho}{2\overline{M}}C_DA_fx_1^2 - \overline{w}_1 + \dot{x}_{1d} - K_1 sat(S_1/\Phi_1)\right]. \tag{3.100}$$

Following the same steps, we can derive the control law for surfaces S_2 as,

$$v_2 = F_{yd} = \overline{M}\left[x_1x_3 - \overline{w}_2 + \dot{x}_{2d} - K_2 sat(S_2/\Phi_2)\right], \tag{3.101}$$

where $K_2 \geq \beta_1\left(\overline{\beta}_1\left|x_1 x_3\right|_m + w_{2u} + \overline{\beta}_1 \bar{\dot{r}}_2 + \eta_2\right)$ needs to be met to guarantee the attractiveness of the sliding surface. $\left|x_1 x_3\right|_m = \max\left(\left|x_1 x_3\right|\right)$, $\left|\dot{x}_{2d}\right| \leq \bar{\dot{r}}_2$ is the upper bound of the derivative of the desired lateral velocity, $\left|w_2 - \frac{\overline{M}}{M}\overline{w}_2\right| \leq w_{2u}$ is the upper bound of the disturbance term. Lastly $\eta_2 > 0$ is a design parameter determining the convergence speed of the sliding surface.

Similarly, for the surface S_3, we can obtain the control law as,

$$v_3 = M_{zd} = \bar{I}_z\left[-\overline{w}_3 + \dot{x}_{3d} - K_3 sat(S_3/\Phi_3)\right], \tag{3.102}$$

where $K_3 \geq \beta_2\left(w_{3u} + \overline{\beta}_2 \bar{\dot{r}}_3 + \eta_3\right)$ is required to ensure the attractiveness of the surface with $\beta_2 = \sqrt{\frac{I_{z\max}}{I_{z\min}}}$, $\overline{\beta}_2 = \max\left(\left|1-\beta_2^{-1}\right|, \left|1-\beta_2\right|\right)$, $\left|\dot{x}_{3d}\right| \leq \bar{\dot{r}}_3$ being the upper bound of the derivative of the desired yaw rate, $\left|w_3 - \frac{\bar{I}_z}{I_z}\overline{w}_3\right| \leq w_{3u}$ being the upper bound of the disturbance term, and $\eta_3 > 0$ is a design parameter determining the convergence speed of the sliding surface.

Note that for the system (3.86) and its control law (3.102), the yaw rate is the only control objective. During the virtual experimental testing of the controller (presented in Chapter 7), we discovered that the yaw rate tracking error could be accumulated to cause vehicle yaw angle or heading error/offset, which is not desirable for vehicle dynamics control. In Chapter 7, we will re-design the control law for $v_3 = M_{zd}$ to eliminate the yaw angle error caused by integrated yaw rate tracking error and compare the corresponding virtual experimental results of these two different control laws for the sliding surface S_3.

3.6 SUMMARY

In this chapter, the nonlinear tracking control methodologies are presented. For a class of nonlinear systems, there are several well-known control design methods such as

sliding mode control and backstepping that can be applied. Under certain circumstances, these methods can be expanded to square MIMO systems. For nonlinear systems with control actuation constraints, the control design needs to be conducted in a case-by-case basis. An example using hyperbolic functions to incorporate actuation saturation is used to show the idea.

For nonlinear systems with redundant and constrained actuations, the modular control structure with control allocation may offer an attractive solution. The overall CVDC structure employing control allocation to deal with vehicle actuation redundancy and constraints is proposed. The higher-level controller in the CVDC system is designed based on the sliding mode control method to enhance system robustness with respect to disturbance and vehicle parametric variations.

In the following chapters, we will describe in detail the remaining elements that form the CVDC control structure.

Chapter 4: Control Allocation

In this chapter, we discuss control allocation, a key technique for solving actuation redundancy under constraints. We will start with a general description of a control allocation scheme for redundantly actuated systems. Then the existing control allocation methods including conventional approaches and optimization based numerical algorithms are compared with emphasis put on computational effort. An improved fixed-point control allocation, called accelerated fixed-point (AFP) control allocation, is proposed to facilitate the convergence rate based on the contraction mapping theory. The reconfigurable control as well as task and actuation prioritizations enabled by control allocation will also be discussed.

Many physical systems are designed with one single actuator (effector) for each controlled system output. Thus the number of independent control actuators equals to the number of controlled outputs, and solutions for the control are thus unique. Additional control actuators may be introduced into systems in order to improve reliability, achieve reconfigurable control, and expand the system operational envelope in extreme situations. Using redundant actuation is a common approach to satisfy the continuously increasing demand on system performance in a large variety of engineering systems such as aircraft, automobiles, and robotic systems [Part etc., 2003], [Hammett 1999], [Bedner and Chen, 2004], [Bishop and Spong, 1998], [Antonelli and Chiaverini, 1998], [Bodson 2002]. For example, modern aircraft typically have more control actuators (control surfaces) than required for generating the three independent moments (yaw, pitch, and roll). However, as the number of actuators increases, appropriately coordinating them to achieve certain control objectives and performance criteria becomes challenging. Research on how to optimally utilize the available actuation redundancy for improving specified performance

criteria remains a relatively new and active research area [Bodson, 2002], [Poonamallee and Yurkovich et al., 2004], [Luo and Serrani et al., 2004], [Peterson and Bodson, 2006].

4.1 CONTROL ALLOCATION FOR REDUNDANTLY ACTUATED SYSTEMS

Control allocation is commonly employed in redundantly actuated (or over-actuated) systems to optimally distribute/allocate the desired generalized controls (typically forces and moments for mechanical systems) among all the available actuators. It provides an approach to coordinate the redundant actuators and ensure they are working towards achieving the same desired control objectives. Often, control allocation is used in conjunction with feedback control laws, which specify the virtual or generalized control efforts, to fulfill the overall control tasks while optimally addressing the actuation redundancy. A general structure for control systems employing CA is shown in Figure 3.5 in Chapter 3.

Consider a general redundantly actuated dynamic system described below,

$$\begin{aligned} \dot{x} &= f(t, x, v) \\ v &= g(t, x, U), \\ y &= h(t, x) \end{aligned} \tag{4.1}$$

where $t \geq 0$ is time, $x \in \Re^n$ is the system state variable vector, $y \in \Re^m$ is the system output vector, $v \in \Re^m$ is a vector of virtual (generalized or resultant) controls, which results from a feedback control law, and $U \in \Re^p$ is the system actuation vector (including all the available actuators) or control element vector. In this dissertation, we use U for the control element vector and u for the individual control element/actuator. Since $p > m$ for over-actuated systems, there is no unique solution for U in general, and control allocation is to address the $\Re^p \to \Re^m$ optimal mapping problem. For autonomous systems, the time can be dropped from the state equations, which results in,

$$\begin{aligned} \dot{x} &= f(x, v) \\ v &= g(x, U) \\ y &= h(x). \end{aligned} \tag{4.2}$$

As we discussed in Chapter 3, for nonlinear control systems with redundant and constrained actuation, the need for control allocation is apparent. The main reason is because the nonlinear control design methods such as feedback linearization, backstepping, and sliding mode control etc. can only be applied for certain systems with "square" property. These control design methods can yield the virtual control or the generalized control efforts but without specifying how to generate them from the actual redundant actuators subject to their constraints. The gap between the generalized virtual control and redundant actuators can be bridged by control allocation. For linear control systems, it is possible to utilize the redundant actuation in a unified manner through a wide range of control design methods such as LQ optimal control and H_∞ [Harkegard and Glad, 2005]. However, control allocation is still attractive for linear control systems as well for several important practical reasons besides resolving actuation redundancy.

- Actuation constraints: in real control systems, actuators do have their own constraints most commonly in the forms of amplitude saturations and rate limits. As will be shown later in this chapter, these actuation constraints can be well addressed by control allocation.
- Reconfigurable control: one of the main motivations for using redundant actuation for practical control systems is to improve reliability. Control allocation provide a good and easy method to reconfigure the control system in case some actuators degrade and/or fail without redesigning the control law [Eberhardt and Ward 1999], [Harkegard and Glad, 2005]. The reconfigurable control will be described in more detail later in this chapter.

- Task prioritization: by using control allocation, it is then possible to prioritize certain control tasks among different ones when they cannot be satisfied simultaneously. For instance, as mentioned in Chapter 3, in ground vehicle control systems, longitudinal/lateral/yaw motions may have different priorities in different driving situations, and control systems will need to be able to organize the available actuators to fulfill the tasks in an order. Same for the aircraft and marine vessel control systems in which some motions may be more important than others in certain circumstances.
- Actuation preference: it is common that the actuators equipped on a system have different utilization preferences and characteristics. Control allocation enables the control systems to utilize the actuators with respect to their characteristics [Davidson, Lallman, and Bundick, 2001].

State-of-the-art control allocation methods are based on the assumption that a linear relationship exists or can be approximated between the virtual controls, v_d, and the amplitudes of the control effectors, U [Harkegard and Glad, 2005], [Petersen and Bodson 2006], [Doman and Oppenheimer, 2002] i.e.,

$$v_d = BU, \tag{4.3}$$

where $B \in \Re^{m \times p}$ is the control effectiveness matrix. So, pragmatically, control allocation can be stated as follows: given a desired virtual control v_d produced by the higher-level control law, determine the system actuation vector, U, obeying the corresponding actuation constraints and satisfying (4.3). If there are several solutions, find the optimal one with respect to certain criteria. If there is no solution, determine U such that BU approaches v_d as well as possible. The linear assumption is necessary in order to ensure the problem can be solved with reasonable computational effort.

4.1.1 Actuation Amplitude and Rate Limit Constraints

In real systems, the equipped actuators usually have their own amplitude (position) limits and most likely the rate limits as well. We refer to these constraints as actuation constraints. One of the main motivations for employing control allocation in control systems is that the actuation constraints can be taken into account. These constraints can be expressed as,

$$U_{\min} \le U \le U_{\max}, \tag{4.4}$$

$$r_{\min} \le \dot{U} \le r_{\max}, \tag{4.5}$$

where, $U \in \Re^p$ is the control element vector, $U_{\min} \in \Re^p$ is the amplitude lower limit vector for actuators, $U_{\max} \in \Re^p$ is the amplitude upper limit vector for actuators, $r_{\min} \in \Re^p$ is the rate of change lower limits for actuators, and $r_{\max} \in \Re^p$ is the rate of change upper limits. The above inequalities apply to each actuator, respectively.

As the control systems are implemented as digital sampled-data systems, if the sampling frequencies are sufficiently fast, it is then appropriate to approximate the $\dot{U}(t)$ as,

$$\dot{U}(t) \approx \frac{U(t) - U(t-T)}{T}, \tag{4.6}$$

where, T is the system sampling period. Thus, the actuator rate limits can be incorporated with the amplitude limits in the following way. From (4.6), we have,

$$r_{\min} \le \frac{U(t) - U(t-T)}{T} \le r_{\max} \;\Rightarrow\; U(t-T) + Tr_{\min} \le U(t) \le U(t-T) + Tr_{\max}. \tag{4.7}$$

Therefore, the actuator amplitude limits can be re-defined as

$$\begin{aligned} \underline{U}(t) &= \max\left[U_{\min}, \quad U(t-T) + Tr_{\min}\right] \\ \overline{U}(t) &= \min\left[U_{\max}, \quad U(t-T) + Tr_{\max}\right], \end{aligned} \tag{4.8}$$

which allow us to consider the actuation constraints in the form of amplitude limits only in control allocation. Equation (4.8) should be interpreted in a component-wise manner.

4.1.2 Nonlinear Actuation

In practical systems, the virtual controls, v_d , are usually nonlinear functions of the control element vector and some related parameters as, $v_d = g(\phi, U)$. The nonlinearities usually increase as the actuators' displacements approach their limits. Conventional control allocation schemes rely on the assumption that virtual controls are linear functions of actuator's deflections [Durham and Bordignon, 1996]. This assumption could often be violated in real systems. Besides, in the case that one or more actuators fail, the remaining actuators could be forced to operate in the regions close to their limits (often likely in the highly nonlinear regions) to produce the desired virtual control. In this case, the linear assumption may not be valid and the control allocation could give results with unacceptable errors. For example, the tire longitudinal force vs. tire slip is shown in Figure 4.1. The longitudinal force is almost a linear function of slip within the small slip region. However, the relationship becomes highly nonlinear when tire slip becomes large.

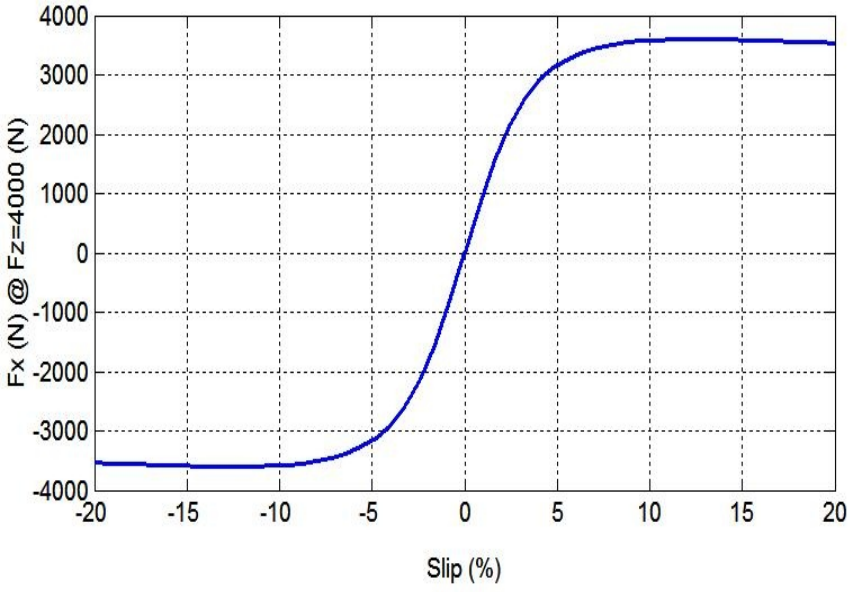

Figure 4.1 The nonlinear relationship between tire slip and longitudinal force.

If we directly use the nonlinear actuation relationship in the control allocation, the computational burden could be prohibitive and turns into an obstacle for real-time control system applications [Poonamallee and Yurkovich et al., 2004]. Doman and Oppenheimer proposed a linearization approach to deal with the nonlinearity [Doman and Oppenheimer, 2002]. The nonlinear function (4.2) is locally approximated with an affine mapping by linearizing it at each sampling instant to obtain the control effectiveness matrix.

$$g(\phi, U_k) \approx g(\phi, U_{k-1}) + \frac{\partial g}{\partial U}(\phi, U_{k-1})(U_k - U_{k-1}) \tag{4.9}$$

Thus, the nonlinear control allocation problem is converted to a linear control allocation problem as

$$\bar{v}_d = B(\phi, U_{k-1})U_k \,. \tag{4.10}$$

with,

$$\bar{v}_d = v_d - g(\phi, U_{k-1}) + B(\phi, U_{k-1})U_{k-1}\,, \tag{4.11}$$

$$B(\phi, U_{k-1}) = \frac{\partial g}{\partial U}(\phi, U_{k-1})\,, \tag{4.12}$$

where k denotes the k^{th} sampling time instant. Given the sampling period being sufficiently small, the linear approximation of the relationship between virtual control and control element vector should provide sufficient accuracy.

4.2 EXISTING CONTROL ALLOCATION METHODS

There are several algorithms for solving the control allocation optimization problem, namely direct control allocation, daisy chaining, pseudo-inverse redistribution (PIR), linear programming (LP) methods, quadratic programming (QP) methods. In this section, we briefly review them.

4.2.1 Direct Control Allocation

The direct control allocation method was mainly proposed and refined by Durham and his group [Durham 1993], [Durham 1994a], [Durham 1994b]. Given a desired virtual control v_d, the method first finds the feasible (within the constraints) control vector $\tilde{U}$ that maximizes the amplitude of the virtual control $\tilde{v} = B\tilde{U}$ in the same direction of v_d and defines,

$$a = \frac{\|\tilde{v}\|_2}{\|v_d\|_2}. \tag{4.13}$$

Then the actual control vector is selected according the following rule,

$$U = \begin{cases} \tilde{U}/a & if \quad a > 1 \\ \tilde{U} & if \quad a \le 1 \end{cases}. \tag{4.14}$$

The direct control allocation method is simple and conducts the control vector saturation while preserving the direction of the virtual control. If the commanded virtual control is not feasible, the actually generated virtual control will be in the same direction of the commanded virtual control but with smaller amplitude. An assumption for the direct control allocation method is that the origin, $U = 0$, has to be a feasible control input [Bodson, 2002]. However, when the actuator rate limits are interpreted in the fashion of (4.8), $U = 0$ may fall outside the feasible region. In the direct control allocation methods, there are no design variables to tune, which makes it hard to achieve task and actuation prioritizations.

4.2.2 Daisy Chain Control Allocation

The main idea of daisy chain control allocation method is to distribute the virtual control among the redundant actuators in a series by grouping the actuators [Buffington and Enns, 1996], [Bordignon, 1996]. The method can be described as the following.

First, the p control actuators (inputs) are divided into L groups,

$$U = \begin{bmatrix} u^1 \\ \vdots \\ u^L \end{bmatrix}. \tag{4.15}$$

Then the control effectiveness matrix is partitioned into L portions correspondingly,

$$B = \begin{bmatrix} B^1 & \cdots & B^L \end{bmatrix}. \tag{4.16}$$

The control allocation equation (4.3) can then be rewritten as,

$$BU = B^1 u^1 + B^2 u^2 + \cdots + B^L u^L = v. \tag{4.17}$$

The algorithm first tries to distribute the virtual control among the first group of actuators only by,

$$u^1 = sat\left(B^{1+} v\right), \tag{4.18}$$

where, $B^{1+} = B^{1T}(B^1 B^{1T})^{-1}$ is the pseudo-inverse of B^1, and *sat* function limits the elements in vector u^1 if position or rate limit violations happen.

If $B^1 u^1 = v$ holds true, then the control allocation task is finished and the process stops. Otherwise, continue the next step to utilize the second group of actuators by calculating,

$$u^2 = sat\left[B^{2+}(v - B^1 u^1)\right]. \tag{4.19}$$

If virtual control is not met in these intermediate steps, the algorithm continues until the last group of actuators,

$$u^L = sat\left[B^{L+}(v - \sum_{i=1}^{L-1} B^i u^i)\right]. \tag{4.20}$$

As determined by the inherent feature of the method, the actuators in the ending groups have less chance to be utilized but the actuators in the beginning groups may be used frequently. It is reported that in aircraft control applications, daisy chain CA is usually used when thrust vectoring system is available, and the conventional control surfaces, such as elevator, aileron, and rudder are often grouped as primary actuators,

with the thrust vectoring vanes grouped as secondary actuators for subsidiary control purposes [Adams et al., 1994], [Enns et al., 1994]. However, Bordignon pointed out that the method could fail to produce virtual controls that are actually feasible [Bordignon, 1996].

Recently, with the increasing computational capability of hardware, numerical optimization algorithms have been introduced to solve the control allocation problems. The control allocation essentially is a constrained sequential optimization problem as stated below.

$$U_s = \arg\min_{U\in\kappa} \left\| W_u (U - U_0) \right\|_h^h, \tag{4.21}$$

$$\kappa = \arg\min_{\underline{U}\le U\le \overline{U}} \left\| W_v (BU - v_d) \right\|_h^h, \tag{4.22}$$

where, U_0 is the preferred control vector usually at the resting positions of the actuators, W_u and W_v are the diagonal weighting matrices for actuators and virtual controls, respectively. So, the first step is to find κ, which is the feasible set (within actuation constraints) of control that minimizes the weighted difference between BU and v_d in the sense of L_h norm. Then choose $U_s \in \kappa$ that minimizes the weighted distance from the preferred control vector in the sense of L_h norm.

In order to solve the problem as a single step optimization to improve associated computational efficiency, it is common to approximately reformulate the sequential optimization problem as a mixed optimization problem [Harkegard, 2002], [Bodson, 2002], [Burken et al., 2001] as,

$$U_m = \arg\min_{\underline{U}\le U\le \overline{U}} \left(\left\| W_v (BU - v_d) \right\|_h^h + \lambda \left\| W_u (U - U_0) \right\|_h^h \right), \tag{4.23}$$

where, λ is a small positive parameter used to balance the efforts between reducing allocation errors and actuators' amplitudes.

For the control allocation problems formulated in this fashion, the primary objective is to minimize the difference between the desired virtual controls and achieved ones, or the control allocation error. The secondary objective is to minimize the amplitudes of the actuator positions, which usually connect with the control energy. The weighting factor λ is usually small. In other words, this mixed optimization problem with small λ can be interpreted as the following. When the virtual controls are attainable or feasible, the one that minimizes the weighted control actuation will be the solution. When virtual controls are not attainable, the weighted control allocation error will be minimized. Different norms can be used in the optimization problem.

4.2.3 L_1-Norm Based Control Allocation Method

When L_1 norms are used in the mixed optimization CA, the cost function becomes,

$$\min_{U} \quad J = \left\| W_v (BU - v_d) \right\|_1 + \lambda \left\| W_u (U - U_0) \right\|_1, \tag{4.24}$$

Subject to

$$\underline{U} \le U \le \overline{U}\,. \tag{4.25}$$

It has been shown that this CA problem can be converted to a linear programming (LP) problem and standard LP techniques such as simplex algorithm can be used to solve it [Buffington et al., 1999], [Doman and Ngo, 2002], [Bodson, 2002]. Linear programs are usually stated in the following standard form:

$$\min \qquad J = c^T z \tag{4.26}$$

$$subject \quad to: \qquad 0 \le z \le h, \qquad Pz = b\,. \tag{4.27}$$

Here we use P and z instead of A and x in the typical LP notation to avoid confusions with previously defined state space notations. The vector inequalities should be interpreted elementally. The challenge of converting the mixed L_1 norm optimization

CA to linear programming is how to appropriately define the objective function for LP to avoid inappropriate reduction of the objective function caused by negative elements in z. In [Bodson, 2002], a specially defined non-negative function is introduced to construct the objective function for LP problem. Define the function $q(z)$,

$$q(z) = \begin{cases} z & z \geq 0 \\ 0 & z < 0 \end{cases}. \tag{4.28}$$

Assume the preferred control vector satisfies,

$$\underline{U} \leq U_0 \leq \overline{U}\ . \tag{4.29}$$

Define

$$U^+ = q(U - U_0),$$

$$U^- = q(U_0 - U)\ . \tag{4.30}$$

Then we can have

$$U = U^+ - U^- + U_0, \tag{4.31}$$

$$0 \leq U^+ \leq \overline{U} - U_0, \tag{4.32}$$

$$0 \leq U^- \leq U_0 - \underline{U}\ . \tag{4.33}$$

Also define the control allocation error as,

$$e = BU - v_d\ ,\ \ e^+ = q(e),\ \ e^- = q(-e)\ . \tag{4.34}$$

Then we can have,

$$e = e^+ - e^-, \tag{4.35}$$

$$0 \leq e^+ \leq e_{\max}, \tag{4.36}$$

$$0 \leq e^- \leq e_{\max}\ . \tag{4.37}$$

where $e_{\max}$ is the upper bound on the control allocation error. Define the optimization variable vector as,

$$z^T = \begin{pmatrix} e^+ & e^- & U^+ & U^- \end{pmatrix}. \tag{4.38}$$

The LP equality constrain becomes

$$e^+ - e^- - BU^+ + BU^- = BU - v_d - BU + BU_0 = BU_0 - v_d . \tag{4.39}$$

The optimization objective function becomes

$$J = \sum_{i=1}^{m} e_i^+ + \sum_{i=1}^{m} e_i^- + \lambda \sum_{i=1}^{p} u_i^+ + \lambda \sum_{i=1}^{p} u_i^- , \tag{4.40}$$

with

$$P = \begin{pmatrix} I_{m\times m} & -I_{m\times m} & -B_{m\times p} & B_{m\times p} \end{pmatrix}, \tag{4.41}$$

$$b = BU_0 - v_d , \tag{4.42}$$

$$c^T = \begin{pmatrix} 1 & \cdots & 1 & \lambda & \cdots & \lambda \end{pmatrix} \in \Re^{1\times(2m+2p)}, \tag{4.43}$$

$$h^T = \begin{pmatrix} e_{\max} & e_{\max} & \overline{U} - U_0 & U_0 - \underline{U} \end{pmatrix}. \tag{4.44}$$

Thus the mixed L_1 norm optimization CA problem is converted into a standard LP problem and numerical LP methods could be applied to solve it.

Remarks:

1) As stated in the assumption, the preferred control vector U_0 needs to satisfy $\underline{U} \le U_0 \le \overline{U}$. In most applications, U_0 is chosen as the resting positions of actuations, which typically are zeros, to reduce control actuation energy. For control allocation problems incorporating actuation rate limits as (4.8), $\underline{U}$ and $\overline{U}$ could be negative or positive, which violates the assumption. One way to avoid this violation is, at each sampling step, choose U_0 as $\underline{U}$ or $\overline{U}$ which ever is closet to zeros in the sense of L_1 norm.

2) Notice that when the original mixed L_1 norm optimization problem is converted to the LP problem, the size of the problem increased significantly. For example, if we want to allocate a $m \times 1$ virtual control vector to p control elements (actuators), then the resultant matrices for the converted LP problem according to this approach will be $P \in \Re^{m\times(2m+2p)}$, $c \in \Re^{(2m+2p)\times 1}$, $h \in \Re^{(2m+2p)\times 1}$. The expansion of the problem dimension increases the

required computational effort and could become undesirable when the dimension of the original CA problem is already large.

4.2.4 L_2-Norm Based Control Allocation Methods

Since the signs of variables can be automatically taken care in L_2 norms, the construction of the optimization cost function will be easier. There are a wider range of selections of methods for L_2 norm based optimization control allocation.

4.2.4.1 Pseudo-Inverse Control Allocation Methods

When actuation constraints are not considered, there is a class of methods for L_2 norm based optimization control allocation with closed-form solutions, which are the pseudo-inverse based CA methods. Pseudo-inverse based control allocation methods are widely used in practice for their computational simplicity [Jin, 2005], [Wang and Longoria, 2006a]. The method provides a closed-form solution to the following weighted optimization problem.

$$\min \qquad J = \frac{1}{2}\left\| W_u (U - U_0) \right\|_2^2 \tag{4.45}$$

$$\textit{subject to} \qquad BU = v_d \,. \tag{4.46}$$

The solution can be easily obtained by defining the Lagrangian function as,

$$L(U,\ \pi) = \frac{1}{2}(U - U_0)^T W_u (U - U_0) + \pi (BU - v_d). \tag{4.47}$$

Take the partial derivative of L with respect to U and π and set them to zero. We can have,

$$\nabla_u L = (U - U_0)^T W_u + \pi B = 0\,, \tag{4.48}$$

$$\nabla_\pi L = BU - v_d = 0\,. \tag{4.49}$$

Post-multiplying W_u^{-1} on (4.48), we can have,

$$U = U_0 - W_u^{-1} B^T \pi^T\,. \tag{4.50}$$

Substitute (4.50) into (4.49), one can get,

$$\pi^T = -\left(BW_u^{-1}B^T\right)^{-1}\left(v_d - BU_0\right). \tag{4.51}$$

Substitute (4.51) back to (4.50), we can have the weighted pseudo-inverse as:

$$U = \left[I - W_u^{-1}B^T\left(BW_u^{-1}B^T\right)^{-1}B\right]U_0 + W_u^{-1}B^T\left(BW_u^{-1}B^T\right)^{-1}v_d. \tag{4.52}$$

Even though no iterations are involved and the method is computationally efficient, a disadvantage of this method is that the actuation constraints are not explicitly included and violations of actuation amplitude and rate limits could happen. The weighting matrix can be selected in such a way to discourage the violations of actuation constraints by placing more penalties on actuators with more restrictive constraints, as demonstrated in [Wang and Longoria, 2006a] for ground vehicle control. Several other methods were also proposed to address the issue of exceeding control constraints.

Virnig and Bodden proposed a pseudo-inverse redistribution (PIR) method to set the saturated controls to their limits and recalculate the pseudo inverse using the remaining unsaturated ones until a solution is reached or all controls are saturated [Virnig and Bodden, 1994]. The algorithm first obtains the optimal control vector by pseudo-inverse as,

$$U = B^T(BB^T)^{-1}v_d \equiv B^+v_d. \tag{4.53}$$

If some elements of the allocated control vector exceed their limits, the elements and control effectiveness matrix are separated into unsaturated and saturated groups as

$$U_m = \begin{bmatrix} U_r & U_s \end{bmatrix}^T, \tag{4.54}$$

$$B_m = \begin{bmatrix} B_r & B_s \end{bmatrix}, \tag{4.55}$$

where U_s are the actuation elements exceed their limits and B_m is the rearranged control effectiveness matrix according to U_m. The following equation is used to redistribute the virtual control among the unsaturated actuation.

$$U_r = B_r^+(v_d - B_s\overline{U}_s), \tag{4.56}$$

where $\overline{U_s}$ is the clipped vector of U_s by setting them at their limits. If some elements in the redistributed vector U_r exceed their limits, then the process of (4.54), (4.55), and (4.56) is repeated until a solution within the limits is obtained or all the controls are saturated.

This PIR method is simple and fast. However, it cannot guarantee either the result is optimal or $BU = v_d$ is met when v_d is actually feasible [Bodson, 2002].

4.2.4.2 Quadratic Programming Based Control Allocations

Quadratic programming (QP) techniques could be also applied to solve the mixed optimization problem under actuation constraints [Page and Steinberg, 2000], [Harkegard, 2002], [Bodson and Pohlchuk, 1998]. The problem statement is as below.

$$\min_{U} \quad J = \left\| W_v (BU - v_d) \right\|_2^2 + \lambda \left\| W_u (U - U_0) \right\|_2^2, \tag{4.57}$$

Subject to,

$$\underline{U} \le U \le \overline{U}, \tag{4.58}$$

where $\lambda > 0$ is the weighting factor to balance the effort between the primary and secondary objectives. The constraint in (4.58) can be rearranged in a unified form as,

$$CU \ge Q, \tag{4.59}$$

with $C = \begin{bmatrix} I_{p\times p} \\ -I_{p\times p} \end{bmatrix}$ and $Q = \begin{bmatrix} \underline{U} \\ -\overline{U} \end{bmatrix}$.

The control allocation problem (4.57) above can be converted to standard QP problem formulation as,

$$\begin{aligned} J &= (BU - v_d)^T W_v (BU - v_d) + \lambda (U - U_0)^T W_u (U - U_0) \\ &= (U^T B^T W_v BU - U^T B^T W_v v_d - v_d{}^T W_v BU + v_d{}^T W_v v_d) + \lambda U^T W_u U \\ &\quad - \lambda U^T W_u U_0 - \lambda U_0^T W_u u + \lambda U_0^T W_u U_0 \\ &= U^T \left[B^T W_v B + \lambda W_u \right] U + U^T (-2B^T W_v v_d - 2\lambda W_u U_0) + v_d{}^T W_v v_d + \lambda U_0^T W_u U_0 \\ &= \frac{1}{2} U^T G U + U^T d + r \end{aligned}, \tag{4.60}$$

where $G = 2\left(B^T W_v B + \lambda W_u\right)$, $d = -2B^T W_v v_d - 2\lambda W_u U_0$, and $r = {v_d}^T W_v v_d + \lambda U_0^T W_u U_0$. Since the term r is constant for a sampling period it can be removed from the cost function without affecting the optimal solution. Thus, the final QP problem can be stated as,

$$\min_u \quad J = \frac{1}{2} U^T G U + U^T d, \tag{4.61}$$

$$\text{Subject to} \quad CU \geq Q. \tag{4.62}$$

For this inequality-constrained quadratic programming problem, there are several classes of optimization algorithms to solve it, such as classical active-set methods and interior-point methods. Some of them have been used in this L_2 norm based control allocation in literature. We provide a brief review of these optimization algorithms with emphasis placed on the fixed-point CA method.

A) Active Set Methods

Active set methods have been the most widely used methods for small- to medium-scale problems since the 1970s [Nocedal and Wright, 1999]. The algorithm starts with an initial guess of working set W_0 and a feasible initial guess U_0. If the guess is correct, the optimal solution can be obtained by solving an equality-constrained quadratic sub-problem. Otherwise, one index from the current estimate of active set is removed and a new index is added using gradient and Lagrange multiplier information. The iteration then repeats in the same manner. The details of the algorithm can be found in many literatures such as [Nocedal and Wright, 1999] and [Fletcher, 2000]. Harkegard investigated using classical active set algorithms to solve the control allocation problem in a quadratic programming format [Harkegard, 2002] for aircraft control applications.

Compared with the pseudo-inverse based CA, the algorithm can provide an exact optimal solution. In each iteration, it yields a feasible iterate U_k that brings the cost

function to a value lower than the previous one. This property can be used as a means to terminate the iteration by setting a maximal number of iterations for each sampling period. However, in [Petersen and Bodson, 2006], it was found that the number of iterations required to bring the allocation error below a certain tolerance level greatly depends on the virtual control commands and can widely vary. The sequence of the iterations also greatly depends on the choice of initial working set and iterate [Nocedal and Wright, 1999]. For large-scale problems, the convergence rate could be slow because the active set and working set change only by a single index for each iteration. More importantly, since an equality-constrained quadratic programming problem has to be solved in each iteration, the computational burden of the active-set algorithms is still heavy for applications in some real-time control systems.

B) Primal-Dual Interior-Point Methods

Another quadratic programming method is the primal-dual interior-point (PDIP) algorithms. They were developed for large-scale quadratic programming problems in 1990's [Potra and Wright, 2000], [Monteiro and Zhou, 1997], and [Zhang 1996]. Details of the algorithms can be found in many literatures such as [Nocedal and Wright, 1999] and [Wright 1997]. The implementation of the PDIP is easier than the active-set methods. Petersen and Bodson proposed to use standard interior-point algorithms for solving the L_2 norm control allocation problem [Petersen and Bodson, 2005]. Simulation results based on linearized aircraft models show that it requires fewer calculations than active-set methods [Petersen and Bodson, 2006]. Its uniform convergence property also makes it possible for implementations with fixed number of iterations. PDIP can also predict the distance from current solution to the optimum and, therefore, allow one exit the algorithm when a solution is reached within a specific tolerance. However, the

drawback is its computational effort is still relatively significant concerning real-time applications.

C) Fixed-Point Method

Computationally efficient algorithms are crucial for control allocation techniques being practically attractive in real-time control systems, such as VDC. A fixed-point algorithm was proposed by Lu [Lu, 1996] and used to solve the quadratic programming problem that minimizes the cost function below [Burken et al., 2001].

$$J = \frac{1}{2}(1-\varepsilon)\left(BU - v_d\right)^T W_v (BU - v_d) + \frac{1}{2}\varepsilon U^T W_u U\,, \tag{4.63}$$

$$\text{Subject to } \underline{U} \le U \le \overline{U}\,, \tag{4.64}$$

where $W_v = diag(w_{v1},\ \ w_{v2},\ \ w_{v3}) > 0$ and $W_u = diag\left(w_{u1},\ \ w_{u2},\ \ \cdots,\ \ w_{up}\right) > 0$ are the weighting matrices. The cost function is similar to (4.57) with the preferred control $U_0 = 0$. The algorithm conducts the iteration according the following equation,

$$U_{k+1} = sat\left[(1-\varepsilon)\eta B^T W_v v_d - (\eta T - I)U_k\right], \tag{4.65}$$

$$T = (1-\varepsilon)B^T W_v B + \varepsilon W_u\,. \tag{4.66}$$

Matrix T is symmetric. $\eta = 1/\|T\|_F$ and t_{ij} is the element of T with $\|T\|_F = \left(\sum_{i=1}^{p}\sum_{j=1}^{p} t_{ij}^2\right)^{\frac{1}{2}}$ being the Frobenius norm of matrix T [Golub and Van Loan, 1996]. $\varepsilon \in (0,\ \ 1)$ is used to balance between control allocation error and control energy. The saturation function, sat, clips the elements of the control vector U_{k+1} at their limits in the fashion below.

$$sat(u_i) = \begin{cases} \overline{u}_i, & u_i \ge \overline{u}_i \\ u_i, & \underline{u}_i \le u_i \le \overline{u}_i\,, \\ \underline{u}_i, & u_i \le \underline{u}_i \end{cases} \quad \text{for } i = 1,\ \ 2,\ \ \cdots,\ \ p\,. \tag{4.67}$$

The saturation function maps the calculated control vector onto the feasible region in a component-wise manner. The proof of the convergence of this fixed point method

was provided by Lu in [Lu, 1996]. Here we present a similar proof with more detailed steps.

First, let us convert the problem into a standard quadratic programming formulation.

$$\begin{aligned} J &= \frac{1}{2}(1-\varepsilon)(BU - v_d)^T W_v (BU - v_d) + \frac{1}{2}\varepsilon U^T W_u U \\ &= \frac{1}{2}(1-\varepsilon)(U^T B^T W_v BU - U^T B^T W_v v_d - {v_d}^T W_v BU + {v_d}^T W_v v_d) + \frac{1}{2}\varepsilon U^T W_u U \cdot \\ &= \frac{1}{2}U^T\left[B^T(1-\varepsilon)W_v B + \varepsilon W_u\right]U + (1-\varepsilon)U^T(-B^T W_v v_d) + \frac{1}{2}(1-\varepsilon){v_d}^T W_v v_d \end{aligned} \tag{4.68}$$

The actuation constraints are equivalent to:

$$\underline{U} \le U \le \overline{U} \quad \Leftrightarrow \quad \underbrace{\begin{pmatrix} 1 & 0 & \cdots & 0 \\ -1 & 0 & \cdots & 0 \\ \vdots & \vdots & \vdots & \vdots \\ 0 & 0 & \cdots & 1 \\ 0 & 0 & \cdots & -1 \end{pmatrix}}_{A} \underbrace{\begin{pmatrix} u_1 \\ u_2 \\ \vdots \\ u_p \end{pmatrix}}_{U} \ge \underbrace{\begin{pmatrix} \underline{u}_1 \\ -\overline{u}_1 \\ \vdots \\ \underline{u}_p \\ -\overline{u}_p \end{pmatrix}}_{b}. \tag{4.69}$$

Since $\frac{1}{2}(1-\varepsilon){v_d}^T W_v v_d$ is constant for one sampling period, it can be removed from the performance index without affecting the optimal solution. Let $G = T = B^T(1-\varepsilon)W_v B + \varepsilon W_u$ and $d = -(1-\varepsilon)B^T W_v v_d$. Thus, the quadratic programming based control allocation problem can be reformulated as:

$$\min_u \qquad J = \frac{1}{2}U^T GU + U^T d\,, \tag{4.70}$$

$$\textit{Subject to} \quad AU \ge b\,. \tag{4.71}$$

Define the Lagrangian of the problem as:

$$L(U,\lambda) = \frac{1}{2}U^T GU + U^T d - \lambda^T(AU - b)\,, \tag{4.72}$$

where $\lambda = \left(\underline{\lambda}_1, \ \overline{\lambda}_1, \ \cdots \ \underline{\lambda}_p, \ \overline{\lambda}_p\right)^T$ is the vector of Lagrange multipliers. Define the active set at an optimal solution U^* as $\Gamma(U^*)$, which are the indices of the constraints at which equality holds, i.e.

$$\Gamma(U^*) = \left\{i \in [1, \quad p]: \quad a_i U^* = b_i \right\}, \tag{4.73}$$

where, $a_i = [0 \ \cdots \ 1 \ \cdots \ 0]$ if $b_i = \underline{u}_i$; or $a_i = [0 \ \cdots \ -1 \ \cdots \ 0]$ if $b_i = -\overline{u}_i$.

Any optimal solution U^* of the problem needs to satisfy the Karush-Kuhn-Tucker (KKT) conditions below if the cost function is convex [Nocedal and Wright, 1999],

$$\begin{aligned} & GU^* + d - \sum_{i \in \Gamma(U^*)} \lambda_i^* a_i^T \\ & = \left[B^T(1-\varepsilon)W_v B + \varepsilon W_u\right]U^* - (1-\varepsilon)B^T W_v v_d - \sum_{i \in \Gamma(U^*)} \lambda_i^* a_i^T = 0 \end{aligned}, \tag{4.74a}$$

$$a_i U^* = b_i, \quad \text{for } i \in \Gamma(U^*), \tag{4.74b}$$

$$a_i U^* \geq b_i, \quad \text{for } i \notin \Gamma(U^*), \tag{4.74c}$$

$$\lambda_i^* \geq 0, \qquad \text{for } i \in \Gamma(U^*). \tag{4.74d}$$

Theorem 4.1 Assume the matrix $G = T = (1-\varepsilon)B^T W_v B + \varepsilon W_u$ is nonsingular, then the unique solution U^* for the quadratic programming problem exists and is the unique solution of the fixed-point equation in U below,

$$U = sat\left[(1-\varepsilon)\eta B^T W_v v_d - (\eta T - I)U\right] \stackrel{\Delta}{=} s(U), \tag{4.75}$$

with $\eta = 1/\|T\|_F$. The fixed-point iteration sequence $\{U^k\}$ generated by

$$U^k = s(U^{k-1}), \quad k = 1, \quad 2, \quad \cdots, \ \forall \ U^0 \in \Re^p \tag{4.76}$$

converges to U^* [Lu, 1996].

Proof: First we can show that $G = B^T(1-\varepsilon)W_v B + \varepsilon W_u$ is positive definite because for any nonzero vector $x \in \Re^p$,

$$\begin{aligned} x^T G x &= x^T [B^T (1-\varepsilon) W_v B + \varepsilon W_u] x \\ &= \underbrace{(1-\varepsilon)(Bx)^T W_v Bx}_{\geq 0} + \underbrace{\varepsilon x^T W_u x}_{>0} > 0 \end{aligned}. \tag{4.77}$$

Thus, the cost function is convex and the quadratic programming problem (4.74) has a global unique solution U^* [Nocedal and Wright, 1999].

Second, we can show that any solution satisfies (4.74) also satisfy the fixed-point equation (4.75). Substitute equation (4.74a) into equation (4.75), we can have

$$sat\left[(1-\varepsilon)\eta B^T W_v v_d - (\eta T - I)U^*\right] = sat[-\eta \sum_{i\in\Gamma(u^*)} \lambda_i^* a_i^T + U^*]. \tag{4.78}$$

From the definition of the constraints, we have $\overline{u}_i > \underline{u}_i$, so $\underline{\lambda}_i$ and $\overline{\lambda}_i$ cannot be positive simultaneously for any $i \in [1, \quad p]$. Namely, constraints $\overline{u}_i$ and $\underline{u}_i$ cannot be active at the same time. For the elements which are active at the solution of (4.74) (i.e. $i \in \Gamma(U^*)$),

$$-\eta \sum_{i\in\Gamma(u^*)} \lambda_i^* a_i^T + U^* = \underbrace{\begin{pmatrix} 0 \\ \vdots \\ -\eta\underline{\lambda}_i^* + \underline{u}_i \\ \vdots \\ 0 \end{pmatrix} or \begin{pmatrix} 0 \\ \vdots \\ \eta\overline{\lambda}_i^* + \overline{u}_i \\ \vdots \\ 0 \end{pmatrix}}_{i\in\Gamma(U^*)} + \cdots + \underbrace{\begin{pmatrix} 0 \\ \vdots \\ u_j^* \\ \vdots \\ 0 \end{pmatrix}}_{j\in[1, \quad p]\setminus\Gamma(U^*)} + \cdots . \tag{4.79}$$

Since $\eta > 0$ and $\underline{\lambda}_i^*, \quad \overline{\lambda}_i^* \geq 0$, one can see that $-\eta\underline{\lambda}_i^* + \underline{u}_i \leq \underline{u}_i$ and $\eta\overline{\lambda}_i^* + \overline{u}_i \geq \overline{u}_i$. In addition, $\underline{u}_j < u_j < \overline{u}_j$ holds because they are not active. Thus, we can have

$$sat\left[(1-\varepsilon)\eta B^T W_v v_d - (\eta T - I)U^*\right] = sat[-\eta \sum_{i\in\Gamma(U^*)} \lambda_i^* a_i^T + U^*] = U^*. \tag{4.80}$$

It means that the unique solution of the quadratic programming problem is also the solution of the fixed-point equation (4.75). If we can prove that the iteration given in equation (4.75) has a unique solution and iteration actually converges to it, then we can conclude that the solution of the fixed-point equation (4.75) is also the unique solution of the quadratic programming problem (4.70-71), therefore, the fixed-point iteration solves the quadratic programming problem [Lu, 1996].

Define $\omega(U) = (1-\varepsilon)\eta B^T W_v v_d - (\eta T - I)U$. From the definition of the mapping $s(\cdot)$, we have that for any U^i and $U^j \in \Re^p$,

$$\begin{aligned} \left\| s(U^i) - s(U^j) \right\| &\le \left\| \omega(U^i) - \omega(U^j) \right\| = \left\| [I - \eta T](U^i - U^j) \right\| \\ &\le \left\| I - \eta T \right\| \ \left\| U^i - U^j \right\| = \alpha \left\| U^i - U^j \right\| \end{aligned} . \tag{4.81}$$

where $\| \cdot \|$ is the L_2 norm. Since $\eta = 1/\|T\|_F > 0$, the matrix $I - \eta T$ is positive definite and then

$$\alpha = \left\| I - \eta T \right\| = \lambda_{\max}[I - \eta T] = 1 - \eta \mu_1 , \tag{4.82}$$

where $\lambda_{\max}(\cdot)$ denotes the largest eigenvalue of the matrix. μ_1 is the smallest eigenvalue of the matrix T. Since $I - \eta T$ and T are both symmetric positive definite, we have $\alpha > 0$, $\mu_1 > 0 \ \Rightarrow \ 0 < \alpha < 1$. Thus, $s(U)$ is a global contraction mapping in $\Re^p$. So the fixed-point equation has a unique solution and the fixed-point sequence converges to this solution as $s(U^*) = U^*$. Here, α is called contraction constant for s in $\Re^p$ [Hille and Phillips, 1957], [Istratescu, 1981], [Granas and Dugundji, 2003]. ■

Remarks:

1) The fixed-point algorithm is numerically simple and requires modest computational effort. Most of the calculations are not involved in the iteration. It is therefore suitable for on-line implementation in real-time control systems.
2) Due to the converging feature of the fixed-point iteration, the selection of the initial guess, U^0 affects the convergence rate. It is shown that using the CA solution of the last sampling cycle provides a good U^0 [Burken et al., 2001].
3) The bound on the error reduction of each iteration is determined by the contraction constant α as

$$\left\| U^n - U^{n-1} \right\| = \left\| s(U^{n-1}) - s(U^{n-2}) \right\| \le \alpha \left\| U^{n-1} - U^{n-2} \right\| \quad \Rightarrow \quad \frac{\left\| U^n - U^{n-1} \right\|}{\left\| U^{n-1} - U^{n-2} \right\|} \le \alpha . \tag{4.83}$$

4) The convergence rate is fast for small virtual control commands (virtual control commands that are well attainable inside the limits of the control vector). However, when the virtual controls are close to the boundary of the attainable set, convergence rate could become slow due to saturations of control vector elements [Petersen and Bodson, 2006].

4.2.5 Comparison of the QP-Based Control Allocation Algorithms

For the seek of applying the control allocation in real-time control systems, computational effort associated with a particular CA method is a very important property due to usually limited computational resources for real-time control systems such as VDC. The algorithms requiring extensive computational efforts will be prohibitive to be applied in real-time systems. A good measure of the computational effort associated with a certain numerical algorithm is the number of *floating point operations* (flops) at each iteration [Asif and Moura, 2005], [Petersen and Bodson, 2006], [Bierlaire and Crittin, 2004]. For the three quadratic programming based control allocation methods described in the previous sub-section, we calculated the theoretical number of flops required for each iteration as below [Wang et al., 2007].

Consider the control allocation problem,

$$v_d = BU, \tag{4.84}$$

where, $v_d \in \Re^m$, $B \in \Re^{m \times p}$, $U \in \Re^p$. For active-set method, since the size of the active set will affect the count of flops, let $n \in [0 \quad p]$ be the dimension of the active set at iteration. The numbers of flops required as a function of the dimensions for each iteration of the three algorithms are listed in Table 4.1. It should be noticed that the flops for the active-set method may slightly vary if different methods are used to solve the equality-constrained sub-quadratic programming problem in the algorithm. However, the

variation is small. In Table 4.1 below, we calculate the flops for the active-set method suggested in [Petersen and Bodson, 2006].

Table 4.1 Number of flops required at each iteration for three different algorithms

CA Algorithm	Number of Flops for Each Iteration
Active-Set	$(m+p)^3 + 2p^3 + (4m-2n+5)p^2 + (2m^2 - 4mn + 6m)p + (m-2mn)m$
PDIP	$p^3 + 4p^2 + 49p$
Fixed-Point	$2p^2 + 3pm$

From the table, one can see that the flops required for the active-set method and primal-dual interior-point method are much greater than that for the fixed-point method. For vehicle dynamics control systems and aircraft control systems, the size of the virtual control is usually 3 (i.e. $m = 3$). The flops for different algorithms as a function of number of control elements (p) are shown in Figure 4.2.

The flops for $p \le 20$ is shown in the upper row as it is the typical range for the size of control elements in ground vehicles, aircraft and marine vessels systems. It is obvious that the fixed-point algorithm offers significantly less computational effort compared with those of active-set and PDIP algorithms. Therefore it is suitable for real-time control systems. The flops differences among different algorithms become more significant when the number of control elements increase as shown in the lower row in the figure.

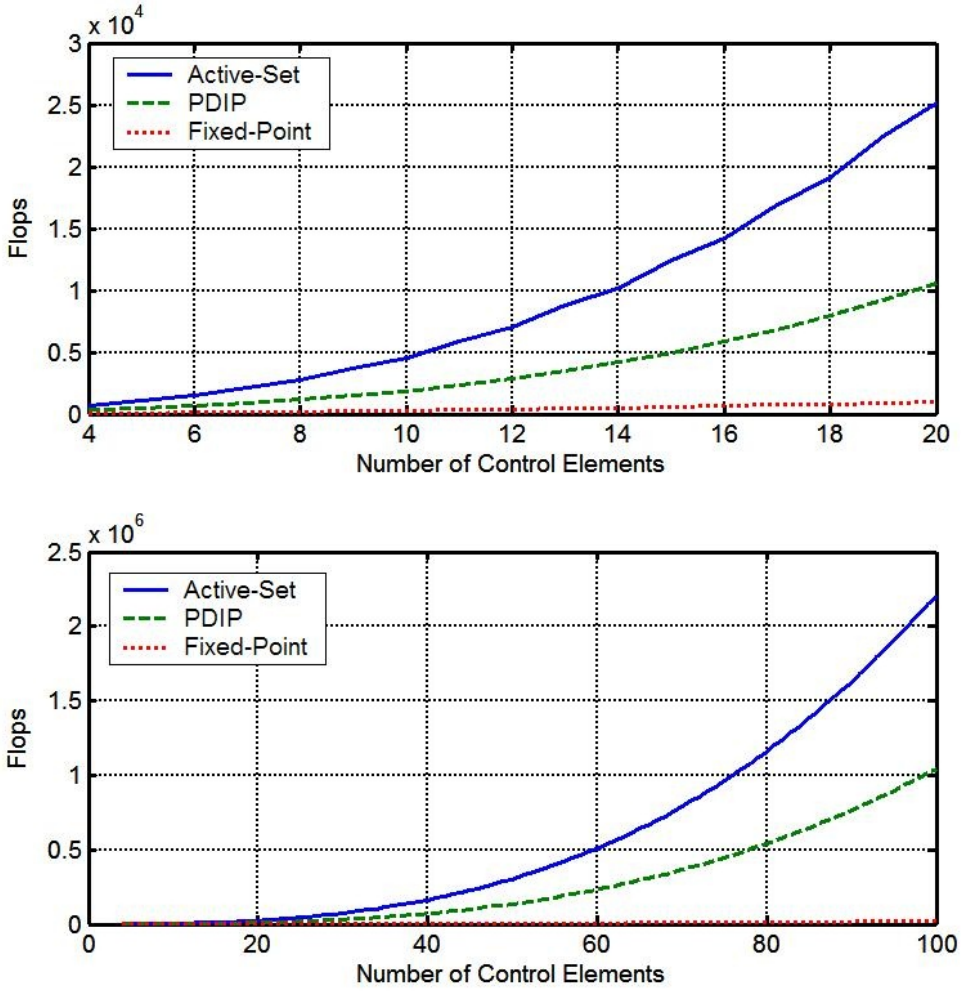

Figure 4.2 Comparison of flops for the three quadratic programming based CA methods.

4.3 ACCELERATED FIXED-POINT CONTROL ALLOCATION

The convergence rate of fixed-point CA algorithm described above could slow down in particular when some elements of the control vector saturate [Petersen and Bodson, 2006]. Hence, we propose some convergence acceleration techniques in this section [Wang et al., 2007]. Let

$$(1-\varepsilon)\eta B^T W_v v_d = M\,, \tag{4.85}$$

$$I - \eta T = H . \tag{4.86}$$

The fixed-point iteration can be re-written as,

$$U = sat\left[M + HU\right] = sat\left[\omega(U)\right]. \tag{4.87}$$

Before moving into the accelerated fixed-point (AFP) algorithm, let's present the Cauchy Interlace Theorem that will be useful in the proof of the AFP algorithm.

Theorem 4.2 (Cauchy Interlace Theorem) If a row-column pair is removed from a real symmetric matrix, then the eigenvalues of the resultant matrix interlace those of the original one.

Let $A \in \Re^{n\times n}$ be a real symmetric matrix with eigenvalues as,

$$\rho_1 \le \rho_2 \le \cdots \le \rho_n . \tag{4.88}$$

Let $A^{ii} \in \Re^{(n-1)\times(n-1)}$ be a principal submatrix resulted from A by removing the i-th row-column pair. The eigenvalues of A^{ii} are

$$\sigma_1 \le \sigma_2 \le \cdots \le \sigma_{n-1} . \tag{4.89}$$

Then we have that

$\rho_1 \le \sigma_1 \le \rho_2 \le \sigma_2 \le \cdots \le \rho_{n-1} \le \sigma_{n-1} \le \rho_n$, i.e. $\sigma_i \in \left[\rho_i, \quad \rho_{i+1}\right]$ for $i = 1, \cdots, n-1$.

Proof of the Cauchy Interlace Theorem could be found in many literatures such as [Horn and Johnson, 1988], [Mercer and Mercer, 2000].

Theorem 4.3 (Invariant Saturation) If the elements, u_i, $i = 1, \quad 2, \quad \cdots, \quad p$, of the control vector saturates in the iteration equation (4.87), they will remain saturated in the rest of the iteration process until the optimal solution is reached if the following conditions are satisfied:

u_i saturates at its upper bound and

$$m_i + \sum_{j\ne i} h_{ij} u_{mj} \ge (1 - h_{ii})\overline{u}_i , \quad u_{mj} = \begin{cases} \underline{u}_j, & h_{ij} \ge 0 \\ \overline{u}_j, & h_{ij} < 0 \end{cases}, \tag{4.90}$$

or

u_i saturates at its lower bound and

$$m_i + \sum_{j \neq i} h_{ij} u_{nj} \leq (1 - h_{ii}) \underline{u}_i, \quad u_{nj} = \begin{cases} \underline{u}_j, & h_{ij} < 0 \\ \overline{u}_j, & h_{ij} \geq 0 \end{cases}. \tag{4.91}$$

Proof: From equation (4.87), at the k-th iteration, we have

$$u_i^k = sat(\omega_i^k) = sat\left[m_i + \sum_{j=1}^{p} h_{ij} u_j^{i-1} \right]. \tag{4.92}$$

Here, the superscript denotes the iteration and subscript denotes the element of the control vector. For example, u_j^{k-1} means the control element j at the $k-1$th iteration. Suppose at the k-th iteration, one of the constraints on u_i is active, then there are two cases.

Case I: $\omega_i^k \geq \overline{u}_i$

Thus, $u_i^k = \overline{u}_i$, and

$$\omega_i^{k+1} = m_i + \sum_{j=1}^{p} h_{ij} u_j^k = m_i + \sum_{j=1, j \neq i}^{p} h_{ij} u_j^k + h_{ii} \overline{u}_i .$$

Since $\sum_{j=1, j \neq i}^{p} h_{ij} u_j^k \geq \sum_{j \neq i} h_{ij} u_{mj}$ with $u_{mj} = \begin{cases} \underline{u}_j, & h_{ij} \geq 0 \\ \overline{u}_j, & h_{ij} < 0 \end{cases}$ holds for all iterations, we have,

$$\omega_i^{k+l} \geq \overline{u}_i, \text{ for } l = 1, \quad 2, \quad \cdots, \text{ if } m_i + \sum_{j \neq i} h_{ij} u_{mj} \geq (1 - h_{ii}) \overline{u}_i .$$

So, if $m_i + \sum_{j \neq i} h_{ij} u_{mj} \geq (1 - h_{ii}) \overline{u}_i, \quad u_{mj} = \begin{cases} \underline{u}_j, & h_{ij} \geq 0 \\ \overline{u}_j, & h_{ij} < 0 \end{cases}$, then $u_i^{k+l} = \overline{u}_i$ will be kept saturated for rest of the iteration.

Case II: $\omega_i^k \leq \underline{u}_i$

Thus, $u_i^k = \underline{u}_i$, and

$$\omega_i^{k+1} = m_i + \sum_{j=1}^{p} h_{ij} u_j^k = m_i + \sum_{j=1, j \neq i}^{p} h_{ij} u_j^k + h_{ii} \underline{u}_i .$$

Since $\sum_{j=1, j\neq i}^{p} h_{ij}u_j^k \le \sum_{j\neq i} h_{ij}u_{nj}$ with $u_{nj} = \begin{cases} \underline{u}_j, & h_{ij} < 0 \\ \overline{u}_j, & h_{ij} \ge 0 \end{cases}$ holds for all iterations, we have,

$\omega_i^{k+l} \le \underline{u}_i$, for $l = 1, \quad 2, \quad \cdots$, if $m_i + \sum_{j\neq i} h_{ij}u_{nj} \le (1 - h_{ii})\underline{u}_i$.

So, if $m_i + \sum_{j\neq i} h_{ij}u_{nj} \le (1 - h_{ii})\underline{u}_i$, $u_{nj} = \begin{cases} \underline{u}_j, & h_{ij} < 0 \\ \overline{u}_j, & h_{ij} \ge 0 \end{cases}$, then $u_i^{k+l} = \underline{u}_i$ will be kept saturated for rest of the iteration. ■

Remarks:

1) In the Theorem 4.3, notice that the saturation conditions (4.90-91) are determined by the matrix M, matrix H, upper and lower bounds of the control elements $\overline{U}$ and $\underline{U}$. Those are all independent of the iteration, so the conditions can be predetermined before the start of iterations.
2) Theorem 4.3 states a condition under which the convergence acceleration technique presented in Theorem 4.4 can be applied.

Now we are ready to present the way to accelerate the convergence when actuation saturations occur.

Theorem 4.4 By removing the saturated control vector elements, u_i, $i = 1, \quad 2, \quad \cdots, \quad p$ that meet the conditions in Theorem 4.3 from the fixed-point iteration, the bound on the convergence rate of the iteration will be improved.

Proof: From the original fixed-point equation, we have

$$\left\| s(U^{k+1}) - s(U^k) \right\| \le \alpha \left\| U^{k+1} - U^k \right\|, \tag{4.93}$$

where $\alpha = \left\| I - \eta T \right\| = \lambda_{\max}[I - \eta T] = 1 - \eta\mu_1 < 1$ is the contraction constant, which determines the convergence rate. $T = (1-\varepsilon)B^T W_v B + \varepsilon W_u \in R^{p\times p}$ is a symmetric positive

definite matrix and all its eigenvalues are positive real numbers. $\lambda_{\max}(\cdot)$ denotes the largest eigenvalue of the matrix. $\mu_1 > 0$ is the smallest eigenvalue of matrix T. $\eta = 1/\|T\|_F = \left(\sum_{i=1}^{p} \sum_{j=1}^{p} t_{ij}^2 \right)^{-\frac{1}{2}} > 0$. So, the convergence rate of this contraction mapping is determined by $\eta\mu_1$. Increasing $\eta\mu_1$ will result in faster convergence rate.

Here, $B = \left[b_1, \ \cdots, \ b_p \right] \in \Re^{m \times p}$ with $m < p$ is the control effectiveness matrix. When the element, u_i, of the control vector is removed, the corresponding column b_i in the control effectiveness matrix B is also removed. $B^i = \left[b_1 \ \cdots \ b_{i-1} \ \ b_{i+1} \ \cdots \ b_p \right] \in \Re^{m \times p-1} \Rightarrow T^{ii} = (1-\varepsilon) B^{iT} W_v B^i + \varepsilon W_u^{ii} \in R^{(p-1)\times(p-1)}$ is the resulted matrix by removing the i-th row-column pair from the matrix T. Then by definition of the Frobenius norm, we have

$$\left\| T^{ii} \right\|_F = \left(\sum_{m=1, m\neq i}^{p} \sum_{n=1, n\neq i}^{p} t_{mn}^2 \right)^{\frac{1}{2}} < \|T\|_F = \left(\sum_{m=1}^{p} \sum_{n=1}^{p} t_{mn}^2 \right)^{\frac{1}{2}} \Rightarrow \eta^{ii} = 1/\left\| T^{ii} \right\|_F > \eta = 1/\|T\|_F . \quad (4.94)$$

Let $\kappa_1 > 0$ be the smallest eigenvalue of the matrix T^{ii}. From Cauchy Interlace Theorem (Theorem 4.2), we can have $\kappa_1 \geq \mu_1$. Thus,

$$0 < \eta\mu_1 < \eta^{ii}\kappa_1 < 1 \ \Rightarrow \ 1 - \eta^{ii}\kappa_1 = \alpha^{ii} < \alpha = 1 - \eta\mu_1 . \quad (4.95)$$

The contraction constant is reduced and the bound on the convergence rate of the iteration is thus improved. ■

Remarks:

1) For the fixed-point CA and accelerated fixed-point CA, the bound on the speed of convergence is determined by the contraction constant. The upper bound of the distance between the n-th iteration solution and the optimal solution can be predicted at the beginning of the iteration process as a function of contraction constant.

2) From Theorem 4.3 and Theorem 4.4, we can conclude that by removing the saturated control elements that meet the conditions in Theorem 4.3, the final optimal solution will not be changed.

Figure 4.3 below shows an example of comparison of the convergence speeds for FP and AFP algorithms in the case of CVDC. Eight control elements (slips and slip angles of four tires) are considered in the example. In the first row of the figure, the allocated controls from the two algorithms are shown in circles and dots, respectively. They are identical. The iteration processes are shown in the second row. Compared with FP, the AFP used considerably less iterations. Notice the AFP can only improve the convergence rate when actuation saturations occur.

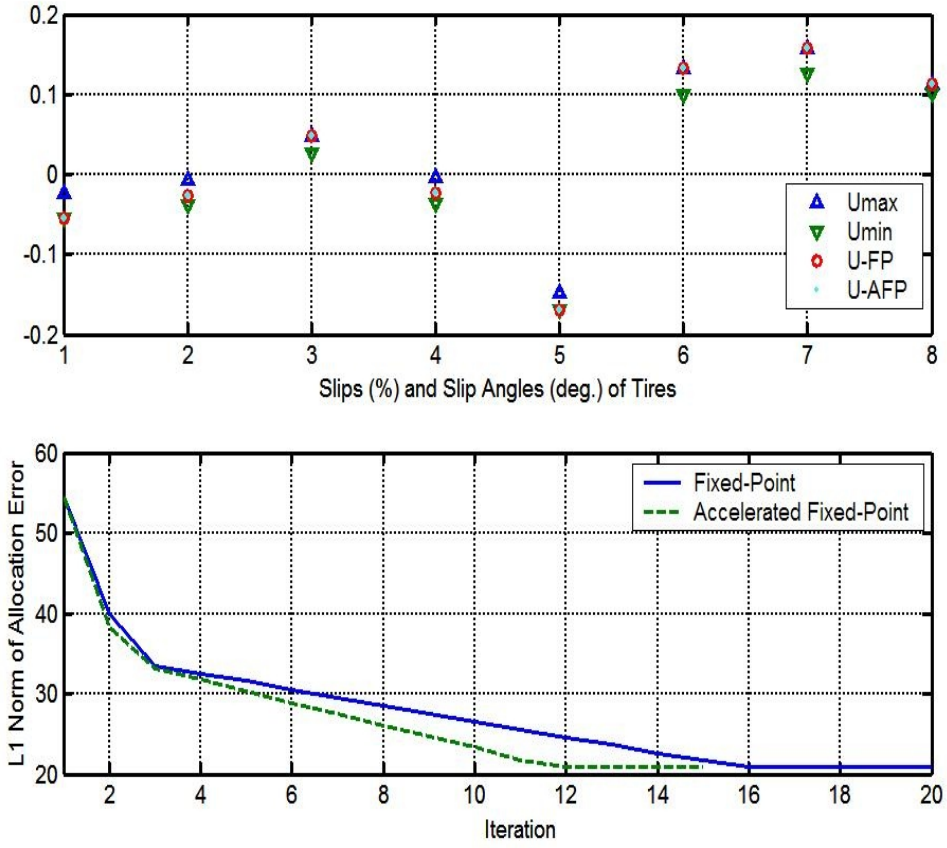

Figure 4.3 Comparison of the convergence for FP and AFP.

4.3.1 Choice of Starting Point

As indicated in [Petersen and Bodson, 2006], the convergence of the fixed-point method may be slow if the starting point of the iteration is not chosen appropriately. For control allocation incorporating actuation rate limits, the actuation amplitude constraints are mostly not active. Therefore, the effective feasible set is centered by the allocated control of the last sampling time. Thus, the allocated control element vector of last sampling time is a good choice of starting point for current sampling time and can effectively reduce the number of iterations [Burken et al., 2001].

Another choice of starting point can be the one with minimal L_2 norm $\|U\|$ as,

$$u_i^0 = \begin{cases} 0.0, & if\ \ \overline{u}_i \geq 0.0\ \ and\ \ \underline{u}_i \leq 0.0 \\ \overline{u}_i, & if\ \ |\overline{u}_i| < |\underline{u}_i| \\ \underline{u}_i, & if\ \ |\overline{u}_i| > |\underline{u}_i| \end{cases} . \tag{4.96}$$

For this choice of starting point, the second term in the cost function (4.63) is already minimized at start of the iteration. Thus the iteration process will be tasked for reducing the allocation errors only.

4.3.2 Termination of the AFP Iteration

The accelerated fixed-point iteration can be terminated by several means, such as allocation error, number of iterations etc. Based on the properties of contraction mapping, the AFP iteration can be terminated by the L_2 norm of the difference between two adjacent control element vectors.

Theorem 4.5 For any two integers $n > m > 0$,

$$\left\|U^n - U^*\right\| \leq \frac{\alpha^{n-m}}{1-\alpha}\left\|U^{m+1} - U^m\right\|, \tag{4.97}$$

where U^* is the solution of the mixed L_2 control allocation problem (4.63), and α is the contraction constant.

Proof: From the properties of contraction mapping, we have,

$$\begin{aligned}\left\|U^n - U^*\right\| &= \left\|s(U^{n-1}) - s(U^*)\right\| \le \alpha\left\|U^{n-1} - U^*\right\| \\ &\le \alpha^2\left\|U^{n-2} - U^*\right\| \le \cdots \le \alpha^{n-m}\left\|U^m - U^*\right\|\end{aligned}. \tag{4.98}$$

We also have,

$$\left\|U^m - U^*\right\| \le \left\|U^m - U^{m+1}\right\| + \left\|U^{m+1} - U^*\right\| \le \left\|U^m - U^{m+1}\right\| + \alpha\left\|U^m - U^*\right\|, \tag{4.99}$$

and thus

$$\left\|U^m - U^*\right\| \le \frac{1}{1-\alpha}\left\|U^{m+1} - U^m\right\|. \tag{4.100}$$

Substitute (4.100) to (4.98), we can then have,

$$\left\|U^n - U^*\right\| \le \frac{\alpha^{n-m}}{1-\alpha}\left\|U^{m+1} - U^m\right\|, \tag{4.101}$$

which proves the Theorem. ■

Remarks:

1) Theorem 4.5 provides a means to terminate the AFP iteration. Based on the L_2 norm of the difference between two adjacent control element vectors and the contraction constant, one can determine the upper bound on the distance (in the sense of L_2) between the current iteration result and the optimal solution.
2) When the contraction constant $\alpha \to 1$, the distance prediction would not be very useful. However, that situation happens only when matrix T is close to singular.

Termination of AFP iteration is a tradeoff between computational effort (number of iterations) and control allocation accuracy.

Theorem 4.6 Suppose the upper bound of the control allocation error that system can tolerate is, $\left\|W_v\left(v_a^t - v_a^*\right)\right\| \le \delta_h$, then, the iteration can be terminated if the following condition is satisfied,

$$\left\|U_k^{t+1} - U_k^t\right\| \le \frac{\mu_1 \delta_h}{\sqrt{p}\,\mu_p \left\|W_v B_{k-1}\right\|}.$$

where, $\mu_1 > 0$ and $\mu_p > 0$ are the smallest and largest eigenvalues of matrix $T = (1-\varepsilon)B^T W_v B + \varepsilon W_u \in \Re^{p\times p}$, respectively.

Proof: Consider the weighted control allocation error as,

$$\begin{aligned}\left\|W_v\left(v_a^t - v_a^*\right)\right\| &\approx \left\|W_v\left(g(\phi,U_{k-1}) + \frac{\partial g}{\partial U}(\phi,U_{k-1})\cdot(U_k^t - U_{k-1}) - g(\phi,U_{k-1}) - \frac{\partial g}{\partial U}(\phi,U_{k-1})\cdot(U_k^* - U_{k-1})\right)\right\| \\ &= \left\|W_v \frac{\partial g}{\partial U}(\phi,U_{k-1})\cdot(U_k^t - U_k^*)\right\| \\ &\le \left\|W_v \frac{\partial g}{\partial U}(\phi,U_{k-1})\right\|\left\|U_k^t - U_k^*\right\| \\ &= \left\|W_v B_{k-1}\right\|\left\|U_k^t - U_k^*\right\|\end{aligned} \quad (4.102)$$

Since matrix $B_{k-1}^T B_{k-1} \in \Re^{p\times p}$ is symmetric positive definite, all its eigenvalues are positive. From Theorem 4.5, we have,

$$\left\|U_k^t - U_k^*\right\| \le \frac{1}{1-\alpha}\left\|U_k^{t+1} - U_k^t\right\|. \quad (4.103)$$

So,

$$\left\|W_v\left(v_a^t - v_a^*\right)\right\| \le \left\|W_v B_{k-1}\right\|\left\|U_k^t - U_k^*\right\| \le \left\|W_v B_{k-1}\right\|\frac{1}{1-\alpha}\left\|U_k^{t+1} - U_k^t\right\|. \quad (4.104)$$

Then, the iteration can be terminated if the following condition is satisfied,

$$\begin{aligned}&\left\|W_v B_{k-1}\right\|\frac{1}{1-\alpha}\left\|U_k^{t+1} - U_k^t\right\| \le \delta_h \\ &\Leftrightarrow \left\|U_k^{t+1} - U_k^t\right\| \le \frac{(1-\alpha)\delta_h}{\left\|W_v B_{k-1}\right\|} = \frac{(1-1+\eta\mu_1)\delta_h}{\left\|W_v B_{k-1}\right\|} = \frac{\mu_1\delta_h}{\left\|T\right\|_F\left\|W_v B_{k-1}\right\|} \\ &\qquad = \frac{\mu_1\delta_h}{\left(\mu_1^2 + \cdots + \mu_p^2\right)^{1/2}\left\|W_v B_{k-1}\right\|},\end{aligned} \quad (4.105)$$

where $\mu_p \geq \mu_{p-1} \geq \cdots \geq \mu_1 > 0$ are the eigenvalues of matrix T. Condition (4.105) will be satisfied if,

$$\left\| U_k^{t+1} - U_k^t \right\| \leq \frac{\mu_1 \delta_h}{\left(\mu_p^2 + \cdots + \mu_p^2\right)^{1/2} \left\| W_v B_{k-1} \right\|} = \frac{\mu_1 \delta_h}{\sqrt{p}\mu_p \left\| W_v B_{k-1} \right\|}. \tag{4.106}$$

It then implies,

$\left\| W_v \left(v_a^t - v_a^* \right) \right\| \leq \delta_h$. ■

Notice that $\frac{\mu_1}{\mu_p}$ is the reciprocal of the condition number of matrix T. For T is not nearly singular, $\frac{\mu_1}{\mu_p}$ will not be very small. Therefore, condition (4.106) provides a guideline for when the iteration of AFP should stop. It is easy to show that when corresponding columns of B_{k-1} are removed, condition (4.106) will be even relaxed, i.e. right hand side of (4.106) will be increased. In Chapter 5, we will use this condition to determine when to terminate the AFP iteration for CVDC system.

The steps of the accelerated fixed-point algorithm we proposed here can be therefore summarized in a pseudo-code format as shown in Figure 4.4 below.

Algorithm for Accelerated Fixed-Point L2-Norm Control Allocation

Inputs:

- $\bar{v}_d$, $B(P,U_{k-1})$ from (4.11) and (4.12) based on system states and allocated control elements of last sampling time.
- $\overline{U}$ and $\underline{U}$ from (4.8) incorporating both actuation amplitude and rate limits.
- U_{k-1}, allocated control element vector of last sampling time.

Preparation:

1. Calculate matrix T, reciprocal of its Frobenius norm η, matrices M and H.
2. Find the set of control elements satisfy the conditions in Theorem 4.3, Θ.
3. Set solution distance, $d = a\tau \in \Re$, $a > 1$, where τ is the allocation tolerance.

Iteration:

While $d > \tau$,

1. Calculate U according to (4.87), let the set of control elements saturated at this iteration as Π.
2. Remove column-row pairs in T and B corresponding to $i \in \Theta \bigcap \Pi$.
3. Recalculate reciprocal of T 's Frobenius norm η, matrices M, and H.
4. Calculate $d = \left\| U_k^{t+1} - U_k^t \right\|$.

End While

Figure 4.4 The pseudo-code for the accelerated fixed-point control allocation algorithm.

4.4 RECONFIGURABLE CONTROL

One of the main benefits of employing control allocation in the redundantly actuated systems is to realize reconfigurable control, which means without redesigning the control law, system closed-loop performance should be best fulfilled even when some of the actuators have degraded or failed. In the control allocation scheme, this can be

easily achieved by adjusting the corresponding columns in the control effectiveness matrix B in (4.3). If some actuators degrade due to attrition or change in working environment, the elements in the corresponding columns in control effectiveness matrix can be readily reduced or set as zeros if actuator failures occur. In Chapter 7, the advantages of the reconfigurable control connected with control allocation are demonstrated by several examples for CVDC systems.

4.5 TASK PRIORITIZATION AND ACTUATION PREFERENCE

When conducting multiple tasks simultaneously with redundant actuators, task prioritization and actuation preference may become desirable. In the following sub-sections, we can find that these functions are facile within the control allocation.

4.5.1 Task Prioritization

As there are usually multiple tasks (virtual control vector has a dimension greater than one) for redundantly actuated systems, needs for task prioritization will surface whenever all the tasks cannot be satisfied simultaneously or, in other words, $v_d = BU$ cannot be satisfied within the constraints $\underline{U} \le U \le \overline{U}$. Here, the tasks refer to producing the generalized control v_d. For systems without control input coupling, it is implicit that the corresponding closed-loop objectives will be better achieved if the associated elements in v_d specified by the control laws can be produced by the redundant actuators with smaller errors. For the L_1-norm and L_2-norm based control allocation method, this kind of task prioritization can be achieved by changing the corresponding elements in the diagonal weighting matrix W_v in the cost function (4.24) and (4.57), respectively. As the optimization is to reduce the value of the cost function, increasing the corresponding weighting factors will raise their priorities.

4.5.2 Actuation Preference

It is also common that actuators equipped in systems may have different preferences, different associated costs, and different characteristics such as bandwidths. For example, some actuators may be expensive to manipulate and some may be easy to drive. Since the actuators are redundant, for a given virtual control vector, the ways to use these actuators are not unique and it is often desired to minimize the "control energy". The diagonal actuation weighting matrix W_u in the control allocation cost functions (4.24) and (4.57) can be adjusted to increase the elements corresponding to the expensive actuators and thus discourage their utilizations.

Davidson et al. proposed a frequency-apportioned control allocation (FACA) [Davidson, Lallman, and Bundick, 2001]. The idea is to use low-pass filters to separate the desired virtual control into high and low frequency components as,

$$v_l = L(s)v_d, \tag{4.107}$$

$$v_h = \left[1 - L(s)\right]v_d, \tag{4.108}$$

where, $L(s) = diag\left\{\left[\frac{1}{T_1 s+1} \quad \frac{1}{T_2 s+1} \quad \cdots \quad \frac{1}{T_m s+1}\right]\right\}$ with m being the dimension of the virtual control, v_l is the low-frequency component of the virtual control and v_h is the high-frequency component. T_1, T_2, $\cdots$, T_m are the filter time constants for the corresponding elements of the virtual control vector. Then v_l and v_h are allocated among the actuators using their position limit and rate limit weighted pseudo-inverses, respectively,

$$U_l = W_p B^T (BW_p B^T)^{-1} v_l = W_p B^T (BW_p B^T)^{-1} L(s) v_d, \tag{4.109}$$

$$U_h = W_r B^T (BW_r B^T)^{-1} v_h = W_r B^T (BW_r B^T)^{-1} \left[1 - L(s)\right] v_d, \tag{4.110}$$

where, W_p is a diagonal matrix populated by squares of the actuator position limits, and W_r is a diagonal matrix populated by squares of the actuator rate limits. The control vector is then given by the sum of U_l and U_h as

$$U = U_l + U_h . \tag{4.111}$$

Thus, the high-frequency commands can be distributed to the actuators with higher rate limits and low frequency commands to the highly effective actuators. This method is evaluated on a Lockheed-Martin Innovative Control Effecter simulation and good tracking performance was shown.

Since the main idea of the above filter-based actuation preference method is to filter the virtual control vector elements, it can be easily extended to all the numerical optimization based control allocation methods discussed in this chapter.

4.6 SUMMARY

In this chapter, we reviewed the state-of-the-art of the control allocation methods including both traditional CA approaches and numerical optimal CA algorithms. Traditional CA approaches typically are computationally simple but have difficulties to ensure optimal solution and achieve task prioritization. Several numerical optimization algorithms have been introduced for control allocation purposes. For real-time control systems, computational effort is a critical criterion for control allocation methods. In order to be attractive for real-time applications such as VDC, CA methods need to be computationally efficient. Compared with other existing quadratic programming based CA methods, the fixed-point algorithm is very computationally efficient.

An improved fixed-point control allocation algorithm is proposed to facilitate the speed of convergence in particular when actuation saturation occurs. Different choices of starting and terminating the iteration are also given.

It is also shown that utilization of the quadratic programming based control allocation makes it possible and convenient for reconfigurable control, task prioritization, and actuator preference, which are desirable for redundantly actuated systems.

In the next chapter, the control allocation scheme specifically for coordinated ground vehicle dynamics control systems will be discussed.

Chapter 5: Control Allocation for Coordinated Ground Vehicle Dynamics Control Systems

In this chapter, we develop the control allocation scheme for coordinated ground vehicle dynamics control systems. Different control allocation algorithms for the CVDC system are also compared.

Control allocation is mostly studied in aircraft and marine vessel control areas. The control allocation approaches described in Chapter 4 are general methods. They are designed to deal with actuator constraints in a component-wise manner, which is appropriate for aircrafts and marine vessels. Also the control actuators are assumed to be individually linear in their effects throughout their actuation ranges and independent of one another. In other words, there is no coupling between actuators [Bordignon and Durham, 1995] [Venkataraman, Oppenheimer, and Doman, 2004] [Bodson, 2002]. For vehicle dynamics control systems, the actuation almost purely relies on the tires, which have nonlinear and coupled constraints because of tire force characteristics as described in Chapter 2.

Recently control allocation approaches have been introduced into ground vehicle control systems to improve system performance and to achieve reconfigurable control [Hac et al., 2006], [Fredriksson et al., 2004], [Plumlee et al., 2004]. In these suggested CA schemes, the virtual controls (i.e. generalized forces/moment) are allocated to longitudinal and/or lateral tire forces. Vehicle motion is governed by forces induced by each tire interacting with the road, and these forces mainly depend on the slip/slip angle and tire-friction coefficient as described in Chapter 2. While allocating the control effort to tires, it is important to take these factors into account, to ensure that the tires can

actually yield the desired forces. In addition, tire forces are difficult to measure in real-time, so it is impractical to implement force-based CA.

Another issue associated with control allocation for CVDC is that solving the optimization problem introduces a significant computational burden and challenges practical real-time implementation on ground vehicles [Fredriksson et al., 2004], [Tondel and Johansen, 2005], [Wang and Longoria, 2006a]. For real-time control applications, computational effort carries a lot of weight in designing and selecting the control allocation algorithms. These aspects of control allocation for CVDC will be resolved in this chapter.

5.1 DERIVATION OF THE CONTROL EFFECTIVENESS MATRIX

In order to conduct the control allocation for CVDC, it is necessary to derive the control effectiveness matrix as in (4.10) from the nonlinear formulation of the virtual control and tire model described in Chapter 2.

The generalized forces/moment are nonlinear function of some configuration parameters and control input elements as

$$v_d = g(\phi, U), \tag{5.1}$$

which can be linearized around an operating point. The vector $\phi = [F_{zi}, \mu_i, \delta_i]^T$ includes tire normal loads, friction coefficients, and steering angles.

$$g(\phi, U_k) \approx g(\phi, U_{k-1}) + \frac{\partial g}{\partial U}(\phi, U_{k-1}) \cdot (U_k - U_{k-1}), \tag{5.2}$$

$$g(\phi, U_k) - g(\phi, U_{k-1}) + \frac{\partial g}{\partial U}(\phi, U_{k-1}) \cdot U_{k-1} \approx \frac{\partial g}{\partial U}(\phi, U_{k-1}) \cdot U_k, \tag{5.3}$$

$$\bar{v}_d = B(\phi, U_{k-1}) U_k, \tag{5.4}$$

$$\bar{v}_d = v_d - g(\phi, U_{k-1}) + \frac{\partial g}{\partial U}(\phi, U_{k-1}) U_{k-1}, \tag{5.5}$$

where $B(\phi, U_{k-1}) = \dfrac{\partial g}{\partial U}(\phi, U_{k-1})$ is the Jacobian matrix at (ϕ, U_{k-1}), which is also the control effectiveness matrix. The derivation process may be tedious but straightforward. Below we show the partial derivatives of the Magic Formula tire model (2.12) with respect to tire slip and slip angle.

The partial derivative of the tire longitudinal force w.r.t. tire slip is,

$$\begin{aligned}\frac{\partial F_{xi}}{\partial s_i} = {} & D_{x\alpha i}\cos[C_{x\alpha i}\arctan(B_{x\alpha i}\alpha_{\mu i})]R_{\mu i}\mu_0 F_{zi} \\ & \cos\left\{C_{xi}\arctan\left[B_{xi}\left(s_i/R_{\mu i}+S_{hxi}\right)-E_{xi}\left(B_{xi}\left(s_i/R_{\mu i}+S_{hxi}\right)-\arctan\left(B_{xi}\left(s_i/R_{\mu i}+S_{hxi}\right)\right)\right)\right]\right\} \\ & C_{xi}\Big/\left\{1+\left[B_{xi}\left(s_i/R_{\mu i}+S_{hxi}\right)-E_{xi}\left(B_{xi}\left(s_i/R_{\mu i}+S_{hxi}\right)-\arctan\left(B_{xi}\left(s_i/R_{\mu i}+S_{hxi}\right)\right)\right)\right]^2\right\} \\ & \left\{\frac{B_{xi}}{R_{\mu i}}-\frac{E_{xi}B_{xi}}{R_{\mu i}}+\frac{E_{xi}B_{xi}/R_{\mu i}}{1+\left[B_{xi}\left(s_i/R_{\mu i}+S_{hxi}\right)\right]^2}\right\}. \end{aligned} \tag{5.6}$$

Figure 5.1 below shows the tire longitudinal force and its partial derivative vs. tire slip.

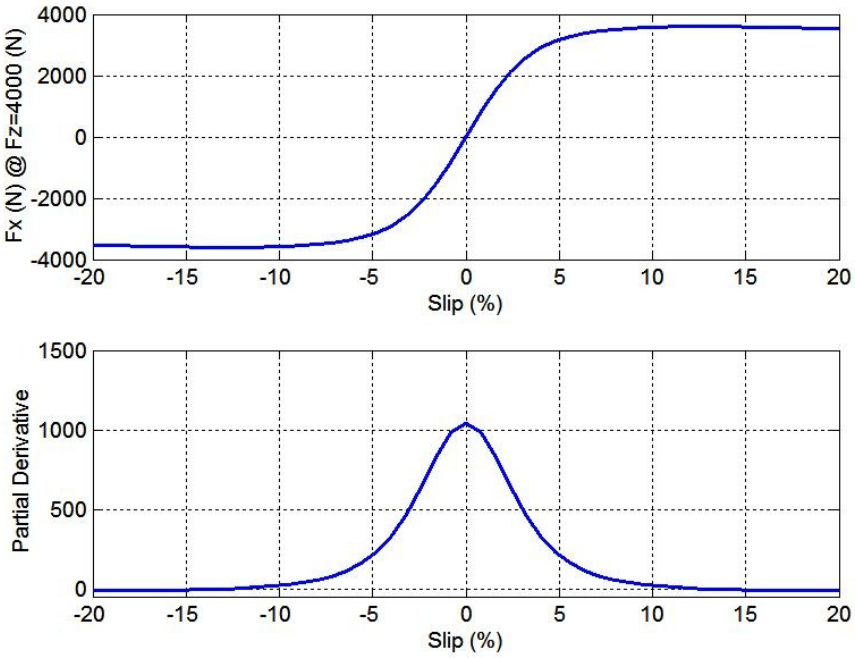

Figure 5.1 Partial derivative of the tire longitudinal force vs. slip at zero slip angle

The partial derivative of the tire longitudinal force w.r.t. tire lateral slip angle is,

$$\frac{\partial F_{xi}}{\partial \alpha_i} = -D_{x\alpha i}\sin\left[C_{x\alpha i}\arctan\left(B_{x\alpha i}\,\alpha_i / R_{\mu i}\right)\right]C_{x\alpha i}B_{x\alpha i}$$
$$\{\mu_0 F_{zi}\sin\{C_{xi}\arctan[B_{xi}s_{\mu xi} - E_{xi}(B_{xi}s_{\mu xi} - \arctan(B_{xi}s_{\mu xi}))]\} + S_{vxi}\}. \qquad (5.7)$$
$$/\left[1 + \left(B_{x\alpha i}\,\alpha_i / R_{\mu i}\right)^2\right]$$

Figure 5.2 below shows the tire longitudinal force and its derivative vs. tire lateral slip angle at 5% longitudinal slip.

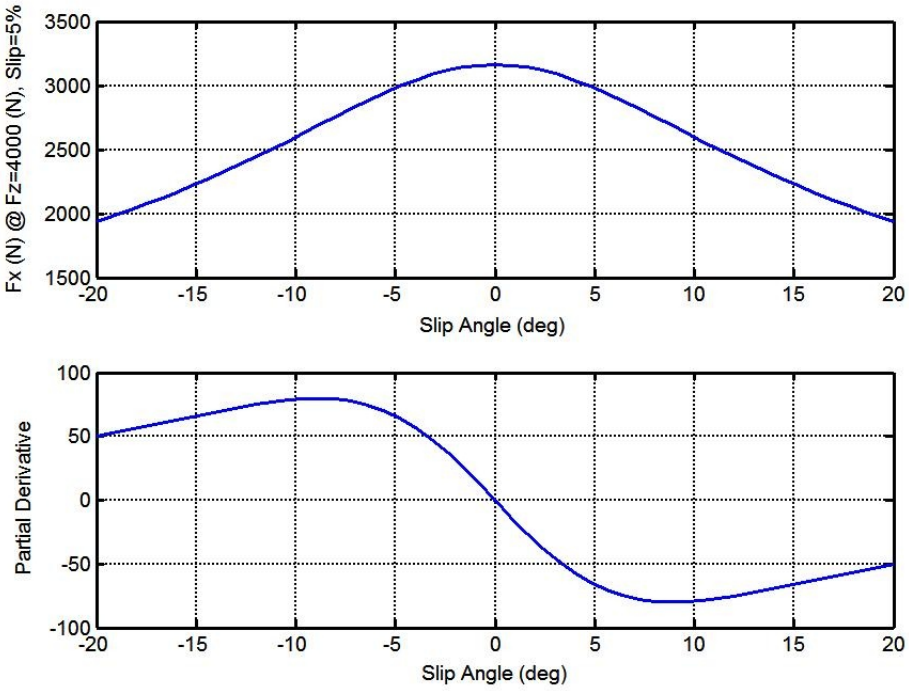

Figure 5.2 Partial derivative of the tire longitudinal force vs. slip angle at 5% slip

The partial derivative of tire lateral force w.r.t. tire longitudinal slip is,

$$\frac{\partial F_{yi}}{\partial s_i} = -D_{ysi}\sin\left[C_{ysi}\arctan\left(B_{ysi}\,s_i / R_{\mu i}\right)\right]C_{ysi}B_{ysi}$$
$$\{\mu_0 F_{zi}\sin\{C_{yi}\arctan[B_{yi}\alpha_{\mu yi} - E_{yi}(B_{yi}\alpha_{\mu yi} - \arctan(B_{yi}\alpha_{\mu yi}))]\} + S_{vyi}\}. \qquad (5.8)$$
$$/\left[1 + \left(B_{ysi}\,s_i / R_{\mu i}\right)^2\right]$$

Figure 5.3 below shows the tire lateral force and its partial derivative vs. tire longitudinal slip at 5.0 deg. slip angle.

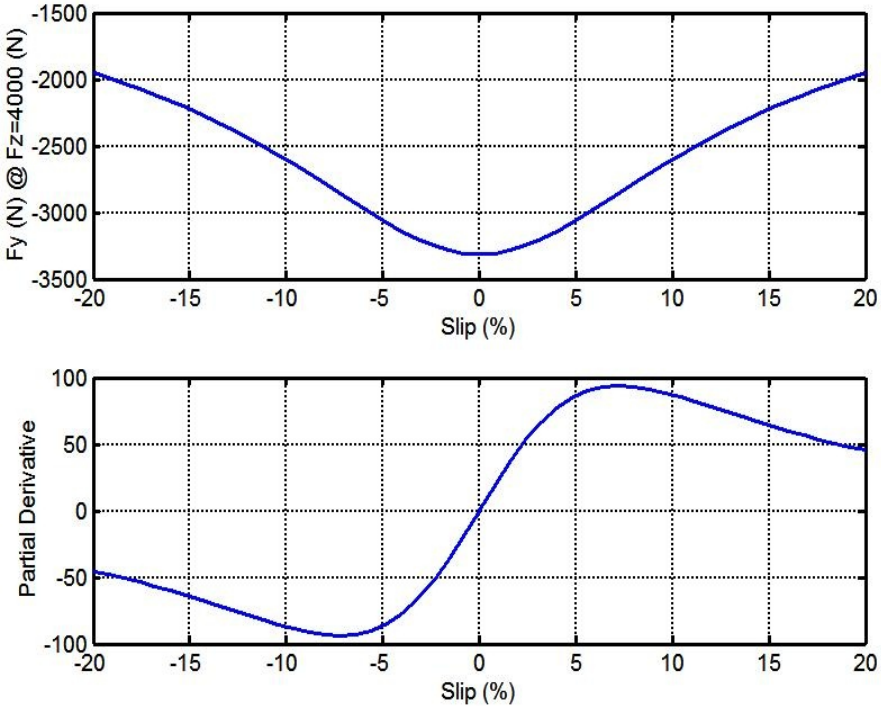

Figure 5.3 Partial derivative of the tire lateral force vs. slip at 5.0 deg. slip angle

The partial derivative of the tire lateral force w.r.t. tire slip angle is,

$$\frac{\partial F_{yi}}{\partial \alpha_i} = D_{ysi}\cos[C_{ysi}\arctan(B_{ysi}s_{\mu i})]R_{\mu i}\mu_0 F_{zi}$$
$$\cos\left\{C_{yi}\arctan\left[B_{yi}\left(\alpha_i/R_{\mu i}+S_{hyi}\right)-E_{yi}\left(B_{yi}\left(\alpha_i/R_{\mu i}+S_{hyi}\right)-\arctan\left(B_{yi}\left(\alpha_i/R_{\mu i}+S_{hyi}\right)\right)\right)\right]\right\}$$
$$C_{yi}/\left\{1+\left[B_{yi}\left(\alpha_i/R_{\mu i}+S_{hyi}\right)-E_{yi}\left(B_{yi}\left(\alpha_i/R_{\mu i}+S_{hyi}\right)-\arctan\left(B_{yi}\left(\alpha_i/R_{\mu i}+S_{hyi}\right)\right)\right)\right]^2\right\}$$
$$\left\{\frac{B_{yi}}{R_{\mu i}}-\frac{E_{yi}B_{yi}}{R_{\mu i}}+\frac{E_{yi}B_{yi}/R_{\mu i}}{1+\left[B_{yi}\left(\alpha_i/R_{\mu i}+S_{hyi}\right)\right]^2}\right\}. \qquad (5.9)$$

Figure 5.4 below shows the tire lateral force and its partial derivative vs. tire lateral slip angle.

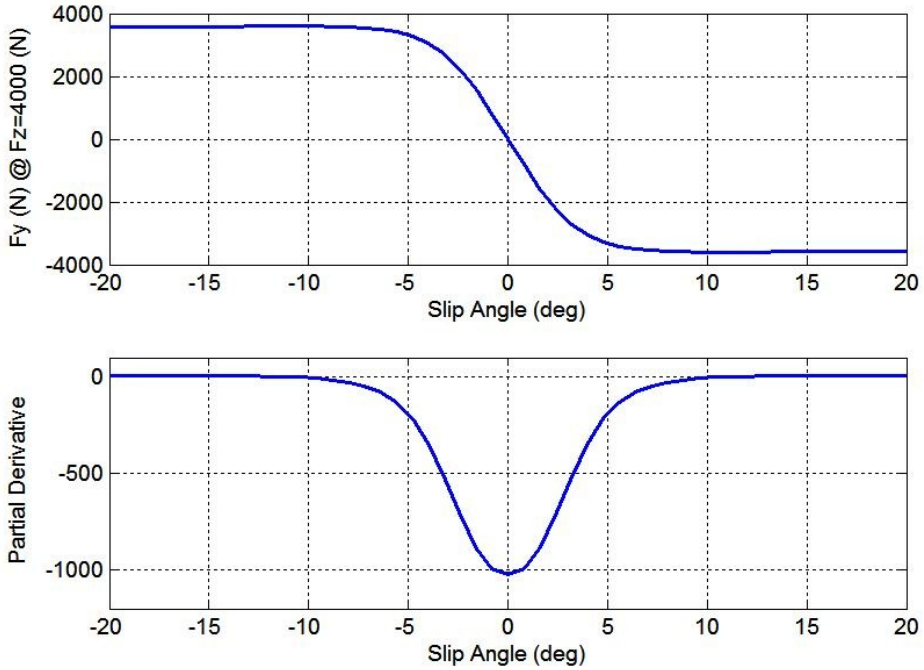

Figure 5.4 Partial derivative of the tire lateral force vs. slip angle at zero slip

With these partial derivatives being defined, the control effectiveness matrix can be readily populated from (3.78-80) as,

$$B = \begin{pmatrix} B_1 \\ B_2 \\ B_3 \end{pmatrix}, \tag{5.10}$$

where,

$$\begin{aligned} B_1 = \frac{\partial F_x}{\partial U} = [&\frac{\partial F_{xfl}}{\partial s_{fl}}\cos\delta_{fl} - \frac{\partial F_{yfl}}{\partial s_{fl}}\sin\delta_{fl}, \quad \frac{\partial F_{xfl}}{\partial \alpha_{fl}}\cos\delta_{fl} - \frac{\partial F_{yfl}}{\partial \alpha_{fl}}\sin\delta_{fl}, \\ &\frac{\partial F_{xfr}}{\partial s_{fr}}\cos\delta_{fr} - \frac{\partial F_{yfr}}{\partial s_{fr}}\sin\delta_{fr}, \quad \frac{\partial F_{xfr}}{\partial \alpha_{fr}}\cos\delta_{fr} - \frac{\partial F_{yfr}}{\partial \alpha_{fr}}\sin\delta_{fr}, \\ &\frac{\partial F_{xrl}}{\partial s_{rl}}\cos\delta_{rl} - \frac{\partial F_{yrl}}{\partial s_{rl}}\sin\delta_{rl}, \quad \frac{\partial F_{xrl}}{\partial \alpha_{rl}}\cos\delta_{rl} - \frac{\partial F_{yrl}}{\partial \alpha_{rl}}\sin\delta_{rl}, \\ &\frac{\partial F_{xrr}}{\partial s_{rr}}\cos\delta_{rr} - \frac{\partial F_{yrr}}{\partial s_{rr}}\sin\delta_{rr}, \quad \frac{\partial F_{xrr}}{\partial \alpha_{rr}}\cos\delta_{rr} - \frac{\partial F_{yrr}}{\partial \alpha_{rr}}\sin\delta_{rr}] \end{aligned} . \tag{5.11}$$

$$
\begin{aligned}
B_2 = \frac{\partial F_y}{\partial U} = [&\frac{\partial F_{xfl}}{\partial s_{fl}}\sin\delta_{fl} + \frac{\partial F_{yfl}}{\partial s_{fl}}\cos\delta_{fl}, \quad \frac{\partial F_{xfl}}{\partial \alpha_{fl}}\sin\delta_{fl} + \frac{\partial F_{yfl}}{\partial \alpha_{fl}}\cos\delta_{fl}, \\
&\frac{\partial F_{xfr}}{\partial s_{fr}}\sin\delta_{fr} + \frac{\partial F_{yfr}}{\partial s_{fr}}\cos\delta_{fr}, \quad \frac{\partial F_{xfr}}{\partial \alpha_{fr}}\sin\delta_{fr} + \frac{\partial F_{yfr}}{\partial \alpha_{fr}}\cos\delta_{fr}, \\
&\frac{\partial F_{xrl}}{\partial s_{rl}}\sin\delta_{rl} + \frac{\partial F_{yrl}}{\partial s_{rl}}\cos\delta_{rl}, \quad \frac{\partial F_{xrl}}{\partial \alpha_{rl}}\sin\delta_{rl} + \frac{\partial F_{yrl}}{\partial \alpha_{rl}}\cos\delta_{rl}, \\
&\frac{\partial F_{xrr}}{\partial s_{rr}}\sin\delta_{rr} + \frac{\partial F_{yrr}}{\partial s_{rr}}\cos\delta_{rr}, \quad \frac{\partial F_{xrr}}{\partial \alpha_{rr}}\sin\delta_{rl} + \frac{\partial F_{yrr}}{\partial \alpha_{rr}}\cos\delta_{rr}]
\end{aligned}
\qquad (5.12)
$$

$$
\begin{aligned}
B_3 = \frac{\partial M_z}{\partial U} = [&\frac{\partial F_{xfl}}{\partial s_{fl}}(-l_s\cos\delta_{fl} + l_f\sin\delta_{fl}) + \frac{\partial F_{yfl}}{\partial s_{fl}}(l_s\sin\delta_{fl} + l_f\cos\delta_{fl}), \\
&\frac{\partial F_{xfl}}{\partial \alpha_{fl}}(-l_s\cos\delta_{fl} + l_f\sin\delta_{fl}) + \frac{\partial F_{yfl}}{\partial \alpha_{fl}}(l_s\sin\delta_{fl} + l_f\cos\delta_{fl}), \\
&\frac{\partial F_{xfr}}{\partial s_{fr}}(l_s\cos\delta_{fr} + l_f\sin\delta_{fr}) + \frac{\partial F_{yfr}}{\partial s_{fr}}(-l_s\sin\delta_{fr} + l_f\cos\delta_{fr}), \\
&\frac{\partial F_{xfr}}{\partial \alpha_{fr}}(l_s\cos\delta_{fr} + l_f\sin\delta_{fr}) + \frac{\partial F_{yfr}}{\partial \alpha_{fr}}(-l_s\sin\delta_{fr} + l_f\cos\delta_{fr}), \\
&\frac{\partial F_{xrl}}{\partial s_{rl}}(-l_s\cos\delta_{rl} - l_r\sin\delta_{rl}) + \frac{\partial F_{yrl}}{\partial s_{rl}}(l_s\sin\delta_{rl} - l_r\cos_{rl}), \\
&\frac{\partial F_{xrl}}{\partial \alpha_{rl}}(-l_s\cos\delta_{rl} - l_r\sin\delta_{rl}) + \frac{\partial F_{yrl}}{\partial \alpha_{rl}}(l_s\sin\delta_{rl} - l_r\cos_{rl}), \\
&\frac{\partial F_{xrr}}{\partial s_{rr}}(l_s\cos\delta_{rr} - l_r\sin\delta_{rr}) + \frac{\partial F_{yrr}}{\partial s_{rr}}(-l_s\sin\delta_{rr} - l_r\cos\delta_{rr}), \\
&\frac{\partial F_{xrr}}{\partial \alpha_{rr}}(l_s\cos\delta_{rr} - l_r\sin\delta_{rr}) + \frac{\partial F_{yrr}}{\partial \alpha_{rr}}(-l_s\sin\delta_{rr} - l_r\cos\delta_{rr})]
\end{aligned}
\qquad (5.13)
$$

Note that the effects due to changes of tire normal load F_{zi} and tire-road friction coefficient μ_i are included in the control effectiveness matrix B in (5.6-9). In this dissertation, the tire normal load is estimated by (2.28-35) with dynamic load transfer calculated by measurement from a typical inertial sensor. Tire-road friction coefficients are assumed available through estimators [Wang et al., 2004], [Gustaffson, 1997] and/or stand-alone sensors [Uno et al., 1994], [Breuer et al., 1992].

The control allocation also provides freedom to apply the same control system to vehicle platforms with different architectures. If a vehicle does not have the fully independent driving/braking/steering actuation for all the wheels, the control effectiveness matrix can be easily modified while keeping the overall control structure the same. For instance, if a vehicle is not equipped with a 4-wheel independent steering mechanism but only have front and rear steering capabilities, then the column 4 and column 8 (or columns 2 and 6) can be removed from the matrix B. It then implies that the two front wheels share one degree of freedom and two rear wheels share another one. The resultant control effectiveness matrix is $B \in \Re^{3\times 6}$.

5.2 CHOICE OF THE VARIABLES ALLOCATE TO

Unlike aircraft control, where control variables or actuators are usually independent, ground vehicle actuation forces (tire forces) are inherently coupled. The coupling between tire longitudinal (driving or braking) force and lateral force is described in Chapter 2, and can also be expressed by the friction ellipse in Figure 5.5.

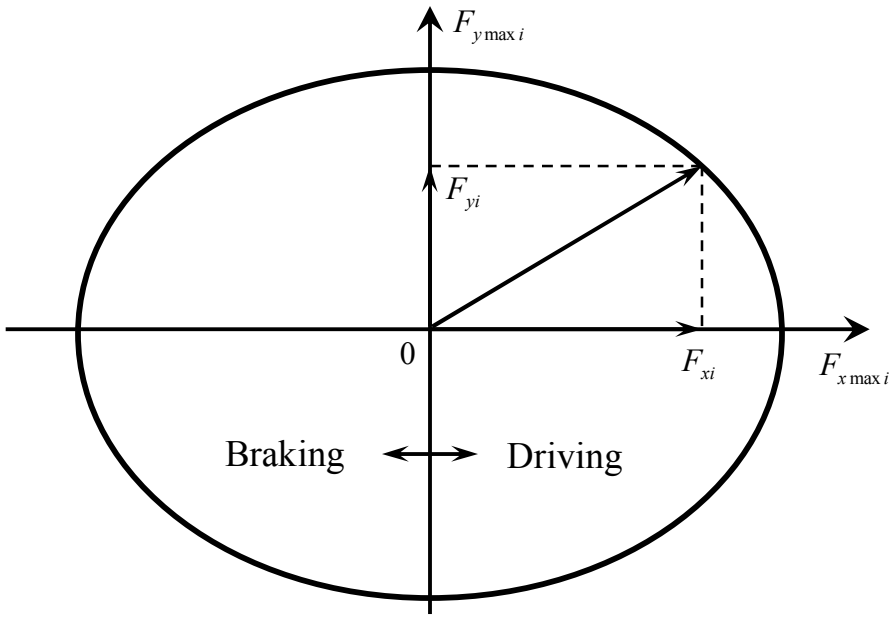

Figure 5.5 Friction ellipse for tire forces.

In the friction ellipse, the tire longitudinal and lateral forces follow the nonlinear constraint,

$$\left(\frac{F_{xi}}{C_{xi}}\right)^2 + \left(\frac{F_{yi}}{C_{yi}}\right)^2 \le (\mu_i F_{zi})^2, \tag{5.14}$$

with $F_{x\max i} = C_{xi}\mu_i F_{zi}$ and $F_{y\max i} = C_{yi}\mu_i F_{zi}$ being the maximum achievable tire longitudinal and lateral forces, respectively. The sum of the weighted squares of tire longitudinal force and lateral force is physically limited by the tire normal load and tire-road friction coefficient.

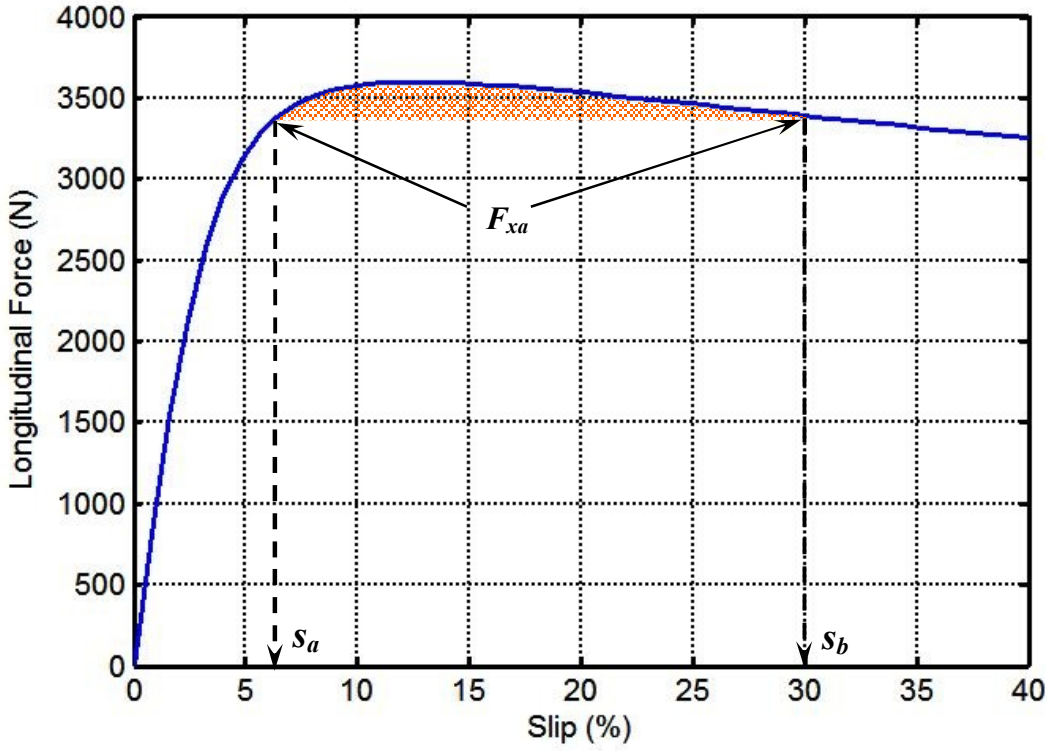

Figure 5.6 Non-monotonic tire longitudinal force vs. slip.

Recently, control allocation approaches have been introduced in the ground vehicle control systems to improve performances and achieve reconfigurable control [Hac et al., 2006], [Mokhiamar and Abe, 2005], [Fredriksson et al., 2004], [Plumlee,

Bevly, and Hodel, 2004]. However, in these suggested control allocation schemes, the virtual controls are allocated to longitudinal and/or lateral forces of tires. Instead of allocating to the tire longitudinal and lateral forces, we propose to allocate the virtual controls to the slip and slip angle of each tire, considering the following:

1) Slip/slip angle can be explicitly constrained in the stable and monotonic regions. Due to the characteristics of the relationships between tire longitudinal/lateral forces and slip/slip angle, allocating to the tire forces may put the tire in the large (unstable) slip/slip angle regions. If operating in the these regions, any need to reduce the tire force requires its state to traverse a "bump" due to the continuity of slip/slip angle, as shown in Figure 5.6, which may cause undesirable behaviors.
2) Slip and slip angle are quantities that can be readily measured or estimated in practice for closed-loop tracking control purposes, while force is difficult to measure in vehicle applications. Chapter 6 presents a combined tire slip and slip angle tracking control system.
3) A nonlinear constraint needs to be considered if the virtual control is allocated to tire forces, due to the friction ellipse as described above. This requires nonlinear programming, which may unduly increase the computational effort in general. If allocating to tire slip and slip angle, the nonlinear constraints can be decoupled into independent linear constraints because tire-slip/slip-angle range depends on friction coefficient only. This simplifies the control allocation optimization problem.

5.3 CVDC SLIP AND SLIP ANGLE AMPLITUDE AND RATE CONSTRAINTS

As shown in the Magic Formula tire model, there is a certain region in which the relationships between slip/slip angle and tire longitudinal/lateral forces are monotonic.

We consider that region as the effective actuation region because if we operate outside that region, the slip and slip angle will need to travel through a "bump" to reduce the tire force, which is not desired. These slip and slip angle limits construct the actuation amplitude limits $U_{\min}$ and $U_{\max}$ in (4.8). They can be derived by setting the partial derivatives of the longitudinal force and lateral force with respect to slip and slip angle to zero.

$$\begin{aligned}
\frac{\partial F_{xi}}{\partial s_i} &= D_{x\alpha i}\cos[C_{x\alpha i}\arctan(B_{x\alpha i}\alpha_{\mu i})]R_{\mu i}\mu_0 F_{zi} \\
&\quad \cos\left\{C_{xi}\arctan\left[B_{xi}\left(s_i/R_{\mu i}+S_{hxi}\right)-E_{xi}\left(B_{xi}\left(s_i/R_{\mu i}+S_{hxi}\right)-\arctan\left(B_{xi}\left(s_i/R_{\mu i}+S_{hxi}\right)\right)\right)\right]\right\} \\
&\quad C_{xi}\Big/\left\{1+\left[B_{xi}\left(s_i/R_{\mu i}+S_{hxi}\right)-E_{xi}\left(B_{xi}\left(s_i/R_{\mu i}+S_{hxi}\right)-\arctan\left(B_{xi}\left(s_i/R_{\mu i}+S_{hxi}\right)\right)\right)\right]^2\right\} \\
&\quad \left\{\frac{B_{xi}}{R_{\mu i}}-\frac{E_{xi}B_{xi}}{R_{\mu i}}+\frac{E_{xi}B_{xi}/R_{\mu i}}{1+\left[B_{xi}\left(s_i/R_{\mu i}+S_{hxi}\right)\right]^2}\right\} \\
&\quad =0 \\
\Rightarrow B_{xi}\left(s_i/R_{\mu i}+S_{hxi}\right)&-E_{xi}\left(B_{xi}\left(s_i/R_{\mu i}+S_{hxi}\right)-\arctan\left(B_{xi}\left(s_i/R_{\mu i}+S_{hxi}\right)\right)\right)=\pm\tan\left(\frac{\pi}{2C_{xi}}\right)
\end{aligned} \quad . (5.15)$$

To obtain the slip limits, we will need to solve this trigonometric equation, which is difficult to do analytically. Fortunately, it is clear that the slip limit is a function of tire-road friction coefficient only and not related to other variables. Thus we can obtain approximate solution. The longitudinal force vs. slip at different friction levels is shown in Figure 5.7. The effective region is shown in shaded area.

Thus, the slip limit $\pm s_{\lim} = f(\mu)$ can be approximated with a 1-D lookup table with sufficient accuracy. Notice that in practice, the positive slip limit, $+s_{\lim}$, may be difficult to achieve due to limitation on the available driving torque from powertrain at driving / traction condition. The negative slip limit, $-s_{\lim}$, however, is often readily achieved by sufficient braking torque.

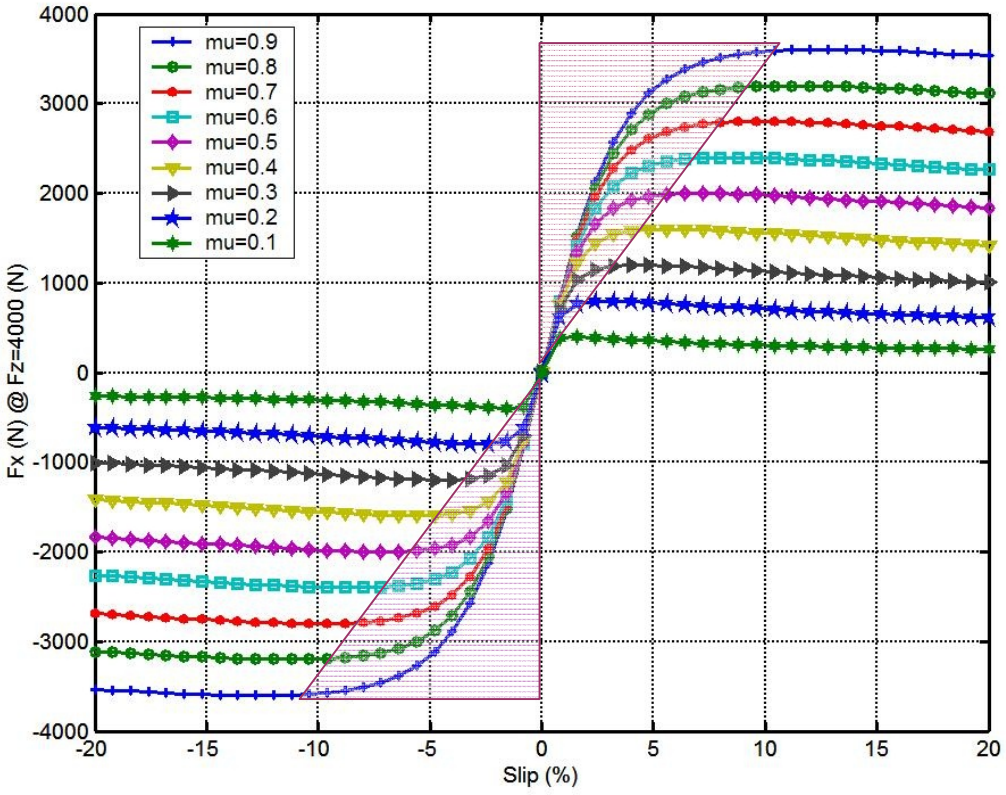

Figure 5.7 Tire longitudinal force vs. slip at different friction levels.

Similarly, we can get the operation region for the slip angle as a function of tire-road friction coefficient by setting the partial derivative as zero.

$$\begin{aligned}\frac{\partial F_{yi}}{\partial \alpha_i} &= D_{ysi}\cos[C_{ysi}\arctan(B_{ysi}s_{\mu i})]R_{\mu i}\mu_0 F_{zi} \\ &\cos\left\{C_{yi}\arctan\left[B_{yi}\left(\alpha_i/R_{\mu i}+S_{hyi}\right)-E_{yi}\left(B_{yi}\left(\alpha_i/R_{\mu i}+S_{hyi}\right)-\arctan\left(B_{yi}\left(\alpha_i/R_{\mu i}+S_{hyi}\right)\right)\right)\right]\right\} \\ &C_{yi}/\left\{1+\left[B_{yi}\left(\alpha_i/R_{\mu i}+S_{hyi}\right)-E_{yi}\left(B_{yi}\left(\alpha_i/R_{\mu i}+S_{hyi}\right)-\arctan\left(B_{yi}\left(\alpha_i/R_{\mu i}+S_{hyi}\right)\right)\right)\right]^2\right\} \\ &\left\{\frac{B_{yi}}{R_{\mu i}}-\frac{E_{yi}B_{yi}}{R_{\mu i}}+\frac{E_{yi}B_{yi}/R_{\mu i}}{1+\left[B_{yi}\left(\alpha_i/R_{\mu i}+S_{hyi}\right)\right]^2}\right\} \\ &=0\end{aligned} \quad . \quad (5.16)$$

$$\Rightarrow B_{yi}\left(\alpha_i/R_{\mu i}+S_{hyi}\right)-E_{yi}\left(B_{yi}\left(\alpha_i/R_{\mu i}+S_{hyi}\right)-\arctan\left(B_{yi}\left(\alpha_i/R_{\mu i}+S_{hyi}\right)\right)\right)=\pm\tan\left(\frac{\pi}{2C_{yi}}\right)$$

Same as the slip limit, the slip angle limit is purely a function of tire-road friction coefficient and we can obtain the approximate solution with sufficient accuracy. The regions of operation for slip angle at different friction levels are shown in Figure 5.8. Notice that the opposite signs for slip angle and lateral force are designed to match with the sign conventions of the CarSim® vehicle dynamics simulation package which will be used to evaluate the control system.

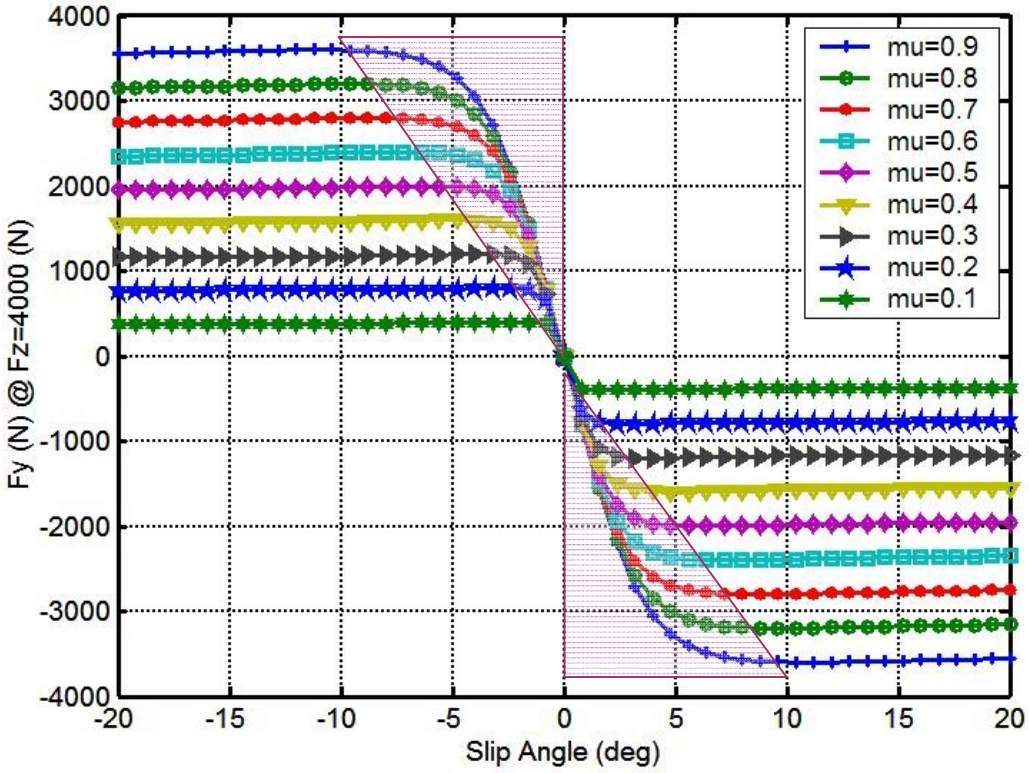

Figure 5.8 Tire lateral force vs. slip at different friction levels.

For vehicle dynamics control system, tire slip and slip angle are not only limited by tire friction ellipse described previously, but also by availabilities of actuation torques, especially for slip as tire driving torque greatly depends on rotational speeds of components coupled with wheel (engine/driveline for conventional automobiles or motor

for electric vehicles). From a physical system perspective, slip is more expensive than slip angle because to generate tire slip, wheel driving/braking torque needs to act against the torque caused by tire longitudinal force; to generate slip angle, wheel steering torque needs to against tire self-aligning moment, which is much smaller. In addition, rate limits of the slip and slip angle also depend on wheel operating conditions and available driving/braking torque.

5.4 APPLICATIONS OF THE AFP CA ON COORDINATED CVDC

In this section, we show some application results of the coordinated vehicle dynamics control specific control allocation using the accelerated fixed-point algorithm developed in Chapter 4.

5.4.1 Starting Point and Termination of the CVDC AFP Iteration

Starting point can be chosen in several different ways. We use the starting point with minimum actuation L_2 norm within the constrained feasible region. The selection method is described in Chapter 4 (4.96). Consider the mixed optimization objective function for the quadratic programming based control allocation.

$$J = \frac{1}{2}(1-\varepsilon)\left(BU - v_d\right)^T W_v (BU - v_d) + \frac{1}{2}\varepsilon U^T W_u U \,. \tag{5.17}$$

As described in Chapter 4, $0 < \varepsilon << 1$ is the weighting factor, which is usually small in order to ensure minimization of the control allocation. By selecting the starting point as the one with minimal L_2 norm, the second term in (5.17) is already minimized at the beginning of the iteration. However, it is not to say that this selection of starting point will give less iterations.

When to terminate the AFP iteration is a tradeoff between computational efforts (number of iterations in this case) and control allocation accuracy as described in Chapter 4. Simulation tests show that terminating the AFP iteration when $\left\|U_k^{t+1} - U_k^t\right\| \le 5e-3$ can

produce satisfactory control performance with manageable computational effort for real-time control system.

5.4.2 Comparisons for Braking through a Split-μ Maneuver

In this sub-section, we will use an adverse driving scenario: hard braking through a split-μ surface, as a case study to show the performance of the control allocation with different termination tolerances.

As shown in Figure 5.9, the vehicle is traveling at 140 km/h and starts braking with a deceleration -5 m/s^2 (~-0.5 g). The friction coefficient at all tires is initially 0.9. The friction coefficient on the right side drops to 0.3, and becomes 0.9 again after 50m. This simulates the case of braking through an icy spot on the right side of the vehicle while left side is dry concrete surface.

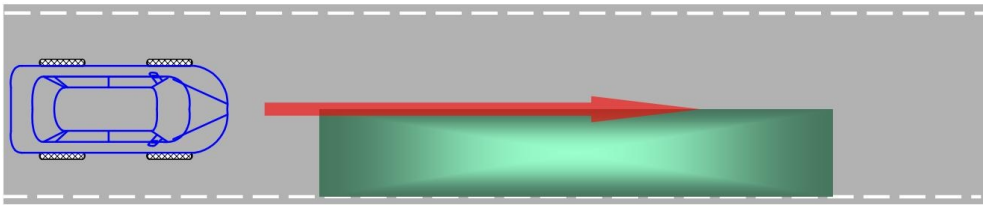

Figure 5.9 Hard braking through a split-μ surface.

Three different CVDC systems are compared with different control allocation methods. The "CVDC: 5e-3" means the CVDC with $\left\|U_k^{t+1} - U_k^t\right\| \le 5e-3$ for AFP CA. The "CVDC: 5e-4" denotes the CVDC with $\left\|U_k^{t+1} - U_k^t\right\| \le 5e-4$ for AFP CA. The "CVDC: M" represents the CVDC using the standard quadratic programming function (active-set algorithm) in Matlab. Notice that other than the control allocation, the higher-level controller and lower-level controller (will be described in Chapter 6) for these three CVDC systems are exactly the same. As shown in Figure 5.10, all the three CVDC systems exhibit similar performance in terms of stable yaw motion and desired

longitudinal deceleration, which are much improved than those of conventional vehicle control systems as will be compared in Chapter 7.

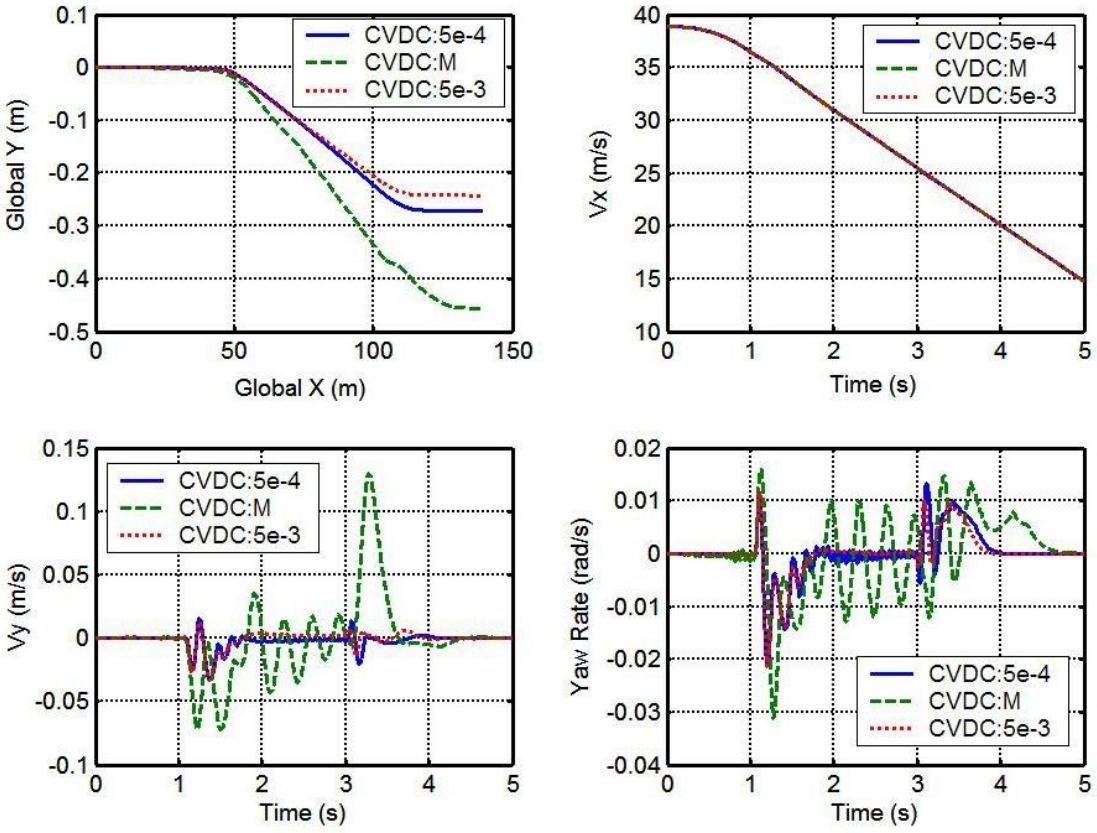

Figure 5.10 Comparisons of different CA schemes for coordinated VDC.

The number of iterations required for the three different control allocation methods are shown in Figure 5.11. The numbers of iterations for "CVDC: 5e-3" are less than 15 for the whole simulation, which are lower than the case of "CVDC: M" and much lower than those of "CVDC: 5e-4". Notice that computational effort (flops) of each iteration for the quadratic programming used in Matlab is much more intense than the fixed-point methods. The small numbers of iterations and low computational effort (flops) associated with each iteration of the AFP make it real-time adaptable. While reducing the AFP allocation tolerance increases the computational effort (more

iterations), it did not show any benefit in terms of system responses. This is because the difference in control allocation error is compensated for by the robustness of the higher-level controller.

Figure 5.11 also shows the desired and achieved virtual controls (generalized forces/moment). At the split- μ surface, the virtual controls are not attainable due to low friction, and therefore, low tire force. For different CVDC systems, both virtual controls and achieved controls are slightly different because of the interaction between higher-level controller and system.

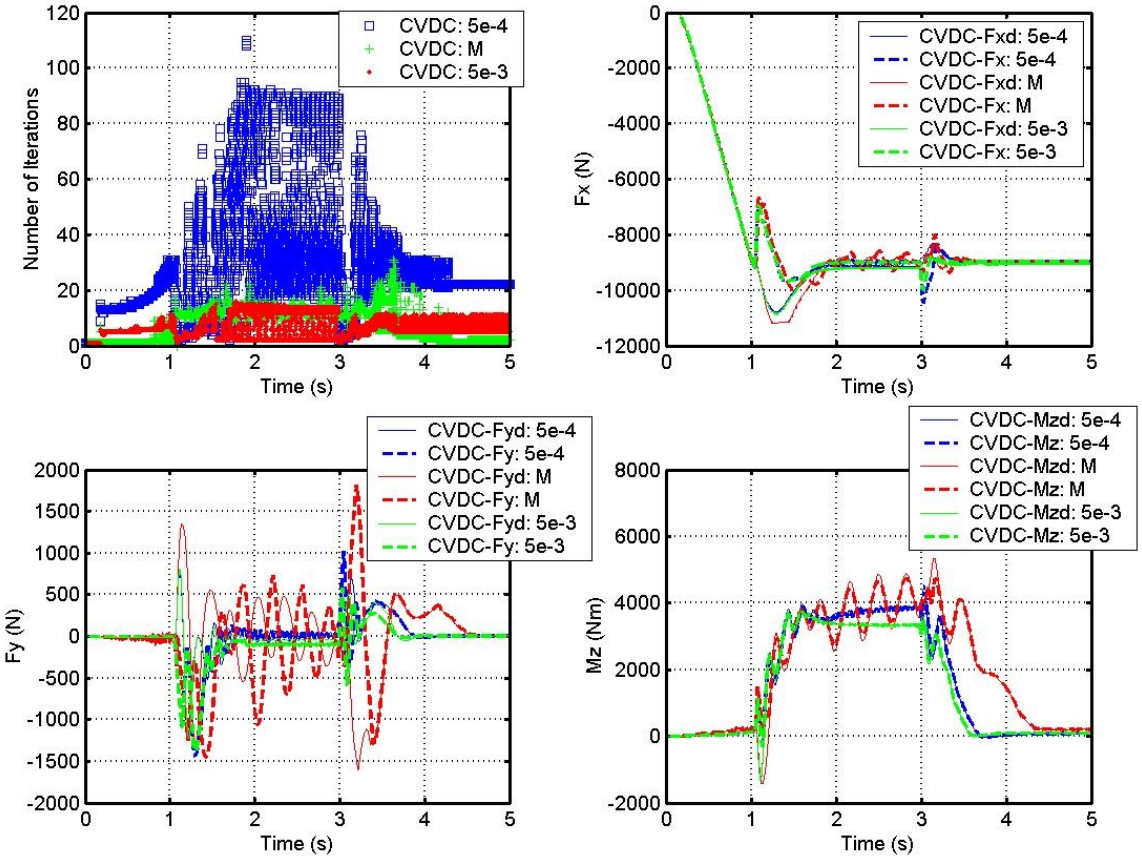

Figure 5.11 Comparisons of numbers of iterations and desired / actual virtual controls.

The allocated tire longitudinal slip and lateral slip angle values for the four tires (FL, FR, RL, RR) are compared in Figure 5.12 and Figure 5.13 respectively for the above three control allocation schemes. Note for comparison of different control allocation schemes, the slip and slip angle values are from the control allocation modules rather than the actual ones. These desired slip and slip angle values are the reference signals for the lower-level tire slip and slip angle tracking controllers as will be presented in Chapter 6.

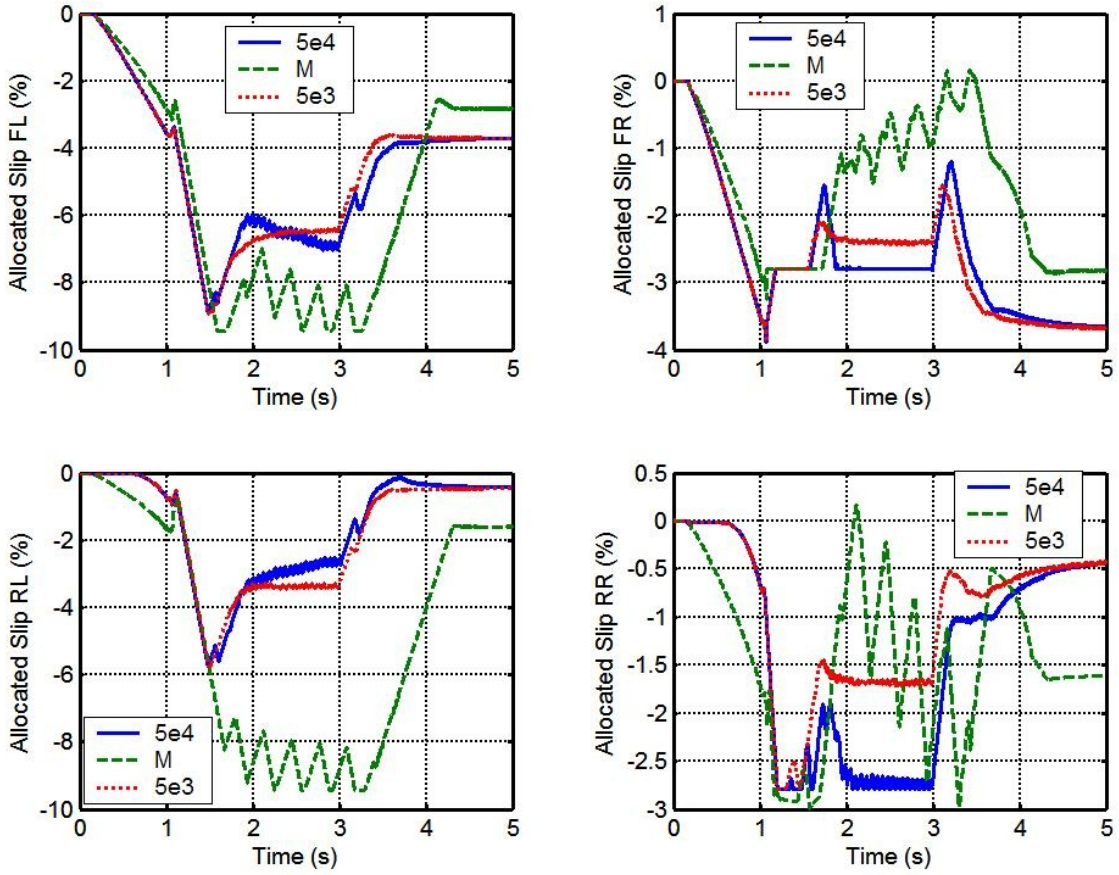

Figure 5.12 Comparisons of the allocated tire longitudinal slips.

As shown in Figure 5.12, the allocated slip values for AFP with different termination tolerances (5e-3 and 5e-4) are similar and gradual. However, they are

considerably different from the ones generated by the quadratic programming algorithm (active-set) in Matlab, which vary greatly especially at the split-μ surface. Similar phenomenon for the active-set CA method is also observed in [Petersen and Bodson, 2006]. For control performance point of view, smoothness of the AFP is more favorable. In Figure 5.13, similar characteristics are noticed for the slip angle case.

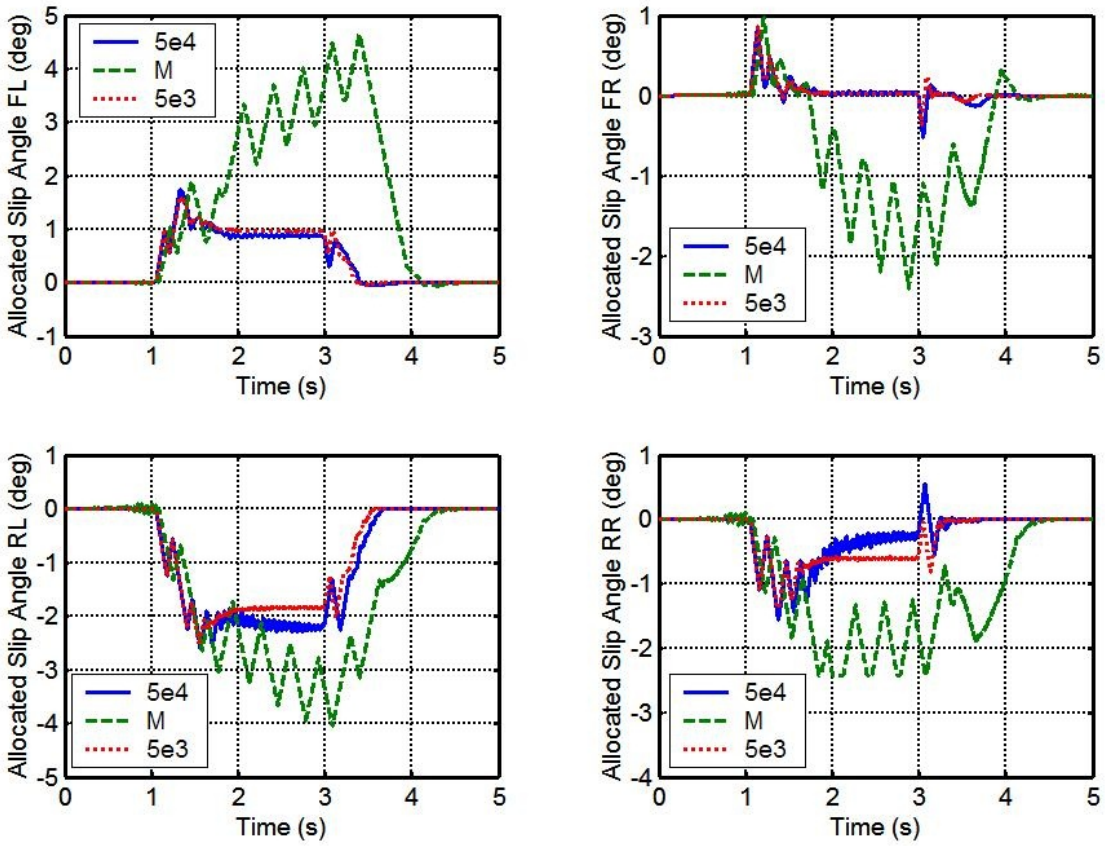

Figure 5.13 Comparisons of the allocated tire lateral slip angles.

5.5 SUMMARY

In this chapter, a vehicle dynamics control allocation scheme has been designed that takes into account vehicle states and tire-road friction coefficient. Instead of tire longitudinal / lateral forces, allocation targets tire slip and slip angle at each tire. This approach converts the nonlinearly coupled constraints to independent linear constraints,

which makes the realization possible by greatly reducing the computational complexity and burden.

The real-time adaptable, computationally efficient accelerated fixed-point control allocation method developed in Chapter 4 is employed for coordinated vehicle dynamics control. Simulation results of the coordinated VDC using the proposed control allocation scheme shows obvious benefits in vehicle response as well as in computational effort.

In the next chapter, we will describe the lower-level tire slip and slip angle tracking control to actually achieve the desired tire slips and slip angles dictated by the control allocation.

Chapter 6: Combined Tire Slip and Slip Angle Tracking Control

In Chapter 5, we explained that for coordinated ground vehicle dynamic control systems, it is more appropriate to allocate the generalized virtual controls to slip and slip angle of each tire rather than directly to tire forces. Thus, it is requisite to have a combined tire slip and slip angle tracking controller (lower-level controller in Figure 3.6) to make each tire achieve the desired slip and slip angle. Here, the desired tire slips and slip angles are dictated by the control allocation. The lower-level controllers manipulate corresponding driving/braking/steering actions to achieve the desired values. As the vehicle systems continuously develop, individual wheel driving/braking/steering control is possible through the advanced sub-systems such as brake-by-wire, torque-vectoring, steer-by-wire, and hybrid/fuel cell vehicles. With each tire running at its corresponding desired slip and slip angle, and therefore, the longitudinal and lateral forces, the resultant forces and moment acting on vehicle's C.G. will be as desired to control the vehicle motions / states. This chapter describes the design of this controller [Wang and Longoria, 2006b].

Several tire slip control methods have been developed in literature for different application purposes. Solyom and Rantzer [Solyom and Rantzer, 2003] studied an ABS controller to regulate tire longitudinal slip at a fixed value. In [Patil et al., 2003], the authors developed an ABS control system to regulate tire longitudinal slip at a desired value and tested using a scaled vehicle. In [Johansen et al., 2003], a vehicle speed based gain-scheduled control system is developed for tire longitudinal slip tracking in an anti-lock braking application. In this work, all the four tires are assumed to have identical slip and zero lateral slip angle. The system thus virtually becomes one single tire. These approaches are not applicable for the coordinated VDC systems in which individual tires

will exercise different slips and slip angles according to their own control effectiveness determined by vehicle body dynamics and environmental factors. In [Taheri and Law, 1990], the authors describe a combined fixed slip regulation and four wheel steering control system based on a bicycle model. Slip is used to control vehicle longitudinal motion, and four-wheel steering is used to control yaw motion. Venkataraman and Waldron proposed an active steering / braking control for individual wheel to improve the vehicle maneuverability based on a linearized vehicle model [Venkataraman and Waldron, 1993]. Constant tire cornering stiffness and constant friction coefficient are assumed in this study.

However, simultaneous tire slip and slip angle tracking control has rarely been reported in literature. When approaching the limits, tire forces are particularly dependent on the coupling effects of slip and slip angle. In order to achieve coordination among all the tires and best possible performance, each tire needs to simultaneously track its own desired slip and slip angle dictated by the control allocation algorithm.

6.1 SYSTEM MODELING

Tire longitudinal slip and lateral slip angle tracking control is realized by manipulating the driving/braking/steering torques of each wheel individually. In this section, we present the dynamic models of those actuation sub-systems for control design purposes.

6.1.1 Steer-by-Wire Dynamics

Steer-by-wire systems have been developed by several manufactures and used on production vehicles [Oh et al., 2004], [Cesiel et al., 2006]. Steer-by-wire replaces the steering column with a fault-tolerant controller and motor that connects to the wheel steering rack. Besides its benefits on vehicle design, safety, and fuel economy, it also

greatly increases the control freedom. The dynamics can be approximately modeled as a second-order system [Yih et al., 2004], [Heinzl et al., 2002],

$$J_{wzi}\ddot{\delta}_i + b_{wzi}\dot{\delta}_i + M_{zi} = T_{wzi}, \tag{6.1}$$

where J_{wzi} is the rotational moment of inertia about the wheel's Z axis, b_{wzi} is the damping, T_{wzi} is applied actuation torque from the motor, M_{zi} is the tire self-aligning moment from the ground, and δ_i is the steering angle of the road wheel. Any steering induced by suspension kinematics and compliance is not modeled here, although these effects are present in the CarSim® model used to evaluate the control system. The dynamics of all tires are assumed to have the same model form, so a controller designed for one can be applied to all other wheels. Specifically, let $x_{1i} = \delta_i$ and $x_{2i} = \dot{\delta}_i$, and steering system dynamics for the *i*th tire is expressed as,

$$\begin{aligned} \dot{x}_{1i} &= x_{2i} \\ \dot{x}_{2i} &= -\frac{b_{wzi}}{J_{wzi}}x_{2i} - \frac{f_{zi}(s_i, \alpha_i, F_{zi}, \mu_i)}{J_{wzi}} + \frac{T_{wzi}}{J_{wzi}}, \end{aligned} \tag{6.2}$$

where $f_{zi}(\cdot)$ denotes tire self-aligning moment as described in the Magic Formula tire model (2.12).

6.1.2 Wheel Longitudinal Slip Dynamics

The rotational motion of the wheel during acceleration and deceleration (about its *Y* axis) is determined by the longitudinal force from the ground and driving/braking torque applied to the wheel. These dynamics are approximated by,

$$J_{wyi}\dot{\omega}_{wyi} = T_{wyi} - R_i F_{xi}, \tag{6.3}$$

where J_{wyi} is the rotational moment of inertia of the wheel, T_{wyi} is the torque (driving or braking) applied to the wheel about its *Y* axis, and F_{xi} is the tire longitudinal force from ground. The effect of rolling resistance is ignored here.

The derivative of the slip can be found from (2.4) as,

$$\dot{s}_i = \frac{\dot{\omega}_{wyi} R_i}{V_{xi}} - \frac{\omega_{wyi} R_i \dot{V}_{xi}}{V_{xi}^2}. \tag{6.4}$$

Notice that the term $\dot{V}_{xi}$ is the derivative of the longitudinal velocity at center of each wheel and involves the dynamics of vehicle body motions such as longitudinal velocity, lateral velocity, and yaw rate. Combining (6.3) and (6.4) provides an equation for the dynamics of the tire longitudinal slip as,

$$\dot{s}_i = -\frac{f_{xi}(s_i, \alpha_i, F_{zi}, \mu_i) R_i^{\,2}}{J_{wyi} V_{xi}} + \frac{T_{wyi} R_i}{J_{wyi} V_{xi}} - \frac{\dot{V}_{xi}}{V_{xi}} s_i - \frac{\dot{V}_{xi}}{V_{xi}}, \tag{6.5}$$

where $f_{xi}(\cdot)$ denotes tire longitudinal force as described in the Magic Formula tire model (2.12). With $x_{3i} = s_i$, (6.2), and (6.5), the system can be rewritten as,

$$\dot{x}_{3i} = -\frac{f_{xi}(x_{3i}, \alpha_i, F_{zi}, \mu_i) R_i^{\,2}}{J_{wyi} V_{xi}} + \frac{T_{wyi} R_i}{J_{wyi} V_{xi}} - \frac{\dot{V}_{xi}}{V_{xi}} x_{3i} - \frac{\dot{V}_{xi}}{V_{xi}}. \tag{6.6}$$

Notice that when $V_{xi} \to 0$, the open loop slip dynamics will be infinitely fast. Thus, the slip controller should be disabled at low speed, which is common in practice for vehicle control systems [Johansen et al., 2003]. Grouping (6.2) and (6.6) yields a MIMO dynamic system in state space form as,

$$\begin{aligned}
\dot{x}_{1i} &= x_{2i} \\
\dot{x}_{2i} &= -\frac{b_{wzi}}{J_{wzi}} x_{2i} - \frac{f_{zi}[x_{3i}, f_{\alpha i}(x_{1i}, \xi), F_{zi}, \mu_i]}{J_{wzi}} + \frac{T_{wzi}}{J_{wzi}} \\
\dot{x}_{3i} &= -\frac{f_{xi}[x_{3i}, f_{\alpha i}(x_{1i}, \xi), F_{zi}, \mu_i] R_i^{\,2}}{J_{wyi} V_{xi}} + \frac{T_{wyi} R_i}{J_{wyi} V_{xi}} - \frac{\dot{V}_{xi}}{V_{xi}} x_{3i} - \frac{\dot{V}_{xi}}{V_{xi}}
\end{aligned}, \tag{6.7}$$

where, $\alpha_i = f_{\alpha i}(\delta_i, \xi)$ represents the slip angle calculated from (3.81) with $\xi = [V_x, V_y, \Omega_z]$. $y_i = [x_{1i} \quad x_{3i}]^T$ is the output vector and $u_i = [T_{wzi} \quad T_{wyi}]^T$ is the input vector.

6.2 CONTROL SYSTEM DESIGN

The goal of the combined tire slip and slip angle tracking control is to manipulate the driving/braking/steering actuation of wheel to track the desired tire slip and slip angle

values dictated by control allocation. Vehicle body states such as V_x, V_y, and Ω_z are considered as exogenous signals rather than states at this controller level, in order to isolate the control tasks. This will become more clearly in a later sub-section.

As mentioned before, there are parametric uncertainties and un-modeled dynamics in the MIMO nonlinear system described in (6.7), arising from rolling resistance, aerodynamics, etc. Therefore, a sliding mode control (SMC) approach is used to design a control system for its robustness.

6.2.1 Relative Degree and Zero Dynamics

It can be shown that for the $y_{1i} = x_{1i}$ channel, the relative degree is 2 and for the $y_{2i} = x_{3i}$ channel, the relative degree is 1; hence,

$$y_{1i}^{(1)} = L_f h_{1i}(x_i) + L_g h_{1i}(x_i) \cdot u_i = x_{2i}, \tag{6.8}$$

$$\begin{aligned} y_{1i}^{(2)} &= L_f^2 h_{1i}(x_i) + L_g L_f h_{1i}(x_i) \cdot u_i \\ &= -\frac{b_{wzi}}{J_{wzi}} x_{2i} - \frac{f_{zi}[x_{3i}, f_{\alpha i}(x_{1i}, \xi), F_{zi}, \mu_i]}{J_{wzi}} + \frac{T_{wzi}}{J_{wzi}}, \end{aligned} \tag{6.9}$$

$$\begin{aligned} y_{2i}^{(1)} &= L_f h_{2i}(x_i) + L_g h_{2i}(x_i) \cdot u_i \\ &= -\frac{f_{xi}[x_{3i}, f_{\alpha i}(x_{1i}, \xi), F_{zi}, \mu_i] R_i^{\,2}}{J_{wyi} V_{xi}} + \frac{T_{wyi} R_i}{J_{wyi} V_{xi}} - \frac{\dot{V}_{xi}}{V_{xi}} x_{3i} - \frac{\dot{V}_{xi}}{V_{xi}}. \end{aligned} \tag{6.10}$$

Equations (6.9) and (6.10) can be rewritten as,

$$\begin{pmatrix} y_{1i}^{(2)} \\ y_{2i}^{(1)} \end{pmatrix} = \begin{pmatrix} -\frac{b_{wzi}}{J_{wzi}} x_{2i} - \frac{f_{zi}[x_{3i}, f_{\alpha i}(x_{1i}, \xi), F_{zi}, \mu_i]}{J_{wzi}} \\ -\frac{f_{xi}[x_{3i}, f_{\alpha i}(x_{1i}, \xi), F_{zi}, \mu_i] R_i^{\,2}}{J_{wyi} V_{xi}} - \frac{\dot{V}_{xi}}{V_{xi}} x_{3i} - \frac{\dot{V}_{xi}}{V_{xi}} \end{pmatrix} + \begin{pmatrix} \frac{1}{J_{wzi}} & 0 \\ 0 & \frac{R_i}{J_{wyi} V_{xi}} \end{pmatrix} \begin{pmatrix} T_{wzi} \\ T_{wyi} \end{pmatrix}. \tag{6.11}$$

For $V_{xi} \neq 0$, the matrix $\begin{pmatrix} \frac{1}{J_{wzi}} & 0 \\ 0 & \frac{R_i}{J_{wyi} V_{xi}} \end{pmatrix}$ is invertible, so this MIMO system has a *vector relative degree* as $(2 \quad 1)^T$. Then, as the total number of coordinates is equal to the

number of system states, there should be no zero dynamics involved within the tire slip / slip angle control system.

6.2.2 Robust Sliding Mode Controller Design

To achieve the slip and slip angle tracking purposes, define the sliding surfaces for the steering angle as,

$$\Omega_{1i} = (\frac{d}{dt} + P_{1i})\tilde{x}_{1i} = \dot{\tilde{x}}_{1i} + P_{1i}\tilde{x}_{1i} = \dot{x}_{1i} - \dot{x}_{1id} + P_{1i}(x_{1i} - x_{1id}), \tag{6.12}$$

where, $\tilde{x}_{1i} = x_{1i} - x_{1id}$ is the error between actual steering angle and desired steering angle, which can be obtained from (3.81) once the desired tire slip angle is specified, and P_{1i} is a positive number determining the dynamics of the surface.

$$\dot{\Omega}_{1i} = \dot{x}_{2i} - \ddot{x}_{1id} + P_{1i}(\dot{x}_{1i} - \dot{x}_{1id}) = -K_{1i}\,\mathrm{sgn}(\Omega_{1i}). \tag{6.13}$$

The attractiveness for sliding surface Ω_{1i} is apparent as there are no exogenous signals and selection of the gain K_{1i} is trivial based on the bounded parametric variations. With (6.7), the appropriate control law for steering angle can be derived as,

$$\begin{aligned} T_{wzi} &= b_{wzi}\dot{x}_{1i} + f_{zi}\left[x_{3i}, f_{\alpha i}(x_{1i}, \xi), F_{zi}, \mu_i\right] + J_{wzi}\ddot{x}_{1id} \\ &\quad - J_{wzi}P_{1i}(\dot{x}_{1i} - \dot{x}_{1id}) - J_{wzi}K_{1i}\,\mathrm{sgn}(\Omega_{1i}) \end{aligned}. \tag{6.14}$$

However, for the slip control law, tire center longitudinal speed V_{xi} and especially its derivative $\dot{V}_{xi}$, which is difficult to measure, need to be treated as time-varying exogenous signals. Otherwise, vehicle body motions will have to be involved because in (6.10) V_{xi} is a function of vehicle C.G.'s longitudinal velocity, lateral velocity and yaw rate described in (6.15a-d). This would make the system too complicated and place obstacles on the design of coordinated control systems.

$$V_{xfl} = (V_x - \dot{\psi} l_s)\cos\delta_{fl} + (V_y + \dot{\psi} l_f)\sin\delta_{fl}, \tag{6.15a}$$

$$V_{xfr} = (V_x + \dot{\psi} l_s)\cos\delta_{fr} + (V_y + \dot{\psi} l_f)\sin\delta_{fr}, \tag{6.15b}$$

$$V_{xrl} = (V_x - \dot{\psi} l_s)\cos\delta_{rl} + (V_y - \dot{\psi} l_r)\sin\delta_{rl}, \tag{6.15c}$$

$$V_{xrr} = (V_x + \dot{\psi} l_s)\cos\delta_{rr} + (V_y - \dot{\psi} l_r)\sin\delta_{rr}. \tag{6.15d}$$

In such a case, the control gain needs to be chosen sufficiently large to ensure the sliding surface is attractive with presence of the exogenous signals, but not too large in order to alleviate chattering effects. As described in Chapter 3, chattering effects could be reduced by introducing the continuous approximation of the switching function in the SMC control law. However, continuous approximation causes bounded steady-state tracking error. Instead of converging to the origin, the tracking error will converge to a neighborhood of the origin whose size is $o(\Phi)$ with Φ being the thickness of the boundary layer [Seshagiri and Khalil, 2002]. The steady-state tracking error can be eliminated by introducing integral actions in sliding surface [Seshagiri and Khalil, 2002], [Mantz et al., 1999], [Cheng and Miu, 1999]. In this particular case, since we treat V_{xi} and its derivative $\dot{V}_{xi}$ as exogenous signals, the control gain has to be sufficiently large. It then increases the tendency of chattering. Thus, continuous approximation and integral action will be both necessary and appropriate in order to avoid chattering as well as ensure sufficient tracking accuracy.

The tracking error can be defined as,

$$e_{3i} = x_{3i} - x_{3id}, \tag{6.16}$$

where x_{3id} is the desired slip. The integral action can be introduced by augmenting the system with a new state whose dynamics is,

$$\dot{\rho}_{3i} = e_{3i}. \tag{6.17}$$

The sliding surface for the slip can be defined as,

$$\Omega_{2i} = P_{2i}(x_{3i} - x_{3id}) + \lambda_{2i}\rho_{3i} = P_{2i}\dot{\rho}_{3i} + \lambda_{2i}\rho_{3i}, \tag{6.18}$$

where P_{2i} and λ_{2i} are positive numbers. The attractive equations are then obtained by differentiating the sliding surfaces,

$$\dot{\Omega}_{2i} = P_{2i}(\dot{x}_{3i} - \dot{x}_{3id}) + \lambda_{2i}e_{3i} = -K_{2i}\,\mathrm{sgn}(\Omega_{2i}). \tag{6.19}$$

Take the nominal wheel center longitudinal speed as the geometric mean of its bounds, $\overline{V}_{xw} = \sqrt{V_{xwl} V_{xwu}} > 0$. V_{xwl} and V_{xwu} are the lower bound and upper bound of the wheel center longitudinal speed for vehicle dynamics control and $0 < V_{xwl} \le V_{xi} \le V_{xwu}$. V_{xwl} is determined by the minimum vehicle speed for VDC being active and V_{xwu} is determined by the maximal vehicle speed, which is physically limited. Set the nominal wheel center longitudinal acceleration as $\dot{\overline{V}}_{xw}$.

The appropriate control law for the surface Ω_{2i} can be derived as,

$$\begin{aligned} T_{wyi} = \frac{1}{R_i} \{ & J_{wyi} \overline{V}_{xw} \dot{x}_{3id} + J_{wyi} \dot{\overline{V}}_{xw} x_{3i} + f_{xi}\left[x_{3i}, f_{\alpha i}(x_{1i}, \xi), F_{zi}, \mu_i\right] R_i^2 \\ & + J_{wyi} \dot{\overline{V}}_{xw} - J_{wyi} \overline{V}_{xw} \frac{\lambda_{2i}}{P_{2i}} e_{3i} - J_{wyi} \overline{V}_{xw} \frac{K_{2i}}{P_{2i}} \operatorname{sgn}(\Omega_{2i}) \} \end{aligned} . \tag{6.20}$$

Consider the Lyapunov function candidate,

$$V_{2i} = \frac{1}{2} \Omega_{2i}^2 \ge 0 . \tag{6.21}$$

$$\begin{aligned} \dot{V}_{2i} &= \Omega_{2i} \dot{\Omega}_{2i} \\ &= \Omega_{2i} P_{2i} \left[\frac{-f_{xi} R_i^2}{J_{wyi} V_{xi}} + \frac{f_{xi} R_i^2}{J_{wyi} V_{xi}} + \frac{\dot{\overline{V}}_{xw} x_{3i}}{V_{xi}} + \frac{\dot{\overline{V}}_{xw}}{V_{xi}} + \frac{\overline{V}_{xw} \dot{x}_{3id}}{V_{xi}} - \frac{\overline{V}_{xw} K_{2i} \operatorname{sgn}(\Omega_{2i})}{P_{2i} V_{xi}} - \frac{\dot{V}_{xi}}{V_{xi}} x_{3i} - \frac{\dot{V}_{xi}}{V_{xi}} - \dot{x}_{3id} - \frac{\overline{V}_{xw} \lambda_{2i} e_{3i}}{P_{2i} V_{xi}} + \frac{\lambda_{2i} e_{3i}}{P_{2i}} \right] \\ &= \Omega_{2i} P_{2i} \left[(x_{3i} + 1) \left(\frac{\dot{\overline{V}}_{xw}}{V_{xi}} - \frac{\dot{V}_{xi}}{V_{xi}} \right) + \left(\frac{\overline{V}_{xw}}{V_{xi}} - 1 \right) \dot{x}_{3id} - \frac{\overline{V}_{xw} K_{2i} \operatorname{sgn}(\Omega_{2i})}{P_{2i} V_{xi}} - \frac{\overline{V}_{xw} \lambda_{2i} e_{3i}}{P_{2i} V_{xi}} + \frac{\lambda_{2i} e_{3i}}{P_{2i}} \right] \\ &= \Omega_{2i} \operatorname{sgn}(\Omega_{2i}) P_{2i} \left[\operatorname{sgn}(\Omega_{2i}) (x_{3i} + 1) \left(\frac{\dot{\overline{V}}_{xw}}{V_{xi}} - \frac{\dot{V}_{xi}}{V_{xi}} \right) + \operatorname{sgn}(\Omega_{2i}) \left(\frac{\overline{V}_{xw}}{V_{xi}} - 1 \right) \dot{x}_{3id} - \frac{\overline{V}_{xw} K_{2i}}{P_{2i} V_{xi}} + \operatorname{sgn}(\Omega_{2i}) \left(1 - \frac{\overline{V}_{xw}}{V_{xi}} \right) \frac{\lambda_{2i} e_{3i}}{P_{2i}} \right] \\ &\le |\Omega_{2i}| \left[P_{2i} |x_{3i} + 1| \frac{|\dot{\overline{V}}_{xw} - \dot{V}_{xi}|}{|V_{xi}|} + P_{2i} \left| \frac{\overline{V}_{xw}}{V_{xi}} - 1 \right| |\dot{x}_{3id}| - \frac{\overline{V}_{xw}}{V_{xi}} K_{2i} + \left| 1 - \frac{\overline{V}_{xw}}{V_{xi}} \right| \lambda_{2i} |e_{3i}| \right] \\ &\le |\Omega_{2i}| \left[2P_{2i} \frac{|\dot{\overline{V}}_{xw} - \dot{V}_{xi}|}{|V_{xi}|} + P_{2i} \left| \frac{\overline{V}_{xw}}{V_{xi}} - 1 \right| |\dot{x}_{3id}| - \frac{\overline{V}_{xw}}{V_{xi}} K_{2i} + \left| 1 - \frac{\overline{V}_{xw}}{V_{xi}} \right| \lambda_{2i} |e_{3i}| \right] \end{aligned} . \tag{6.22}$$

In order to achieve $\dot{V}_{2i} \le -\eta_{2i} |\Omega_{2i}|$ for asymptotical stability, it is required that

$$K_{2i} \ge \left(2P_{2i} \frac{|\dot{\overline{V}}_{xw} - \dot{V}_{xi}|}{|V_{xi}|} + P_{2i} \left| \frac{\overline{V}_{xw}}{V_{xi}} - 1 \right| |\dot{x}_{3id}| + \eta_{2i} + \left| 1 - \frac{\overline{V}_{xw}}{V_{xi}} \right| \lambda_{2i} |e_{3i}| \right) \frac{V_{xi}}{\overline{V}_{xw}} , \tag{6.23}$$

for all the time. Let,

$$\beta_{wv} = \sqrt{V_{xwu}/V_{xwl}}\,, \tag{6.24}$$

and

$$\dot{\overline{V}}_{xw} = 0\,. \tag{6.25}$$

Then we have,

$$\beta_{wv}^{-1} \le \frac{V_{xi}}{\overline{V}_{xw}} \le \beta_{wv}\,, \tag{6.26}$$

and

$$\beta_{wv}^{-1} \le \frac{\overline{V}_{xw}}{V_{xi}} \le \beta_{wv}\,. \tag{6.27}$$

Here, $\left|\dot{V}_{xi}\right| \le g$ is physically upper bounded with g being the acceleration due to gravity. $\dot{x}_{3id}$ is the rate of the desired tire slip which is dictated by the control allocation algorithm incorporating rate limits as discussed in Chapter 5. Assume $\left|e_{3i}\right| \le e_{3im}$. So,

$$\left|\dot{x}_{3id}\right| \le r_m = \max\left[\left|r_{\min}\right|, \quad \left|r_{\max}\right|\right]. \tag{6.28}$$

Then from the right side of (6.23),

$$\begin{aligned}
&\left(2P_{2i}\frac{\left|\dot{\overline{V}}_{xw} - \dot{V}_{xi}\right|}{\left|V_{xi}\right|} + P_{2i}\left|\frac{\overline{V}_{xw}}{V_{xi}} - 1\right|\left|\dot{x}_{3id}\right| + \left|1 - \frac{\overline{V}_{xw}}{V_{xi}}\right|\lambda_{2i}\left|e_{3i}\right| + \eta_{2i}\right)\frac{V_{xi}}{\overline{V}_{xw}}\,. \\
&\le \left(2P_{2i}\frac{g}{V_{xwl}} + P_{2i}(\beta_{wv}+1)r_m + (\beta_{wv}+1)\lambda_{2i}e_{3im} + \eta_{2i}\right)\beta_{wv}
\end{aligned} \tag{6.29}$$

Thus, the control gain can be selected as $K_{2i} = \left(\frac{2P_{2i}g}{V_{xwl}} + P_{2i}(\beta_{wv}+1)r_m + (\beta_{wv}+1)\lambda_{2i}e_{3im} + \eta_{2i}\right)\beta_{wv}$, which gives us $\dot{V}_{2i} = \left|\Omega_{2i}\right|\frac{d\left|\Omega_{2i}\right|}{dt} \le -\eta_{2i}\left|\Omega_{2i}\right| \;\Rightarrow\; \frac{d\left|\Omega_{2i}\right|}{dt} \le -\eta_{2i}$, whenever $\Omega_{2i} \ne 0$. So the surface Ω_{2i} will be attractive, which means Ω_{2i} is asymptotically stable. In other words, $\Omega_{2i} = P_{2i}\dot{\rho}_{3i} + \lambda_{2i}\rho_{3i} \to 0$ as $t \to \infty$. From the Final-Value Theorem, we can have $\dot{\rho}_{3i},\ \rho_{3i} \to 0$ as $t \to \infty$, and thus $e_{3i} \to 0$ as $t \to \infty$. Subsequently, the tracking objectives are fulfilled.

Practical implementation of the control laws that involve $\text{sgn}(\Omega_{1i,2i})$ might be problematic because the controller would need infinitely-fast switching around $\Omega_{1i,2i}=0$, which may cause chattering. To avoid this, $\text{sgn}(\cdot)$ function can be replaced by an approximation such as a saturation function [Slotine and Li, 1991],

$$\text{sgn}(\Omega_{1i,2i}) \approx sat\left(\frac{\Omega_{1i,2i}}{\Phi_{1i,2i}}\right), \tag{6.30}$$

where $\Phi_{1i,2i}$ are the boundary layer thicknesses around the sliding surface $\Omega_{1i,2i}$. This continuous approximation can smooth out the control discontinuity. The saturation function is defined as,

$$sat\left(\frac{\Omega}{\Phi}\right)=\begin{cases}1 & \Omega \geq \Phi \\ \dfrac{\Omega}{\Phi} & -\Phi < \Omega < \Phi \\ -1 & \Omega \leq -\Phi\end{cases}. \tag{6.31}$$

The selection of the sizes of the boundary layers $\Phi_{1i,2i}$ is a tradeoff between reducing chattering effect and increasing residual steady-state error. With the integral action being introduced in the sliding surface, the residual tracking error will diminish. As $\dot{\overline{V}}_{xw}=0$, the modified control laws are,

$$\begin{aligned}T_{wzi} = {} & b_{wzi}\dot{x}_{1i} + f_{zi}\left[x_{3i}, f_{\alpha i}(x_{1i},\xi), F_{zi}, \mu_i\right] + J_{wzi}\ddot{x}_{1id} \\ & - J_{wzi}P_{1i}(\dot{x}_{1i}-\dot{x}_{1id}) - J_{wzi}K_{1i}sat\left(\frac{\Omega_{1i}}{\Phi_{1i}}\right)\end{aligned}, \tag{6.32}$$

$$T_{wyi}=\frac{1}{R_i}\left\{J_{wyi}\overline{V}_x\dot{x}_{3id} + f_{xi}[x_{3i}, f_{\alpha i}(x_{1i},\xi), F_{zi}, \mu_i]R_i^2 - J_{wyi}\overline{V}_{xw}\frac{\lambda_{2i}}{P_{2i}}e_{3i} - J_{wyi}\overline{V}_x\frac{K_{2i}}{P_{2i}}sat\left(\frac{\Omega_{2i}}{\Phi_{2i}}\right)\right\}, \tag{6.33}$$

where, the T_{wzi} and T_{wyi} are actuation torques (from current-controlled electric motors). The vehicle body motion-free control laws can improve system immunity to measurement noise as well.

It can be noted that V_{xi} is indeed calculable from measured vehicle longitudinal speed, lateral speed, and yaw rate along with vehicle dimension parameters, and could be

directly utilized in the control law. However, $\dot{V}_{xi}$ needs to be treated as an unknown exogenous signal in order to avoid the involvement of the vehicle body dynamics in this lever of control.

6.3 PERFORMANCE EVALUATION

In this section, the simulation evaluation of the control system described above is presented. A commercial vehicle dynamics simulation package, CarSim®, is used to provide a virtual test platform of a passenger car. The models in CarSim® are much more complete and complex than those used for control design. Thus, their use provides a realistic test platform for evaluating the robustness of the controller w.r.t. un-modeled dynamics and parametric uncertainties. Figure 6.1 shows the overall structure for the simulation studies of the coordinated VDC system. A combined tire slip and slip angle tracking controller described above is dedicated for each tire. The AFP control allocation developed in Chapter 4 and Chapter 5 are utilized in the simulations.

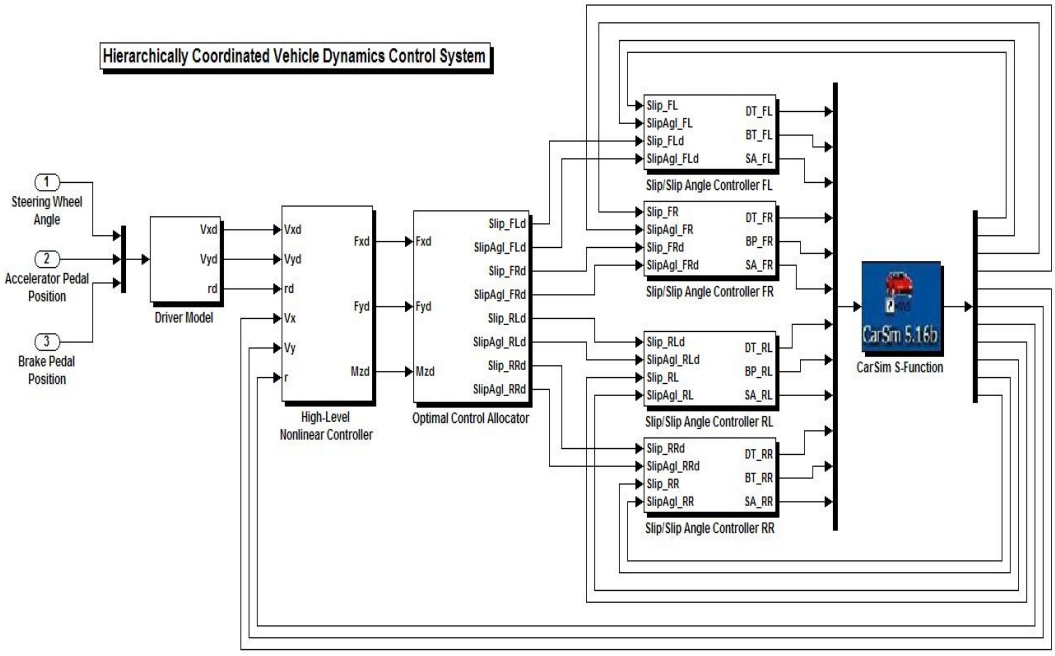

Figure 6.1 The overall simulation diagram for the coordinated VDC system

Two adverse driving scenarios are considered. One is a braking during high-speed double lane-changing on a slippery road surface and another is a hard braking through a split-μ surface maneuver. In these two situations, utilizing both tire longitudinal and lateral forces is desirable.

6.3.1 Braking during High-Speed Double Lane-Changing on a Slippery Road

A braking during high-speed emergency double lane-changing scenario is considered. High-speed double lane-changing is a common test to evaluate vehicle handling performance. The test is usually done at constant vehicle longitudinal speed. Here we introduce braking to this test maneuver to make tires experience both slip and slip angle. To increase the challenge for control systems, the road friction coefficient is set as 0.4, which is analogous to a slippery hard snow surface. Vehicle initial speed is 110 km/h. The double lane-changing steering command starts at 1 second with a deceleration demand for about -0.2 g. Figure 6.2 illustrates the situation.

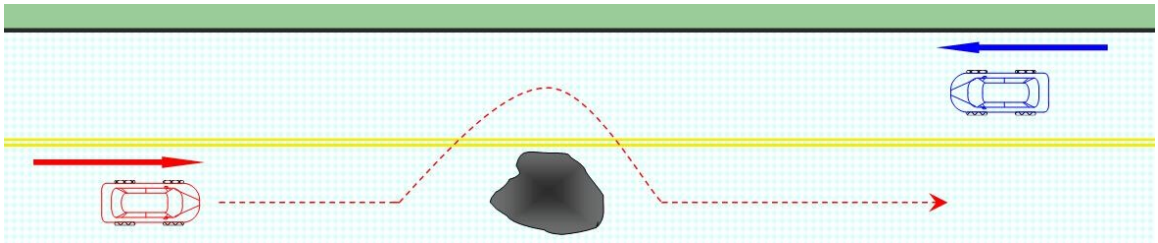

Figure 6.2 Braking during a high-speed DLC on a slippery surface.

The vehicle planar motion responses (longitudinal speed, lateral speed, and yaw rate) are compared with the corresponding desired values in Figure 6.3. As one can see, despite the un-modeled dynamics, the system shows very good tracking performance during this very adverse maneuver. As will be shown in Chapter 7, the CVDC system

control performance is much better compared with those of the existing vehicle control systems such as 2-wheel steering (2WS) and 4-wheel steering (4WS).

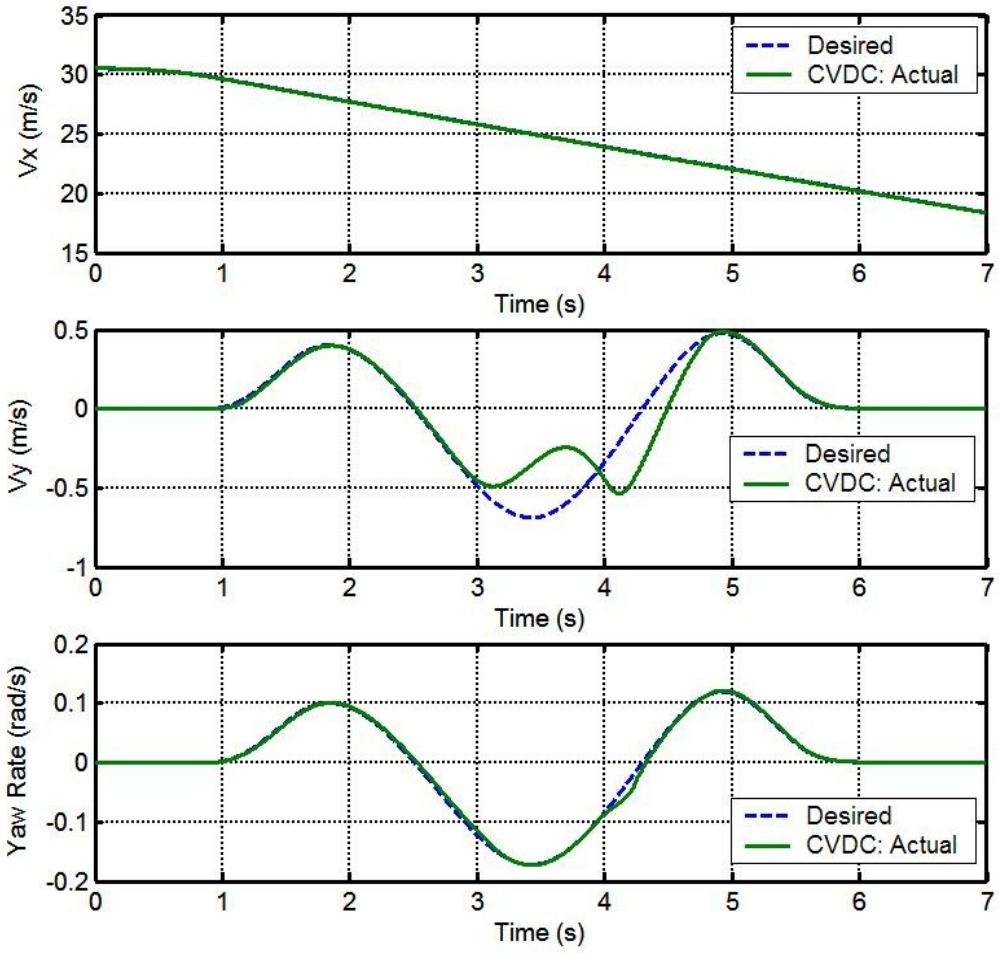

Figure 6.3 Vehicle planar motion responses during the double lane-changing with braking on a slippery surface.

Tire desired tire slips from control allocation and the actual slips for the four wheels during the maneuver are compared in Figure 6.4. As we can see from it, the lower-level controllers can make the slips of all the wheels track their desired values well.

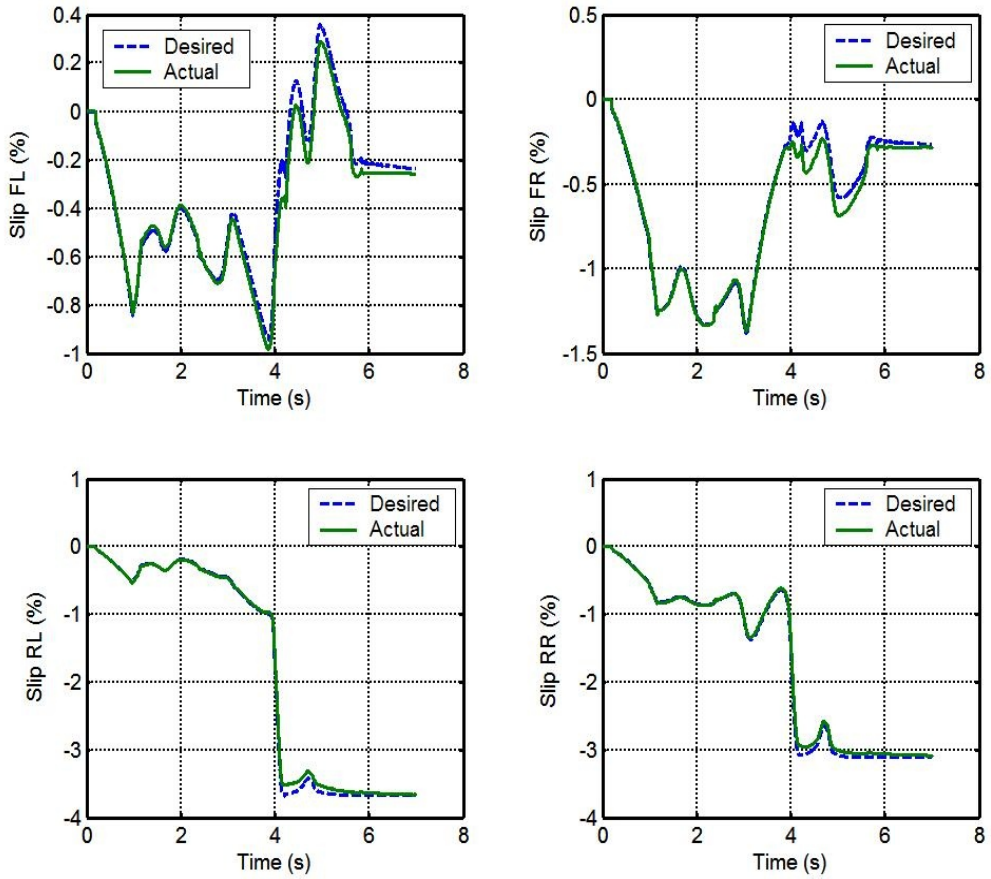

Figure 6.4 Comparisons of the tire desired slips and actual ones during the double lane-changing with braking on a slippery surface.

Similarly, desired tire slip angles from control allocation and the actual slip angles for the four wheels during the maneuver are compared in Figure 6.5. The lower-level controllers can make the slip angles of all the wheels track their desired values well. It is interesting to note that in this maneuver, the slip angles of all the four tires were saturated at about 3.5 deg due to low friction coefficient of the road. The tire longitudinal forces then provide assistance for the yaw motion control as shown in the following figure.

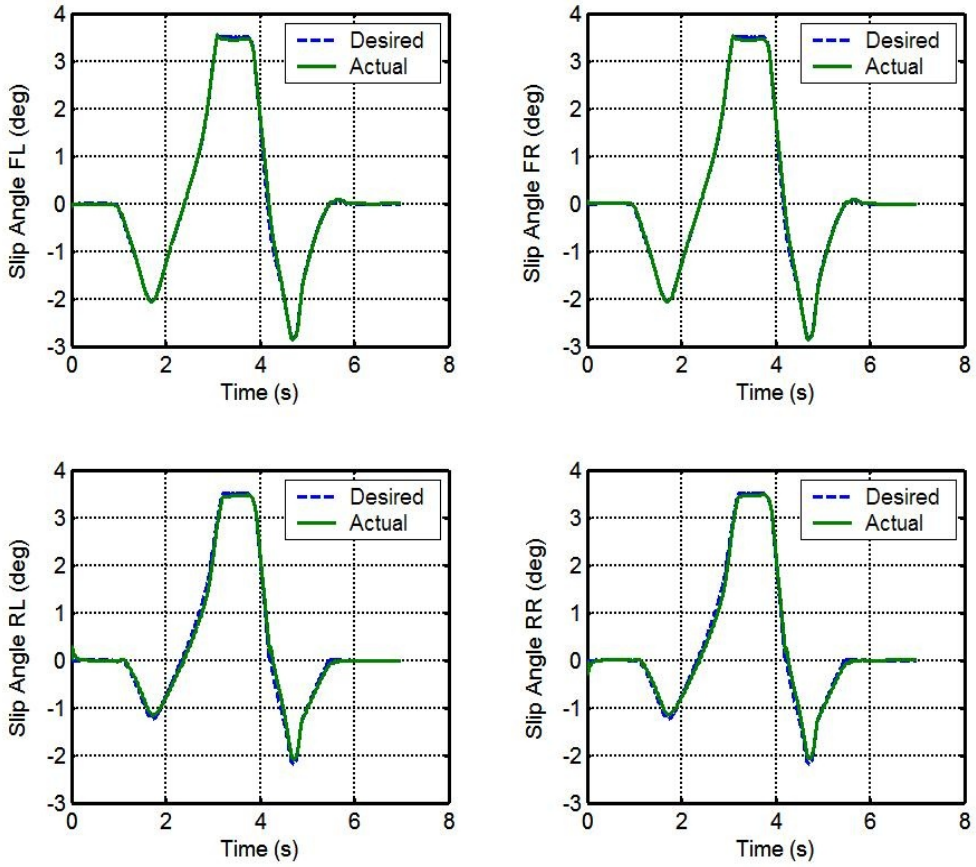

Figure 6.5 Comparisons of the tire desired slip angles and actual ones during the double lane-changing with braking on a slippery surface.

The applied braking torque, driving torque, and steering torque during the maneuver for each wheel are shown in Figure 6.6. Note that during this adverse driving condition, the front-left wheel experiences driving torque (as shown in the dashed green line) while other three wheels perform braking. This increases system control capability on the vehicle yaw motion when the tire lateral forces are saturated. This kind of feature can be realized on hybrid/fuel cell vehicles where individual wheel driving/braking is possible.

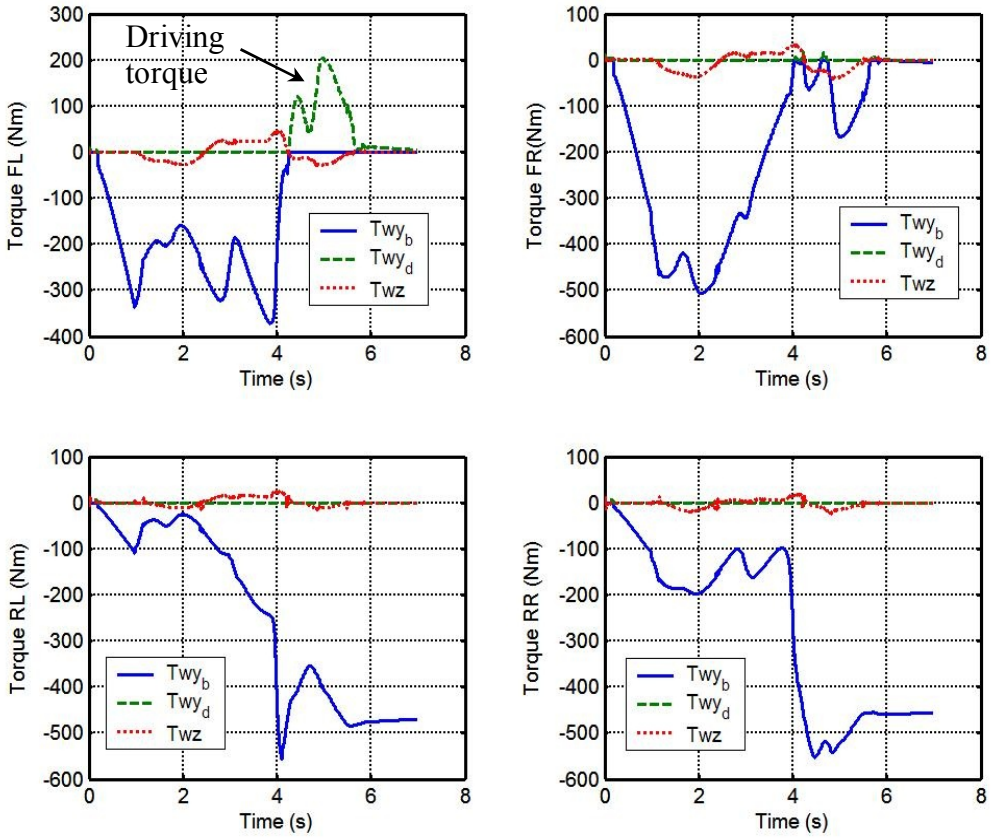

Figure 6.6 Braking, driving, and steering torques for each wheel during the double lane-changing with braking on a slippery surface.

Figure 6.7 shows the comparisons of the slips of right-left tire for the cases with and without integral action in the sliding surface Ω_{2i}. The blue dashed line is the desired tire slip, solid green line is the actual tire slip for the controller with integral action, and dotted red line is the actual tire slip for the controller without integral action ($\lambda_{2i} = 0$). It is clear that the integral action helps to reduce the steady-state tracking error and ensure asymptotic stability (the solid green line converges to the desired value at steady-state while the dotted red line does not).

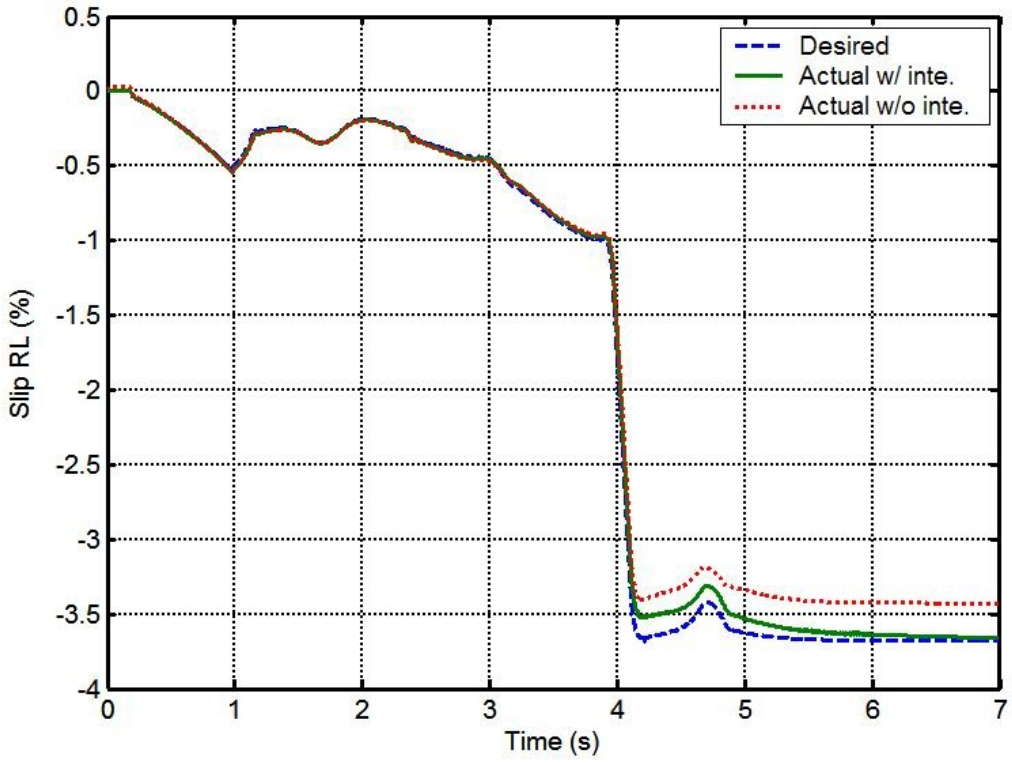

Figure 6.7 Illustration of the effectiveness of the integral action.

6.3.2 Hard Braking through a Split-μ Surface

A hard braking maneuver through a split-μ surface is considered, similar to the case study in Chapter 5. This is analogous to braking through an icy spot on the right side, while the left is on a dry concrete surface. The road surface friction coefficient is 0.9 at the beginning, suddenly drops on the right side of the vehicle to 0.3 between 50 m to 100 m, and then back to 0.9. The friction coefficient on the left side is constant at 0.9 at all times. The test vehicle initial speed is at 140 km/h, and a hard braking command (about -0.5 g) is issued at 0 second and the vehicle passes through the split-μ surface.

Figure 6.8 shows the vehicle planar motions compared against their corresponding desired values. For the vehicle longitudinal motion, the system can track

the desired one very well. During the friction changing boundaries, vehicle lateral and yaw motions exhibit some small derivation from the desired values due to the abrupt external disturbance. However, as will be shown in Chapter 7, the CVDC system control performance is significantly improved compared with those of the existing vehicle control systems such as ABS and DYC.

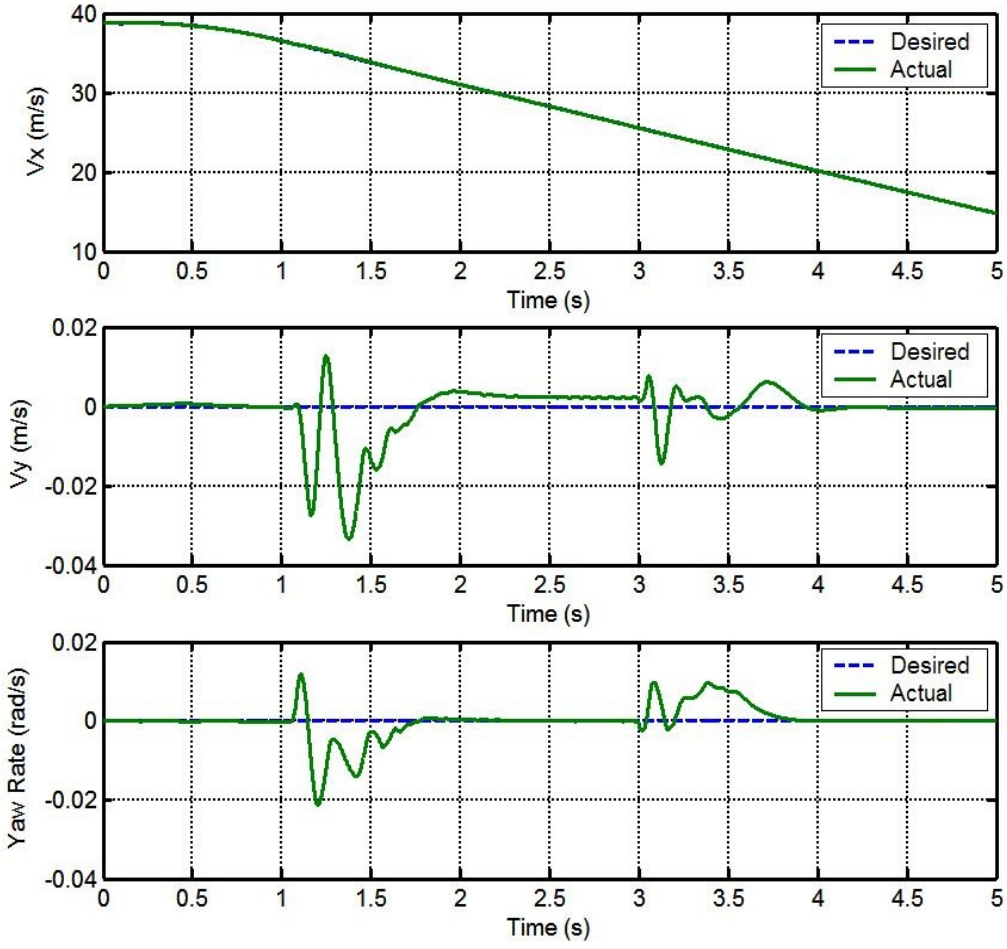

Figure 6.8 The vehicle motions of the three different vehicles during the hard braking through a split-μ surface.

Figure 6.9 and Figure 6.10 show the desired and actual slip angle and slip for the front left and front right tire which travels through the low friction surface, respectively. In the upper rows of the two figures, the tire-road friction coefficient is also plotted against time. The front-left tire travels on the constant friction and the front-right tire experiences the friction variation. The applied braking torques and steering torques are also shown in the corresponding figures.

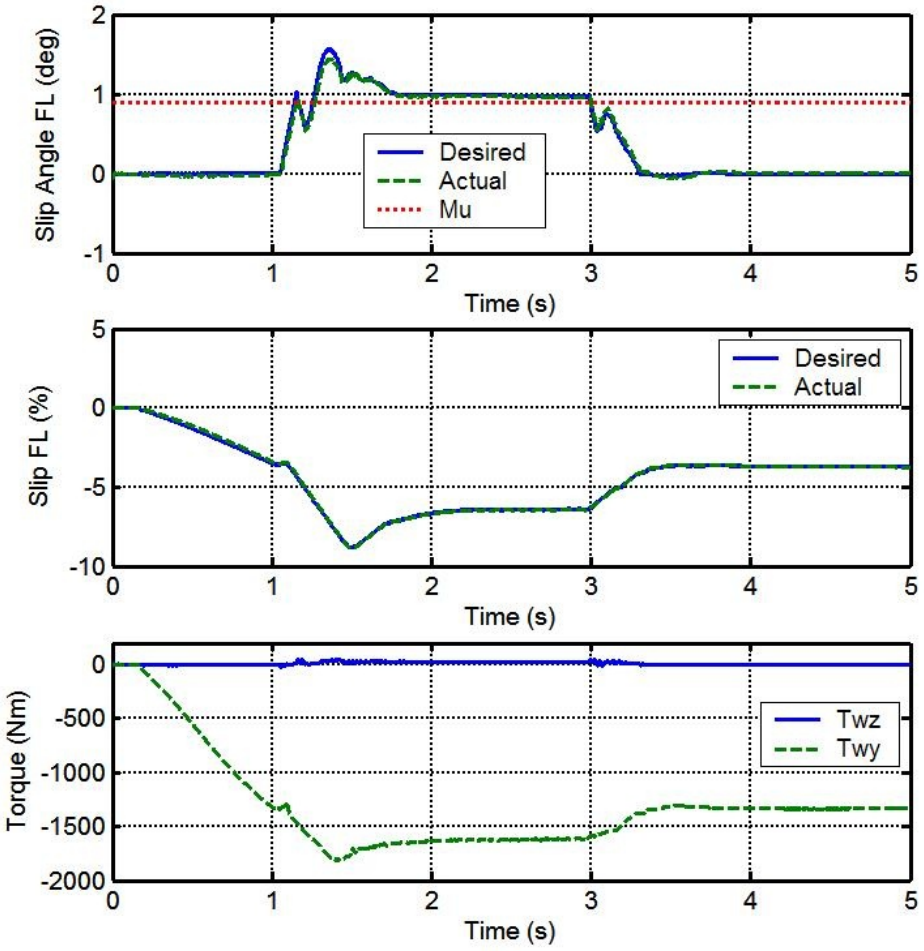

Figure 6.9 The actuation of the front-left tire for the coordinated VDC during the hard braking through a split-μ surface.

The tracking controller can make the actual slip and slip angle track the desired ones well. Notice that the slip and slip angle experience relatively big errors at the boundaries of the split-μ surface, which is due to the abrupt change of the friction coefficient. Since the overall system is in a closed-loop fashion, the effects of these short duration errors on the system performance will not be noticeable.

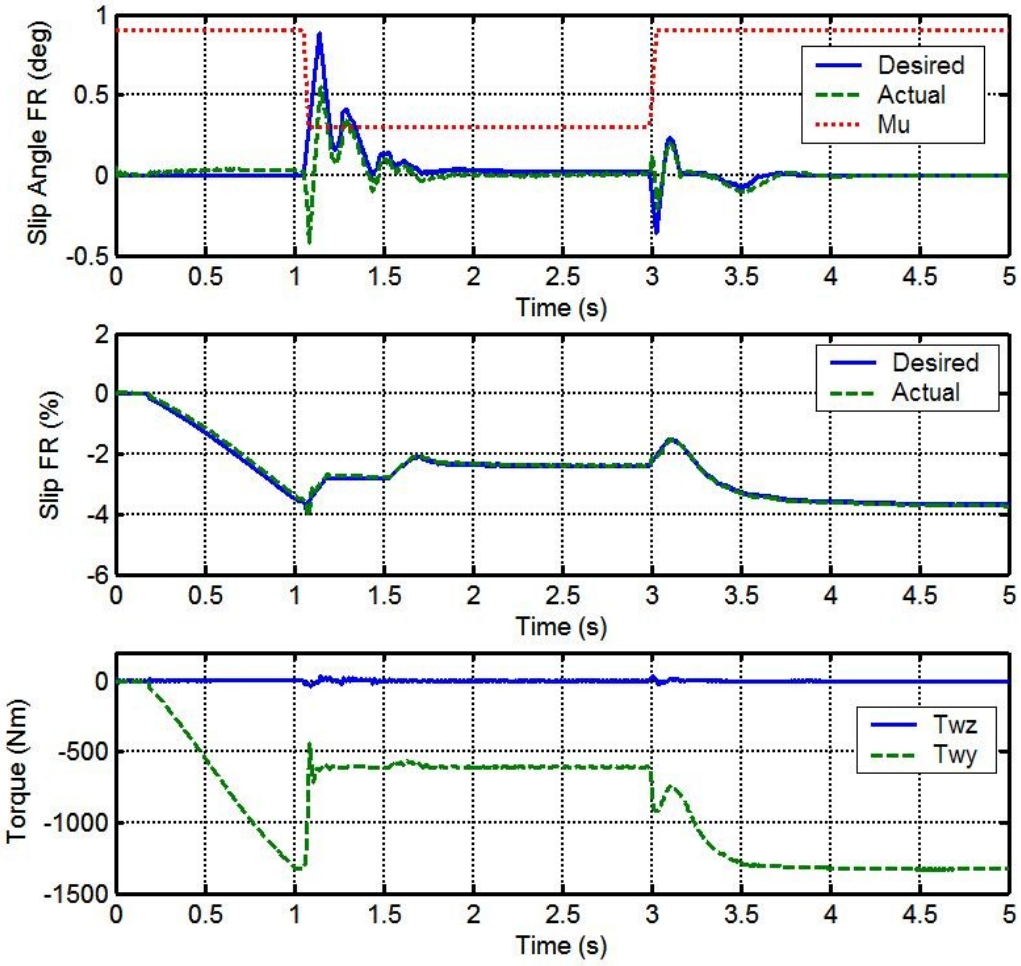

Figure 6.10 The actuation of the front-right tire for the coordinated VDC during the hard braking through a split-μ surface.

6.4 SUMMARY

As tire slips and slip angles are treated as the actuation in this coordinated vehicle dynamics control system, effective tire slip and slip angle tracking control is very critical. A combined tire slip and slip angle tracking control system has been described in this chapter. The system is indispensable for advanced coordinated vehicle dynamics control where both tire longitudinal and lateral forces need to be simultaneously utilized to achieve desired vehicle motions. A MIMO robust sliding mode control approach is employed for the system while vehicle body states are treated as exogenous signals to isolate and simplify the control design tasks as well as enable coordinated control. Integral action is introduced in the sliding surface to reduce residual tracking error caused by continuous approximation of the switching function. The controller manipulates the wheel steering/driving/braking torques to make tire slips and slip angles track the values dictated by the control allocation algorithm. Simulation results based on a complete and complex commercial vehicle simulation package have been used to demonstrate the performance of the control system under adverse driving conditions.

The system developed in this chapter is useful not only for the CVDC presented in this dissertation but also for other advanced control systems in autonomous and non-autonomous vehicles.

Chapter 7: Overall System Analysis and Evaluation

In the previous chapters, we have described the critical elements of the entire CVDC system. In this chapter we present some minor aspects of the system such as overall stability analysis, reference models, and modification of the higher-level yaw motion controller. The main emphasis is put on the evaluation of the system performance by comparing with existing vehicle dynamics control systems under various adverse driving conditions.

7.1 OVERALL SYSTEM STABILITY ANALYSIS

It is worth to point out that the desired virtual control specified by the higher-level control laws may not be exactly met due to control allocation error tolerance and lower-level controller tracking errors. The actual generalized control can be written as,

$$v_{ai} = v_i + \delta v_i, \qquad \text{for } i = 1, 2, 3, \tag{7.1}$$

where δv_i are bounded errors between the desired generalized controls and the corresponding actual ones. However, as will be shown below, it turns out that these effects act on the overall system as disturbances and can be tolerated by the robustness of the higher-level controller provided that there are sufficient actuation potentials. For instance, consider the longitudinal motion control law. For the derivative of the SMC Lyapunov function $\dot{V}_1$ (3.91), if we substitute (7.1) in to it, we can get,

$$\dot{V}_1 = S_1\left[\left(1-\frac{\overline{M}}{M}\right)x_2x_3 + w_1 - \frac{\overline{M}}{M}\overline{w}_1 + \frac{\delta v_1}{M} + \left(\frac{\overline{M}}{M}-1\right)\dot{x}_{1d} - \frac{\overline{M}}{M}K_1\,\mathrm{sgn}(S_1)\right]. \tag{7.2}$$

We notice that (7.2) is the same as the original derivative (3.93) except one additional term $\frac{\delta v_1}{M}$, which is associated with the error of the generalized control. Its effect on the system is the same as the disturbance w_1. If there are sufficient actuation potentials (i.e. actuation is not saturated), a sufficiently large K_1 can overwhelm the effect

of δv_1 and ensure the asymptotical stability of the sliding surface. The stability of the other two surfaces can be shown in the similar manner.

7.2 REFERENCE MODELS

The reference models in the structure of the CVDC presented in Chapter 3 provide the desired vehicle longitudinal speed, lateral speed, and yaw rate by interpreting driver intentions based on the accelerator/braking pedal positions and hand steering wheel input. For the desired yaw rate reference model, we use a model suggested in [Horiuchi et al., 1999] as below,

$$\frac{\Omega_d(s)}{\Theta_{sw}(s)} = \frac{\hat{V}_x}{(\tau_r s + 1)(\tau_d s + 1)}, \tag{7.3}$$

where $\hat{V}_x = \frac{k_r V_x}{(1 + k_a V_x^2) l} GR$, k_r is the gain of the reference model, k_a is the stability factor, l is the vehicle wheelbase, and GR is the gear ratio of the front steering mechanism linkage. τ_r and τ_d are time constants.

The reference model for the desired longitudinal speed can be simply described as,

$$V_{xd} = V_{x0} + \int_{t_0}^{t} a_{xdf}\, dt, \tag{7.4}$$

where V_{x0} is the initial vehicle longitudinal speed at time t_0, a_{xdf} is the desired longitudinal acceleration (or deceleration) after a low-pass filter, which can be obtained by,

$$a_{xd} = \begin{cases} f_a(u_a), \text{ for acceleration} \\ f_d(u_b), \text{ for deceleration} \end{cases} \quad \text{and } a_{xdf} = \frac{a_{xd}}{\tau_a s + 1}, \tag{7.5}$$

where u_a and u_b are the driver's accelerator pedal and brake pedal inputs. Monotonic functions f_a and f_b are used to convert the pedal inputs to desired acceleration or deceleration. In this project, we simply used two linear functions. τ_a is the time constant

for the filter. Of course, there are some physical limits on the maximum acceleration and deceleration considered in the corresponding functions.

The desired vehicle lateral speed can be obtained based on a steady-state bicycle model as [Wong, 2001],

$$V_{yd} = \Omega_d \left(l_r - \frac{M l_f V_x^2}{C_{r0} l} \right), \text{ and } V_{ydf} = \frac{V_{yd}}{\tau_y s + 1}, \tag{7.6}$$

where l_f and l_r are distances from the vehicle center of gravity to the front and rear axles, C_{r0} is the constant cornering stiffness, and τ_y is the time constant for the low-pass filter.

Here, the reference models we used are the common ones, other different reference models can be adapted into the system as well.

7.3 MODIFICATION OF THE HIGHER-LEVEL YAW MOTION CONTROLLER

As mentioned in Chapter 3, yaw rate is the only control objective for vehicle yaw motion in the originally proposed higher-level controller. Since there is no damping factor in the yaw rate controller as shown in Chapter 3, chattering effect can easily be triggered. The induced actual yaw rate error could lead to offset on the vehicle yaw angle (integration of the yaw rate) and cause vehicle heading deviation. For example, Figure 7.1 below shows the test results of a double lane-changing maneuver at 120 km/h using the original higher-level yaw motion controller described in Chapter 3. As one can clearly see, the accumulated yaw rate error causes offset of yaw angle and deviation of the vehicle heading during the maneuver, which are highly undesirable.

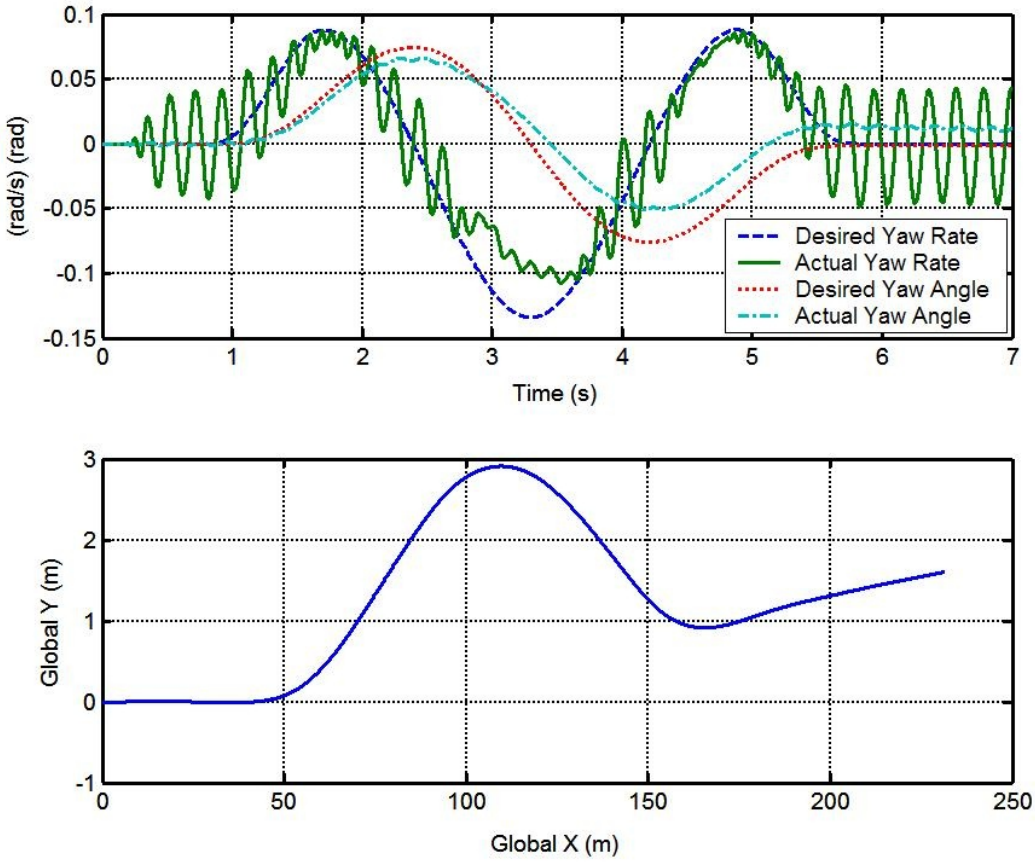

Figure 7.1 Performance of the yaw motion controller without yaw angle control

To mitigate this effect and ensure desired vehicle heading, we added the yaw angle control effort in conjunction with the yaw rate control. This is done by augmenting the system with a new state, yaw angle as

$$\begin{aligned} \dot{x}_3 &= \frac{1}{I_z} v_3 + w_3 \\ \dot{x}_4 &= x_3 \end{aligned}, \tag{7.7}$$

where, $x_3 = \Omega_z$ is the vehicle yaw rate as before, $x_4 = \Phi_z$ is the vehicle yaw angle, $v_3 = M_{zd}$ is the generalized yaw moment, and w_3 is the disturbance. It then becomes a double-integrator-like system. Sliding mode control can be applied for this system by defining a new sliding surface as,

$$S_3 = (x_3 - x_{3d}) + \lambda_3 (x_4 - x_{4d}), \tag{7.8}$$

where x_{3d} is the desired yaw rate from the reference model as usual and x_{4d} is the desired yaw angle which is obtained by integrating x_{3d} over time. Resetting of x_{4d} could be conducted at normal driving conditions such as straight cruising etc. $\lambda_3 > 0$ is the parameter used to determine the dynamics of the sliding surface. The derivative of the surface is,

$$\dot{S}_3 = \dot{x}_3 - \dot{x}_{3d} + \lambda_3 \dot{x}_4 - \lambda_3 \dot{x}_{4d} = \frac{1}{I_z} v_3 + w_3 - \dot{x}_{3d} + \lambda_3 x_3 - \lambda_3 x_{3d}. \tag{7.9}$$

The control law can be derived in a similar way with continuous approximation as presented in Chapter 3 as,

$$v_3 = M_{zd} = \bar{I}_z \left[-\overline{w}_3 + \dot{x}_{3d} - \lambda_3 x_3 + \lambda_3 x_{3d} - K_3 sat(S_3 / \Phi_3) \right], \tag{7.10}$$

which can guarantee the attractiveness of the surface. This modified control law was implemented and tested at the same high-speed double lane-changing maneuver to verify its effectiveness. Figure 7.2 below shows the results. Compared with the previous results, both yaw rate and yaw angle control performances are significantly improved. The introduction of the integral element in the sliding surface greatly reduces the chattering effect. As the yaw angle is included in the closed-loop, its behavior is well controlled, which in turn gives us desired vehicle heading and trajectory as shown in the second row in Figure 7.2.

It should be noted that this modified higher-level controller has been used for the tests results presented in Chapter 5 and Chapter 6. Those results also demonstrated the good performance of the controller, and here we specifically show the performance difference.

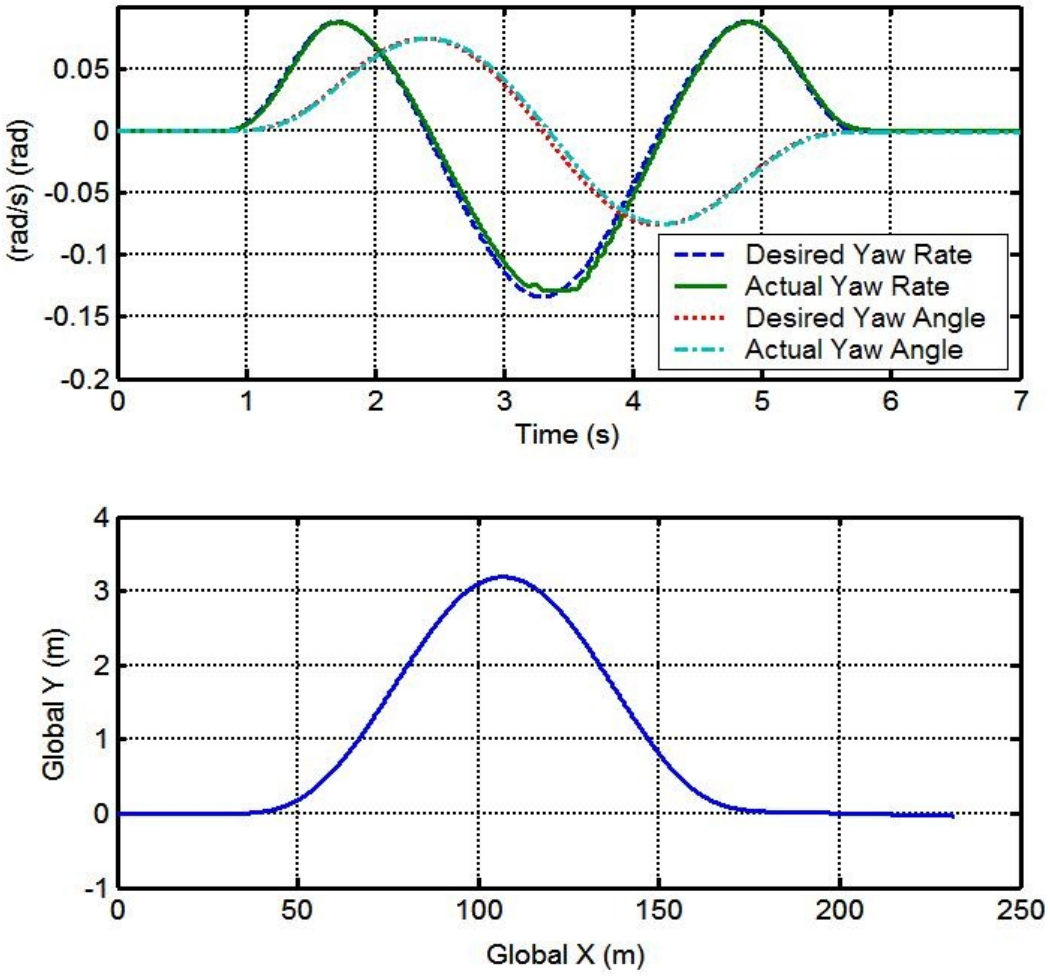

Figure 7.2 The performance of the yaw motion controller with yaw angle control.

7.4 OVERALL SYSTEM PERFORMANCE EVALUATION

In this section, we evaluate the performance of the CVDC by comparing with the existing vehicle control systems under various adverse driving conditions. From the vehicle dynamics control system point of view, the difference between the desired reference signals and the actual system state outputs are of great interest. It is referred to as closed-loop performance here and denoted e_s as shown in Figure 7.3. We will use this e_s to quantify the performance differences among different vehicle control systems.

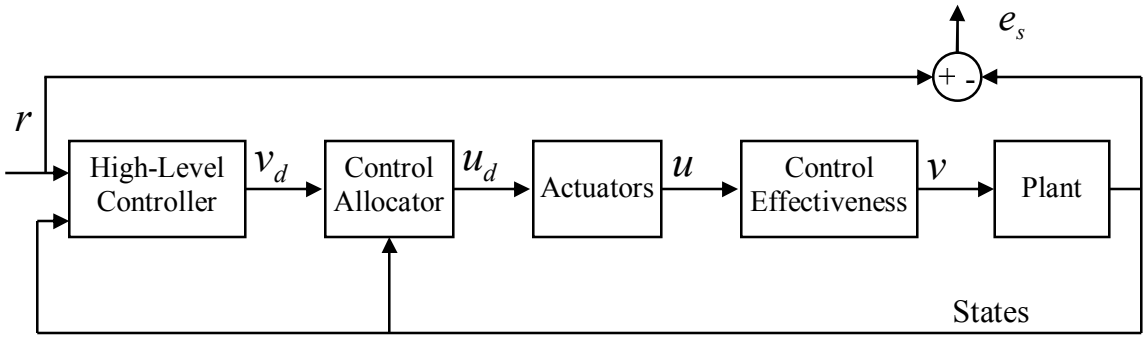

Figure 7.3 Closed-loop system performance measure with control allocation

In this evaluation study, the CarSim® vehicle dynamics simulation package is used to provide a full-vehicle test platform model. CarSim® is a commercial vehicle multi-body dynamics simulation software package which models the dynamics of the vehicle using the most significant components. It is claimed that validation testing has shown that CarSim® produces the same kinds of outputs that are measured in physical tests involving instrumented vehicles with respect to control inputs and environment (road and wind) [CarSim User Manual, 2003]. The CarSim® model is much more complex and complete than the simplified model used for control design, and therefore provides a realistic test platform to evaluate the robustness of the controller with respect to un-modeled dynamics and parameter variations.

When comparing the performances of different vehicle control systems, identical driver inputs are used to keep the driver effects outside the loop for objective comparison among different systems.

7.4.1 Hard Braking through a Split-μ Surface

In this sub-section, a hard braking maneuver through a split-μ surface is considered, similar to the case study in Chapter 5. This is analogous to braking through an icy spot on the right side, while the left is on a dry concrete surface. The road

surface friction coefficient is 0.9 at the beginning, drops on the right side of the vehicle to 0.3 between 50 m to 100 m, and then back to 0.9. The friction coefficient on the left side is constant at 0.9 at all times. The test vehicle initial speed is set as 140 km/h, and a hard braking command (about -0.5 g) is issued at 0 second and the vehicle passes through the split-μ surface.

Three different vehicle control systems are compared in this test: ABS, direct yaw-moment control (DYC), and CVDC. To provide a good comparison among these systems, the driver is not involved in the loop, the hand steering wheel is kept at the rest position, and identical deceleration demand is used for all three cases. A typical ABS control strategy, which releases the braking pressure of a wheel when its slip is higher than a preset threshold value, is used for the ABS car. In the DYC car, a proportional-integral (PI) controller is used (in addition to ABS controller) to offset the applied braking pressures of the wheels at the left and right sides in order to control the vehicle yaw rate. The coordinated VDC system refers to the one described in this dissertation.

The "ABS" car tries to meet the deceleration demand even at the split-μ surface but without steering compensation. Due to the road friction difference, more braking force will be generated on the left side than the right side, which creates a yaw moment that can cause unstable vehicle motion. For the "DYC" car, the left side braking force is intentionally reduced to match that of the right side in order to reduce undesired yaw moment. However, this may sacrifice the longitudinal deceleration demand. In the "CVDC", the tire longitudinal and lateral forces are coordinated in a unified fashion to meet the desired longitudinal velocity, lateral velocity, and yaw rate simultaneously. At the split-μ surface, slip values on the right side tires are reduced and the slip values on the left side tires are increased to meet the deceleration demand. The four wheels are automatically steered to help maintaining the desired yaw motion in the presence of the

yaw moment generated by the differential braking. Figure 7.4 shows the global trajectories and planar motions for these three systems in this test. As indicated, the "ABS" vehicle loses stability and goes off the track while the "DYC" performs better in terms of reduced deviation from the track. The "CVDC" system yields the smallest deviation from the track and the best yaw motion.

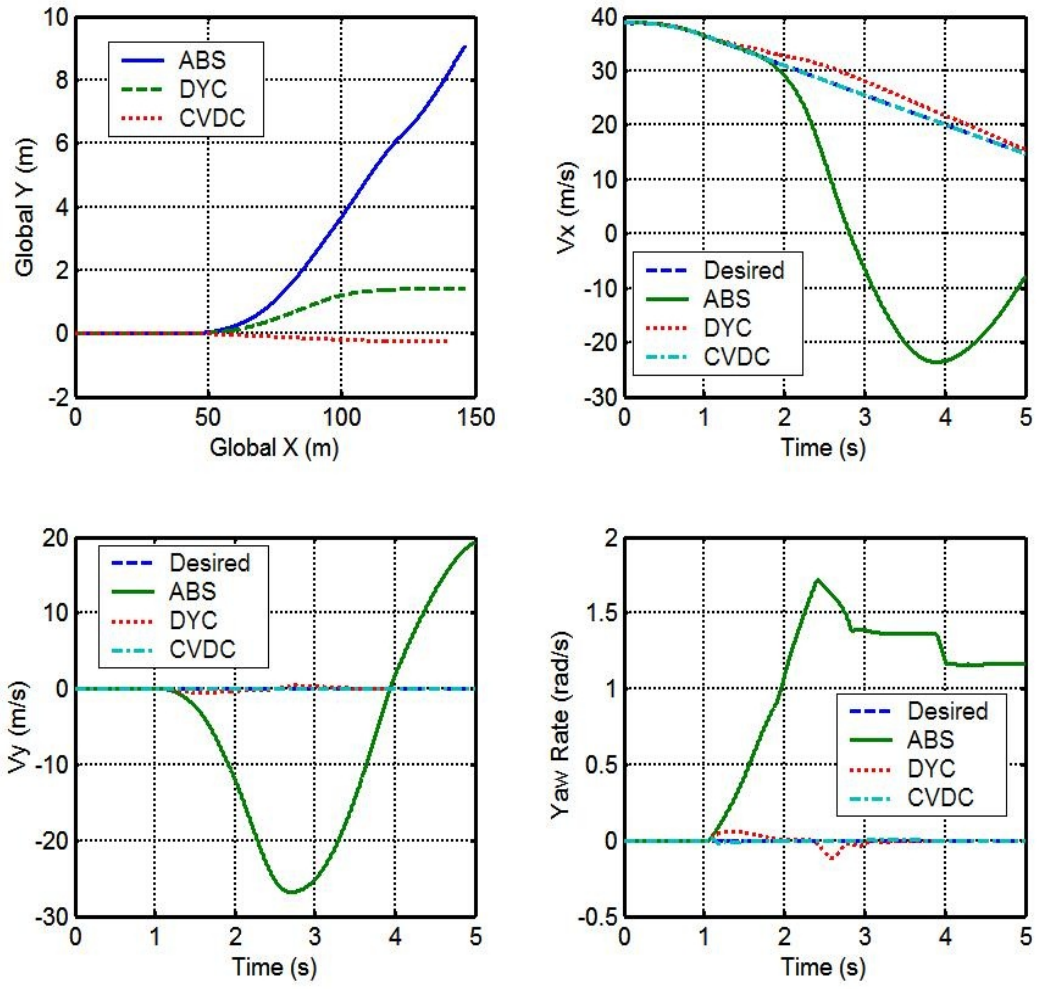

Figure 7.4 The global trajectories and planar motions of the three different vehicles during hard braking through a split-μ surface maneuver.

On the other hand, from the deceleration point of view, the "DYC" system cannot satisfy the deceleration demand of the driver on the split-μ surface, which can be seen

from both figures in the upper row of Figure 7.4 as the traveled distance is longer and longitudinal speeds are higher than for "CVDC". Performance is significantly improved by the "CVDC" system, which optimally utilizes all the tire forces.

Quantitatively, the performances of the three different vehicle control system can be compared in terms of root-mean-square-error (RMSE) and peak error (PE) as summarized in Table 7.1.

Table 7.1 Comparison of the system performances at hard braking through a split-μ surface

Measures / Systems	V_x (m/s)		V_y (m/s)		Ω_z (rad/s)	
	RMSE	PE	RMSE	PE	RMSE	PE
ABS	18.3524	44.6009	10.3595	26.8236	0.8922	1.7151
DYC	1.3421	2.7588	0.1355	0.4813	0.0149	0.1172
CVDC	0.0219	0.2710	0.0042	0.0294	0.0019	0.0211

It is clear that the CVDC significantly improved the system performance compared with ABS and DYC at this case.

It should be noted that in this maneuver, the tire-road friction coefficient is assumed known. In practice, uncertainties can arise in the friction estimation that can affect the performance of CVDC. Incorporating a means for dealing with this uncertainty is a topic of future work.

7.4.2 High-Speed Double Lane-Changing

Another example to evaluate the system is a high-speed double lane-changing maneuver. This is a common vehicle testing used to emulate an emergency double lane-changing to avoid an unexpected obstacle as illustrated in Figure 7.5.

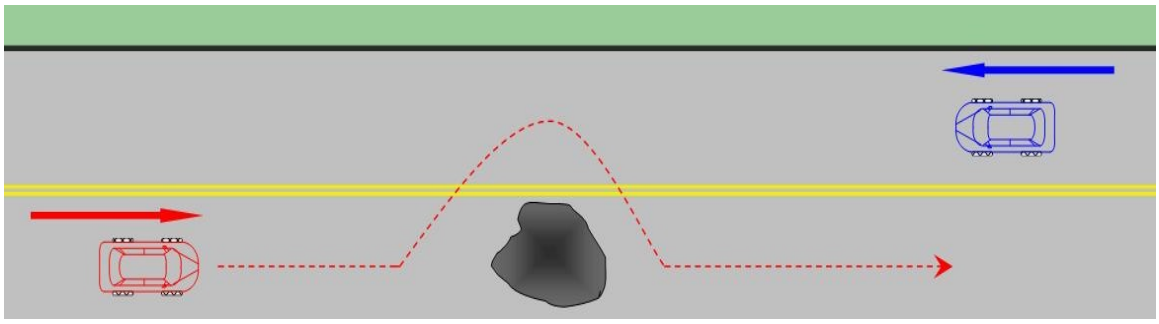

Figure 7.5 High-speed double lane-changing scenario.

In this scenario, the vehicles are initially traveling straight at 120 km/h constant speed and suddenly conduct an emergency double lane-changing maneuver within less than 5 seconds. The road surface is dry concrete with tire-road friction coefficient as 0.9.

Three vehicles with different control systems are compared. The "2WS" is a regular vehicle with conventional mechanical front wheel steering. The "4WS" is a vehicle equipped with four-wheel steering control system, which means its rear wheels can steer as well. The "CVDC" is a vehicle with coordinated vehicle dynamics control developed in this dissertation. The longitudinal motions of the "2WS" and "4WS" are controlled by the CarSim® built-in cruise controller for maintaining constant vehicle speed. Identical hand-steering wheel signal is used for all the three vehicles. Figure 7.6 shows the global trajectories and planar motions of the three vehicles during the maneuver.

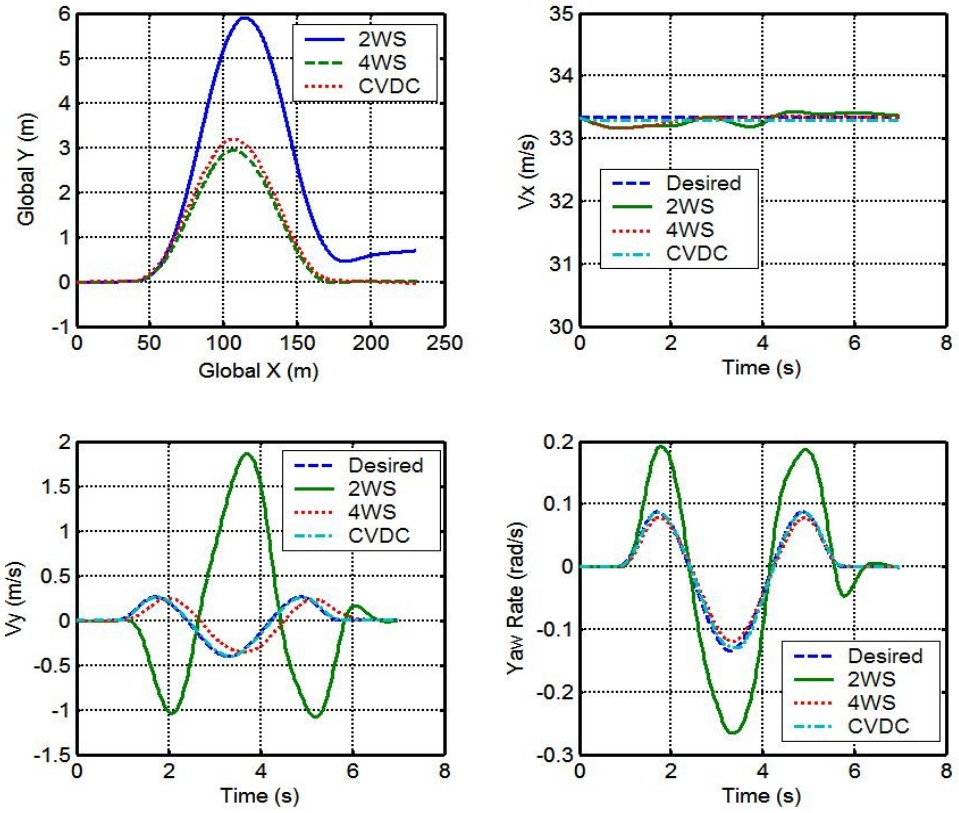

Figure 7.6 Global trajectories and planar motions of the three different vehicles during the high-speed double lane-changing maneuver.

It is clear that for this adverse driving condition, the "2WS" vehicle cannot fulfill the tasks as its trajectory, lateral and yaw motions significantly deviated from the desired ones compared with the "4WS" and "CVDC". Also the heading of the "2WS" departed from the desired track after the maneuver. This poor performance is mainly due to the lack of maneuverability for the front-wheel steering vehicle. In contrast, the lateral and yaw responses of the "4WS" and "CVDC" are similar and much improved due to the enhanced steerability of the four-wheel steering system. However, regarding the vehicle longitudinal motions, the CVDC vehicle can maintain its speed better than the other two thanks to the coordinated tire longitudinal and lateral control.

The quantified error comparisons are listed in the Table below.

Table 7.2 Comparisons of the performances for the high-speed double lane-changing maneuver

Measures / Systems	V_x (m/s)		V_y (m/s)		Ω_z (rad/s)	
	RMSE	PE	RMSE	PE	RMSE	PE
2WS	0.0848	0.1654	0.6765	2.1736	0.0524	0.1346
4WS	0.0460	0.1654	0.0729	0.1806	0.0056	0.0171
CVDC	0.0348	0.0449	0.0096	0.0208	0.0028	0.0110

Both 4WS and CVDC out-performed the 2WS vehicle on lateral and yaw motions. The CVDC still shows the best performance of the three systems on every aspect. As this test is mainly for lateral handling, the 4WS exhibits similar performance as that of CVDC. In the next test, we conduct a more adverse maneuver: braking during a high-speed DLC on a very slippery surface where the tire lateral forces are saturated, to further show the superior performance of the CVDC.

7.4.3 Braking during High-Speed Double Lane-Changing on a Slippery Road

This maneuver is same as the one presented in Chapter 6. A braking during high-speed emergency double lane-changing (BDLC) scenario is considered. Here we introduce braking to this test maneuver to make tires experience both slip and slip angle. To increase the challenge for control systems, the road friction coefficient is set as 0.4, which is analogous to a slippery hard snow surface. Vehicle initial speed is 110 km/h. The double lane-changing steering command starts at 1 second with a deceleration demand for about -0.2 g. As in the last case study, three different vehicle control systems are considered, namely 2WS, 4WS, and CVDC. Identical driver's inputs are used for all

the three test vehicles. The global trajectories and planar motions of the three vehicles are compared in Figure 7.7.

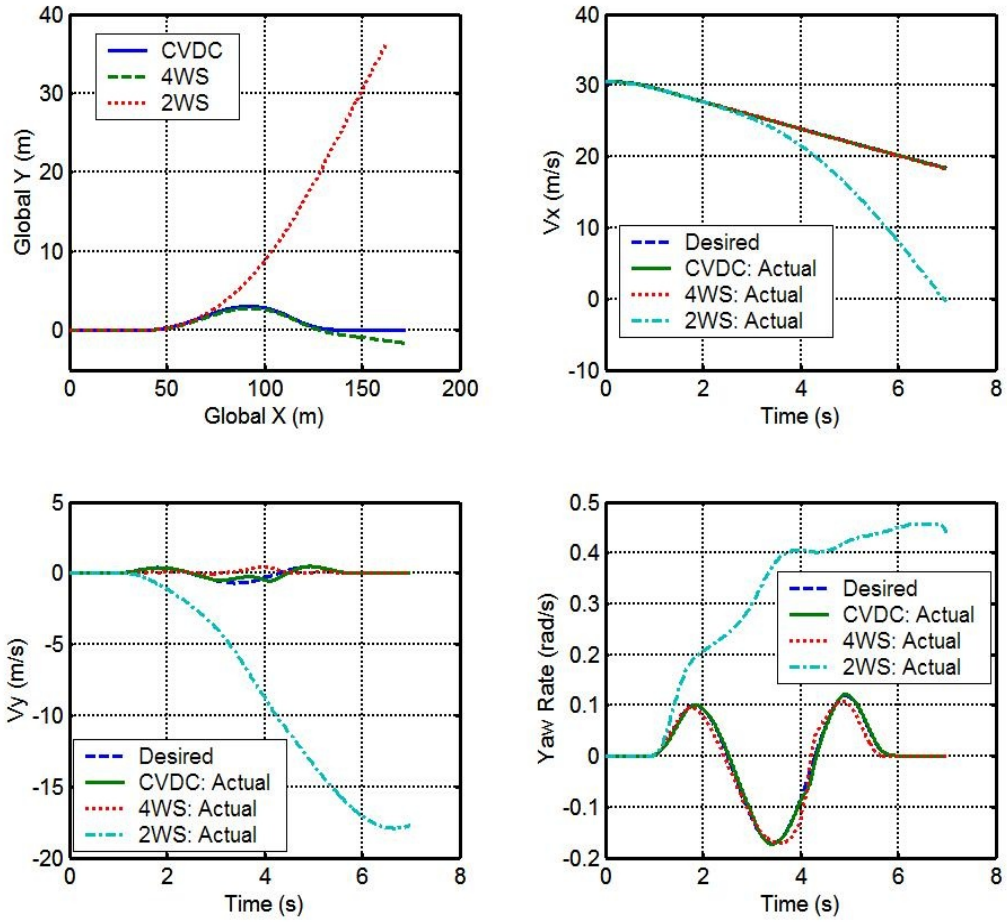

Figure 7.7 The global trajectories and planar motions of the three vehicles at BDLC maneuver on a slippery surface.

For this maneuver, since the tire-road friction coefficient is very low and the vehicle tire's lateral forces are saturated as shown in Figure 6.5, it is a very challenging test. It is obvious that the 2WS cannot pass this test and loses stability. The 4WS system can finish the test but there is considerable vehicle heading offset and the vehicle trajectory deviates from the desired track. Of the three systems, CVDC shows the best

performance in terms of trajectory tracking and planar motion. The quantitative comparisons are presented in the Table below.

Table 7.3 Comparisons of the three systems for a BDLC on a slippery surface.

Measures / Systems	V_x (m/s)		V_y (m/s)		Ω_z (rad/s)	
	RMSE	PE	RMSE	PE	RMSE	PE
2WS	4.3331	18.8471	7.5676	17.9142	0.2903	0.5568
4WS	0.0599	0.2037	0.2387	0.9417	0.0095	0.0401
CVDC	0.0263	0.2066	0.0633	0.3896	0.0023	0.0229

It is clear that CVDC shows the best lateral and yaw motion control performances for this very adverse driving condition. The main reason is that the CVDC coordinately utilizes the available tire longitudinal forces to help controlling vehicle lateral and yaw motion when tire lateral forces are saturated.

7.4.4 Maintain Stability in Cross Wind

Maintaining vehicle lateral stability in cross wind is another test for vehicle dynamics control. The vehicle is running straight at high speed and a strong cross wind is applied, which is analogous to passing by windy mountain gaps along the highway. The desired vehicle longitudinal speed is 120 km/h. CarSim® has a built-in controller for cross wind test with 4WS system, which was used here to compare with the CVDC. To show the effect of the cross wind, another CarSim® built-in 4WS system is used with disabled hand-wheel steering action.

In the upper row of Figure 7.8, the cross wind speed is shown with time. We used a pulse wind with 40 km/h to emulate passing through some gaps along the highway. The second row of Figure 7.8 shows the hand-wheel steering for the three test vehicles. The hand-wheel steering for CVDC and "4WS W/O Steering" are zero all the time,

which means the driver does not put effort to maintain the vehicle lateral motion. The hand-wheel steering of the "4WS W/ Steering" is from the CarSim® built-in controller, which means the driver needs to execute the steering wheel in such a fashion in order to maintain the lateral motion in cross wind.

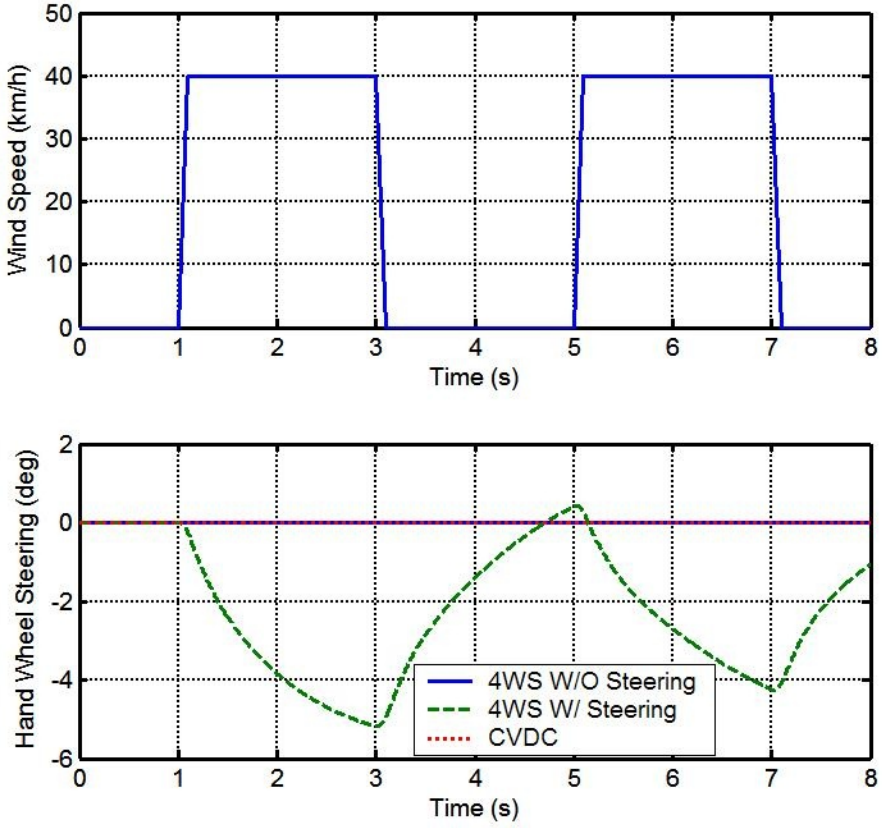

Figure 7.8 Wind speed and the drivers' hand-wheel steering during the test.

The global trajectories and planar motions of the three test vehicles are compared in Figure 7.9. As we can see, without steering the vehicle experiences considerable lateral deviation. The "4WS W/ Steering" and CVDC can maintain the lateral stability while the lateral and yaw deviations of the CVDC are the smallest.

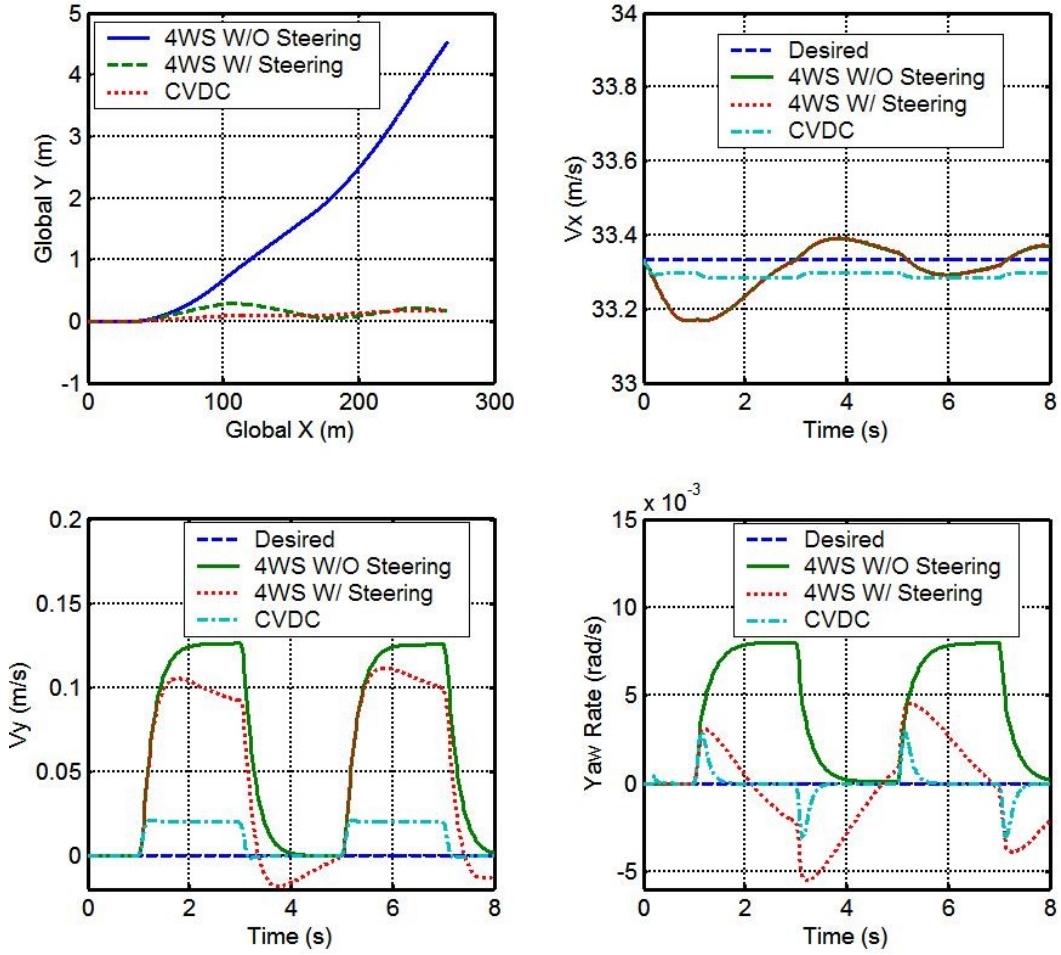

Figure 7.9 Global trajectories and planar motions of the three test vehicles during the cross-wind test scenario.

The planar motion tracking errors of the three vehicles are listed in the table below. It is clear that CVDC demonstrated the best stability performance. It should be noted that CVDC achieved the lateral stability in cross wind without driver's effort while considerable driver's effort is required for the "4WS W/ Steering" system to attain a similar performance. In reality, driver may be panic in this situation and may not be able to conduct the correct steering operation as shown in Figure 7.8, which may results in worsen vehicle behavior.

Table 7.4 Comparisons of the system performance for cross wind scenario

Measures / Systems	V_x (m/s)		V_y (m/s)		Ω_z (rad/s)	
	RMSE	PE	RMSE	PE	RMSE	PE
4WS W/O Steering	0.0573	0.1654	0.0626	0.1262	0.0040	0.0080
4WS W/ Steering	0.0581	0.1654	0.0535	0.1116	0.0021	0.0055
CVDC	0.0421	0.0499	0.0101	0.0211	0.0004	0.0031

7.4.5 Reconfigurable Control

As mentioned in Chapter 4, one of the advantages of using control allocation to resolve the actuation redundancy is that reconfigurable control can be easily achieved. More specifically, a diagonal *actuation status matrix* can be introduced into the control allocation to adjust the corresponding column of each actuation in the control effectiveness matrix as,

$$B_a(\phi, U_{k-1}) = B(\phi, U_{k-1})S, \tag{7.11}$$

where, $S = diag\left(\begin{bmatrix} s_1 & s_2 & \cdots & s_p \end{bmatrix}\right) \in \Re^{p\times p}$ is the diagonal actuation status matrix with $s_i \in [0 \quad 1]$, $i = 1, 2, \cdots, p$ representing the status of each actuation. If an actuation fails, its status can be set as zero, which will automatically turn the corresponding column of $B_a(\phi, U_{k-1})$ to zero. By doing that, the control allocation will not utilize this actuation and meanwhile leverage the control burdens to other remaining ones. In the following two sub-sections, we demonstrate the reconfigurable control enabled by the CA for CVDC for two adverse driving conditions. Comparisons with existing vehicle control systems are used to show the benefits.

7.4.5.1 Hard Braking with an Actuator Failure

This test is for the situation where the braking actuator of the front-right (FR) wheel fails during a hard braking. The vehicle initial speed is 140 km/h and a hard braking command (about -0.5 g) is issued at 0 second. The hand-wheel is kept at rest position, and the driver's intention is to keep traveling straight while decelerating. The FR braking actuator of each test vehicle suddenly fails at 1.0 second, i.e. no braking torque can be applied on the FR wheel. The tire-road friction coefficient is 0.9 for a dry concrete surface. Figure 7.10 shows the global trajectories and planar motions of the three vehicles during the test.

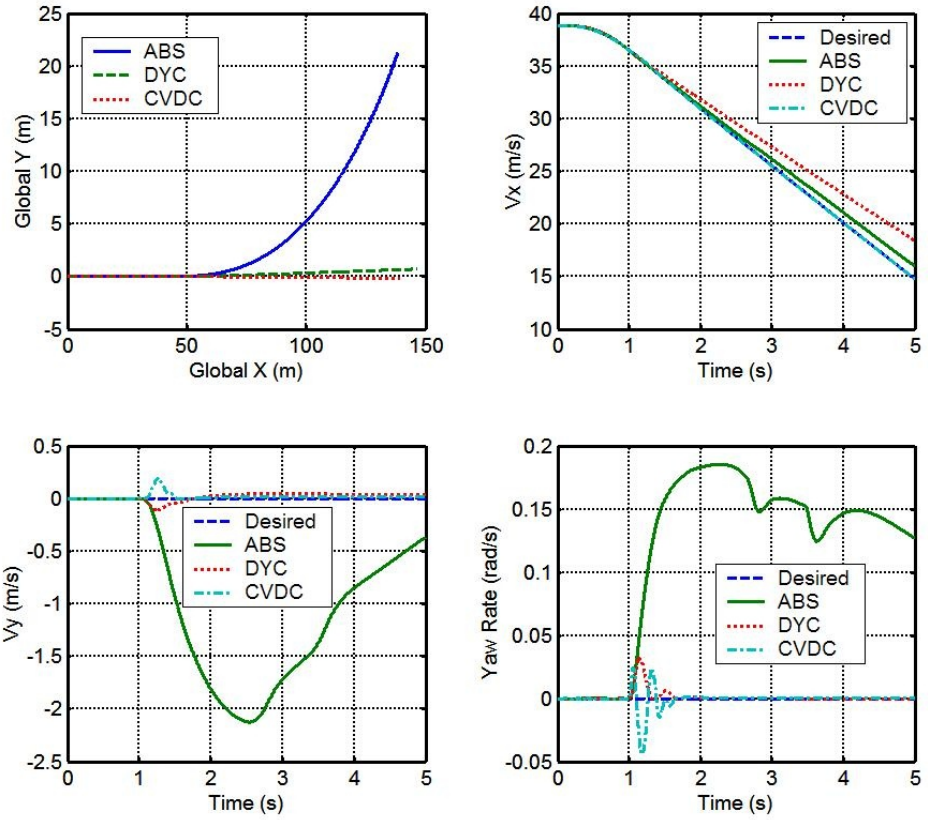

Figure 7.10 Global trajectories and planar motions of the three vehicles at straight line braking with a failed actuator.

Again, the ABS vehicle loses stability due to lack of yaw motion control even though its longitudinal motion is closer to the desired one than that of DYC. DYC behaves better than ABS in terms of lateral and yaw motions. However, we can note that its longitudinal motion was sacrificed and resulted in less deceleration and longer stopping distance (as shown in the first row of Figure 7.10), which may not be desirable in some emergency situations. We can clearly see that the CVDC still exhibits the best performance of the three with the smallest deviation from the track and satisfied longitudinal deceleration. Table 7.5 shows the errors of the three vehicles at this maneuver with a failed FR braking actuator.

Table 7.5 Comparisons of the performance for the three vehicles during the maneuver with an actuator failure.

Measures / Systems	V_x (m/s)		V_y (m/s)		Ω_z (rad/s)	
	RMSE	PE	RMSE	PE	RMSE	PE
ABS	0.4768	1.2143	0.9588	2.1243	0.1184	0.1856
DYC	1.4213	3.6267	0.0319	0.1102	0.0013	0.0319
CVDC	0.0268	0.2710	0.0171	0.1878	0.0021	0.0447

CVDC achieved similar lateral and yaw motion control as the DYC with improved performance on the longitudinal motion.

7.4.5.2 High-Speed Double Lane-Changing with an Actuator Failure

This test is same as the one in sub-section 7.4.2 except that the rear-right (RR) steering actuators of all the test vehicles suddenly fail at 1.0 second, i.e. no steering angle can be exercised on the RR wheel. The desired vehicle longitudinal speed is 120 km/h. We only compare the performances between 4WS and CVDC as the RR wheel of the 2WS vehicle does not steer by nature.

Figure 7.11 shows the global trajectories and planar motions of these two vehicles during the maneuver. Compared with the DLC without actuator failure presented in sub-section 7.4.2, we note that the 4WS exhibit some vehicle trajectory deviation and heading offset due to the lose of RR wheel steering capability while CVDC can maintain on the desired track fairly well.

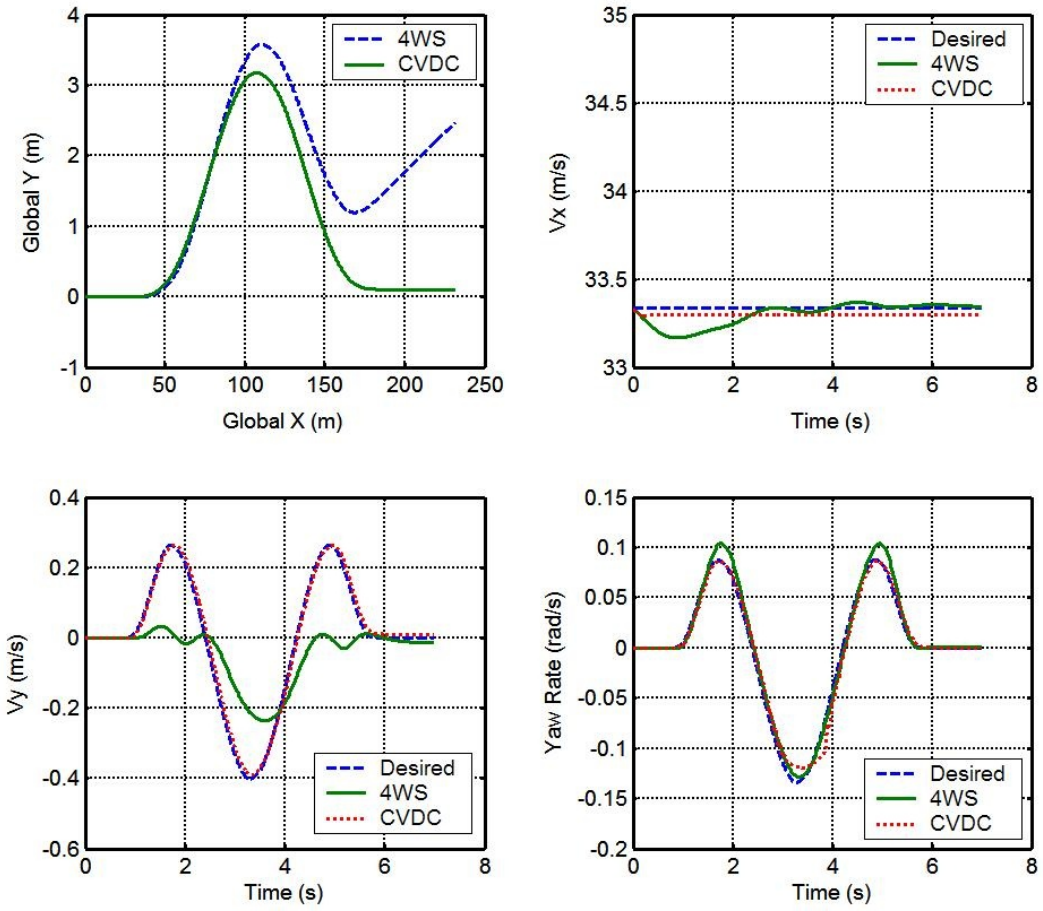

Figure 7.11 Global trajectories and planar motions of the two vehicles at DLC maneuver with a failed actuator

The planar motion tracking errors of the two vehicles are compared in Table 7.6. CVDC's longitudinal and lateral motions control are much better than those of 4WS as

can be seen from Figure 7.11 as well. In terms of yaw motion, 4WS and CVDC exhibit comparable responses.

Table 7.6 Comparisons of the performance for the two vehicles during the maneuver with an actuator failure.

Measures / Systems	V_x (m/s)		V_y (m/s)		Ω_z (rad/s)	
	RMSE	PE	RMSE	PE	RMSE	PE
4WS	0.0482	0.1654	0.0981	0.2670	0.0052	0.0203
CVDC	0.0352	0.0449	0.0113	0.0322	0.0051	0.0306

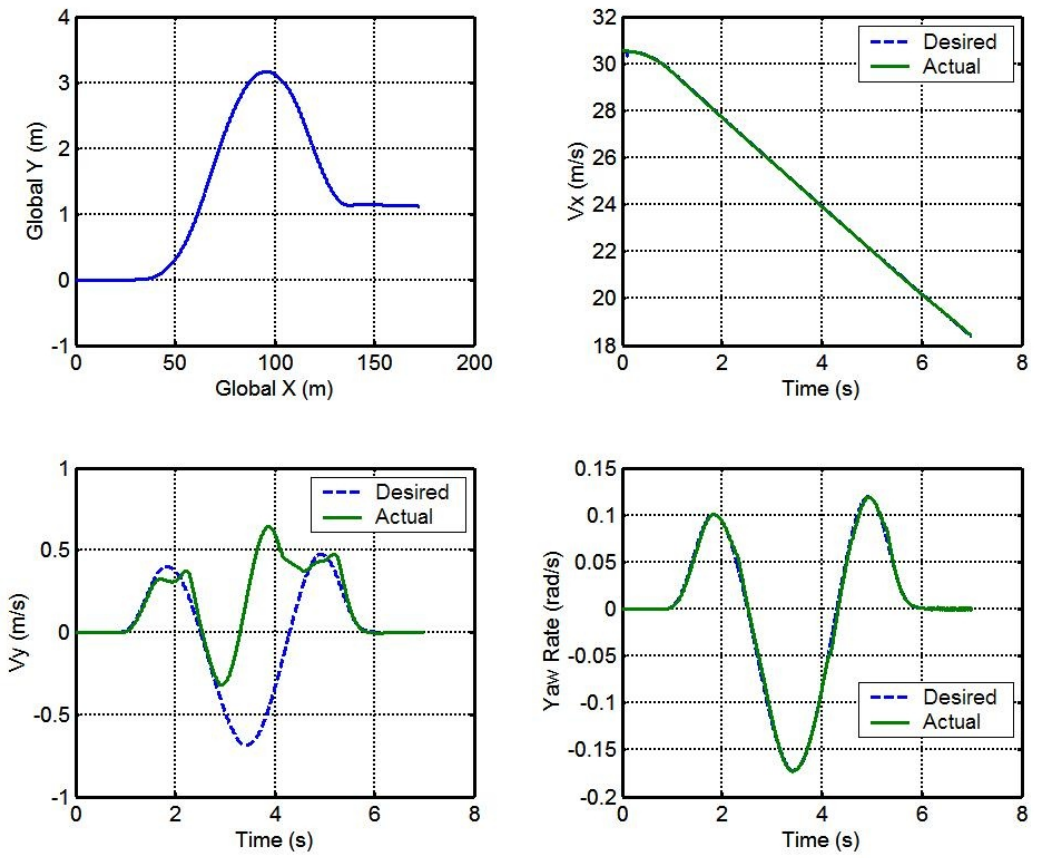

Figure 7.12 Global trajectories and planar motions of the BDLC maneuver with friction as 0.3.

Note that in the above benchmarking test maneuvers, CVDC exibits superior performances compared with different existing vehicle control systems under various adverse driving conditions. However, the operational envelop of CVDC is naturally limited by environmental conditions as well. For instance, it was found that the CVDC could not maintain stability or follow the desired trajectory in testing braking during double lane-changing on a slippery surface (see Section 7.4.3) when tire-road friction coefficient is less than 0.3. Figure 7.12 shows the CVDC vehicle global trajectory and planar motions during this maneuver. Note that even though vehicle longitudinal velocity and yaw rate are met, vehicle lateral velocity demand was not fulfilled, which caused the deviation of the vehicle global trajectory from the desired path.

7.5 SUMMARY

In this chapter, we showed a simple analysis on the overall system stability. Reference models for CVDC are briefly described. Yaw angle control is augmented to the original higher-level yaw control to reduce chattering effect, yaw angle offset and vehicle heading deviation.

The CVDC system performance evaluation is presented by comparing with other existing vehicle control systems under various adverse driving conditions. From the test results, we can draw the following conclusions.

- The proposed CVDC can greatly expand the system operational envelope under adverse driving conditions by coordination of all the tire forces.
- CVDC can greatly reduce driver work load especially under adverse driving condition where otherwise driver has to be much involved and the results may not be desirable depending on driver's control behavior.

- Reconfigurable control can be easily realized by the control allocation utilized in the CVDC. Remarkable performances were still realized even when some actuator fails during adverse maneuvers.

Chapter 8: Conclusions and Future Work

This chapter summarizes this dissertation as well as outlines some directions for future work.

8.1 SUMMARY AND CONCLUSIONS

The goal of this dissertation work is to find a systematic approach to address the control problems for nonlinear constrained redundantly-actuated ground vehicle dynamics control systems. Planar motions (longitudinal, lateral, and yaw) are typically of primary interest for vehicle dynamics control systems. However, there are many actuation sub-systems available on the vehicle and ultimately each tire can produce longitudinal and lateral forces independent of others, which makes VDC a redundantly-actuated system.

The current nonlinear control design methods such as sliding mode control, backstepping, and feedback linearization often require systems to have "square" properties and cannot be directly applied to MIMO systems with constrained and redundant actuation, where the number of actuation is greater than the number of controlled outputs. To resolve this design perplexity, for a class of systems, it is feasible to virtually divide the systems into two parts as shown in (4.1). The system outputs can be controlled by a set of virtual/generalized control efforts, which satisfy the "square" requirement to utilize nonlinear control design methods. These generalized control efforts are then constructed by the actual redundant actuation. For this kind of systems, control allocation techniques can provide attractive solutions to optimally resolve the actuation redundancy subject to their constraints as well as realize reconfigurable control.

Ground vehicle planar motions are determined by the generalized longitudinal force, lateral force, and yaw moment, which are comprised of ground forces from all the

tires. It thus is suitable for control allocation to be exercised for resolving the actuation redundancy.

A SMC-based higher-level controller is designed to specify the generalized forces/moment which make the vehicle planar motion track the desired reference trajectories. An integral action is introduced into the vehicle yaw motion control to effectively reduce the vehicle heading residual caused by yaw rate tracking error.

Among the control allocation approaches, quadratic programming based CA methods are more suitable for systems where both actuation amplitude and rate constraints are present. However, a major burden typically associated with QP-based CA method is the intensive computational effort requirement. Fixed-point CA is a computationally efficient method and could be real-time adaptable. We proposed a modified fixed-point CA which improves the convergence speed when actuation saturation happens.

A vehicle dynamics control allocation scheme has been designed that takes into account vehicle states and tire-road friction coefficient. Instead of tire longitudinal/lateral forces, allocation targets tire slip and slip angle at each tire. This approach converts the nonlinearly coupled constraints to independent linear constraints, which makes the realization possible by greatly reducing the computational complexity and burden. The real-time adaptable, computationally efficient accelerated fixed-point control allocation method is employed for coordinated vehicle dynamics control. Simulation results of the coordinated VDC using the proposed control allocation scheme shows obvious benefits in terms of computational effort.

As tire slips and slip angles are treated as the actuation in this coordinated vehicle dynamics control system, effective tire slip and slip angle tracking control is very crucial. A combined tire slip and slip angle tracking control system is thus developed. The

system is indispensable for advanced coordinated vehicle dynamics control systems where both tire longitudinal and lateral forces need to be simultaneously utilized to achieve desired vehicle motions. A MIMO robust sliding mode control approach is employed for the system while vehicle body states are treated as exogenous signals to isolate and simplify the control design tasks as well as enable actuation coordination. Integral action is introduced in the sliding surface to reduce residual tracking errors caused by continuous approximation of the switching function. The controller manipulates the wheel steering/driving/braking torques to make tire slips and slip angles track the ones dictated by the control allocation algorithm.

Compared with existing vehicle control systems under various adverse driving conditions, the CVDC developed in this dissertation exhibits superior performance in terms of significantly expanding the operational envelope and greatly reducing driver workload.

8.2 FUTURE DIRECTIONS

There are many interesting topics motivated by this dissertation for future research efforts. In the sub-sections followed, we briefly list some of them.

8.2.1 Dynamic Control Allocation

For most of the engineering systems, it is usually reasonable to assume that the dynamics of the actuators are much faster than the dynamics of the system states. Therefore, they can be ignored, which results in the *static* control allocation (SCA). However, for some systems, the actuators are relatively slow and their dynamics may not be ignored. Then control allocation approaches need to take into account the actuator dynamics, which is referred to as *dynamic* control allocation (DCA). As the relationships between generalized control and actuator commands are no longer a mapping function,

they comprise a dynamic system where commanded actuator amplitudes are the system inputs and actual actuator amplitudes are the states. Constrained optimization should also be incorporated in this dynamic allocation scheme. Its complexity is more intense than SCA. However, since the actuator dynamics could be addressed, it is expected that DCA can yield better performance for systems in which slow actuators are involved.

8.2.2 Implementation Related Topics

Some aspects associated with the implementation of the control system developed in this dissertation are also interesting. For example, individual tire slip angle estimation could be an attractive research topic. In this dissertation, we use the measurable longitudinal velocity, lateral velocity, yaw rate of the vehicle C.G. along with geometric parameters to calculate the tire slip angle. However, when considering situations where these signals are contaminated by measurement noise, optimal estimation of the slip angles would become beneficial.

Furthermore, fast and reliable tire-road friction coefficient estimation is very valuable for any vehicle control systems. Uncertainties in the friction coefficient estimation can affect the system performance. Improvement of the friction coefficient estimation technique will be undoubtly beneficial for vehicle dynamics control systems. Application scopes of the vehicle dynamics-based estimation approaches are often limited. Some additional sensing mechanisms may be useful to improve the friction estimations

8.2.3 Extension to other Redundantly Actuated Systems

Besides ground vehicles, there are many other redundantly actuated engineering systems such as aircrafts, marine vessels, and robotic systems. With the continuously increasing computational power, control allocation techniques are being researched more

and more and employed in those systems as well. Since different systems have different characteristics, profound understanding of the systems themselves would be very profitable in deriving attractive solutions.

Bibliography

[Adams et al., 1994] R. J. Adams, J. M. Buffington, and S. S. Banda. Design of Nonlinear Control Laws for High-Angle-of-Attack Flight. Journal of Guidance, Control, and Dynamics, Vol. 17, No. 4, pp. 737 – 746, 1994.

[Akella, 2006] M. R. Akella. ASE 396 Nonlinear Dynamics and Adaptive Control Theory: Class Notes. University of Texas at Austin, 2006.

[Angeli et al., 2000] D. Angeli, E. Mosca, and A. Casavola. Output Predictive Control of Linear Plants with Saturated and Rate Limited Actuators. Proceedings of the 2000 American Control Conference, pp. 272 – 276, 2000.

[Antonelli and Chiaverini, 1998] G. Antonelli and S. Chiaverini. Task-Priority Redundancy Resolution for Underwater Vehicle-Manipulator Systems. Proceedings of the 1998 IEEE International Conference on Robotics & Automation, pp. 768 – 773, 1998.

[Asif and Moura, 2005] A. Asif and J. M. F. Moura. Block Matrices With L-Block-banded Inverse: Inversion Algorithms. IEEE Transactions on Signal Processing, Vol. 53, No. 2, pp. 630 – 642, 2005.

[Bakker et al., 1989] E. Bakker, H. B. Pacejka, and L. Lidner. A New Tire Model with an Application in Vehicle Dynamics Studies. SAE Paper 890087, 1989.

[Bedner and Chen, 2004] E. J. Jr. Bedner and H. H. Chen. A Supervisory Control to Manage Brake and Four-Wheel-Steer Systems. SAE Paper 2004-01-1059, 2004.

[Bemporad et al., 1997] A. Bemporad, A. Casavola, and E. Mosca. Nonlinear Control of Constrained Linear Systems via Predictive Reference Management. IEEE Transactions on Automatic Control, Vol. 42, No. 3, pp. 340 – 349, 1997.

[Bemporad, 1997] A. Bemporad. Control of Constrained Nonlinear Systems via Reference Management. Proceedings of the 1997 American Control Conference, pp. 3343 – 3347, 1997.

[Bevly et al., 2000] D., Bevly, J. Gerdes, C. Wilson, and G. Zhang. The Use of GPS Based Velocity Measurements for Improved Vehicle State Estimation. Proceedings of 2006 the American Control Conference, pp. 2538 – 2542, 2000.

[Bierlaire and Crittin, 2004] M. Bierlaire and F. Crittin. An Efficient Algorithm for Real-Time Estimation and Prediction of Dynamic OD Tables. Operations Research, Vol. 52, No. 1, pp. 116 – 127, 2004.

[Bishop and Spong, 1998] B. E. Bishop and M. W. Spong. Control of Redundant Manipulators Using Logic-Based Switching. Proceedings of the 37th IEEE Conference on Decision and Control, pp. 1488 – 1493, 1998.

[Bodson and Pohlchuk, 1998] M. Bodson and W. A. Pohlchuk. Command Limiting in Reconfigurable Flight Control. Journal of Guidance, Control, and Dynamics, Vol. 21, No. 4, pp. 639 – 646, 1998.

[Bodson, 2002] M. Bodson. Evaluation of Optimization Methods for Control Allocation. Journal of Guidance, Control, and Dynamics, Vol. 25, No. 4, pp. 703 – 711, 2002.

[Bordignon and Durham, 1995] K. A. Bordignon and W. C. Durham. Closed-Form Solutions to Constrained Control Allocation Problem. Journal of Guidance, Control, and Dynamics, Vol. 18, No. 5, pp. 1000 – 1007, 1995.

[Bordignon, 1996] K. A. Bordignon. Constrained Control Allocation for Systems with Redundant Control Effectors. Ph.D. Dissertation, Virginia Polytechnic Institute and State University, 1996.

[Bozdog and Olson, 2005] D. Bozdog and W. W. Olson. An Advanced Shell Theory Based Tire Model. Tire Science and Technology, Vol. 33, No. 4, pp. 227 – 238, 2005.

[Brenna and Alleyne, 2001] S. Brennan and A. Alleyne. Integrated Vehicle Control via Coordinated Steering and Wheel Torque Inputs. Proceedings of the 2001 American Control Conference, pp. 7 – 12, 2001.

[Breuer et al., 1992] B. Breuer, U. Eichhorn, and J. Roth. Measurement of Tyre/Road Friction Ahead of the Car and Inside the Tyre. Proceedings of AVEC (International Symposium on Advanced Vehicle Control), pp. 347 – 353, 1992.

[Buffington and Enns, 1996] J. Buffington and D. Enns. Lyapunov Stability Analysis of Daisy Chain Control Allocation. Journal of Guidance, Control, and Dynamics, Vol. 19, No. 6, pp. 1226 – 1230, 1996.

[Buffington et al., 1999] J. Buffington, P. Chandler, and M. Pachter. On-line System Identification for Aircraft with Distributed Control Effectors. International Journal of Robust and Nonlinear Control, Vol. 9, No. 14, pp. 1033 – 1049, 1999.

[Burken et al., 2001] J. J. Burken, P. Lu, Z. Wu, and C. Bahm. Two Reconfigurable Flight-Control Design Methods: Robust Servomechanism and Control Allocation. Journal of Guidance, Control, and Dynamics, Vol. 24, No. 3, pp. 482 – 493, 2001.

[Cafvert and Svendenius, 2005] M. Gafvert and J. Svendenius. A Novel Semi-Empirical Tyre Model for Combined Slips. Vehicle System Dynamics, Vol. 43, No. 5, pp. 351 – 384, 2005.

[CarSim User Manual, 2003] Mechanical Simulation Corporation. CarSim User Manual, Version 5.11, 2003.

[Cesiel et al., 2006] D. Cesiel, M. C. Gaunt, and B. Daugherty. Development of a Steer-by-Wire System for the General Motors Sequel. SAE Paper 2006-01-1173, 2006.

[Chen and Tomizuka, 2000] C. Chen and M. Tomizuka. Lateral Control of Commercial Heavy Vehicles. Vehicle System Dynamics, Vol. 33, pp. 391 – 420, 2000.

[Cheng and Miu, 1999] C.-C. Cheng and L. Miu. Design of MIMO Integral Variable Structure Controllers. Journal of Franklin Institute, Vol. 336, No. 7, pp. 1119 – 1134, 1999.

[Claeys et al., 2001] X. Claeys, J. Yi, L. Alvarez, R. Horowitz, and C. Canudas de Wit. A New 3D Dynamic Tire/Road Friction Model for Vehicle Control and Simulation. Proceedings of 2001 ASME International Mechanical Engineering Congress and Exposition, pp. 221 – 227, 2001.

[Davidson, Lallman, and Bundick, 2001] J. B. Davidson, F. J. Lallman, and W. T. Bundick. Integrated Reconfigurable Control Allocation. Proceedings of 2001 AIAA Guidance, Navigation, and Control Conference and Exhibit, pp. 1 – 11, AIAA Paper 2001-4083, 2001.

[Deur, Asgari, and Hrovat, 2001] J. Deur, J. Asgari, and D. Hrovat. A Dynamic Tire Friction Model for Combined Longitudinal and Lateral Motion. Proceedings of 2001 ASME International Mechanical Engineering Congress and Exposition, pp. 229 – 236, 2001.

[Doman and Ngo, 2002] D. B. Doman and A. D. Ngo. Dynamic Inversion-Based Adaptive/Reconfigurable Control of the X-33 on Ascent. Journal of Guidance, Control, and Dynamics, Vol. 25, No. 2, pp. 275 – 284, 2002.

[Doman and Oppenheimer, 2002] D. B. Doman and M. W. Oppenheimer. Improving Control Allocation Accuracy for Nonlinear Aircraft Dynamics. Proceedings of AIAA Guidance, Navigation, and Control Conference and Exhibit, pp. 1 – 10, 2002.

[Drakunov et al., 2000] S. V. Drakunov, B. Ashrafi, and A. Rosiglioni. Yaw Control Algorithm via Sliding Mode Control. Proceedings of the 2000 American Control Conference, pp. 580 – 583, 2000.

[Dugoff et al., 1970] H. Dugoff, P. S. Fancher, and L. Segel. An Analysis of Tire Traction Properties and Their Influence on Vehicle Dynamic Performance. SAE Paper 700377, 1970.

[Durham 1993] W. Durham. Constrained Control Allocation. Journal of Guidance, Control, and Dynamics, Vol. 16, No. 4, pp. 717 – 725, 1993.

[Durham 1994a] W. Durham. Constrained Control Allocation: Three Moment Problem. Journal of Guidance, Control, and Dynamics, Vol. 17, No. 2, pp. 330 – 336, 1994.

[Durham 1994b] W. Durham. Attainable Moments for the Constrained Control Allocation Problem. Journal of Guidance, Control, and Dynamics, Vol. 17, No. 6, pp 1371 – 1373, 1994.

[Durham and Bordignon, 1996] W. C. Durham and K. A. Bordignon. Multiple Control Effector Rate Limiting. Journal of Guidance, Control, and Dynamics, Vol. 19, No. 1, pp. 30 – 37, 1996.

[Elbeheiry et al., 2001] E. M. Elbeheiry, Y. F. Zeyada, and M. E. Elaraby. Handling Capabilities of Vehicles in Emergencies Using Coordinated AFS and ARMC Systems. Vehicle System Dynamics, Vol. 35, No. 3, pp. 195 – 215, 2001.

[Enns et al., 1994] D. Enns, D. Bugajski, R. Hendrick, and G. Stein. Dynamic Inversion: An Evolving Methodology for Flight Control Design. International Journal of Control, Vol. 59, No. 1, pp. 71 – 91, 1994.

[Esfandiary and Khalil, 1991] F. Esfandiary and H. K. Khalil. Stability Analysis of a Continuous Implementation of Variable Structure Control. IEEE Transactions on Automatic Control, Vol. 36, No. 5, pp. 616 – 619, 1991.

[ESP-NHTSA] National Highway Traffic Safety Administration (NHTSA), http://www.nhtsa.dot.gov.

[Feng et al., 1998] K. T. Feng, H. S. Tan, and M. Tomizuka. Automatic Steering Control of Vehicle Lateral Motion with the Effect of Roll Dynamics. Proceedings of the 1998 American Control Conference, pp. 2248 – 2252, 1998.

[Fernandez and Hedrick, 1987] B. R. Fernandez and K. J. Hedrick. Control of Multivariable Nonlinear Systems by the Sliding Mode Method. International Journal of Control, Vol. 46, No. 3, pp. 1019 – 1040, 1987.

[Fletcher, 2000] R. Fletcher. Practical Methods of Optimization. John Wiley & Sons, Second edition, 2000.

[Fredriksson et al., 2004] J. Fredriksson, J., Andreasson, and L. Laine. Wheel Force Distribution for Improved Handling in a Hybrid Electric Vehicle Using Nonlinear Control. Proceedings of 43rd IEEE Conference on Decision and Control, pp. 4081 – 4086.

[Furukawa and Abe, 1997] Y. Furukawa and M. Abe. Advanced Chassis Control Systems for Vehicle Handling and Active Safety. Vehicle System Dynamics, Vol. 28, pp. 59 – 86, 1997.

[Gilbert et al., 1995] E. G. Gilbert and I. Kolmanovsky. Discrete-Time Reference Governors for Systems with State and Control Constraints and Disturbance Inputs. Proceedings of the 34th IEEE Conference on Decision and Control, pp. 1189 – 1194, 1995.

[Golub and Van Loan, 1996] G. H. Golub and C. F. Van Loan. Matrix Computations. John Hopkins University Press, 3rd edition, 1996.

[Granas and Dugundji, 2003] A. Granas and J. Dugundji. Fixed Point Theory. Springer-Verlag, New York, 2003.

[Gustaffson, 1997] F. Gustaffson. Slip-based Tire-Road Friction Estimation. Automatica, Vol. 33, No. 6, pp. 1087 – 1099.

[Guvenc et al., 2003] B. A. Guvenc, T. Acarman, and L. Guvenc. Coordination of Steering and Individual Wheel Braking Actuated Vehicle Yaw Stability Control. Proceedings of IEEE Intelligent Vehicle Symposium, pp. 288 – 293, 2003.

[Hac et al., 2006] A. Hac, D. Doman, and M. Oppenheimer. Unified Control of Brake- and Steer-by-Wire Systems Using Optimal Control Allocation Methods. SAE Paper 2006-01-0924.

[Halanay et al., 1994] A. Halanay, A. Ionita, and V. Rasvan. Stability and Maneuverability Analysis of Vehicle with Four Wheel Steering System. Proceedings of the Third IEEE Conference on Control Applications, pp. 385 – 390, 1994.

[Hallowell and Ray, 2003] S. J. Hallowell and L. R. Ray. All-Wheel Driving Using Independent Torque Control of Each Wheel. Proceedings of the 2003 American Control Conference, pp. 2590 – 2595, 2003.

[Hammett 1999] C. R. Hammett. Ultra-Reliable Real-Time Control System – Future Trends. IEEE Aerospace and Electronic Systems Magazine, Vol. 14, No. 8, pp. 31 – 36, 1999.

[Harkegard and Glad, 2005] O. Harkegard and S. T. Glad. Resolving Actuator Redundancy – Optimal Control vs. Control Allocation. Automatica, Vol. 41, pp. 137 – 144, 2005.

[Harkegard, 2002] O. Harkegard. Efficient Active Set Algorithms for Solving Constrained Least Squares Problems in Aircraft Control Allocation. Proceedings of the 41st IEEE Conference on Decision and Control, pp. 1295 – 1300, 2002.

[Hayama et al., 2000] R. Hayama, K. Nishizaki, S. Nakano, and K. Katou. The Vehicle Stability Control Responsibility Improvement Using Steer-by-Wire. Proceedings of the 2000 IEEE Intelligent Vehicle Symposium, pp. 596 – 601.

[Hebden et al., 2004] R. G. Hebden, C. Edwards, and S. K. Spurgeon. Automotive Steering Control in a Split-u Maneuver Using an Observer-Based Sliding Mode Control. Vehicle System Dynamics, Vol. 41, No. 3, pp. 181 – 202, 2004.

[Heinzl et al., 2002] P. Heinzl, P. Lugner, and M. Plochl. Stability Control of a Passenger Car by Combined Additional Steering and Unilateral Braking. Vehicle System Dynamics Supplement, Vol. 37, pp. 221 – 233.

[Hille and Phillips, 1957] E. Hille and R. S. Phillips. Functional Analysis and Semigroups. American Mathematical Society, Providence, 1957.

[Hisaoka et al., 1999] Y. Hisaoka, M. Yamamoto, and A. Okada. Closed-Loop Analysis of Vehicle Behavior During Braking in a Turn. JSAE Review, Vol. 20, pp. 537 – 542, 1999.

[Horiuchi et al., 1999] S. horiuchi, K. Okada, and S. Nohtomi. Improvement of Vehicle Handling by Nonlinear Integrated Control of Four Wheel Steering and Four Wheel Torque. JSAE Review, Vol. 20, pp. 459 – 464, 1999.

[Horn and Johnson, 1988] R. A. Horn and C. R. Johnson. Matrix Analysis. Cambridge University Press, 1988.

[Ikenaga et al., 2000] S. Ikenaga, F. L. Lewis, J. Campos, and L. Davis. Active Suspension Control of Ground Vehicle Based on a Full-Vehicle Model. Proceedings of the 2000 American Control Conference, pp. 4019 – 4024, 2000.

[Istratescu, 1981] V. I. Istratescu. Fixed Point Theory, An Introduction. D. Reidel, Holland, 1981.

[Johansen et al., 2003] T. A. Johansen, I. Petersen, J. Kalkkuhl, and J. Ludemann. Gain-Scheduled Wheel Slip Control in Automotive Brake Systems. IEEE Transactions on Control System technology, Vol. 11, No. 6, pp. 799 – 811, 2003.

[Kageyama and Jo, 1997] I. Kageyama and H. Y. Jo. An Advanced Vehicle Control Method Using Independent Four-Wheel-Steering System. Proceedings of the 1997 IEEE Conference on Intelligent Transportation System, pp. 954 – 959, 1997.

[Li, 2002] P. Y. Li. ME8281 Advanced Control Systems: Class Notes. University of Minnesota, 2002.

[Lin et al., 2004] M. Lin, A. A. Popov, and S. McWilliam. Stability and Performance Studies of Driver-Vehicle Systems with Electronic Chassis Control. Vehicle System Dynamics Supplement, Vol. 41, pp. 477 – 486, 2004.

[Liu et al., 2002] C. S. Liu, v. Monkaba, H. Tan, C. McKenzie, H. Lee, and S. Suo. Driveline Torque-Bias-Management Modeling for Vehicle Stability Control. SAE Paper 2002-01-1584, 2002.

[Lu, 1996] P. Lu. Constrained Tracking Control of Nonlinear Systems. Systems & Control Letters, Vol. 27, pp. 305 – 314, 1996.

[Luo and Serrani et al., 2004] Y. Luo, A. Serrani, S. Yurkovich, D. B. Doman, and M. W. Oppenheimer. Model Predictive Dynamic Control Allocation with Actuator Dynamics. Proceedings of the 2004 American Control Conference, pp. 1695 – 1700.

[Mammar and Koenig, 2002] S. Mammar and D. Koenig. Vehicle Handling Improvement by Active Steering. Vehicle System Dynamics, Vol. 38, No. 3, pp. 211 – 242, 2002.

[Mantz et al., 1999] R. J. Mantz, P. F. Puleston, and H. De Battista. Output Overshoots in Systems with Integral Action Operating in Sliding Mode. Automatica, Vol. 35, No. 6, pp. 1141 – 1147, 1999.

[Mercer and Mercer, 2000] A. M. Mercer and P. R. Mercer. Cauchy's Interlace Theorem and Lower Bounds for The Spectral Radius. Internat. J. Math. & Math. Sci., Vol. 23, No. 8, pp. 563 – 566, 2000.

[Mokhiamar and Abe, 2002] O. Mokhiamar and M. Abe. Effects of Model Response on Model Following Type of Combined Lateral force and Yaw Moment Control Performance for Active Vehicle Handling Safety. JSAE Review, Vol. 23, pp. 473 – 480, 2002.

[Mokhiamar and Abe, 2005] O. Mokhiamar and M. Abe. Experimental Verification Using a Driving Simulator of the Effect of Simultaneous Optimal Distribution of Tyre Forces for Active Vehicle Handling Control. Proceedings of Institution of Mechanical Engineers, Part D: Journal of Automobile Engineering, Vol. 219, pp. 135 – 149, 2005.

[Monteiro and Zhou, 1997] R. Monteiro and F. Zhou. On Superlinear Convergence of Infeasible Interior Point Algorithms for Linearly Constrained Convex Programs. Comput. Optimiz. Applicat., Vol. 8, pp. 245 – 262, 1997.

[Nagai et al., 2002] M. Nagai, M. Shino, and F. Gao. Study on Integrated Control of Active Front Steer angle and Direct Yaw Moment. JSAE Review, Vol. 23, pp. 309 – 315, 2002.

[Nguyen and Jabbari, 2000] T. Nguyen and F. Jabbari. Output Feedback Controllers for Disturbance Attenuation with Actuator Amplitude and Rate Saturation. Automatica, Vol. 36, pp. 1339 – 1346, 2000.

[Niu and Tomizuka, 2001] W. Niu and M. Tomizuka. A New Approach of Coordinated Motion Control Subject to Actuator Saturation. ASME Journal of Dynamic Systems, Measurement, and Control, Vol. 123, pp. 496 – 504, 2001.

[Nocedal and Wright, 1999] J. Nocedal and S. J. Wright. Numerical Optimization. Springer, 1999.

[Oh et al., 2004] S. W. Oh, H. C. Chae, S. C. Yun, and C. S. Han. The design of a Controller for the Steer-by-Wire System. JSME International Journal, Series C, Vol. 47, No. 3, pp. 896 – 907, 2004.

[Oosten and Bakker, 1993] J. J. M. van Oosten and E. Bakker. Determination of Magic Tyre Model Parameters. Vehicle System Dynamics, Vol. 21 No. SUPPL, Tyre Models for Vehicle Dynamics Analysis, pp. 19 – 29, 1993.

[Pacejka and Bakker, 1993] H. B. Pacejka and E. Bakker. Magic Formula Tyre Model. Vehicle System Dynamics, Vol. 21, No. Suppl: Tyre Models for Vehicle Dynamics Analysis, pp. 1 – 18, 1993.

[Page and Steinberg, 2000] A. B. Page and M. L. Steinberg. A Closed-Loop Comparison of Control Allocation Methods. Proceedings of AIAA Guidance, Navigation, and Control Conference and Exhibit, pp. 1 – 11, 2000.

[Pasterkamp and Pacejka, 1994] W. R. Pasterkamp and H. B. Pacejka. On-line Estimation of Tyre Characteristics for Vehicle Control. Proceedings of AVEC'94, International Symposium on Advanced Vehicle Control, pp. 521 – 526, 1994.

[Pasterkamp and Pacejka, 1997] W. R. Pasterkamp and H. B. Pacejka. The Tyre as a Sensor to Estimate Friction. Vehicle System Dynamics, Vol. 27, pp. 409 – 422, 1997.

[Patil et al., 2003] C. B. Patil, R. G. Longoria, and J. Limroth. Control Prototyping for an Anti-Lock Braking Control System on a Scaled Vehicle. Proceedings of the 42nd IEEE Conference on Decision and Control, pp. 4962 – 4967, 2003.

[Petersen and Bodson, 2002] J. A. M. Peterson and M. Bodson. Fast Implementation of Direct Allocation with Extension to Coplanar Controls. Journal of Guidance, Control, and Dynamics, Vol. 25, No. 3, pp. 464 – 473, 2002.

[Petersen and Bodson, 2005] J. Petersen and M. Bodson. Interior Point Algorithms for Control Allocation. Journal of Guidance, Control, and Dynamics, Vol. 28, No. 3, pp. 471 – 480, 2005.

[Petersen and Bodson, 2006] J. A. M. Peterson and M. Bodson. Constrained Quadratic Programming Techniques for Control Allocation. IEEE Transactions on Control Systems Technology, Vol. 14, No. 1, pp. 91 – 98, 2006.

[Plumlee, Bevly, and Hodel, 2004] J. H. Plumlee, D. M. Bevly, and A. S. Hodel. Control of a Ground Vehicle Using Quadratic Programming Based Control Allocation Techniques. Proceedings of the 2004 American Control Conference, pp. 4704 – 4709, 2004.

[Poonamallee and Yurkovich et al., 2004] V. L. Poonamallee, S. Yurkovich, A. Serrani, D. B. Doman, and M. W. Oppenheimer. A Nonlinear Programming Approach for Control Allocation. Proceedings of the 2004 American Control Conference, pp. 1689 – 1694, 2004.

[Potra and Wright, 2000] F. Potra and S. Wright. Interior-Point Methods. Journal of Computational and Applied Mathematics, Vol. 124, pp. 281 – 302, 2000.

[SAE J670e] Vehicle Dynamics Terminology. SAE J670e, Society of Automotive Engineers, 1978.

[Sastry and Bodson, 1989] S. S. Sastry and M. Bodson. Adaptive Control: Stability, Convergence, and Robustness. Prentice-Hall, 1989.

[Seshagiri and Khalil, 2002] S. Seshagiri and H. K. Khalil. On Introducing Integral Action in Sliding Mode Control. Proceedings of the 41st IEEE Conference on Decision and Control, pp. 1473 – 1478, 2002.

[Shibahata et al., 1993] Y. Shibahata, K. Shimada, and T. Tomari. Improvement of Vehicle Maneuverability by Direct Yaw Moment Control. Vehicle System Dynamics, Vol. 22, No. 5, pp. 465 – 481, 1993.

[Shifrin 2006] B. M. Shifrin. An Analytic Model of a Rolling Pneumatic Tire. International Applied Mechanics, Vol. 42, No. 4, pp. 479 – 485, 2006.

[Shim and Margolis, 2001] T. Shim and D. Margolis. Using μ Feedforward for Vehicle Stability Enhancement. Vehicle System Dynamics, Vol. 35, No. 2, pp. 103 – 119, 2001.

[Shimada and Shibahata, 1994] K. Shimada and Y. Shibahata. Comparison of Three Active Chassis Control Methods for Stabilizing Yaw Moments. SAE Paper 940870, 1994.

[Slotine and Li, 1991] J.-J. E. Slotine and W. Li. Applied Nonlinear Control. Prentice Hall, 1991.

[Solyom and Rantzer, 2003] S. Solyom and A. Rantzer. ABS Control – A Design Model and Control Structure. Nonlinear and Hybrid Systems in Automotive Control, R. Johansson and A. Rantzer, Eds. London: Springer-Verlag, pp. 85 – 96, 2003.

[Sussmann et al., 1994] H. J. Sussmann, E. D. Sontag, and Y. Yang. A General Result on the Stabilization of Linear Systems Using Bounded Controls. IEEE Transactions on Automatic Control, Vol. 39, pp. 2411 – 2424, 1994.

[Taheri and Law, 1990] S. Taheri and H. E. Law. Investigation of a Combined Slip Control Braking and Closed Loop Four Wheel Steering System for an Automobile During Combined Hard Braking and Severe Steering. Proceedings of the 1990 American Control Conference, pp. 1862 – 1867, 1990.

[Tondel and Johansen, 2005] P. Tondel and T. A. Johansen. Control Allocation for Yaw Stabilization in Automotive Vehicles using Multiparametric Nonlinear Programming. Proceedings of the 2005 American Control Conference, pp. 453 – 458, 2005.

[Tsiotras et al., 2004] P. Tsiotras, E. Velenis, and M. Sorine. A LuGre Tire Friction Model with Exact Aggregate Dynamics. Vehicle System Dynamics, Vol. 42, No. 3, pp. 195 – 210, 2004.

[Utkin, 1992] V. I. Utkin. Sliding Modes in Control Optimization. Springer-Verlag, Berlin, pp. 111 – 130, 1992.

[Venkataraman and Waldron] S. C. Venkataraman and K. J. Waldron. Performance Improvement with Active Control of Steering angles and Wheel Torques During a Combined Braking and Steering Maneuver. ASME Dynamic Systems and Control Division, V 52, Advanced Automotive Technologies, pp. 39 – 48, 1993.

[Virnig and Bodden, 1994] J. Virnig and D. Bodden. Multivariable Control Allocation and Control Law Conditioning When Control Effectors Limit. AIAA Paper 94-3609, 1994.

[Wallsgrove and Akella, 2005] R. J. Wallsgrove and M. R. Akella. Globally Stabilizing Saturated Attitude Control in the Presence of Bounded Unknown Disturbances. Journal of Guidance, Control, and Dynamics, Vol. 28, No. 5, pp. 957 – 963, 2005.

[Wang and Longoria, 2006a] J. Wang and R. G. Longoria. Coordinated Vehicle Dynamics Control with Control Distribution. Proceedings of the 2006 American Control Conference, pp. 5348 – 5353, 2006.

[Wang and Longoria, 2006b] J. Wang and R. G. Longoria. Combined Tire Slip and Slip Angle Tracking Control for Advanced Vehicle Dynamics Control Systems. Proceedings of the 45th IEEE Conference on Decision and Control, pp. 1733-1738, 2006.

[Wang and Longoria, 2006c] J. Wang and R. G. Longoria. Effect of Computational Delay on the Performance of a Hybrid Adaptive Cruise Control System. SAE Transactions: Journal of Passenger Cars – Electronic & Electrical Systems, Vol, 115, 2007.

[Wang et al., 2004] J. Wang, L. Alexander, and R. Rajamani. Friction Estimation on Highway Vehicles Using Longitudinal Measurements. Journal of Dynamic Systems, Measurement, and Control, Vol. 126, Issue 2, pp. 265 – 275, 2004.

[Wang et al., 2007] J. Wang, J. Solis, and R. G. Longoria. On the Control Allocation for Coordinated Ground Vehicle Dynamics Control Systems. Proceedings of the 2007 American Control Conference (to appear), 2007.

[Wong, 2001] J. Y. Wong. Theory of Ground Vehicles. 3rd edition, John Wiley & Sons, New York, 2001.

[Wright 1997] S. Wright. Primal-Dual Interior-Point Methods. SIAM, 1997.

[Yih et al., 2004] P. Yih, J. Ryu, and J. C. Gerdes. Vehicle State Estimation Using Steering Torque. Proceedings of the 2004 American Control Conference, pp. 2116 – 2121.

[Yu and Moskwa, 1994] S. H. Yu and J. J. Moskwa. A Global Approach to Vehicle Control: Coordination of Four Wheel Steering and Wheel Torques. Journal of Dynamic Systems, Measurement, and Control, Vol. 116, pp. 659 – 667, 1994.

[Zanten, 2000] A. T. V. Zanten. Bosch ESP Systems: 5 Years of Experience. SAE Paper 2000-01-1633, 2000.

[Zhang 1996] Y. Zhang. Solving Large-Scale Linear Programs by Interior-Point Methods under the MATLAB Environment. Technical Report TR96-01, Department of Mathematics and Statistics, University of Maryland, Baltimore, 1996.

[Zhang et al., 2003] Y. Zhang, J. H. Chung, and S. A. Velinsky. Variable Structure Control of a Differentially Steered Wheeled Mobile Robot. Journal of Intelligent and Robotic Systems: Theory and Applications, Vol. 36, No. 3, pp. 301 – 314, 2003.

Vita

Junmin Wang was born in Shanxi, China in 1974. He received Bachelor of Engineering in Automotive Engineering and M.S. degree in Power Machinery and Engineering from Tsinghua University (Beijing, China) in 1997 and 2000, respectively.

He then entered The University of Minnesota, Twin Cities (UMN) as a Ph.D. student/Research Assistant in fall 2000. In fall 2002, he decided to quit his Ph.D. program and start commercial work. He graduated with two M.S. degrees from both Electrical Engineering and Mechanical Engineering at UMN in spring 2003. Upon graduation from UMN, he started working as a full-time Engineer at Southwest Research Institute (SwRI) where he is a Senior Research Engineer now.

In fall 2004, Junmin resumed his Ph.D. program at The University of Texas at Austin while maintaining full-time position/responsibility at SwRI. His research interests are dynamic systems and control in general.

This dissertation was typed by the author.